École doctorale ENGSYS-632 : Sciences de l'Ingénierie et des Systèmes

Doctorat IEMN Lille
THÈSE

pour obtenir le grade de docteur délivré par
l'Université de Lille
Spécialité doctorale « Micro-nanosystèmes et capteurs »

présentée et soutenue publiquement par
Saher H. Barsoum
Le 2 Février 2024

Hybrid Surface and Bulk Acoustic Waves Resonators

Résonateurs hybrides à ondes acoustiques de surface et de volume

Jury:

M. Olivier BOU MATAR	Professeur, École Centrale de Lille	Président du Jury
M. Guillermo VILLANUEVA	Professeur, Ecole Polytechnique Fédérale de Lausanne	Rapporteur
M. Emmanuel LE CLEZIO	Professeur, Université De Montpellier	Rapporteur
Mme. Claire PRADA	Directrice de Recherche, Institut Langevin	Examinatrice
Mme. Marie BOUSQUET	Ingénieure-Chercheuse, CEA-LETI	Invitée
M. Thierry LAROCHE	R&D Manager, Soitec Besançon	Invité
M. Alexandre REINHARDT	Ingénieur-Chercheur, CEA-LETI (Co-encadrant de thèse)	Examinateur
M. Bertrand DUBUS	Directeur de Recherche, IEMN	Directeur de thèse

IEMN UMR 8520, Villeneuve d'Ascq,
JUNIA-ISEN, 41 Boulevard Vauban, 59800 Lille

Résumé

Le concept des résonateurs hybrides SAW/BAW (HSB) a été introduit en 2013. Il se base sur un arrangement périodique de transducteurs piézoélectriques sur un substrat, combinant les avantages des dispositifs à ondes de volume et des dispositifs à ondes de surface. Une étude initiale portant sur l'AlN a permis d'optimiser deux modes de résonance et a été confirmés par deux cycles de fabrication atteignant respectivement des coefficients de couplage électromécanique de 1.6% et 1,8% à environ 600 MHz et 1.8 GHz. Ces résultats mettent en évidence des facteurs de qualité élevés, allant jusqu'à 3700 à la résonance et 3300 à l'antirésonance pour le premier mode à 600 MHz, et jusqu'à 1900 à la résonance et 1700 à l'antirésonance pour le second mode à 2,8 GHz.

Afin d'améliorer ces coefficients de couplage électromécanique, nous avons évalué l'utilisation de matériaux piézoélectriques tels que le AlScN et le niobate de lithium (LNO). Une étude théorique a été réalisée, montrant la possibilité d'atteindre un coefficient de couplage électromécanique de 38% à 500 MHz et de 14% à 1,5 GHz pour le LNO. De nouveaux procédés de fabrication sont introduits, et des résultats préliminaires sont présentés. Enfin, nous avons mis en évidence l'existence d'un nouveau mode qui peut atteindre, sous certaines conditions spécifiques, des fréquences supérieures à 4 GHz avec des coefficients de couplage électromécaniques de 7% pour l'AlN et 16% pour le LNO.

Synopsis

The concept of hybrid SAW/BAW (HSB) resonators was introduced in 2013. It is based on a periodic arrangement of piezoelectric transducers on a substrate, combining the advantages of bulk- and surface-wave devices. An initial study on AlN optimized two resonance modes and were confirmed by two manufacturing cycles to achieve electromechanical coupling coefficients of 1.6% and 1.8% respectively at around 600 MHz and 1.8 GHz. These results demonstrated quality factors up to 3700 at resonance and 3300 at anti-resonance for the first mode at 600 MHz, and up to 1900 at resonance and 1700 at anti-resonance for the second mode at 2.8 GHz.

In order to improve the electromechanical coupling, we have investigated other piezoelectric materials such as scandium-doped AlN and lithium niobate (LNO). A theoretical analysis have shown that an electromechanical coupling coefficient of 38% at 500 MHz and 14% at 1.5 GHz can be attained with LNO. A new manufacturing process is introduced, and preliminary results are presented. Finally, we demonstrate the existence of a new mode that can reach frequencies above 4 GHz with electromechanical coupling coefficients of 7% for AlN and 16% for LNO, under certain specific conditions.

I am dedicating this Ph.D. to my most
beloved late aunt, Eman Wahib Barsoum (1957-2021).

Your words of encouragement still fill
my heart with tears, your prayers
sustain me when my strength wanes,
and your memory reminds me who
I am when I lose all sense of direction.
You remain with me today.

Acknowledgements

General Introduction

The RF front-end module serves as a critical gateway in modern telecommunication systems, acting as the interface between the antenna and the digital baseband processing components. It plays a pivotal role in the efficient transmission and reception of wireless signals. As the demand for faster data rates and increased connectivity continues to surge, the importance of RF filters, a key element within the RF front-end module, cannot be overstated. These filters are tasked with selectively passing certain frequency bands while attenuating unwanted interference, ensuring the integrity of wireless communications.

In the past three decades, the landscape of RF filters has witnessed a transformative shift with the introduction of Surface Acoustic Wave (SAW) and Bulk Acoustic Wave (BAW) technologies. These innovations have revolutionized the field of resonator technologies, enhancing the performance and versatility of RF filters. SAW and BAW devices were introduced as a response to the escalating demand for higher frequencies, increased miniaturization, and improved overall filter performance. By harnessing the unique properties of acoustic waves on piezoelectric materials, SAW and BAW technologies have added a new dimension to resonator-based devices, enabling engineers to achieve unprecedented levels of selectivity, miniaturization, and bandwidth control in RF filters. This evolution has not only paved the way for more compact and powerful wireless devices but has also opened new frontiers in telecommunications and beyond.

Surface Acoustic Wave (SAW) resonators have undergone significant advancements in recent years, driven by the need for enhanced performance in various applications. One notable progress involves the development of novel SAW resonator structures and the utilization of advanced materials. Engineers and researchers have explored complex designs such as interdigitated transducers (IDTs) with varying electrode geometries and multi-layered structures to achieve improved frequency responses and reduced insertion loss. These innovations have not only expanded the operational frequency range of SAW devices, now up to 2.5 GHz, with prospects towards 4 GHz, but have also allowed for the creation of highly sensitive sensors and precise frequency control components. However, SAW resonators still face certain limitations. The miniaturization of SAW devices, although achieved to a great extent, presents fabrication challenges, particularly as feature sizes reach nanoscale dimensions.

Bulk Acoustic Wave (BAW) resonators traditionally exploit the thickness vibration of thin films of aluminum nitride (AlN), or more recently scandium-doped AlN (AlScN). These materials exhibit excellent piezoelectric properties, enabling BAW devices to achieve low loss, critical for applications like RF filtering at frequencies beyond 2.5 GHz. The utilization of novel fabrication techniques has allowed for precise control over BAW resonator dimensions, resulting in improved frequency stability and miniaturization.

Despite their remarkable progress, BAW resonators are not without challenges. Fabrication complexity increases as the operating frequency rises, making it challenging to achieve the desired performance at higher frequencies (above 5 GHz). To address these challenges, researchers continue to explore new materials and manufacturing techniques to further improve BAW resonators' performance.

Hybrid Surface Acoustic Wave-Bulk Acoustic Wave (SAW/BAW) Resonators (HSBR) represent an emerging class of acoustic devices that attempts to merge the advantages of both SAW and BAW

technologies. These resonators leverage the surface-confined nature of SAW and the high frequency capabilities of BAW, offering a unique blend of miniaturization, high-Q factors, and photolithographic tunability. Their development was proposed to open up exciting possibilities as they combine the strengths of each technology to address the increasingly complex demands of modern electronics.

Despite their theoretical promising attributes, challenges to explore these structure exist in the design and fabrication of HSB resonators. These include the need for complex manufacturing processes, precise control over materials, and the potential for increased device complexity compared to conventional SAW or BAW resonators.

The primary aim of this thesis is to thoroughly explore the practical capabilities of hybrid SAW/BAW devices and assess their true potential in comparison to established SAW and BAW technologies. Given the initial suboptimal results reported in the existing literature, a critical need arose to establish a robust fabrication process for these structures. This process serves a dual purpose: firstly, to enable the initial assessment of resonator performance, and secondly, to unveil any technological limitations. Once these limitations are identified, they can be incorporated into theoretical models, helping to define the design parameters for hybrid SAW/BAW resonators within the bounds of physical feasibility.

This research was conducted as part of a collaborative effort involving frec|n|sys (now Soitec Besançon), CEA-LETI, and IEMN. Members of frec|n|sys were among the pioneers in the exploration of hybrid SAW/BAW structures. CEA-LETI contributed its extensive knowledge and clean-room expertise in developing acoustic devices based on piezoelectric thin films, initially using AlN and later expanding to AlScN or LiNbO$_3$. This expansion was made possible through the development of Piezoelectric-On-Insulator substrates, a joint endeavor between CEA and Soitec. IEMN played a crucial role in deepening the understanding of the physics behind periodic piezoelectric structures and the mechanisms governing the hybridization of surface and bulk modes, employing advanced simulation methods.

In Chapter 1, we provide a comprehensive introduction to the concept of hybrid SAW/BAW resonators. We delve into the expectations associated with these structures and explore early attempts to implement them.

Chapter 2 centers on the establishment of a periodic finite element model tailored for simulating AlN hybrid SAW/BAW resonators while considering technological limitations. This model is employed to examine how resonator metrics, such as frequency and electromechanical coupling factor, depend on the transducer geometry as well as the substrate and electrode materials. This analysis aims to define the attainable frequency ranges and electromechanical coupling factors for these devices.

Moving on to Chapter 3, we shift our focus to the experimental realization of AlN hybrid SAW/BAW resonators. We detail the developed process flow and outline the electrical characterization methodology. The performance of various resonator designs is presented and compared against the theoretical expectations outlined in Chapter 2.

Chapter 4 investigates the enhancement of electromechanical coupling factors in hybrid SAW/BAW resonators through the utilization of lithium niobate thin films as opposed to AlN. We

discuss the necessary adjustments to the periodic finite element model to account for new wave polarizations induced in lithium niobate transducers. Furthermore, we examine the crystal orientation dependence of various modes and optimize resonators for the most promising crystal cuts. This chapter concludes with a preliminary process flow for implementing lithium niobate hybrid SAW/BAW resonators and provides initial trial results.

Finally, Chapter 5 focuses on the frequency scaling of hybrid SAW/BAW resonators. We particularly explore a novel mode resulting from the hybridization of bulk modes in thin film transducers with surface modes of the substrate when transducers are excited in phase. This investigation considers the performance dependence on transducer geometry using both AlN and lithium niobate piezoelectric films.

A final conclusion is added to highlight the main results of this thesis and to discuss future prospects. Further theoretical and manufacturing investigations of similar structures would be possible beyond this work either by changing key geometrical features or changing the piezoelectric material of the transducer.

Chapter 1: Introduction to HSBR

This chapter is made up of two parts; the first part describes RF acoustic filters and how they make up the largest portion of the RF-front end market. We then provide an introduction to piezoelectricity followed by an introduction to the physics of Surface Acoustic Waves (SAW) and Bulk Acoustic Waves (BAW) and how they are utilized to build resonators. The description of these phenomena and physics allow us to define the performance indices for a resonator especially the electromechanical coupling factor (k^2). We are then able to provide a summary of the state of the art of available SAW and BAW resonators.

We then present the basic concept of HSBR. We highlight how the idea of etched pillars was first presented and the expectations from it. We discuss different design parameters and show how they were explored theoretically in the literature to increase performance including the aspect ratio, reflective layers, and the use of reflectors for the addition of acoustic cavity. The discussion is extended to cover different materials such as AlN, AlScN, ZnO and LiNO$_3$.

We finally discuss the attempts to physically fabricate HSBR and discuss the different process flow charts followed by different research groups. These attempts can be grouped based on the piezoelectric material used starting with AlN and AlScN and then based on lithium niobate or grouped based on the research group and their distinct process flow.

1   Context

1.1   RF front-end module and RF filters

The telecommunications industry has witnessed an unprecedented surge in demand for wireless communication in recent times, driven by the ever-increasing data traffic. This rapid growth has brought forth the need for advanced technologies to support higher data rates and ensure seamless connectivity. As a result, the industry has turned its attention towards the development of the fifth generation of wireless communication (5G) and beyond.

The electromagnetic spectrum encompasses various bands, each designated for specific applications such as WiFi, military communication, cellular communication, consumer radio, and other applications. These bands consist of smaller sub-bands known as channels and are standardized to be adhered to by wireless communication system users. The RF front-end module is a vital component that enables the transmission and reception of wireless signals, ensuring the seamless integration of smartphones, tablets, and other wireless devices into the telecommunications infrastructure. As the frequency spectrum dedicated to mobile communication becomes overcrowded, there are more requirements on the RF Front-End devices and in particular on filtering technologies.

A sample of a front-end module is presented in Figure 1. Input signal received by the antenna carries various frequencies. A band selection filter is then used to isolate the desired frequency band from the received signals. The selected signal is then amplified to boost its strength. Next, an oscillator generates a local oscillation signal that is mixed with the amplified signal. The mixer produces intermediate frequencies, which are then passed through a channel filter to further isolate the specific frequency channel of interest. Finally, the treated signal is ready for further processing and utilization in the wireless communication system.
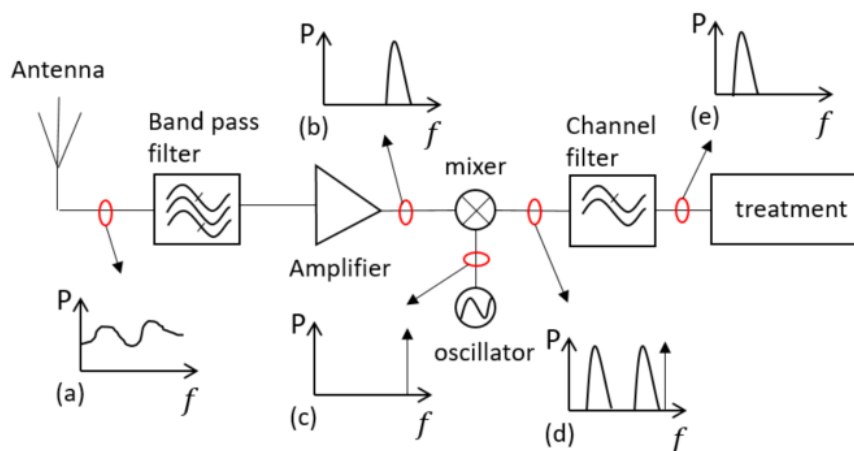
Figure 1: description of a Front-end module (redrawn adapted from [1])

RF filters serve as the backbone of RF front-end modules, providing the essential function of isolating and filtering different frequency bands. RF filters selectively pass or reject specific frequency bands as demonstrated in Figure 2. Band-pass filters allow signals within a certain frequency range to pass through while attenuating frequencies outside this range. High-pass filters, on the other hand, permit frequencies above a certain threshold, blocking lower frequencies. Conversely, low-pass filters pass signals below a specified frequency while attenuating higher frequencies. Lastly, band-reject filters, also known as notch filters, reject a specific frequency range while allowing all other frequencies to pass through unaffected.
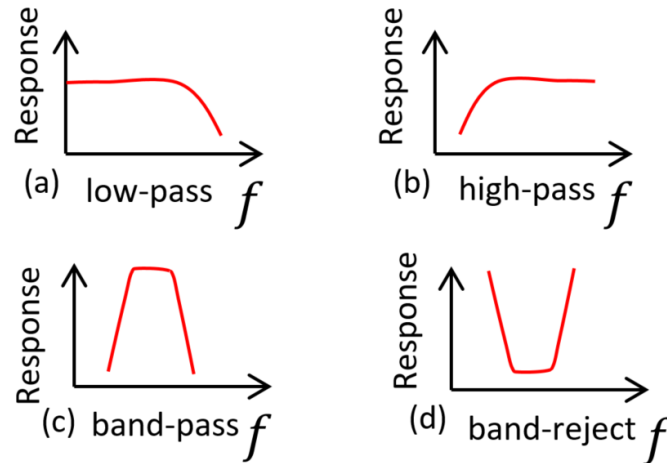
Figure 2: Basic RF filter types

Several challenges facing RF filter technologies are listed below and highlighted in Figure 3.

1- Center frequency range demands: RF filters are designed to operate within specific frequency ranges. This parameter is crucial as it defines the applications and environments in which the filter can be employed. **Challenge**: The ever-increasing demand for higher data rates and the proliferation of wireless devices require RF filters operating on bands spread from 600 MHz to currently near 6 GHz. Designing filters that can operate efficiently in the sub-6 GHz range while maintaining low losses and a high selectivity (see below) is a significant challenge.

2- Insertion loss is a measure of the reduction in signal power that occurs when a signal passes through a device or component, such as an RF filter, as shown in Figure 3. **Challenge:** Lower insertion loss is desirable, as it indicates that the filter efficiently transmits the desired signal without significant power loss. In contrast, higher insertion loss can degrade signal quality and limit the effective range of RF communication systems.

3- Bandwidth and Selectivity: Bandwidth refers to the range of frequencies over which an RF filter allows signals to pass with minimal attenuation or loss. Selectivity measures an RF filter's ability to discriminate between desired signals within its passband and unwanted signals outside its passband. **Challenge:** RF filters need to provide sufficient bandwidth to accommodate the desired frequency range, while also offering excellent selectivity to reject unwanted signals. This is particularly challenging because a wider bandwidth often leads to reduced selectivity, and vice versa. The ability of the filter to reject unwanted frequencies outside its passband is crucial to avoid interference from neighboring frequency bands or other sources of electromagnetic interference. High out-of-band rejection is vital for maintaining the signal integrity and preventing interference.

4- Miniaturization refers to the reduction of the component size being integrated to the circuit. **Challenge:** With the trend towards smaller and more compact electronic devices, RF filters need to be miniaturized without sacrificing their performance. Achieving high performance in a small form factor is a complex engineering challenge.
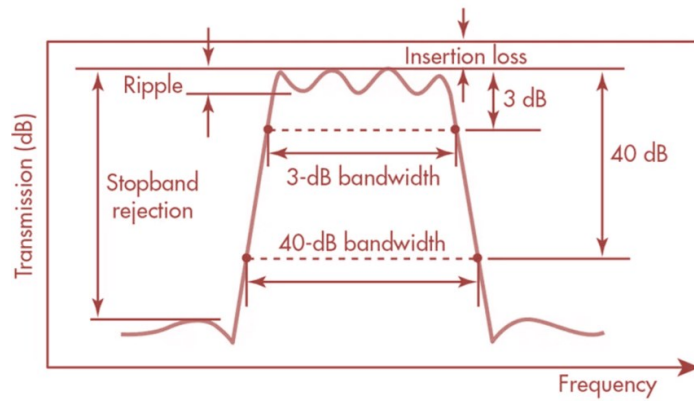
Figure 3: typical filter response highlighting the meaning of insertion loss, bandwidth and stopband rejection [2].

Other challenges include temperature stability, production cost and integration in the RF module. Overcoming these challenges is essential for advancing RF filter technologies. Various filtering technologies with distinct characteristics, including operating frequencies, bandwidths, power handling, and insertion losses, can be employed. These technologies encompass Multi-Layered Ceramic (MLC), Integrated Passive Devices (IPD), Surface Acoustic Wave (SAW) filters (standard SAW, Temperature-Compensated SAW, and Multi-Layer SAW), and Bulk Acoustic Wave (BAW) filters (Film Bulk Acoustic Resonator and Solidly Mounted Resonator).
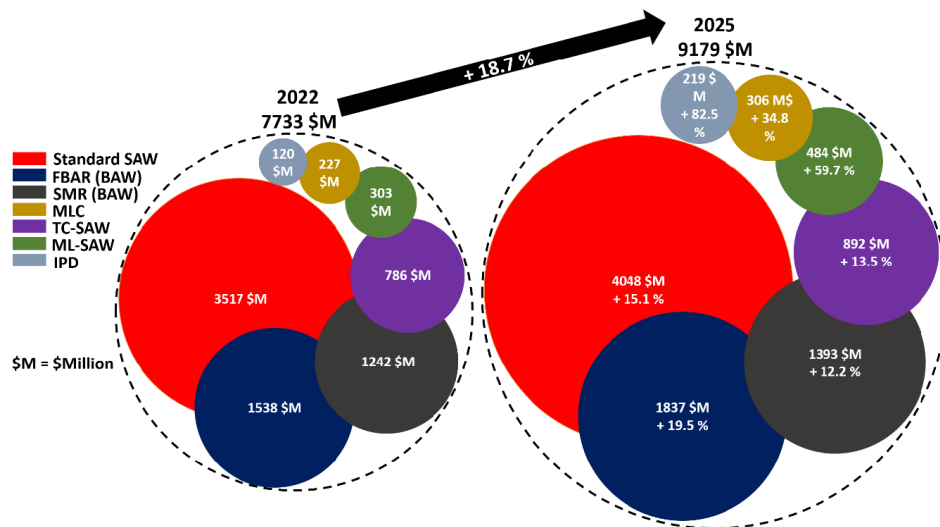
Figure 4: RF Filter Market value Forecast. For each year, the area circle is proportional to the market value [3].

The respective market portion of each of these technologies and their market volume forecast by 2025, based on data from Yole group [3], is depicted in Figure 4. SAW and BAW devices appear as the most important components in the RF filters market, representing more than a half of the market value. In 2022, standard SAW devices captured 45% of the value while BAW technologies (FBAR and SMR) captured 36% of the value. In 2025, the market value is expected to grow around 19%, with standard SAW filters likely still dominating the market but BAW technology growing at a faster pace The new requirements induced by the development of new wireless communication standards should lead to a higher growth of BAW technologies since it is currently the only viable acoustic approach able to operate at high frequency (today up to 5 GHz). BAW devices unfortunately have their own limitations including higher cost, and complex fabrication.

1.2   Acoustic wave filters

In the past three decades, SAW and BAW technologies have been continuously capable of producing filters with satisfying performances to follow the evolution of RF Front Ends [4]. Resonators play a crucial role in the design and construction of RF filters. They are devices designed to exhibit an electrical resonance at a specific frequency. Even though there are various other types of resonators such as mechanical, electrical, optical and magnetic resonators, acoustic resonators dominate the RF filter technologies. These resonators are composed of piezoelectric materials, such as AlN or lithium niobate. Discussions on the meaning of piezoelectricity and some major piezoelectric materials are added to Appendix A

The electric admittance of a single acoustic resonator response is plotted as a function of frequency in Figure 5(a). The base line of the admittance is a capacitive contribution $Y = jC_0\omega$, where C_0 is the static capacitance of the resonator. The resonator displays a resonance frequency f_r and antiresonance frequency f_a, at which the admittance becomes respectively very large or very small.

In ladder circuits, such as the one shown Figure 5(b), one exploits these large admittance variations to reorganize the electric signal flow as a function of frequency. The series components S01 and S02 have the same resonance and antiresonance frequencies $f_m^{(S)}$ and $f_n^{(S)}$ identified by the green curve in Figure 5(c). The parallel components P01 and P02 have the same resonance and antiresonance frequencies $f_m^{(P)}$ and $f_n^{(P)}$ identified by the blue curve in Figure 5(c). The resonators are selected in order to have $f_m^{(S)} \approx f_n^{(P)}$. As a result of this assembly, filters can be constructed with characteristic bandwidths (red curve) that depend on these resonance and anti-resonance frequencies. S_{21} (red line) is the s transmission parameter (T) between input and output. It is expressed in decibel (dB).
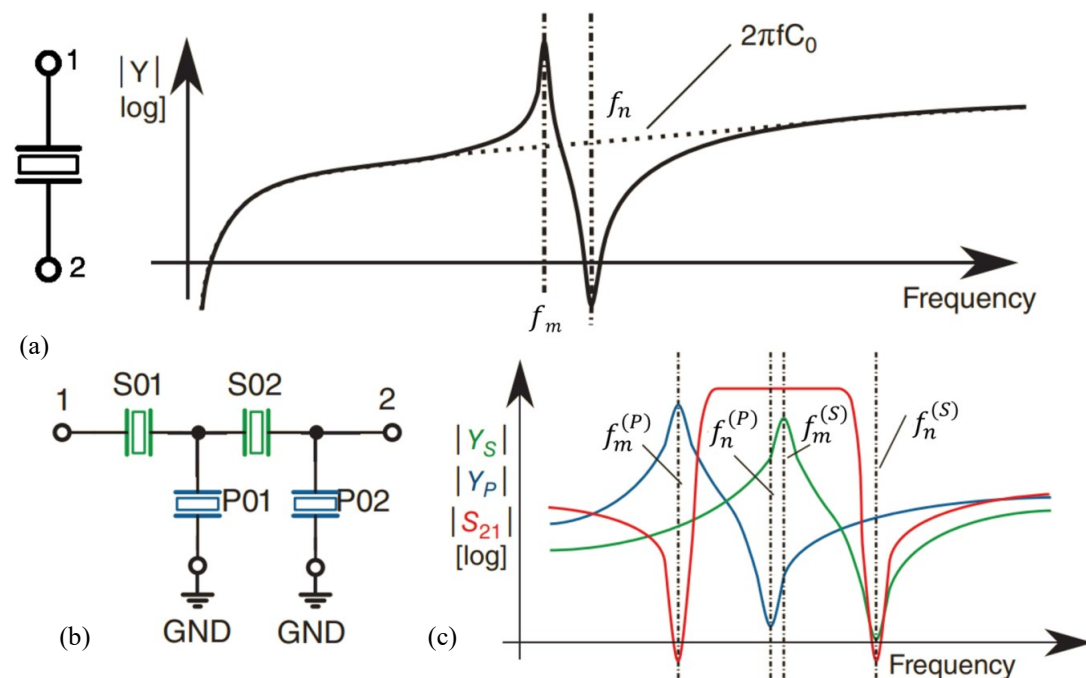
Figure 5: principle of a filter using an acoustic resonator as an impedance element. Typical admittance response of a resonator (a), ladder type filter circuit (b) and typical filter response showing the contributions of the parallel and series resonators (c).

As a consequence, when designing a resonator, we are primarily interested in its resonance and antiresonance frequencies, since they define the center frequency and bandwidth of the filter.

Electromechanical coupling

The electromechanical coupling factor (k²) is a key parameter that characterizes the efficiency with which a piezoelectric material can convert electrical energy to mechanical energy and vice versa. In the context of RF resonators, the electromechanical coupling factor is defined as the ratio of the power converted from electrical to mechanical form during one oscillation period over the sum of the energy stored inside the resonator in mechanical and electrical form [5]. It is expressed as a dimensionless quantity between 0 and 1. k^2 translates in practice into the strength of the electrical resonance of an acoustic resonator, and affects therefore the insertion loss and bandwidth of a filter made of such resonators [6]–[8].

Its expression depends on the type of resonance mode (thickness or width resonance of a plate, resonance of a disk or a rod, etc.) and does therefore differ according to the technology. In specific cases, such as BAW resonators with infinitely thin electrodes, for instance, it can be expressed in terms of material properties when the acoustic wave propagates along the thickness of the piezoelectric layer (longitudinal mode). Piezoelectric thin films have a small thickness relative to their lateral dimensions, which makes their expression simpler [9]. In practice, it is more common to define the electromechanical coupling factor k_t^2 in terms of the resonance and anti-resonance frequencies [8]

$$k_t^2 = \frac{\pi}{2} \frac{f_p}{f_s} \tan\left(\frac{\pi}{2} \frac{f_s - f_p}{f_s}\right),$$ (1)

where f_s is the series resonance frequency (the frequency at which the conductance of the resonator is maximum) and f_p the parallel resonance frequency (the frequency at which the resistance is maximum) [10]. It is common to assume that the difference between f_s and f_p is small, enabling to approximate this expression to

$$k_t^2 \approx \frac{\pi^2}{4} \frac{f_p}{f_s} \frac{(f_s - f_p)}{f_s} \approx \frac{\pi^2}{4} \frac{(f_p - f_s)}{f_p}.$$ (2)

The later expression is customary for BAW resonators. In the general case, one calculates the *effective coupling factor* [10]

$$k_{eff}^2 = \frac{f_p^2 - f_s^2}{f_p^2}.$$

Quality factor and FOM

The quality factor (Q) is another performance index to consider for piezoelectric resonators. It is a measure of the damping or energy loss in the resonator. It is defined as the ratio of the energy stored in the resonator to the energy dissipated per cycle of oscillation [11].

$$Q = 2\pi \frac{E_{stored}}{E_{lost}}.$$ (3)

The higher the quality factor, the lower the energy loss per cycle and the more efficient the resonator. As a consequence, it impacts directly the insertion loss of a filter, as visible in Figure 6, which shows the attenuation characteristics for an acoustic filter for four different values of resonator Q.
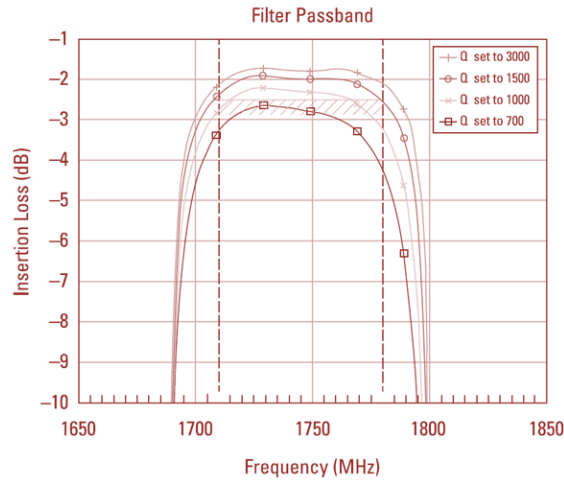
Figure 6: Attenuation characteristics of an acoustic RF filter with different resonator Q factors [12].

Quality factors (Q factors) of resonators can be evaluated using different methods, with two common approaches being the full width at half maximum (FWHM) and phase measurements [13], [14].

The full width at half maximum method involves measuring the width of the resonance peak at half of its maximum amplitude. A narrower resonance peak indicates a higher Q factor, signifying a more precise and selective resonance at the resonant frequency. This method is widely used for quick and practical Q factor estimations in various resonator systems.

$$Q_s = \frac{f_s}{FWHM_{resonance}} . \tag{4}$$

Another approach, proposed by Lakin *et al.* [15] involves analyzing the phase response of the resonator admittance:

$$Q_s = \frac{f_s}{2} * \left| \frac{d}{df} (\varphi(\mathrm{Y})) \right|_{f=f_s} . \tag{5}$$

The same is repeated to calculate Q_p at f_p. These methods can be used depending on the available data and their accuracy will depend on the resolution of the measurement.

The Figure of Merit (FOM) is a criterion to compare different devices that might be using different mechanisms or designs. The IEEE Standard on Piezoelectricity suggests [10]:

$$M = \frac{Q k_{eff}^2}{1 - k_{eff}^2} . \tag{6}$$

For filtering applications, we are often interested in the maximum and minimum admittances reached by a resonator. This is calculated from the impedance ratio:

$$Z_{ratio} = \frac{Z_{max}}{Z_{min}} = \frac{Y_{max}}{Y_{min}} = Q_s Q_p k_{eff}^4 . \tag{7}$$

For this reason, one often consider the square root of the impedance ratio as the figure of merit:

$$FOM = k_{eff}^2 \sqrt{Q_s Q_p} . \tag{8}$$

1.3   Acoustic Waves Resonators

In elastic wave components, electromagnetic waves are replaced by elastic waves to achieve the same function. Piezoelectric materials are the most popular solution for these devices. Due to the relative slowness of elastic waves (a few km/s) compared to electromagnetic waves (some 100 km/s), structures such as waveguides or resonant cavities can be considerably miniaturized. As a result, resonators operating in the GHz range can be produced with micrometric dimensions using manufacturing techniques inherited from microelectronics. This makes them the elements of choice for miniaturized radio frequency systems.

An acoustic wave is a vibrational perturbation which propagates through time and space in a material carrying along its travel mechanical energy that can be transformed into electrical energy through the piezoelectric effect. There are two types of plane acoustic waves (Figure 7): longitudinal and transverse waves. The longitudinal waves or the compressive mode waves travel and carry energy in the same direction as the direction of its media oscillation. The transverse waves or the shear waves exhibit displacements in an orthogonal direction with respect to the propagation direction [7]. Most waves are combinations of longitudinal and transverse waves. In piezoelectric media, the strains associated with these waves induce a polarization of the material, which in turns results in an electric field which propagates along the wave.
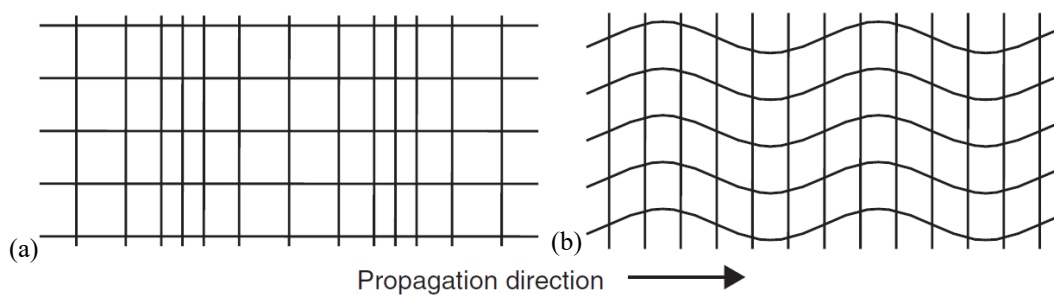
Figure 7: Displacement of a rectangular grind during propagation of bulk acoustic waves. Longitudinal wave (a) and transverse (shear) wave (b).

Surface Acoustic Waves Resonators

There are various types of Surface acoustic waves [1]. The most classic type was first discovered by Rayleigh back in 1885, and is depicted in Figure 8 (a). The displacement of these waves is elliptical. They result from the coupling of a longitudinal wave and a quasi-transverse wave with vertical polarization due to the stress-free boundary condition on the surface [16]. These waves are trapped on the surface, travel parallel to it and decay exponentially within depth [17]. SAWs are commonly used in electronic devices for filtering, sensing, and signal processing applications.
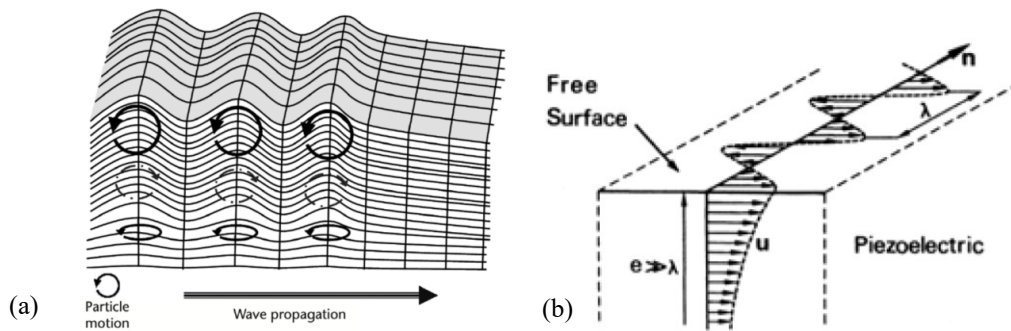
Figure 8 Rayleigh wave propagation: The displacement of these waves is elliptical (a) [7] Displacement for shear-horizontal surface acoustic waves [18] (b)

Another type is the Shear horizontal surface acoustic waves (SH-SAW) depicted in Figure 8 (b). These waves are transverse waves polarized horizontally with respect to the surface. When an electric field is applied to the surface of a piezoelectric material, the SH-SAW is generated by the coupling of an elastic shear wave with the electric field [19]. The displacement of the SH-SAW is mostly transverse horizontal, and the energy is confined to the surface of the substrate material.

In 1965, the invention of the Inter-Digital Transducer (IDT) by White and Voltmar [20] made Rayleigh surface acoustic waves popular as SAW resonators were used for a wide diverse range of sensors and filters. SAW devices are primarily made of a set of interdigitated metallic electrodes deposited on the surface of a piezoelectric material, as shown in Figure 9.
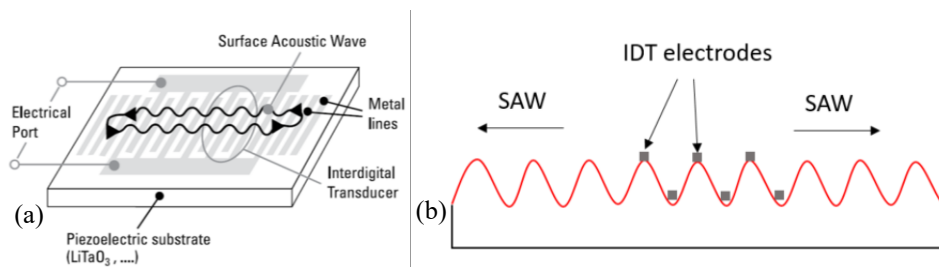
Figure 9: Typical SAW devices with IDT electrodes [12] (a) and operational schematic of SAW resonator with IDT on top (b).

The operation of SAW resonators can be divided into three main stages [21]:

1- Generation: An external electrical signal is applied to one of the IDTs. The alternating voltage creates an electric field that induces mechanical deformation in the piezoelectric material. This mechanical deformation generates surface acoustic waves that propagate along the surface of the substrate.

2- Propagation: The surface acoustic waves propagate along the surface of the piezoelectric substrate, carrying the mechanical vibrations induced by the IDTs. These waves travel at a specific velocity, which depends on the material properties of the substrate and the frequency of the applied signal.

3- Detection: The second IDT, located at a certain distance from the first one, acts as a receiver (in case of a delay-line). When the surface acoustic waves reach this IDT, they induce a voltage in the metal electrodes. This voltage signal corresponds to the mechanical vibrations of the waves and is detected as an electrical output. SAW devices can also either by standing waves or delay lines devices.

SAW devices are either one-port or two-ports devices. In a one-port configuration the drive or excited and sensing or emitted surface waves go through the same IDT. In a two-port device these waves are uncoupled and processed by two different IDTs [21].

Different special types of surface acoustic waves arise in resonators with metal electrodes IDT on top. Surface Transverse Waves (STW) arise from the slowing down of a bulk wave propagating near the surface (Surface Skimming Bulk Wave, SSBW) [22]. Love waves are another type of transverse wave that propagate along the surface of a substrate. Their displacement is purely horizontal and perpendicular to the direction of propagation. Love waves are guided by the substrate and are sensitive to the properties of the substrate [23]. The different types of surface acoustic waves have different properties and are used for different applications. For example, Rayleigh waves are commonly used in surface acoustic wave devices for filtering and sensing applications, while Love waves are used for sensing applications that require high sensitivity.

The fabrication process of SAW devices typically starts with the deposition of thin films of piezoelectric and conductive materials on a substrate, which is often made of quartz, lithium tantalate or lithium niobate. The next step is photolithography, where a patterned photoresist mask is created on top of the thin films to define the desired shape of the IDT. This mask is then used in the etching process, where the unwanted metal is removed, leaving behind the desired IDT pattern. After etching, additional layers may be added, such as the passivation layer, to protect the resonator from environmental factors [24], [25].

SAW devices exhibit excellent performance, small size and low cost since they are fabricated on wafers in large volumes, but are traditionally limited to applications up to 2 GHz. Beyond that frequency, the width and spacing of the interdigitated electrodes become sub-micron, which increases the complexity of fabrication, raises concerns regarding yield, losses and power handling and degrades filter performance. In addition, fabrication problems may arise due to the very thin and delicate IDT electrode pattern. Nevertheless, SAW devices currently lead the market share of electric acoustic components.

Bulk Acoustic Wave Resonators

Bulk acoustic waves (BAW) can be excited by an alternating electrical signal applied perpendicularly to opposite surfaces of a piezoelectric layer. The acoustic wave propagates through the entire thickness of the material, giving rise to a stationary wave at specific frequencies [26], [27]. Depending on the crystalline orientation of the material, BAW can be generated in different modes of propagation. One mode is the thickness-extension mode (Figure 10 (a)), in which the piezoelectric material can expand and contract perpendicularly to the surface. The wave polarization is longitudinal, as the mechanical displacement is parallel to the propagation direction. Another mode is the thickness-shear mode (Figure 10 (b)), in which the piezoelectric material deforms in a direction parallel to the surface.
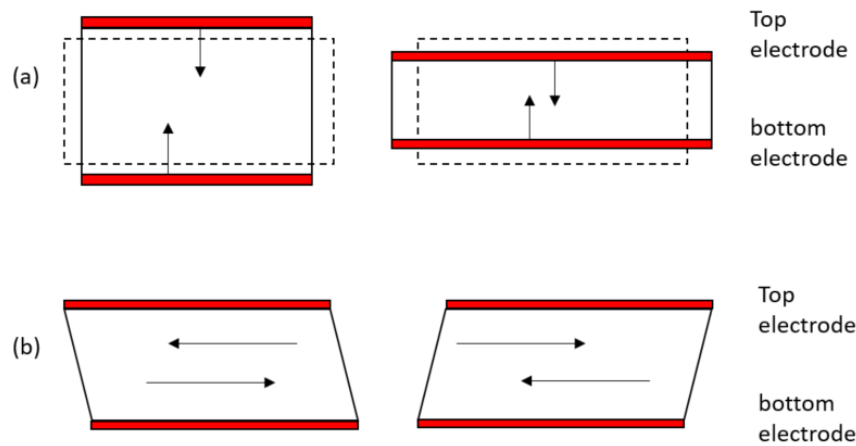
Figure 10: thickness-extensional mode (a) and thickness-shear mode (b) of a BAW device

The limitations of SAW devices have motivated the research for BAW components operating at high frequency above (2 GHz). At higher frequencies, BAW devices, which take the form of a piezoelectric thin film sandwiched between two planar electrodes, are preferred for their traditionally higher quality factors (exceeding Q= 1500) and larger power handling capabilities compared to conventional SAW devices [28], [29].
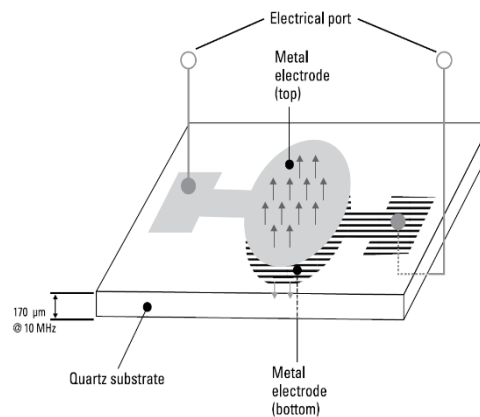
Figure 11: A typical BAW device made up of a piezoelectric material sandwiched between two electrodes [12].

To reach such high quality factors in this structure, waves need to be kept from escaping beyond the bottom electrode through one of two methods conventionally: film bulk acoustic wave resonators (FBARs) and solidly mounted resonators (SMRs). SMR utilize a Bragg reflector to trap the acoustic wave, preferably with stacked thin-film layers featuring alternating low and high acoustic impedances [30]. The layers usually have thicknesses equal to a quarter of the wave wavelength. Two to four alternations are usually enough to achieve a reflection coefficient of 99%. This technology is considered superior to FBARs in terms of power handling and mechanical durability since it is less fragile to handle than the membrane technology. However, the drawback of SMRs is an increase in the number of fabrication process steps that need precise control over film thickness and properties [31], [32].

The second method which relies on the creation of air cavity under the bottom electrode is known as Film Bulk Acoustic Resonator (FBAR). The cavity can be created through the etching of the back side of the substrate or through the use of a sacrificial layer that is later removed before the end of the process forming a gap under the active area. This configuration allows the air/electrode interface

to trap more acoustic waves between the electrodes compared to the Bragg quarter-wavelength acoustic mirror in SMRs, resulting in improved effective electromechanical coupling (k_{eff}^2). Additionally, FBAR provides slightly higher Q (quality factor) than SMR due to the absence of additional reflector layers that could attenuate or escape the acoustic wave [33]–[35].
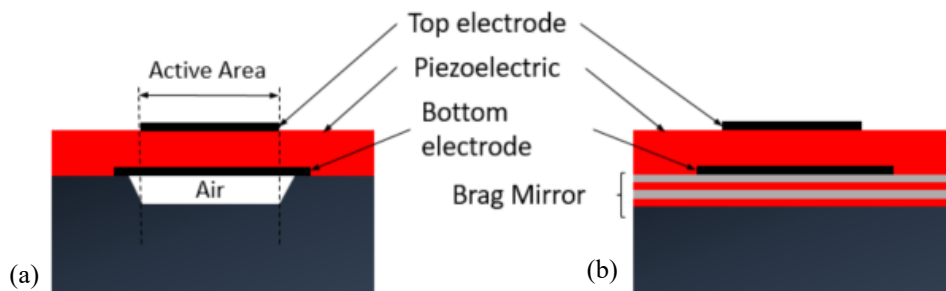
Figure 12: structure of the film bulk acoustic resonator (FBAR) formed over an air gap (a) and solidly mounted resonator (SMR) formed over a Bragg reflection layer (b).

Recent trends for SAW and BAW devices

According to the Microwave Journal [36], there are multiple major competitors in the world of RF filters. For BAW, Qorvo and Qualcomm are the biggest manufacturer of SMR, while Avago, muRata and SKYWORKS dominate the FBAR market. At low frequencies, SAW filter technologies are well established and manufacturers include smaller companies like WiSOL, Sawnics, Shoulder and Kyocera. Other note-worthy commercial technologies include Incredibly High Performance (I.H.P) SAW devices which operate at the range of 2.5 GHz with good performance and the single crystal (AlN and AlScN) BAW devices otherwise called XBAW which are exclusively manufactured by Akoustis. I.H.P SAW devices can trap the leaky SAW by using a Bragg mirror, and achieve a higher quality factor and coupling factor of SAW resonators [37] while XBAW is a single crystal BAW resonator suspended on an air cavity and is optimized to address frequencies in the sub-6 GHz range [38] .

In the past decade, research on thin film Lithium Niobate (LNO)-based components [39]–[44] has gained significant momentum due to its exceptional properties, such as its large electromechanical coupling coefficient. Additionally, the performance of resonators and filters can be efficiently tailored by varying the direction of wave propagation due to the material's strong anisotropy and different stiffness, coupling factor, temperature dependency, etc. along different crystal orientations and cuts [45]. $LiNO_3$ has been used to increase the coupling in FBAR devices based on their longitudinal waves. Gorisse *et al.* [46] were the very first ones to publish on LNO FBARs to be followed by others later [47], [48].

Aside from the I.H.P. SAW devices mentioned above, the possibility to bond single crystal lithium niobate or lithium tantalate layers on high velocity substrates offers possibilities to exploit guided waves. For example, Zhang *et al.* [49] demonstrated the feasibility of the SH_0-mode of $LiNbO_3$ mounted on SiC substrate.

$LiNbO_3$ has also been used to increase the electromechanical coupling factor of FBAR or SMR devices up to 40% [46]–[48]. An alternative structure, called XBAR, exploits laterally excited (i.e. through interdigitated electrodes located on top of the piezoelectric substrate) bulk wave. These devices have the highest operational frequencies and are developed by Resonant Inc.
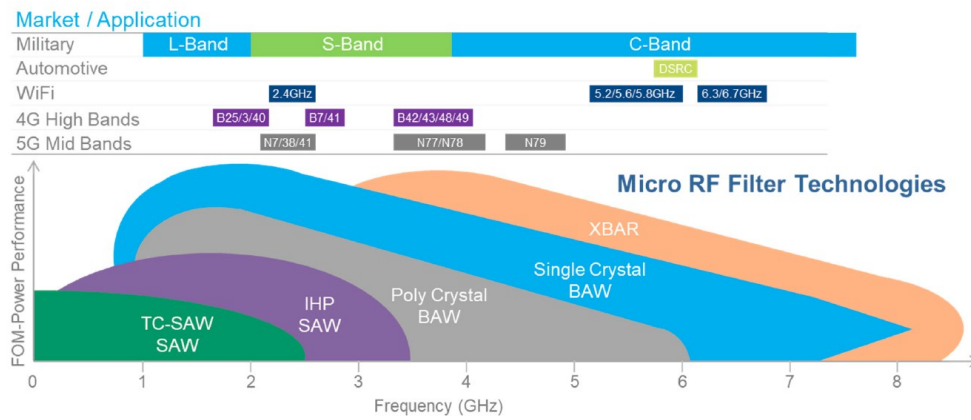
Figure 13: Market application and band allocation of radio frequency (RF) filter technologies [50].

As shown in Figure 13, SAW filters operate at low ranges while BAW filters are the standard for applications higher than 3 GHz. A conventional SAW resonator fabricated on $LiTaO_3$ has $k^2 \sim 6 - 8 \%$ [51] and $Q \sim 800$, while the new generation of Incredibly High Performance SAW (IHP SAW) has $k^2 \sim 9 - 10 \%$ and $Q = 4000$ [52].

	SAW	TC-SAW	TF-SAW	BAW-SMR	BAW-FBAR	BAW-XBAR
		Lateral Propagation			Vertical Propagation	
Application						
	4G	4G	4G/5G)	4G/5G	4G/5G	4G/5G
Cost (– High Cost, + Low Cost)						
	+++	++	+	+	–	(Est.) ++
Process Steps (+ Complex, – Simple)						
	–	+	++	+++	++	+++
Structure						
	Air Cavity	Oxide	Air Cavity	Air Cavity	Air Cavity	Air Cavity
	Single Crystal Piezo	Single Crystal Piezo	Single Crystal Piezo	Polycrystal Piezo	Polycrystal Piezo	Polycrystal Piezo
			Backside Parasitic	Backside Parasitic	Air Cavity	Air Cavity
Substrate						
	Single Crystal Piezo	Single Crystal Piezo	Piezo on Insulator	Silicon	Silicon	Piezo on Insulator

Figure 14: qualitative comparison of different SAW and BAW technologies in terms of application, cost of fabrication and process complexity [36].

Comparatively, a state of the art BAW resonator exhibits an electromechanical coupling factor of close to 8 % and Q between 2000 and 3500 close to $2\ GHz$, however at the expense of a very complex and expensive fabrication process. Figure 14 shows how the BAW technologies compare to SAW devices in terms of cost and complexity of manufacturing. A summary of k_t^2 and Q-factor of the available SAW and BAW solutions at 2 GHz is provided at Table 1.

Table 1: State of the art of SAW and BAW resonators **at 2 GHz**

State of the art resonators	k_t^2	Q-factor	FOM
Classical SAW (bulk LiTaO₃)	8%	800	64
Temperature-compensated SAW (bulk LiNbO₃ / SiO₂)	7%	1500	105
LiNbO₃ BAW	20%	250	125
IHP SAW (bulk Si / SiO2 / LiTaO₃)	10%	4000	400
AlN BAW	6%	3000	18
AlScN BAW	15%	700	105

There is still an ever-growing need to expand the range of operation frequency while maintaining the maximum possible electromechanical coupling factor (k^2) and quality factor (Q). Specifications of 5G filters for example (n77, n78, and n79) demand high frequency (3-5 GHz) and very large bandwidth (13-24%), beyond the limits of conventional SAW or FBAR technologies [53].

2 Hybrid SAW/BAW resonators

2.1 Initial concept

Aside from this very competitive context, a new mode of propagation was proposed a few years ago, combining both operation concepts of SAW and BAW resonators in a so-called Hybrid SAW/BAW device [54].
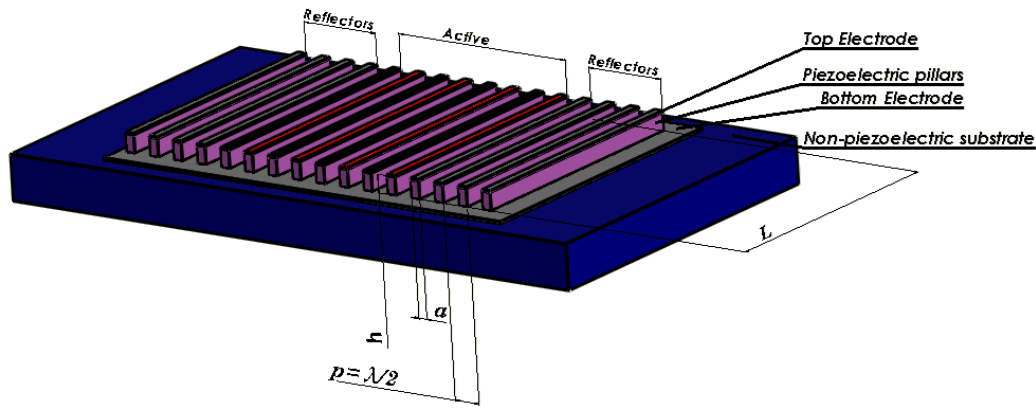
Figure 15: A simplified 3D drawing of Hybrid SAW/BAW resonators with key parameters and structures indicated.

The goal was to combine low wave attenuation and high wave velocity at the surface of stiff but non-piezoelectric substrates like silicon or sapphire while taking advantage of a high quality piezoelectric material like AlN to maintain a relatively large coupling factor (k^2).

2.2 Theoretical analysis based on AlN/ AlScN and ZnO

The structure proposed is made of a substrate suitable for surface wave propagation, a metal layer deposited on the substrate and followed by micro acoustic transducers in the shape of bars. These transducers are made of AlN and arranged in an array spaced out evenly at a distance equal to a half of the propagating wavelength. Unlike standard FBAR where the piezoelectric material is deposited as a continuous layer of thin film, bar shaped transducers benefit in theory from a larger coupling factor than planar transducers ($k_{33}^2 = \frac{k_t^2}{1-k_t^2}$), since they are free to extend or contract as the transducer elongates or shrinks according to Rouffaud *et al.* [55] These individual transducers are connected mechanically via the substrate. Thus, the array is composed of individual piezoelectric elements with interdigitated top electrodes (IDTs). The authors considered sinusoidal potential of opposite phase on neighboring fingers while the continuous bottom surface deposited on the substrate is kept at the zero electric potential.

Figure 16: Proposed SAW/BAW device (a) new resonance at 1 GHz (b) [54]

Their simulations identify different resonance modes and locate their approximate frequency ranges. They find that the resonance mode related to the surface wave on top of the silicon substrate (its Rayleigh wave) appears at 1 GHz when covered by a plane AlN layer. Alternatively, it appears at 350 MHz when covered by a patterned AlN layer (Figure 16 (b)) but a new mode occurs at 1 GHz corresponding to the fundamental bulk longitudinal wave in the AlN. They show its admittance without showing the mode shape.
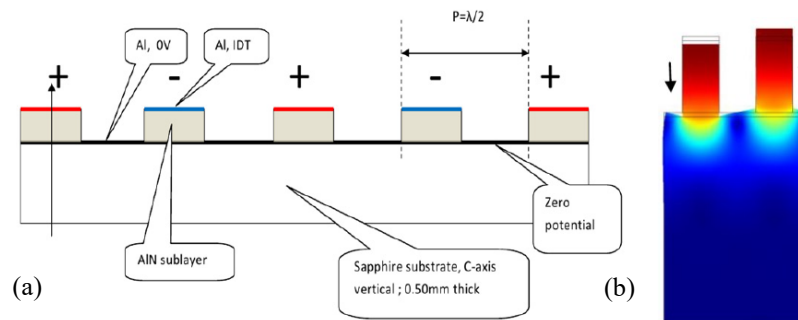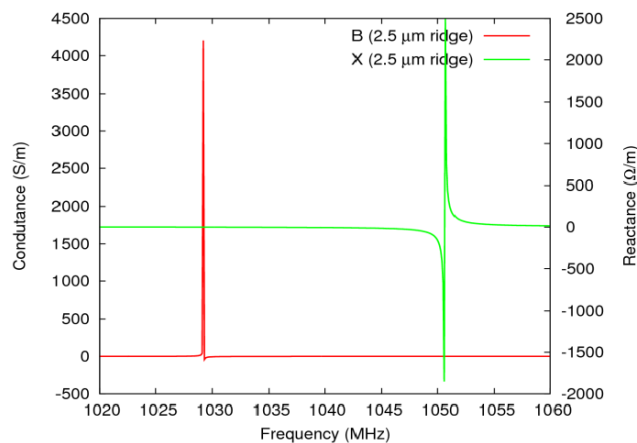

Figure 17: Electric response of the patterned AlN configuration, new mode, $k^2 = 4.0\%$ [54]

While they demonstrate the concept of micro-machined pillars, their simulations also consider variation of different parameters like the thickness of the transducers (e.g 2.5 μm or 5 μm) at a fixed width, and the material of the substrate (e.g silicon or sapphire). Their study concludes that the surface wave propagating under the array of transducers does in fact provide an electromechanical coupling factor 3.5 times larger than the one of a surface wave propagating on a planar AlN/Si substrate. For a piezoelectric layer thickness of 2.5 μm, k^2 reaches 0.29% for a continuous piezoelectric layer and 1% for machined pillars (3.5 times bigger).

It also mentions that the new resonance mode exhibits an electromechanical coupling factor at least 10 times larger than the surface wave on the same layered substrate. This new mode only appears under the condition that the longitudinal bulk resonance of the piezoelectric transducers occurs at a frequency below the bulk radiation threshold of the substrate. For a thickness of 5 μm, k^2 is equal to 0.26% for a continuous piezoelectric layer and increases to 2.33% for mode 1 and 4% for mode 2 (Figure 17) in the case of machined pillars.

In 2016, Pashchenko *et al.* [56] provided new simulations considering new electric configurations using alternating IDTs on top and out-of-phase potentials on the bottom as shown in Figure 18 (a).
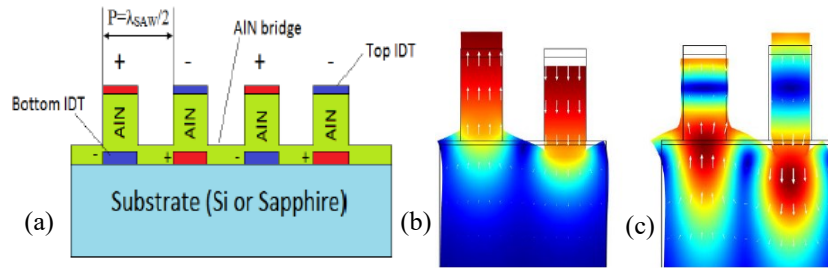
Figure 18 Unbalanced design: with top and bottom IDTs connected in crossed polarity [56] (a) Mode shape of quasi-SAW mode (ab) and Quasi-BAW mode (c) [57]

- They identified 5 resonance modes and selected the two desirable modes which are shown in Figure 18 (b, c) called "Quasi-SAW" and "Quasi-BAW" modes.
- The effective electromechanical coupling factor for the Quasi-BAW mode was found higher than for the Quasi-SAW mode, reaching a maximum of 6.8% at $h/\lambda=0.6$ (ratio of AlN film thickness to wavelength) and $t/h=0.75$ (etching ratio) with the proposed electric configuration, on Si substrate.
- For all simulated electrical configurations the best k^2 were always observed for both modes when the piezoelectric layer was only partially etched over between 60 and 80% of its thickness (Figure 19). This result suggests the existence of an interaction between the pillars beneficial to the electromechanical coupling and that contributes to wave confinement in the transducers.
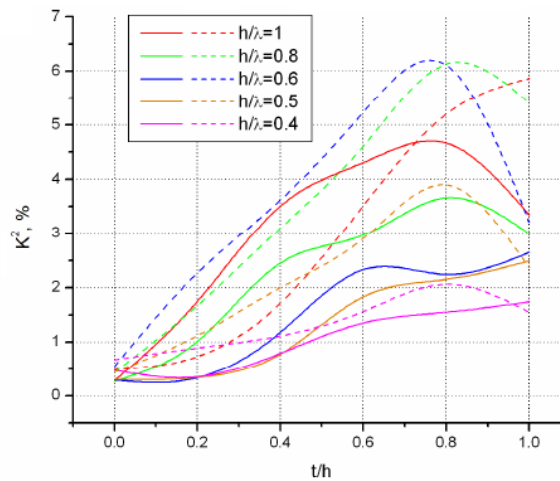
Figure 19: Effective coupling factors varied with the etching ratio for HSBR with IDT/AlN/Pt/Si. Solid lines correspond to the pseudo-SAW mode and dashed lines correspond to the pseudo-BAW mode [56]

Improving wave confinement

Integrating an acoustic reflective layer beneath the pillars of HSBR offers a significant engineering advantage. These layers, with their elevated acoustic velocity, effectively curtail the radiation of high-frequency waves into the substrate, effectively entrapping and concentrating the energy within the resonator structure. This suggests that such an approach can substantially augment the quality factor, and to some extent also the electromechanical coupling factor, leading to more efficient resonator performance. While these considerations would suggest a high acoustic velocity substrate could be all together advantageous like demonstrated below, Silicon remains a reasonably stiff substrate and much less expensive than other substrates such as sapphire or diamond. Si was thus a reasonable substrate to start with.

Pashchenko *et al.* [58] investigated the effect of the acoustic impedance mismatch between the transducer and the non-piezoelectric substrate on the travelling surface acoustic wave. As they were also interested in delay lines, their goal was to maximize the coupling between the transducers excitation and the surface waves travelling on top of the substrate. Thus, they attempted to match the acoustic impedance between the transducers and the Si substrate by inserting an acoustic matching multilayer consisting of 200 nm of SiO_2 and 1100 nm of Si_3N_4 below the 200 nm of *Pt* bottom electrode. Their results show the possibility to achieve $\underline{k^2}$ of 7% (considering AlScN instead of AlN) and were able to increase it to 10.3% by appropriately matching the piezoelectric film and substrate.
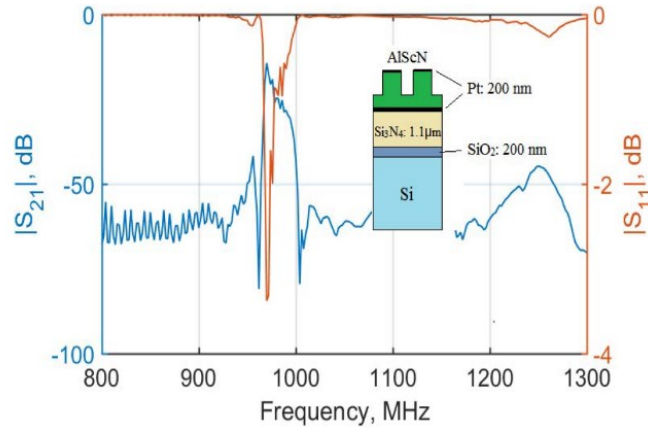
Figure 20: Calculated reflection and transmission coefficients of the delay line with acoustic matching layers Pt/ Si_3N_4/SiO_2 using hybrid SAW/BAW resonators [58]

In 2019, Qamar *et al.* [59] considered a GaN layer inserted between the silicon substrate and the transducers. In their simulations, they consider a 4.3 µm thick layer of GaN grown on Si (111), a 100 nm-thick Mo bottom electrode, an AlN thickness of 1 μm and 150 nm-thick Ni top electrode of Ni. The advantage of Ni is that it acts as a hard mask for the patterning of the AlN layer. They consider transducers width of 500 nm, 100 IDT with an aperture of 100 µm. The top electrodes are alternately connected to signal and ground while the bottom electrode is kept floating. Their device is arranged as a delay line, with a length of 50 μm. All design parameters are shown in Figure 21 (a). This show that the pseudo-SAW mode is observed both on samples with or without the GaN layer (Figure 21 b).
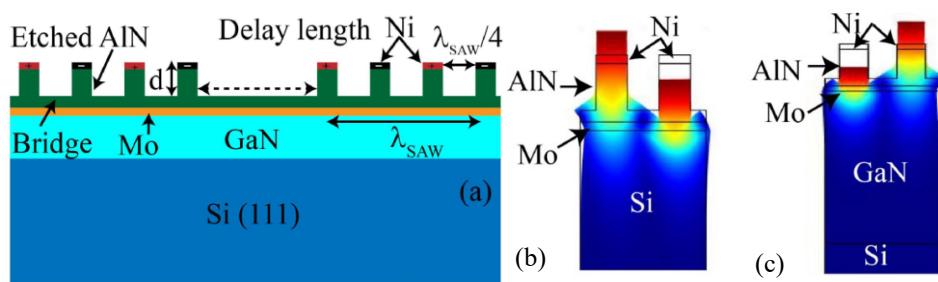
Figure 21: Schematic of the coupled BAW/SAW resonator with a GaN substrate (a), excited mode of vibration, which induces a SAW in Si (b) and in GaN (c) [59]

They consider also the influence of the depth of etching in between transducers: they show the evolution of the coupling factor as the etching depth changes. A maximum of $k^2 = 2.4\%$ is obtained for the AlN/Mo/Si arrangement and $k^2 = 3.2\%$ for the AlN/Mo/GaN/Si arrangement at approximately an etching depth of 70 % to 80 % of the AlN thickness. These results are less than the ones reported by Pashchenko *et al.* since they consider a different geometry and electrode materials but

they confirm the same trend concerning the need for optimization of the etching ratio at 0.6 to 0.8 (Figure 22).
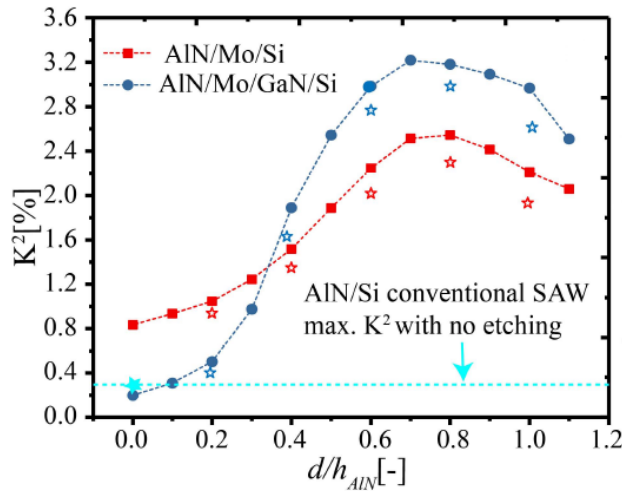
Figure 22: Effective coupling factor reported by Qamar *et al.* [59] marked stars show the experimental results

In 2020, Liu *et al.* [57] considers the same stack as Qamar *et al*. Positive and negative potentials are alternately applied to IDT fingers, while the bottom electrode keeps a floating potential. They however investigate other layers than GaN, focusing on high velocity layers, more capable of confining waves in the transducers than Si or GaN: diamond, SiC and AlN.
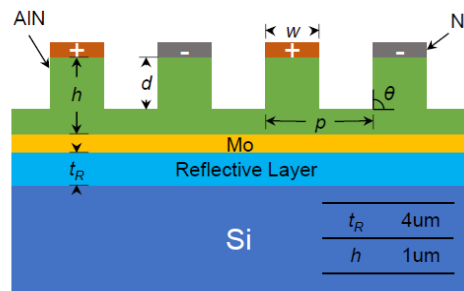
Figure 23: SAW/BAW device with an inserted reflective layer [57].

Two results may be highlighted:

1. when the thickness of the reflective layer is increased beyond one wavelength, k^2 and wave velocity reach a maximum, and then show no change (Figure 24).
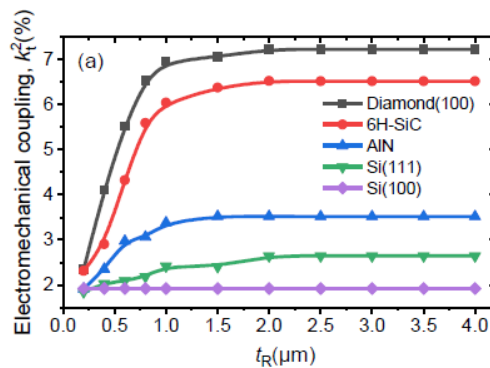
Figure 24: Electromechanical coupling k_t^2 of pseudo-SAW mode (coverage a/p = 50%, θ=90°, etching d/h=1 and aspect h/λ=0.5).

2. increasing the depth of the trenches separating the transducers (parameter d in Figure 21) decreases the wave velocity, but also increases k^2 for the quasi-SAW mode. For the quasi-

BAW mode, on the contrary, the wave velocity increases, while the electromechanical coupling factor has a more complex dependency, and is maximum for an etching depth 80% of the initial AlN layer, which is consistent with the previous studies (Figure 25). This is also confirmed by other groups [60].
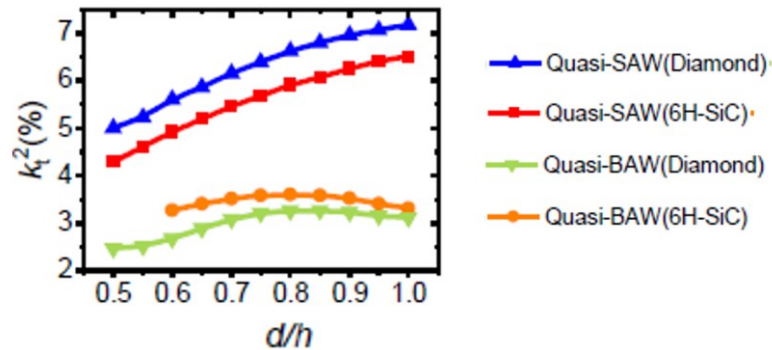
Figure 25: Electromechanical coupling (k_t^2) variation with etching ratio d/h

With multiple optimization and a reflective layer having a high acoustic velocity material such as diamond, they simulate a resonator reaching k^2= 7% at 1.7 GHz and k^2= 4% at 4.2 GHz.

Lateral reflectors

In 2021, Liu *et al.* [61] expanded their work by extending the array of transducers with a series of short-circuited transducers acting as reflectors. The proposed structure is shown in Figure 26.
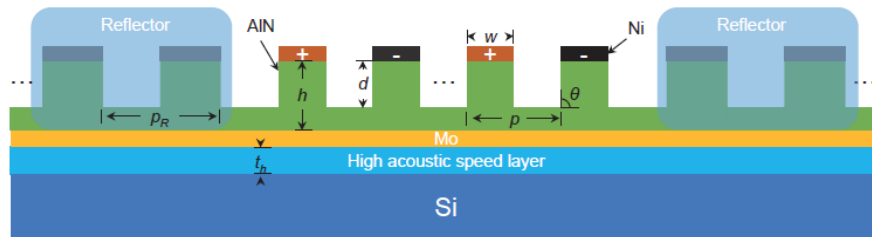
Figure 26 Cross-section view of the proposed structure of the resonator, which consists of the IDT and reflectors [61]

Two designs of the reflectors are being investigated: a synchronous reflector with a periodicity matching the one of the transducers (p = 1 μm) and an asynchronous reflector structure with p = 1.4 μm, optimized so that the resonance frequency falls in the middle of the stop-band of the reflector array. They evaluate the reflection coefficients to reach 86.3% without reflector, 94.8% with the Bragg reflector and 99.9% with the asynchronous reflectors. These reflection coefficients are calculated using domain probes in comsol to evaluate E_c: the mechanical elastic strain energy around the active pillars (including the IDT) and E_t: the total mechanical elastic strain energy in the whole device. The reflection coefficient is taken to be the ratio of these two quantities: $\eta = E_c/E_t$. Figure 27 shows the calculated surface displacement at the top of the high velocity layer at resonance.

Under the same excitation, the reflectors clearly enhances the vibration in the IDT region while reducing it strongly elsewhere. Thus, the quality factors show significant improvement: without any reflector, k^2=5.69%, Q_s=1436 and Q_p=448 without reflector, k^2=5.91%, Q_s=1780 and Q_p=1310 with synchronous reflector and k^2=5.41%, Q_s=3146 and Q_p=2166 with asynchronous reflector. These Q factor calculations are inferred from the same eigenfrequency analysis mentioned before giving rise to questions concerning
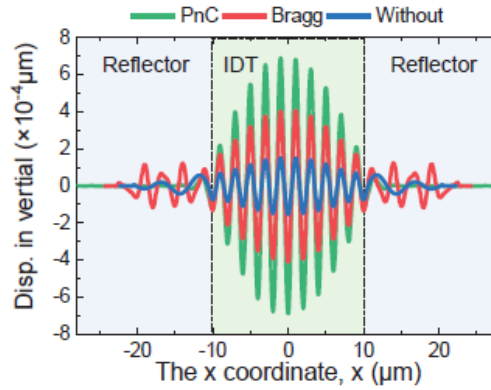
Figure 27: vertical displacement at the surface of the high velocity layer with for different reflector designs.

Lateral field excitation of hybrid SAW/BAW resonators

Another approach to improve the electromechanical coupling factor is to modify the excitation of the piezoelectric transducers. Sandwiching the piezoelectric film between two electrodes leads to excitation of waves by a vertical electric field, which mostly favors longitudinal strains in AlN or similar materials. However, exciting these piezoelectric layers with a horizontal electric field favors the excitation of shear waves.

Santosh *et al.* [62] presented in 2015 the first theoretical analysis of a ZnO-based structure similar to a HSBR, but with a structure having electrodes located in between the piezoelectric pillars (Figure 28). Under such an excitation, they identify two families of resonance modes i.e. transverse wave modes and longitudinal wave modes. Figure 28 (c,d,e) show the displacement fields of these modes. The first two modes result from shear deformation of the piezoelectric pillar, while the second group bears some similarity with the typical quasi-SAW mode.
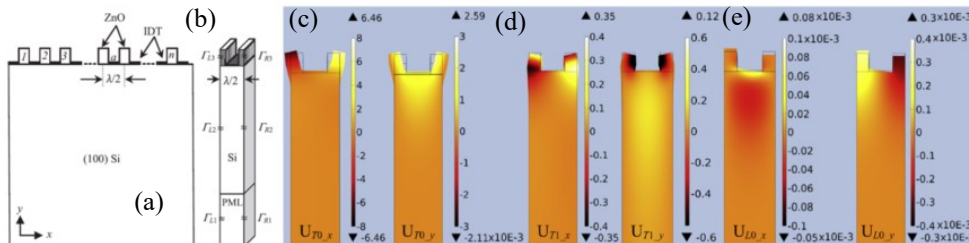
Figure 28: Laterally excited hybrid SAW/BAW resonators. Schematic of the device structure (a), geometry considered with periodic boundary conditions (b) for the simulation of the first transverse mode (c) the second transverse mode (d) and the first longitudinal mode (e) [62].

As was done for thickness-excited transducers by the other group, the authors investigated the evolution of k^2 as a function of the ZnO thickness to wavelength ratio. They also evidence an optimum k^2 of 8.37% at $h/\lambda= 0.13$ for the first transverse mode and $k^2= 6.4\%$ at $h/\lambda= 0.19$ for the second transverse mode. These electromechanical coupling factors are twice the value reported for conventional ZnO/Si layered SAW devices for similar stacks.

The same group extended this work [63] providing experimental results and focusing their theoretical analysis on the transverse mode shown in Figure 29 (b) for a metallization ratio of 0.5 and $\lambda= 8\mu m$. They also considered the addition of a SiO$_2$ layer of thickness of $h_{SiO_2}/\lambda = 0.2$ on top of the silicon substrate. Unlike what could be observed for thickness excited longitudinal modes, k^2

is found to decrease from 8.37% at h_{SiO_2}/λ =0.12 to 3.2% for $h_{SiO_2}/\lambda = 0.3.$ In the meanwhile, very little variation of phase velocity is observed.
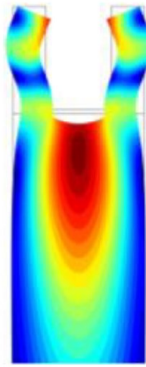
Figure 29: Displacement profile of the first order transverse mode surface acoustic wave generated in the silicon substrate. [63]

Xu *et al.* [64] simulated a structure with *ZnO* pillars on *SiC* substrate shown in Figure 30 (a). Top electrodes are located above the pillars restoring somehow the original design of the HSBR researchers used in *AlN* and *AlScN* studies. But no bottom electrode is located under the piezoelectric film. However, due to the channeling of the electric field inside the piezoelectric pillars, the excitation relies primarily on a vertical field, as is conventional. They identify therefore the same: pseudo-SAW and pseudo-BAW modes as for AlN shown in Figure 30 (b, c). They also reported that the quasi-SAW mode appears at 1.12 GHz while the quasi-Sezawa mode appears at 2.77 GHz which is in agreement with studies on AlN. With this configuration, they obtain for the quasi-SAW mode a maximum k^2 of 11.82% with Cu electrodes and V_p=1975 m/s. For the quasi-BAW mode, the maximum k^2 is 9.26% with Al electrodes and V_p=4754.8 m/s.
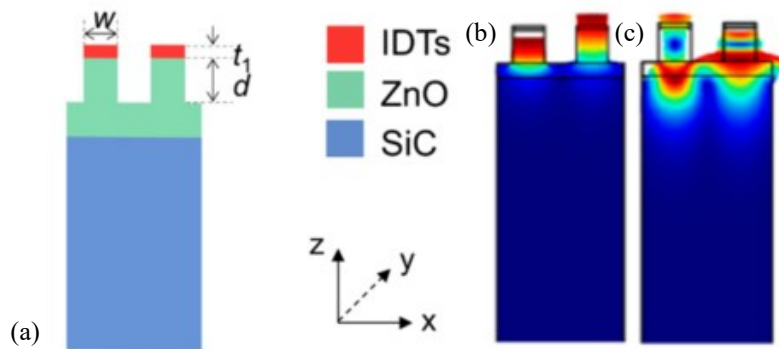
Figure 30: Schematic of the structure made up of IDTs, partially etched ZnO/ SiC (a) pseudo-Rayleigh mode (b) pseudo-Sezawa mode (c)

As in [63], but unlike what was observed on AlN or AlScN devices, k^2 drops significantly and the velocity decreases slightly when the thickness of a SiO₂ layer (t2) located under the piezoelectric layer increases as demonstrated in Figure 31.
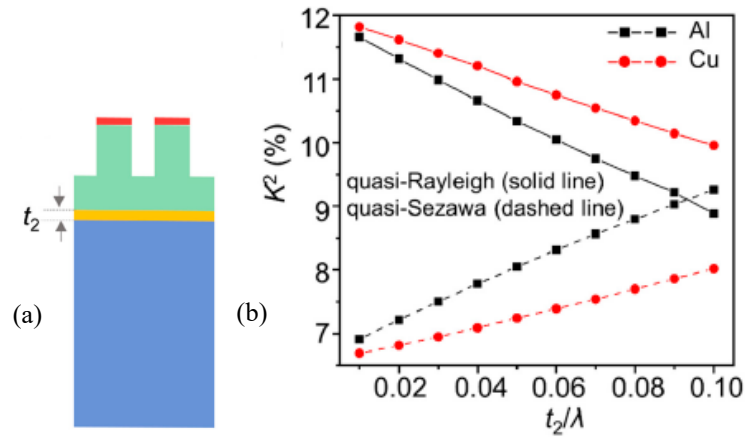
Figure 31 Schematic (a) and k^2 of pseudo-SAW and pseudo-BAW modes as functions of bottom electrode material and thickness t2/l based on the partially etched ZnO/metal/SiC structure (b) [64]

Finally, Han *et al.* [65] published a parametric study on the same structures, with ZnO, AlN or lithium niobate, but on a diamond substrate, and with the piezoelectric pillars located atop another continuous piezoelectric layer (in red in Figure 32), also either ZnO, AlN or lithium niobate. Their paper analyses different HSBR stack arrangements. They found that the use of the two layers of piezoelectric films of different sizes increases k^2. They theoretically show the possibility to reach a k^2 of 8.26% was achieved at a high frequency of 3.4 GHz using ZnO/ZnO/Diamond with h$_{first}$/λ = h$_{second}$/λ = 0.5 which is basically the same as one ZnO layer with a 50% etching ratio.
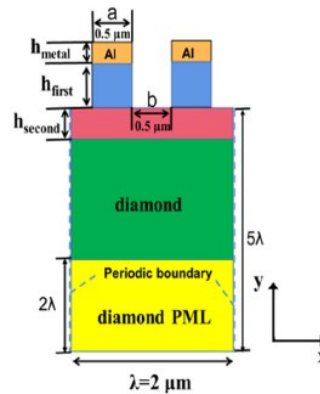
Figure 32: schematic of the "tree shape" structure proposed by [65]

In 2020 Zhang *et al.* [60] were the first to present an extended theoretical discussion on HSBR using AlScN. They investigated several structures (Figure 33), and discussed the effect of doping AlN with Sc on performance.
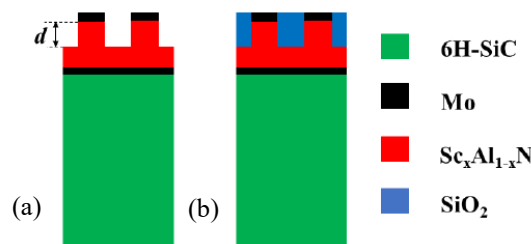
Figure 33 Different designs considered by Zhang *et al.* [60]

The maximum achievable k^2 reaches 10.49% and 13.69% for the quasi-SAW and the quasi-BAW modes respectively with Al$_{0.6}$Sc$_{0.4}$N in the configuration of Figure 33(a). This is higher than

the 7 and 10.3% reported by Pashchenko *et al.* [58] when using $Al_{0.85}Sc_{0.15}N$ we reported earlier, confirming that an increase in Sc concentration improves the piezoelectric properties of the film and benefits to the electromechanical coupling factor of the resonators (Figure 34).
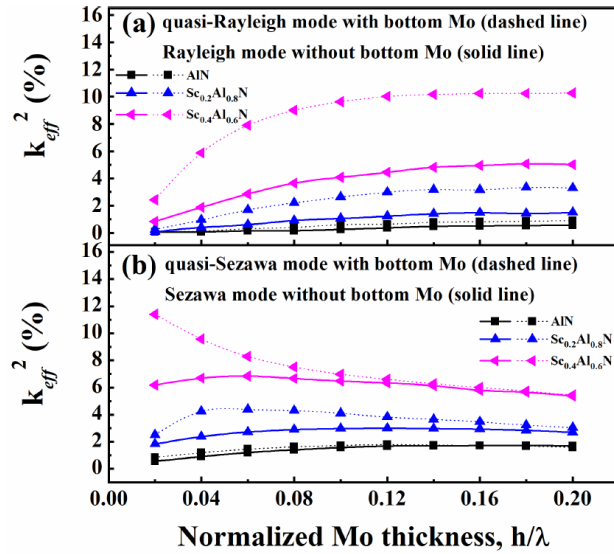
Figure 34: k^2 of the pseudo-SAW (denoted quasi-Rayleigh) (a) and the pseudo-BAW (denoted quasi-Sezawa) (b) of the Mo/AlScN/Mo/6H-SiC structure as a function of the normalized bottom Mo thickness.

Zhang *et al.* also consider filling the trenches separating the transducers with SiO_2 [60], as shown in Figure 33(b). This increases the maximum k^2 of the quasi-BAW mode to 14.55%, but decreases the one of the quasi-SAW mode to 6.84%. In the meantime, filling the trenches with SiO2 increases the velocity of the quasi-BAW mode while it decreases the one of the pseudo-SAW mode (Figure 35). Either with or without SiO_2 filling, the velocity of both the quasi-Rayleigh and the quasi-Sezawa modes are above 5000 and 7500 m/s respectively which makes them suitable for high-frequency devices. Since the shear wave velocity in Si is 5680 m/s, it means only the pseudo-SAW mode is confined and that the pseudo-BAW mode will experience radiation losses.
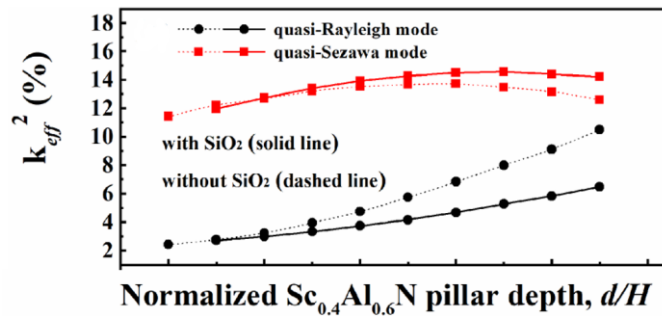
Figure 35: k^2 of the pseudo-SAW (denoted quasi-Rayleigh) and the pseudo-BAW (denoted quasi-Sezawa) for HSBR with and without SiO2 filling.

Lang *et al.* [66] studied a structure using $Al_{0.6}Sc_{0.4}N$ as the piezoelectric material and SiC as a high acoustic velocity substrate. They confirmed that the large shear wave velocity of SiC allows to confine the mechanical energy in the piezoelectric material at 1.3 GHz. Their optimal design (AlScN thickness to pitch ratio of 0.6 and etching ratio of 0.95) set a new reference in term of figure of merit (FOM): $k^2 = 23.72\%$, Q = 2130, FOM=504

The theoretical studies that considered AlScN confirmed that an increase in the intrinsic piezoelectric properties of the pillar material would lead to significantly higher k^2 for HSBR.

2.3   Alternative structures based on lithium niobate

Plessky *et al.* [44], [53] considered an alternative to their XBAR (mentioned in section 1.3) which rely on the vertical field excitation of shear-horizontal modes in rotated Y-cut lithium niobate membranes, which they called YBAR. This device may be considered as a set of series-and-parallel connected FBARs, operating on shear mode in Y-cut of LN membrane. It has a floating bottom electrode, and alternating top side electrodes, which simplifies manufacturing. They suggested partially etching the piezoelectric film, as shown in Figure 36, to suppress spurious lateral modes. This confines the main mode (the shear horizontal mode) in the region between trenches, essentially stopping any travelling waves in the piezoelectric plate [67]. This produces structures very close to hybrid SAW/BAW resonators, except that they are suspended. The interest of these structures is that they are capable of exhibiting extremely large electromechanical coupling factors of above 50% at frequencies close to 4 GHz.
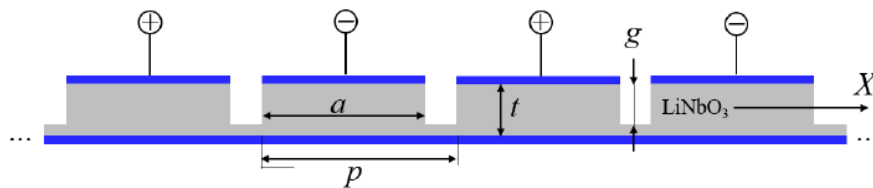
Figure 36: YBAR structure [53].

3   Fabrication of HSBR

The previous section reviewed theoretical expectations for hybrid SAW/BAW or similar devices. The promises offered by these structures have motivated works towards their implementation into practical devices. We review here the major attempts reported in the literature.

3.1   HSBR fabrications based on sputtered films

The relatively high k^2 of AlN (6.5% for longitudinal bulk waves) has made it the material of choice for the bulk acoustic wave resonators and filters used in radio frequency communication systems [68], while low insertion loss and high-quality factor resonators realized using AlN have greatly advanced time reference applications [69]–[72]. Scandium doped Aluminum Nitride (AlScN) [73], [74] is a thin film alloy that has been developed to offer a higher electromechanical coupling coefficient compared to AlN but potentially at the cost of quality factor [75]. This unique combination of properties makes AlScN an ideal choice for RF front-end applications. Because of their wide use in acoustic devices, most works on hybrid SAW/BAW resonators considered this material as the piezoelectric layer.

The most popular deposition techniques for AlN include physical vapor deposition (PVD), in particular reactive sputtering, and chemical vapor deposition (CVD) [76]. Reactive sputtering is a thin film deposition technique that involves ionizing and accelerating inert gas atoms to bombard a target material, namely aluminum, and form a thin film in the presence of a reactive gas, namely nitrogen. The choice of deposition technique depends on factors such as the desired film thickness, quality, and substrate material.

Etching techniques used for AlN typically involve wet etching with basic solutions (KOH, H_3PO_4), reactive ion etching. Wet etching is a cost-effective and efficient method for etching AlN, but can result in a rough surface finish if the film contains disoriented grains [77], [78]. Dry etching, on the other hand, produces smoother surfaces and allows for finer control over etch depth and shape,

but is more expensive and time-consuming [78]. Dry etching techniques include Reactive Ion Etching (RIE), Inductively Coupled Plasma (ICP) and Ion Beam Etching (IBE) are three commonly used techniques for etching AlN in the microfabrication of SAW and BAW resonators. RIE couples an ion bombardment with chemical reactions made possible by the introduction of chlorine gases in the plasma along with neutral gases such as Argon. ICP is a variation of the previous technique that increases the density of the plasma through the use of an RF electromagnetic field. IBE, on the other hand, uses only a beam of neutral ions to physically etch the AlN material [79]. The choice of etching technique usually depends on the desired resolution, aspect ratio, and surface finish. Overall, the deposition and etching techniques for AlN have been well-established and optimized over the years, making them relatively mature processes in the fabrication of SAW and BAW resonators and thus a natural first step material for the realization of hybrid SAW/BAW devices.

Initial realizations

The first attempt at an experimental implementation of HSBR devices was provided by Pashchenko *et al.* [56] from the École Polytechnique Fédérale de Lausanne (EPFL). They used polycrystalline AlN and $Al_{0.85}Sc_{0.15}N$ as piezoelectric material deposited using reactive magnetron sputtering. They used (111)-oriented Platinum as the bottom electrode on which AlN grows with preferential (0001) orientation. The patterning of the AlN pillars was performed using an Inductively Coupled Plasma (ICP) with Cl_2/Ar gases, while the patterning of the AlScN pillars was performed using Ion Beam Etching (IBE) with an Argon plasma. IBE can result in some damage to the AlN material due to the ion bombardment, which can affect its piezoelectric properties [80].
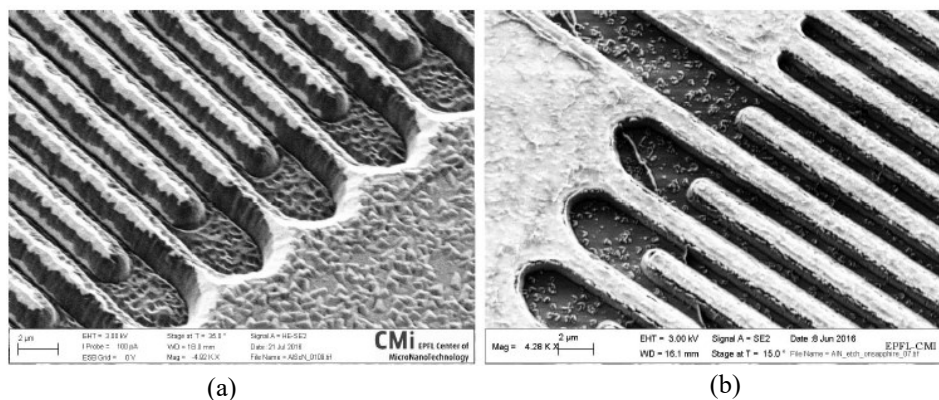
Figure 37: SEM view of the patterned AlScN film by IBE (a) and AlN film by ICP (b) growth on Pt/Sapphire [56].

Frustum shaped damaged electrodes and pillars were observed, resulting probably from the etching of the photoresist mask during the ion beam exposure.

In 2017, the same authors reported the manufacturing of new HSBR AlScN based resonator on sapphire (001) substrates [81]. The thickness of AlScN was 3 μm and it was etched using inductively coupled plasma. The resulting patterned transducers and the resulting electric response are shown in the SEM image in Figure 38. Two resonances appear at around 642 MHz and 796 MHz, with electromechanical coupling factors of respectively 1.1% and 4.3%.
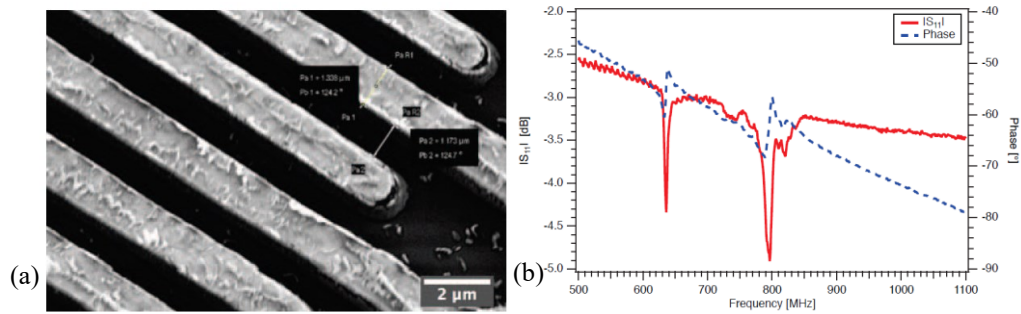
Figure 38: SEM image of the patterned AlScN film by ICP etching, grown on Sapphire (a) Electrical response of a SAW/BAW device of AlScN on Sapphire (b) [81]

Finally, the same authors manufactured and tested delay lines using $Al_{0.85}Sc_{0.15}N$ (2.5 µm)/Pt (200 nm)/Si_3N_4/SiO_2/Si structures [58]. They manufactured two identical transducers containing each 20 pillars, 1.25 µm wide and with a pitch of 2.5 µm and separated by 1 mm. IDTs (electrode aperture of 300 µm) were patterned using Ion Beam Etching. However, Argon ion bombardment damaged the transducers and roughened surface in between, leading to SAW scattering and signal attenuation, as shown in Figure 39. Moreover, some over-etching resulted in the thinning of the electrodes leading to irregular shapes and increased electrical resistance.
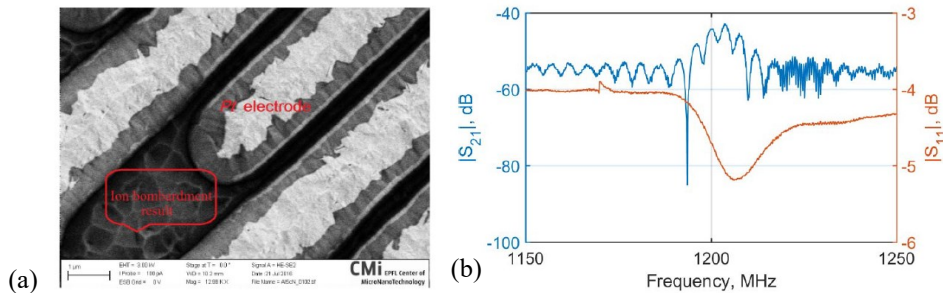
Figure 39: (a) SEM image of the AlScN pillars. Roughening is shown due to Ar ion bombardment. Etching depth ~ 1 µm (b) Experimental measured data of delay line [56]

The observed transmission lobe is centered around 1.2 GHz, 200 MHz higher than expected by simulation. The authors attribute it to a lower etching depth than expected (1 instead of 1.5 µm). The passband width is 16.3 MHz and k^2 reaches 3%. They suggested that manufacturing could be improved by using ICP despite its unfavorable etching ratio.

Use of a hard mask for the patterning of the piezoelectric film

Damages to the electrodes can be prevented by employing a metal which acts as an etch mask when patterning the piezoelectric layer, such as Ni. Actually, Ni is resistant to Cl_2 based dry etching of AlN: Ni is etched at 4.5 nm/min, while AlN is etched at 100 nm/min.

Qamar *et al.* [59] employed this technique to manufacture in 2019 a set of AlN hybrid SAW/BAW devices on GaN/Si and Si substrates. The crystallinity of AlN grown on GaN was confirmed by X-Ray diffraction with a rocking curve full width at half maximum of close to 1.3° for the AlN (0002) diffraction peak. This intermediary verification step is important to confirm the good crystalline quality of the grown AlN since AlN deposed on Mo and on GaN/Si may exhibit lower crystalline quality than AlN grown on Si.

Figure 40 shows the electrical response of delay lines fabricated on top of Si and GaN/Si substrates, with insets showing SEM images of the transducers. Clearly, the patterning of these transducers seems cleaner than those obtained by Pashchenko *et al.* on AlScN [56] (see section 4.2.1). Especially, the edges are better defined compared to the rough edges visible in Figure 37 and Figure 38. The reported coupling factors (3.2%) are in line with theoretical expectations, although they remain well below the initial theoretical expectations ($\approx$7%) [54], [56].
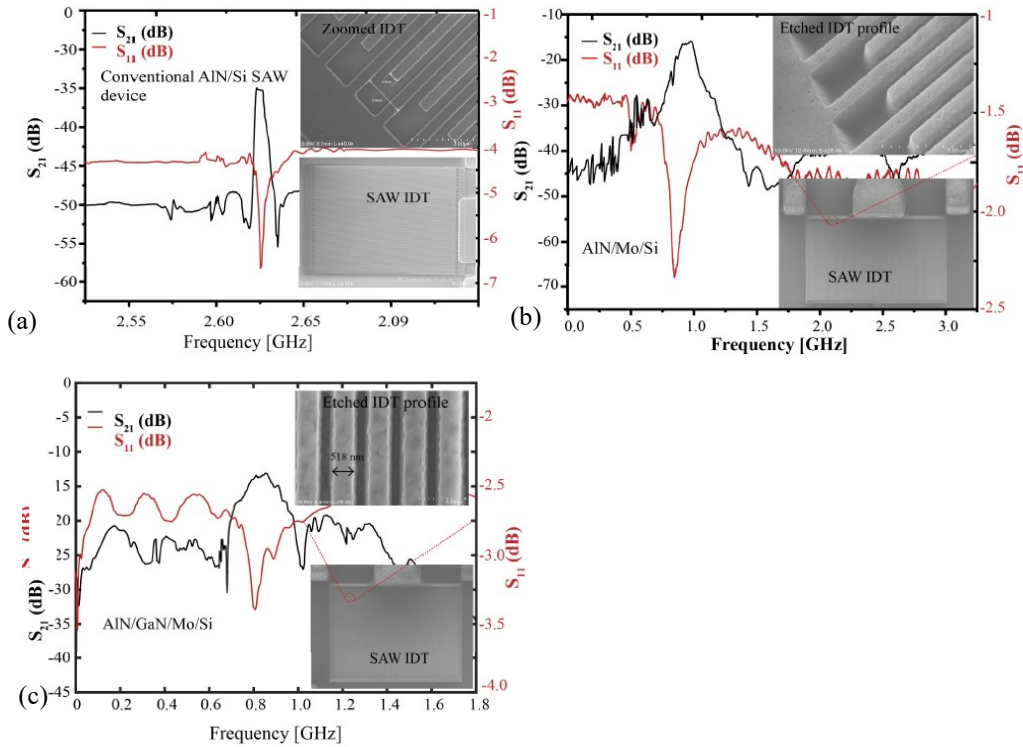
Figure 40: Transmission response and SEM images of (a) conventional SAW AlN/Si (b) AlN/Mo/Si and (c) AlN/Mo/GaN/Si hybrid SAW/BAW delay lines

The coupling factor obtained for the conventional SAW devices on Si was 0.3% and their insertion loss 35 dB while the coupling factor and insertion loss for the coupled SAW/BAW on the same Si substrate were significantly improved at 2.4% and 16 dB respectively. Finally, the coupling factor for the coupled SAW/BAW device on the GaN/Si substrate was 3.2% with insertion losses of 13 dB, which represents the best performance among the developed devices.

Xie *et al.* [82] relied instead on the wet etching of AlN, and use Ag top electrodes as a hard mask. They fabricated AlN based HSBR with an acoustic aperture of 80λ, and IDT with 30, 60 or 90 pairs of electrodes. The Ag/AlN/Mo/Diamond multi-layer films were deposited on 10x10 mm silicon dies, with the 30.02 µm thick polycrystalline diamond (PCD) film deposited by DC arc jet plasma CVD method. The rough diamond film was smoothed by polishing down to a roughness Ra lower than 2 nm. Mo (190 nm-thick) and AlN (0002) (3.04 µm-thick) were then deposited. A thin (111) oriented Ag film with thickness of 306 nm was deposited using DC sputtering method. The Ag IDTs were patterned by ion beam etching. The AlN film was fully etched to the surface of Mo layer by wet etching, with the Ag IDT serving as the hard mask of wet etching, and Mo layer serving as the etching stop layer.

The fabricated device exhibited a smooth Mo/Diamond surface between IDTs after AlN wet etching, and eroded AlN IDT line profile showing 500–800 nm thick white sidewalls on both sides due

to inevitable side reaction in etchant. However, the authors reported an electromechanical coupling coefficient of 2.16% and quality factor of 913 for a resonance at 913 MHz.
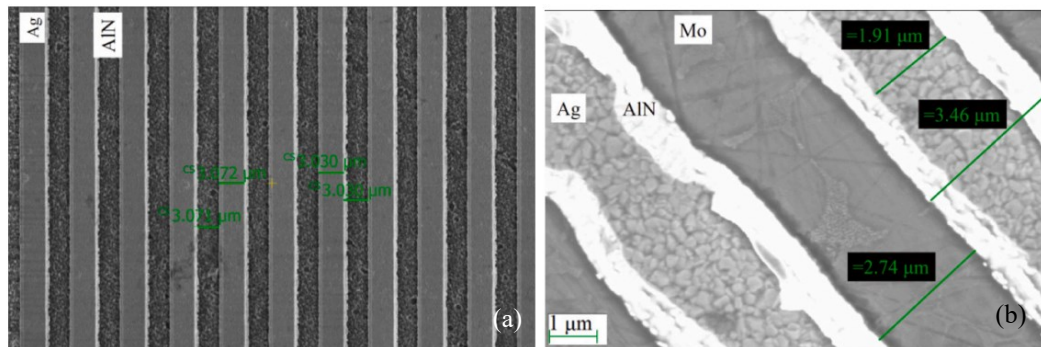
Figure 41: SEM top view of resonator IDT lines after Ag etching (a) and after AlN etching (b) [82]
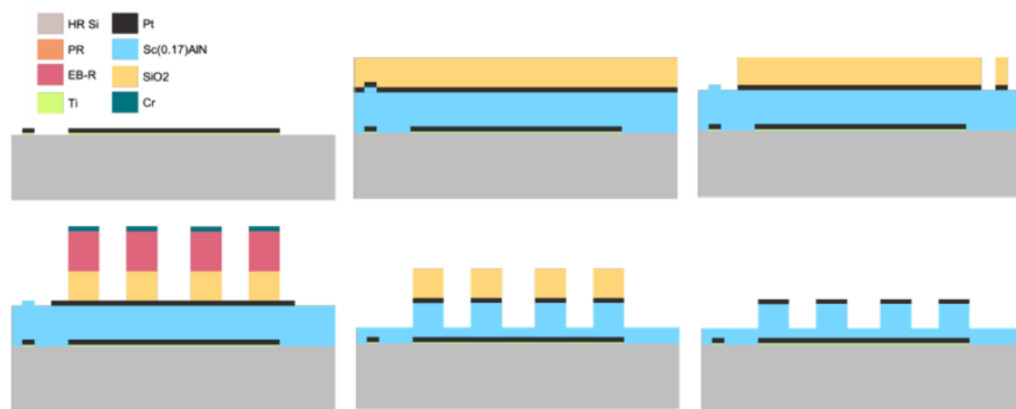
Figure 42: process flow proposed at EPFL for the fabrication of HSBR using AlScN [83]

Gollapudi *et al.* [63] used nearly the exact same process to fabricate their laterally excited ZnO hybrid SAW/BAW resonators on a Si substrate. They start by the deposition of Chromium (10 nm) / gold (100 nm) electrodes using electron beam evaporation. Gold is used since it is insensitive to the etchants used for ZnO. Then, (002) oriented ZnO thin film is deposited using RF magnetron sputtering on these electrodes. The thickness of the ZnO layer was respectively 3.8-4.3 μm for devices where on Si substrates and 3-3.2 μm for devices on SiO_2/Si. A SiO_2 hard mask is employed to pattern the ZnO transducers by wet etching of ZnO using dilute acetic acid of 0.2 M. A dominant vertical etching and reduced lateral etching are obtained by forcing a convection flow of the etchant perpendicular to the sample surface. A SEM view of the transducers, shown Figure 43(a), indicates relatively vertical sidewalls. Overall, the fabrication process involves only two UV lithography steps, one for IDT development and the other to have a hard mask for the patterning of ZnO film.
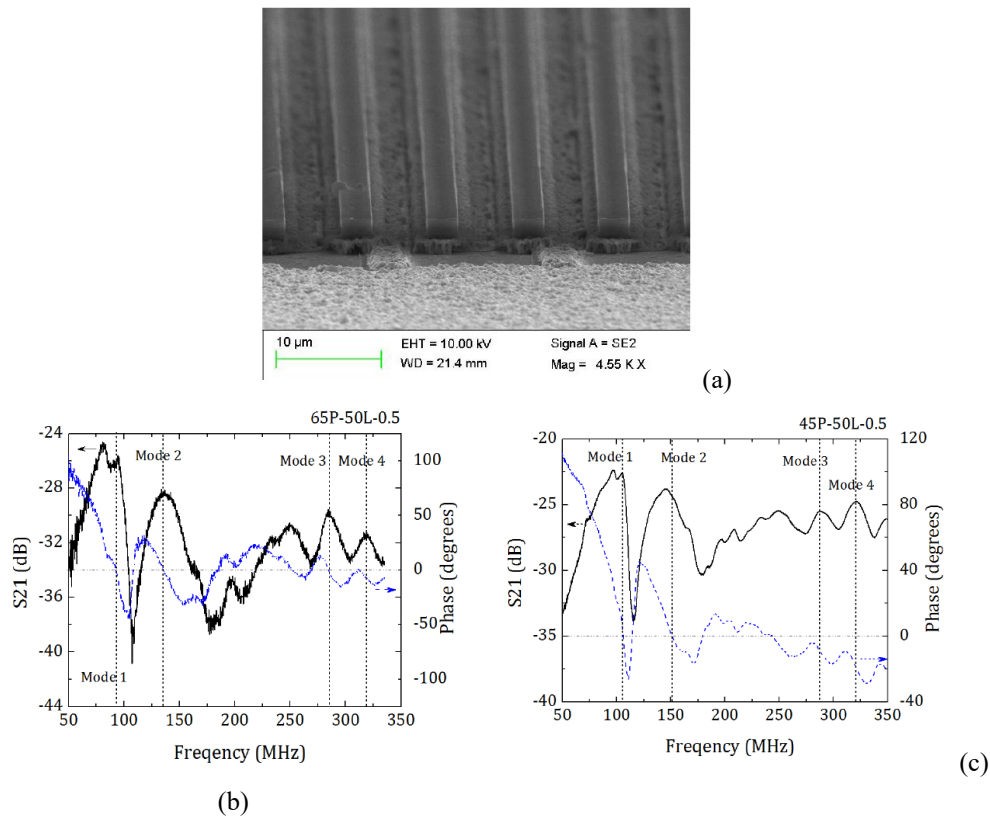
Figure 43: (a) SEM view of the resulting ZnO pillars. (b) Electric response without SiO_2 layer and (c) electric response with SiO_2 layer, both showing S_{12} in modulus and phase [63].

Electrical measurements of the fabricated devices are shown Figure 43 (b, c).On the devices located directly on silicon, they reveal four resonance modes, the first three of them corresponding to the modes depicted Figure 28(c-e):

- Mode 1, at 93 MHz with -26 dB insertion loss (IL)
- Mode 2 at 136 MHz, corresponding to the mode depicted Figure 28 (d), with IL = -31 dB
- Mode 3, corresponding to the pseudo-SAW mode, at 285 MHz with IL= -29 dB exhibits an effective coupling of k^2= 15.2%
- Mode 4 at 320 MHz with IL = -31 dB

When adding the SiO_2 layer, all modes become slightly faster and their insertion losses decrease.

A more conventional approach relies on using a thick SiO_2 layer as a hard mask independent of the electrodes. This was used for example to pattern relatively small holes with almost vertical sidewalls in AlN films [84]. This approach was used in a new process flow carried at EPFL, for the fabrication of HSBR based on AlScN [83]. It involves using a hard mask for the patterning of the top electrodes and the piezoelectric layer, instead of only photoresist which gets easily consumed. The process flow thus consists in several steps (Figure 42):

- substrate preparation,
- photolithography,
- bottom electrode sputtering over the photoresist,
- lift-off
- deposition of the piezoelectric layer
- top electrode and hard mask sputtering
- hard mask and top electrode dry etching to pattern large features of the top electrode,
- e-beam photolithography
- dry etching of the hard mask,
- dry etching of the top electrode and piezoelectric layer at a depth of 50/300 nm,
- hard mask removal using an HF bath or dry etch.

Figure 44 shows a microscope image of a resonator after fabrication. It shows that the bottom electrodes exhibits some defects, attributed to the poor lift-off conditions of the bottom electrode during the fabrication process. Therefore, no acoustic response was recorded when the manufactured devices were measured.
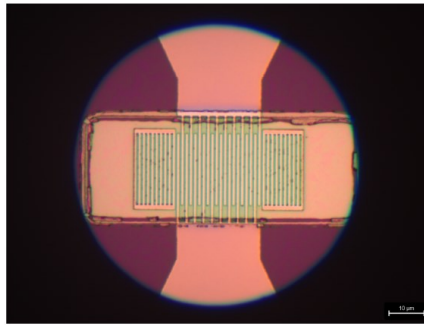
Figure 44: Optical observation of test devices resulting from the process flow sketched in Figure 42 [83]

3.2   HSBR fabrications based on LNO

This process flow is suitable for suspended resonators. In the case where one needs a bottom electrode while remaining attached to the substrate, one can no longer deposit it through a backside opening. One has then to rely on more elaborate process flows, such as for example the ones employed for LiNbO$_3$. Recently, our group at CEA-LETI presented a process flow for the fabrication of solidly mounted BAW filters, starting from an existing Piezoelectric-On-Insulator (POI) wafer [85], [179]. This process, shown Figure 45, starts by depositing and patterning the bottom electrode on the POI substrate. SiO$_2$ is then deposited and planarized by chemical-mechanical polishing. In the meantime, a carrier silicon wafer sees the deposition of Bragg mirror layers. The last layer of this mirror, SiO$_2$, is smoothed. The two wafers are then bonded using hydrophilic direct bonding at room temperature. The Si substrate and SiO$_2$ layer of the POI wafer are then removed. The fabrication of the resonators can then resume by depositing and patterning the top electrode, and by patterning the piezoelectric film.

Figure 46 shows a SEM cross section of a resonator after fabrication: both electrodes sandwiching the piezoelectric film are patterned. It also shows the electric filter of a filter based on such a resonator, highlighting the functionality of these devices.
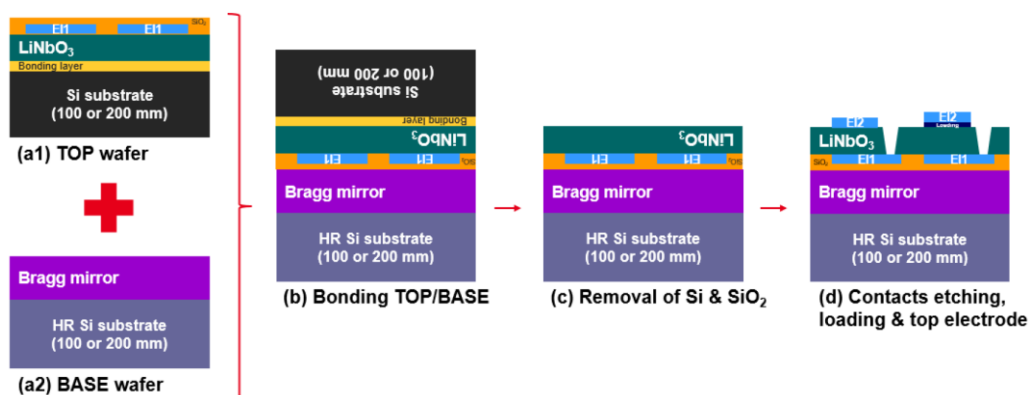
Figure 45: Fabrication of a LiNbO3 solidly mounted BAW resonator starting from a POI substrate [85]
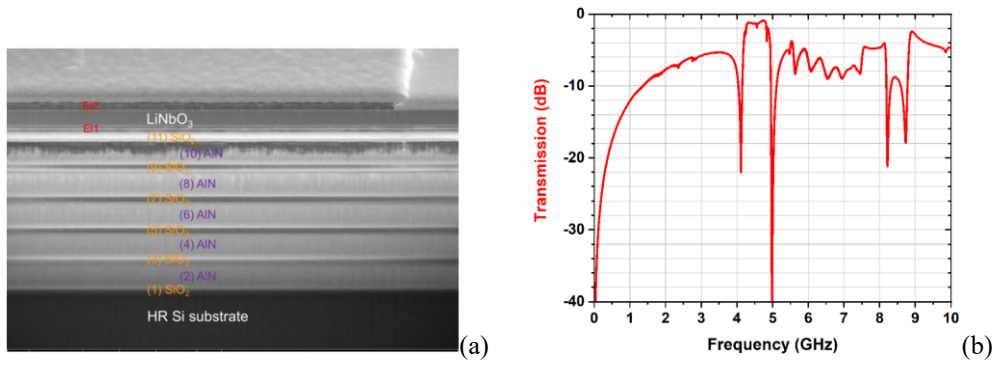
Figure 46: LiNbO$_3$ solidly mounted resonator [85] (a) SEM cross section of the resonator stack and (b) electric response of a band-pass filter.

4 Conclusions

In this chapter, we presented the concept of Hybrid SAW BAW Resonators, and reviewed studies reported on the influence of the nature of the piezoelectric material and the dependency of their performances, namely operation frequency and electromechanical coupling factor, as a function of the piezoelectric material employed (AlN, AlScN, ZnO and LiNbO$_3$), the geometric parameters of the transducers (periodicity, thickness) and the nature of the substrate. We also presented the experimental attempts at implementing these structures and discussed their fabrication processes. A summary of the reported performances is provided in Table 2 and demonstrated in Figure 47 grouped by the piezoelectric material used. To synthesize the table, only the best coupling factors reported by each paper are listed. If a paper report on different stacks, both stacks are listed.

Table 2: Summery of the reported theoretical and experimental results in literature on HSBR using AlN, AlScN, and ZnO

Source	Patterned Structure	f (GHz)	k^2	Q
Theoretical results				
Plessky 2013 [54]	Al/AlN/Al/Si	1	4	
Pashchenko 2016 [56]	Pt/AlN/Pt/Si	1	6.8	
Qamar 2019 [59]	Mo/AlN/Mo/Si	1	2.4	
Qamar 2019 [59]	Mo/AlN/Mo/GaN/Si	0.8	3.2	
Liu 2020 [57]	AlN/diamond/Si	4.2	4	
Liu 2021 [61]	Ni/AlN/Mo/Si	1.7	5.41	2610
Pashchenko 2017 [81]	Pt/AlScN/Pt/(Si or Sapphire)	0.98	7	
Pashchenko 2017 [58]	Pt/AlScN/Pt/Si$_3$N$_4$/SiO$_2$/Si	0.98	10.3	
Zhang 2020 [60]	Mo/AlScN/Mo/SiC	2.3	13.69	
Lang 2021 [66]	Mo/AlScN/Mo/SiC	1.358	23.72	2130
Santosh 2015 [62]	ZnO/Si (no electrodes)	0.332	8.37	
Santosh 2019 [63]	ZnO/SiO$_2$/Si (no electrodes)	0.332	3.2	
Xu 2021 [64]	Al/ZnO/Si	2.77	9.26	
Han 2022 [65]	Al/ZnO/Diamond	3.4	8.26	
Experimental results				
Pashchenko 2016 [56]	Pt/AlN/Pt/sapphire	1	0.6	
Qamar 2019 [59]	Ni/AlN/Mo/Si	0.9	2.4	
Qamar 2019 [59]	Ni/AlN/GaN/Mo/Si	0.8	3.2	
Xie 2023 [82]	Ag/AlN/Mo/Diamond/Si	0.9	2.16	913

Pashchenko 2016 [56]	Pt/AlScN/Pt/sapphire	0.613	3.8	
Pashchenko 2017 [81]	Pt/AlScN/Pt/sapphire	0.796	4.3	
Pashchenko 2017 [58]	Pt/AlScN/Pt/Ti/Si$_3$N$_4$/SiO$_2$/Si	1.2	3	
Santosh 2019 [63]	Au/(c-axis)ZnO/Cr/Si	0.285	15.2	

Figure 47 shows how the HSBR structures are yet to fill the gap over 3 GHz with k^2 higher than 10%.
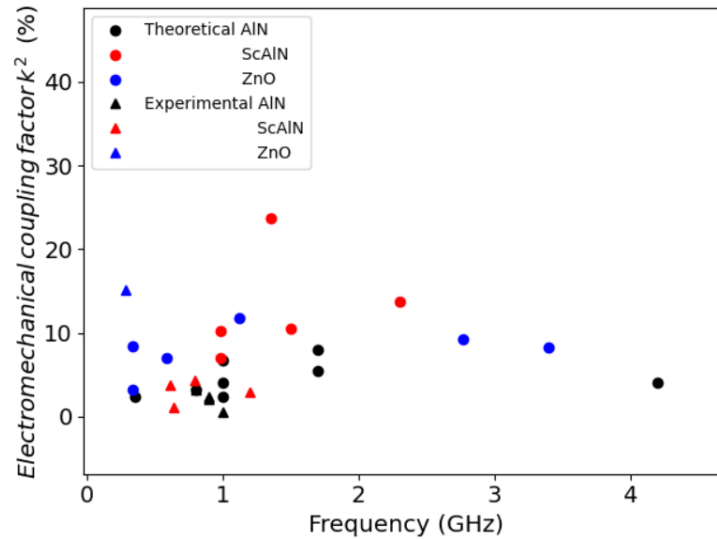
Figure 47: Summery of the reported theoretical and experimental results in literature on HSBR using AlN, AlScN, and ZnO.

As discussed in section 1, the filtering technologies in the 600 MHz – 2.5 GHz range are now very mature and well established. Current needs focus on applications above 3 GHz and for wide bands. We are therefore interested in the investigation of structures capable of reaching high frequency (more than 4 GHz) and high electromechanical coupling factors (at least 10%). The solutions to reach frequencies above 4 GHz reported in [57], [86] consider using stiff substrates to increase the operation frequency, such as diamond or a confinement layer of AlN.

In this manuscript, we will first focus on the investigation of AlN hybrid SAW/BAW resonators. This is the most mature material available at CEA-LETI, having been introduced nearly two decades ago. Its modelling and its integration constraints are well known. Therefore, in Chapter 2 we will revisit the theoretical investigations performed on AlN hybrid SAW/BAW resonators to evaluate realistic geometries in order to establish the necessary tradeoffs between manufacturability, reachable frequencies, and achievable electromechanical coupling factors and quality factors. This will be also the occasion of analyzing and building an understanding on the mechanisms of hybridization between modes of bulk wave transducers and the surface waves propagating on top of a semi-infinite substrate, which can guide the investigation.

Then, in Chapter 3, we will focus on the fabrication of prototypes. For the first realizations, we will consider relatively conservative structures, making use of the materials already available in the clean room of CEA-LETI. The goal will be both to validate the process flow developed for the fabrication of hybrid SAW/BAW resonators, to confirm experimentally the performances expected from the models developed in chapter 2.

Chapter 4 will address the issue of improving electromechanical coupling factors through the use of lithium niobate thin films. We will investigate theoretically the capabilities of LiNbO$_3$ hybrid SAW/BAW resonators, considering again realistic structures and the impact of technological constraints on the frequency/performance tradeoffs. In the meanwhile, we will discuss a possible implementation of such devices and present some first experimental validations for this process.

Eventually, in Chapter 5, we will address high frequency applications. While the literature suggests relying on other substrates than silicon, we will maintain or relatively conservative technological approach, but rather exploit a new hybrid SAW/BAW mode, of higher order than the conventional pseudo-SAW and pseudo-BAW modes, which appeared on electrical responses under some particular condition. We will investigate the conditions to exploit it on purpose using AlN and LiNbO$_3$ HSBR and again try to identify the necessary tradeoffs in realistic implementations.

Chapter 2: Theoretical analysis of AlN based HSBR

Introduction

In this chapter, our primary objective is to investigate what kind of performances in terms of frequencies, electromechanical coupling factor, and potentially quality factors, can be achieved with reasonably realistic and simple hybrid SAW/BAW resonators. We initially consider Aluminum Nitride (AlN) as the piezoelectric material, as its properties are well known, unlike those of the less mature Sc-doped AlN. The trends derives for AlN HSBR can be later transposed to the more piezoelectrically coupled AlScN, which exhibits similar crystal symmetries. To achieve this, we employ a combination of theoretical tools to gain a comprehensive understanding of these resonators.

The first section of this chapter focuses on describing a periodic Finite Element Model (FEM) used to study the acoustic wave propagation in hybrid SAW/BAW structures. The aim here is to identify the different acoustic modes that can be excited and get insights into their behavior and characteristics, in particular their velocities, electromechanical coupling factors and propagation losses.

Moving on to the second section, we investigate the impact of different geometric parameters and materials on the characteristics of these modes. These parameters are interconnected and can have contrasting effects on the different acoustic modes. The dependency of each mode on each parameter is therefore discussed independently for the different acoustic modes. Through this analysis, we can determine the most promising HSBR structures to explore.

1 Finite Element Model

The finite element method (FEM) is a numerical technique used to solve partial differential equations and analyze the behavior of systems with complex geometries. For systems that exhibit periodicity, where the entire system is built by repeating a pattern or a unit cell, periodic FEM is usually well suited. By modeling and analyzing a single unit cell, the behavior of the entire periodic structure can be understood. This approach is especially useful when studying waves, vibrations, and resonances in periodic systems, as it allows for the efficient analysis of their properties.

1.1   Implementation in Comsol Multiphysics

COMSOL® Multiphysics [87] is a software platform that provides capabilities for multiphysics FEM simulations. It is widely used in the field of MEMS to simulate and analyze various physical phenomena such as filter resonators as well as gyroscopes and sensors for example [84], [88]–[90]. One of the key physics interfaces used for the purposes of HSBR within COMSOL Multiphysics is the Structural Mechanics module. It implements a finite element formulation for elastic solids based on Hooke's law:

$$T_{ij} = c_{ijkl}S_{kl}, \tag{9}$$

where T_{ij}, c_{ijkl} and S_{kl} are respectively components of the stress, elastic and strain tensors, where they adopt conventional tensor notation, in particular Einstein's convention for the implicit summation over repeated indices. When considering small displacements and strains, the mechanical strain writes as a function of the displacements u_i:

$$S_{kl} = \frac{1}{2}\left(\frac{\partial u_k}{\partial x_l} + \frac{\partial u_l}{\partial x_k}\right). \tag{10}$$

The dynamic behavior of the solid is described using Newton's law:

$$\rho\frac{\partial^2 u_i}{\partial t^2} = -\frac{\partial T_{ij}}{\partial x_j} + F_{i,ext}, \tag{11}$$

where $F_{i,ext}$ are the components of external forces applied to the volume considered. Merging the three previous relationships and taking into account the symmetries of the elastic tensor, one obtains the differential equation for displacements:

$$\rho\frac{\partial^2 u_i}{\partial t^2} = -c_{ijkl}\frac{\partial^2 u_k}{\partial x_j \partial x_l} + F_{i,ext}. \tag{12}$$

Comsol also implements an electrostatic formulation for solving Poisson's equation in dielectric media:

$$\frac{\partial D_i}{\partial x_i} = 0, \tag{13}$$

where

$$D_i = \varepsilon_{ij}E_j \tag{14}$$

D is the dielectric displacement and **E** the electric field. We consider here the electrostatic behavior rather than a full electromagnetic problem because electromagnetic waves propagate about 10^5 times faster than acoustic waves. This means that one can consider that at the time scales of acoustic waves, any transient electromagnetic phenomenon has reached equilibrium. Hence, the quasi-static approximation for electromagnetic fields is sufficient and one can write that the electric field derives from the electric potential [91]:

$$E_j = -\frac{\partial \Phi}{\partial x_j}.$$
(15)

Again, merging the three previous relations leads to

$$-\varepsilon_{ij} \frac{\partial^2 \Phi}{\partial x_i \partial x_j} = 0.$$
(16)

Eventually, HSBR are piezoelectric devices. Piezoelectricity is represented in Comsol Multiphysics as a multi-physics coupling between elastic solids and dielectric media in the electrostatic approximation. In agreement with classical equations for piezoelectricity [10], the equations are modified so that mechanical stresses result also from the application of an electric field, and conversely that the electric displacement has also an additional contribution resulting from mechanical strains:

$$\begin{aligned}
T_{ij} &= c^E_{ijkl} S_{kl} - e_{kij} E_k, \\
D_i &= \varepsilon^S_{ik} E_k + e_{ikl} S_{kl},
\end{aligned}$$
(17)

where e_{kij} are components of the piezoelectric tensor. Introducing Newton's and Poisson's laws, the set of differential equations solved in the piezoelectric case become:

$$\begin{aligned}
\rho \frac{\partial^2 u_i}{\partial t^2} &= -c_{ijkl} \frac{\partial^2 u_k}{\partial x_j \partial x_l} - e_{kij} \frac{\partial^2 \Phi}{\partial x_j \partial x_k} + F_{i,ext}, \\
0 &= e_{jkl} \frac{\partial^2 u_k}{\partial x_j \partial x_l} - \varepsilon_{ik} \frac{\partial^2 \Phi}{\partial x_i \partial x_k}.
\end{aligned}$$
(18)

It is often convenient to consider in this case generalized displacements written as [92]

$$\boldsymbol{u} = \begin{pmatrix} u_1 \\ u_2 \\ u_3 \\ \Phi \end{pmatrix}.$$
(19)

and to write the differential equations as

$$\begin{pmatrix} c_{1j1l} & c_{1j2l} & c_{1j3l} & e_{l1j} \\ c_{2j1l} & c_{2j2l} & c_{2j3l} & e_{l2j} \\ c_{3j1l} & c_{3j2l} & c_{3j3l} & e_{l3j} \\ e_{j1l} & e_{j2l} & e_{j3l} & -\varepsilon_{jl} \end{pmatrix} \frac{\partial^2 \boldsymbol{u}}{\partial x_j \partial x_l} + \begin{pmatrix} \rho & 0 & 0 & 0 \\ 0 & \rho & 0 & 0 \\ 0 & 0 & \rho & 0 \\ 0 & 0 & 0 & 0 \end{pmatrix} \frac{\partial^2 \boldsymbol{u}}{\partial t^2} = \boldsymbol{F}_{ext}.$$
(20)

Considering a variational formulation, the interpolation of fields from their values at nodal points, and time harmonic fields, one assembles the differential equation into the generic finite element matrix [93]:

$$(K - \omega^2 M)\overline{u} = \overline{F_{ext}} \,. \tag{21}$$

where K is the generalized stiffness matrix, M the generalized mass matrix, $\overline{u}$ the vector of the generalized nodal displacements and $\overline{F_{ext}}$ the vector of generalized external forces.

Boundary conditions are added to this finite element equations and either force directly the value of some unknowns in $\overline{u}$, or introduce relationships between them and therefore modify the K and M matrices.

Once the problem is assembled into a finite element matrix, it can be solved in two ways:

1. The calculation of the (generalized) eigenvalues of the finite element problem (Equation (21)) provides the eigenfrequencies ω_i, which represent the natural frequencies at which a structure or system can enter in resonance. The corresponding eigenvectors $\overline{u_i}$ provide the spatial distribution of displacement fields and electric potentials defining the mode shapes.

   The eigenfrequency analysis is particularly useful when one wants to analyze the modal properties of a structure.

2. Solving the finite element system for nodal field values $\overline{u}$, on the other hand, allows for the investigation of the response of the model under harmonic excitation at specific frequencies ω. It is particularly useful when one wants to understand how the structure responds to different excitations.

Mathematically, the two approaches are complementary. The solution to the frequency domain analysis can write as a linear combination of the eigenvalues of the finite element system. This combination takes into account how much power each eigenmode gets under the excitation specified by the $\overline{F_{ext}}$ term, although the distribution of power among the various modes is not explicit.

1.2   Geometry considered

Hybrid SAW/BAW resonators are made of piezoelectric pillars arranged in a periodic array and deposited on top of a non-piezoelectric substrate. This geometry leads to the following assumptions:

1. The interdigitated transducers are characterized by a much greater aperture compared to their width or height. Therefore, the pillars are assumed to extend infinitely in the aperture direction, allowing the model to be simplified to a two-dimensional simulation with plane strain conditions. Under such conditions, the strains in the out of plane direction are assumed to be zero. This implies that mechanical displacement and electric fields are assumed uniform along the out of plane direction. Considering these fields in the two-dimensional plane only is sufficient to characterize the behavior of the structure [94] when dealing with c-axis oriented AlN as the piezoelectric material, as it does not cause the excitation of shear horizontal modes that would not be represented under plane strain condition with the current implementation of Comsol Multiphysics.

2. The substrate, considered to be semi-infinite, is represented by a section of material augmented with a Perfectly Matched Layer (PML). A PML is a computational technique used in numerical simulations as an artificial absorbing medium that is added to the edges of the computational domain. The primary purpose of a PML is to mimic an infinite domain by effectively absorbing any outgoing waves before they reach the end of the computation domain, where they would be reflected otherwise. It achieves this by gradually attenuating and absorbing the waves as they approach the boundary, ensuring minimal reflection and preventing them from reflecting back into the computational domain [95].

3. To account for the periodic nature of the system, we make the simplifying assumption that the array of pillars is infinite. This is achieved through the application of periodic boundary conditions at both edges of the computational domain along the periodicity axis of the structure, which is regarded as the propagation direction of the acoustic waves.

We apply more particularly Floquet conditions between the lateral edges of the computation domain. These conditions are derived from the Floquet theorem, which states that the solutions to a linear ordinary differential equation with periodic coefficients can be written as a product of a periodic function and a complex exponential term [96]:

$$\psi(x + d) = e^{ik_p d} \, \psi(x). \tag{22}$$

In this equation, $\psi(x)$ represents the periodic function, x the spatial coordinate, d is the period of the system, and k_p is the Bloch wave vector. The Floquet boundary condition states accordingly that the calculated mechanical or electric fields $\psi(x)$ must satisfy (Equation (22)), which essentially says that for the calculated fields to be solution of the periodic problem, they must be phase-shifted by $e^{ik_p d}$ when moving by one period. The Bloch wave vector k_p determines the spatial variation and propagation properties of the periodic solutions.

The structures we consider exhibit a structural periodicity p, corresponding to the periodicity of transducers. These transducers are usually excited with alternate polarities. Hence, only one every two transducers has the same excitation. Therefore, we have an electrical periodicity of *2p*. If we choose to simulate only one transducer, the behavior of the infinite array is considered by applying $k_p = \pi/p$ in order to represent the fact that the excitation of two adjacent transducers is in opposite phase. To ease the visualization of the solution, it is sometimes convenient to simulate two adjacent transducers. In this case, the unit cell made of these two transducers exhibit both the mechanical and the electrical periodicity. It is therefore repeated as is in the infinite array, and one should therefore consider $k_p = 0$, or equivalently $k_p = 2\pi/2p$ (the exponential term being 2π-periodic). It is interesting to note that the later corresponds to the same Bloch wavenumber as in the previous case, meaning that the calculation is equivalent and will provide the same Bloch mode.
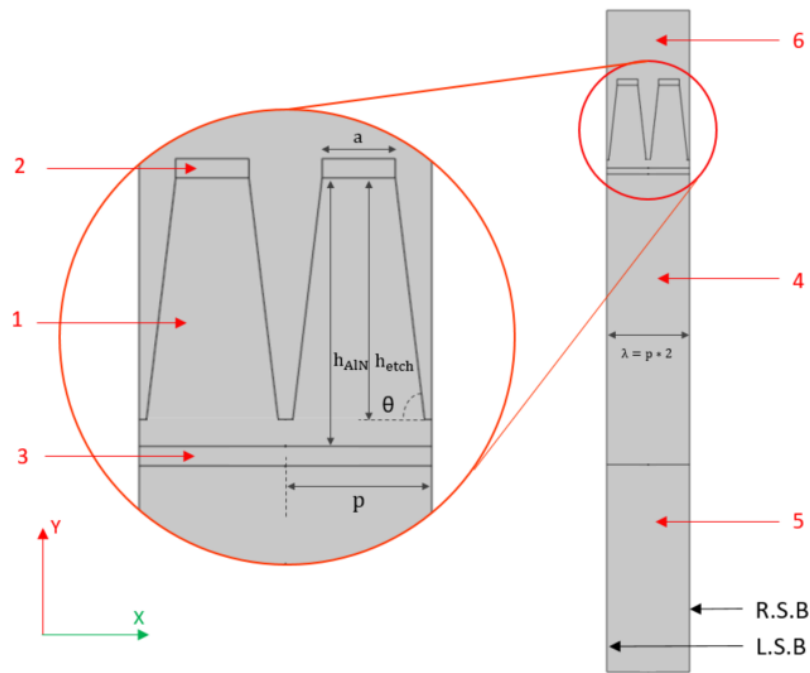
Figure 48: Unit cell considered for the analysis of hybrid SAW/BAW resonators.

Under these considerations, Figure 48 shows a slice made up of two pillars constituting a unit cell for representing this periodic structure. It comprises six domains. Domain 1 represents the piezoelectric material, enclosed between the top and bottom electrodes (domains 2 and 3, respectively). The pillars have a width a on their top, and are repeated with a spatial periodicity p. The piezoelectric pillars may not be fully patterned. Therefore we define an etching depth h_{etch} and leave some residual piezoelectric material at the bottom. For technological reasons, the pillars are usually not patterned with perfectly vertical sidewalls [84]: hence, the pillars sidewalls are considered slanted, with a sidewall angle θ. Finally, domains 4 and 5 encompass the substrate material (e.g., Silicon) which is extended by a Perfectly Matched Layer (PML), whose role is to avoid any reflection of acoustic waves at the bottom of the geometry, and thus to consider the substrate as semi-infinite.

Domain 6 encompasses the vacuum or air region around and between the pillars. This domain does not support mechanical fields and stress-free boundary conditions are therefore applied at the interface between the pillars and the vacuum. Vacuum however supports electric fields and an electric displacement. For the purpose of properly considering the continuity of the electric displacement at the boundaries between pillars and the vacuum, and thus not constraining the electric field only in the piezoelectric medium (what would artificially overestimate the effective electromechanical coupling of the modes considered), one needs therefore to consider this domain.
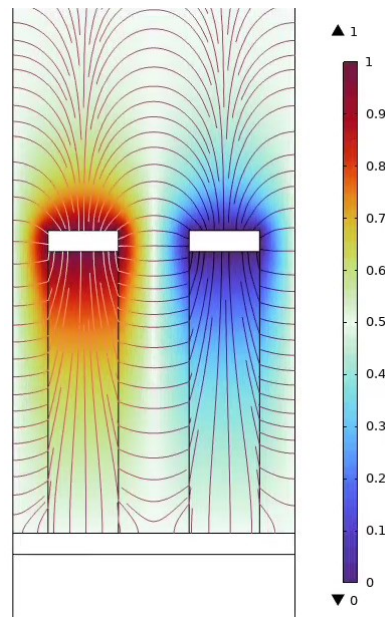
Figure 49: Electric potential (colors: red represents the maximum and blue the minimum potential) and electric field (arrows) propagating in the area between the pillars.

Figure 49 shows the electric potential distribution in and around two AlN pillars excited with opposite polarities. The color bar represents the electric potential : 1 V around the top left electrode, 0 V around the top right electrode, and the floating potential sets at 0.5 V. The arrows represent the electric field direction and magnitude in the dielectric and piezoelectric media. This plot shows that the electric field lines are quite confined in the piezoelectric medium (they are more vertical in-between the electrodes than above), but in the end they still escape the AlN and loop through air to reach the other electrode to which an electric potential is applied.

The electric field lines are concentrated in the piezoelectric pillars because of the higher dielectric permittivity of AlN ($\varepsilon_{33}^S = 9.5 \ 10^{-11}$ F/m) compared to vacuum ($\varepsilon \approx 0.88 \ 10^{-11}$ F/m), but not fully. The electric field lines leave the pillars laterally to follow more direct paths towards the other electrode to which an electric potential is applied, and some loop above the top electrodes. Without considering the vacuum, the electric field lines would be fully confined in the piezoelectric material, which would modify the static capacitance as well as overestimate the electromechanical coupling factor of the modes. This confirms the need to consider the vacuum. Failure to do so has led to inaccurate predictions for the performance of HSBR at the early stages and during the work of this thesis. The harmonic admittance lines with and without the consideration of air are shown in Figure 50 for the exact same structure. The static capacitance and the coupling factors of the different modes are visibly different.
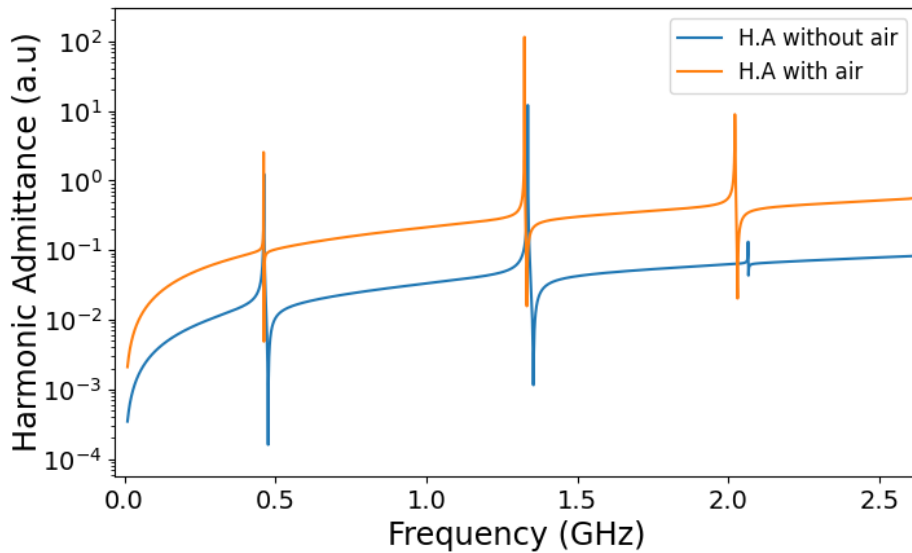
Figure 50: Harmonic Admittance with and without the consideration of air around the pillars. (this figure is produced for a Mo/AlN/Mo/Si structure with h/p=4, a/p=1 and etching ratio of 1)

For the sake of the analysis, we describe this geometry by normalized dimensions shown in Figure 48:

- the ratio between the piezoelectric thickness to the width of the pillars (h_{piezo}/p) is called the *thickness to pitch ratio* ,
- the ratio of the pillar height to the initial piezoelectric layer thickness (h_{etch}/h_{piezo}) is called the *etching ratio*
- the ratio of the pillar width a to the pitch p (a/p) is the *coverage ratio*.

1.3 Hybridization between surface waves and modes of a transducer

Before we consider a complete HSBR structure, we start by an analysis of the hybridization between a surface wave propagating atop an infinite substrate and bulk modes of a piezoelectric transducer. A simple slab of AlN can be used to identify the modes of a piezoelectric pillar with no substrate underneath.
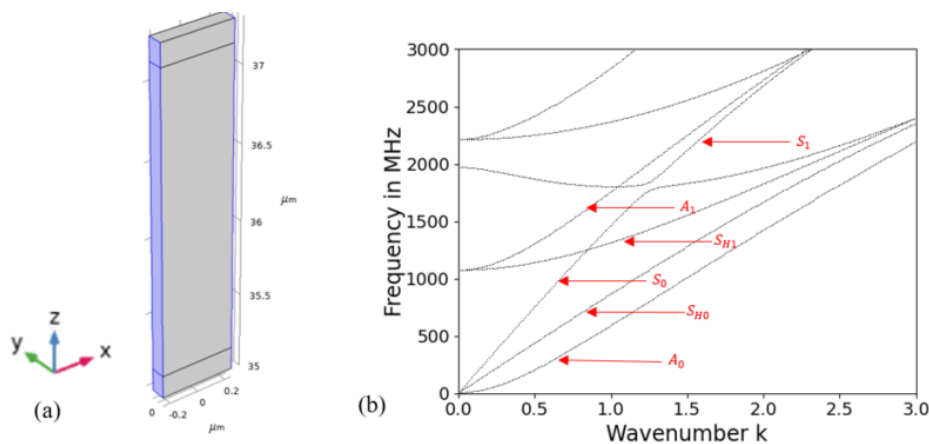
Figure 51: Analysis of an AlN transducer slab (a) and the corresponding dispersion curves revealing the supported Lamb wave modes (b) emphasis on the lowest order modes.

Figure 51 shows the dispersion curves of Lamb and shear horizontal modes in a metal/AlN/metal slab with propagation in the x-direction.

Here is a brief explanation of each of the resonance modes demonstrated in Figure 48:

1- A0 Mode: This refers to the fundamental or lowest-order anti-symmetric Lamb wave mode. It represents an anti-symmetric vibration pattern with respect to the middle XY surface.

2- A1 Mode: This is the first-order anti-symmetric Lamb wave mode. It represents an anti-symmetric vibration pattern in the XZ plane with respect to the middle XY surface.

3- S0 Mode: The S0 mode corresponds to the fundamental symmetric Lamb mode. It represents a symmetric deformation of the resonator in the XZ plane with respect to the middle XY surface.

4- S1 Mode: The S1 mode is the first-order symmetric Lamb wave mode. It represents a symmetric deformation of the resonator along in the XZ plane with respect to the XY surface. This mode is of special interest in the design of HSBR.

5- SH0 Mode: The SH0 mode represents the fundamental symmetric thickness-shear wave mode. It involves a shear deformation in the YZ plane which is symmetric with respect to the XY middle surface.

6- SH1 Mode: The SH1 mode is the first-order antisymmetric thickness-shear wave mode. It involves a shear deformation in the YZ plane which is anti-symmetric with respect to the XY middle surface.

Figure 52 shows sketches of their respective mode shapes.
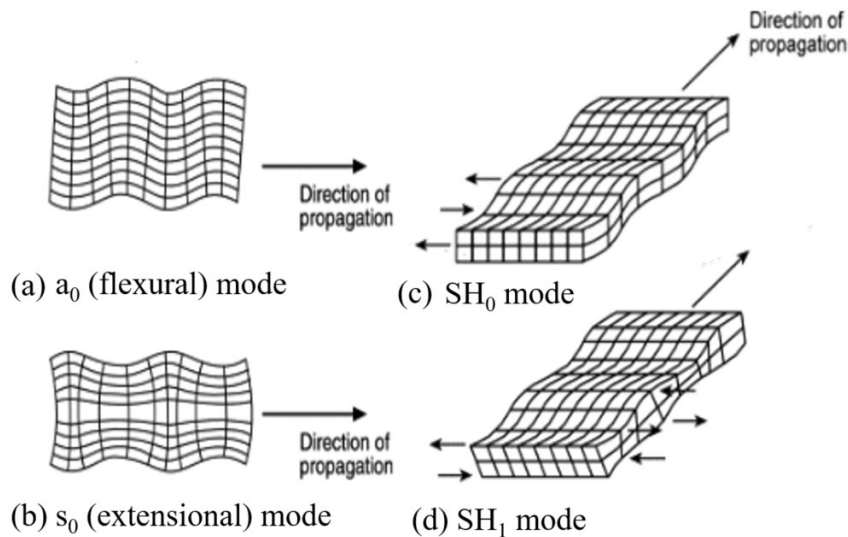
Figure 52: Schematic of the displacement and propagation directions of the length extensional (S0), flexural (A0) Lamb wave modes and fundamental and first order shear horizontal modes (SH0 and SH1) [97].

When a semi-infinite substrate is added underneath the slab, the calculation becomes more intricate. First, the PML representing its infinite extent fails to properly absorb waves when their wavelength becomes large compared to the artificial layer thickness. This causes the finite element model to consider the substrate as of finite size on the low frequency side. As a consequence, the structure appears as a thick slab, which supports many modes in the frequency range of interest. Eventually, for modes with a wave velocity faster than the slowest of the bulk shear waves of the substrate (i.e. located above the *sound line* [98]), radiation into the substrate excites in principle a continuum of modes. In practice, therefore, one can see the emergence of numerous eigenmodes that are closely spaced, making it challenging to discern them individually. Presenting dispersion curves, as done previously, therefore becomes impractical and lacks informative value apart from a limited region of the wavenumber – frequency space.
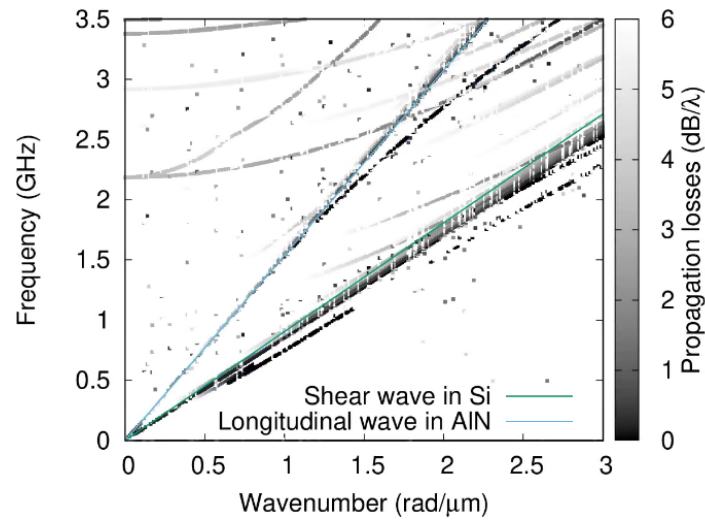
Figure 53: Dispersion curve for a Mo(150 nm)/AlN(2 µm)/Mo(150 nm) slab located on top of a semi-infinite Si substrate.

To address this issue, Figure 53 shows the resulting dispersion curves calculated by a modal analysis for the case of a Mo/AlN/Mo/semi-infinite Si continuous structure with colors related to the propagation losses calculated from the damping of the various modes related to their absorption by the PML. Darker lines represent the modes the best confined near the surface. They correspond mostly to the Rayleigh and shear horizontal surface waves propagating immediately below the sound line (green line in Figure 53). One can also distinguish some of the Lamb wave modes that appeared in Figure 51, but they are now strongly attenuated because they leak in the substrate.

Eventually, we define pillars in the AlN layer, with a periodicity p=1 µm. This now makes the structure fully periodic, resulting in mirroring the dispersion curves at $\pi/p = 3.4\ \mu m^{-1}$ due to the periodicity of the exponential term in the Floquet condition (Equation (22)). Aside from the periodicity, Figure 54 reveals some relatively flat bands that exit the sound cone, labelled 1 to 4. The corresponding mode shapes are plotted in Figure 55. They correspond respectively to the first flexural mode of the transducers, the so-called pseudo-SAW mode in the literature [54], the second order flexural mode of the transducers, and the so-called pseudo-BAW mode.
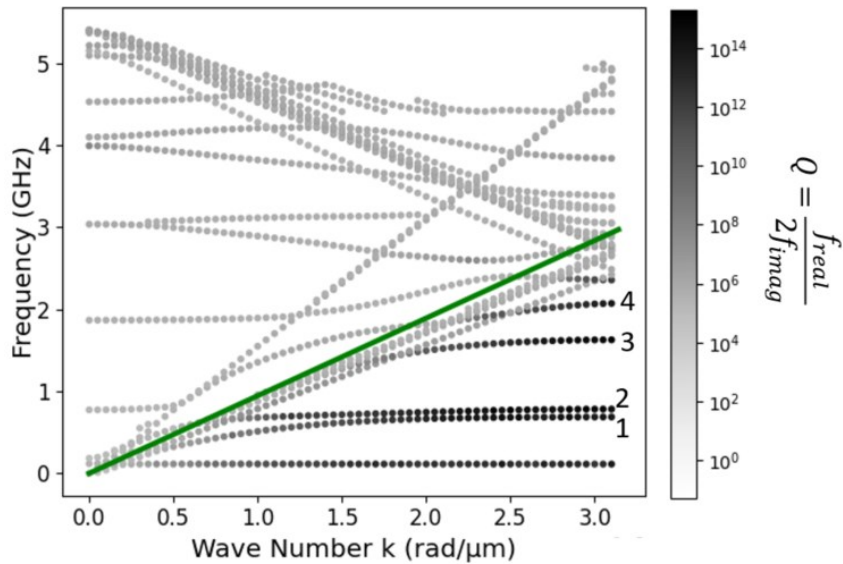
Figure 54: Dispersion curve of an AlN HSB based on the same stack Mo(150 nm)/AlN(2 μm)/Mo(150 nm) with patterning of p=1 μm. The green line is the sound line with equation: $f = k * (V_{Si} / 2 * \pi)$
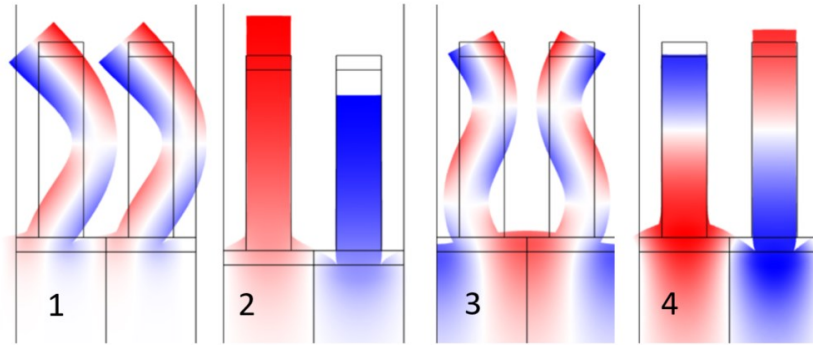
Figure 55: Mode shape of the 4 lowest order modes identified in Figure 54, calculated at the edge of the first Brillouin zone for $k_p = \pi/p$. Colors represent the vertical displacement fields.

A frequency domain analysis is more convenient to reveal modes of the structure, despite possible radiation into the substrate. In addition, it also provides information about which modes are really excited, and how they contribute to the electric response. However, the electric configuration of the structure affects significantly the way the various modes are excited. The configuration classically proposed in the literature [56] is represented in Figure 56. This constitutes the excitation by an alternate voltage applied to the top electrodes, while the common bottom electrode is floating. We represent this by modelling two adjacent transducers with Floquet boundary conditions set to a wavenumber $k_p = \pi/p$, and applying a 1 V voltage to one of the top electrodes, and grounding the second one. The common bottom electrode is floating: its electric potential is uniform, and the net charge accumulated at the level of the electrode is forced to zero.
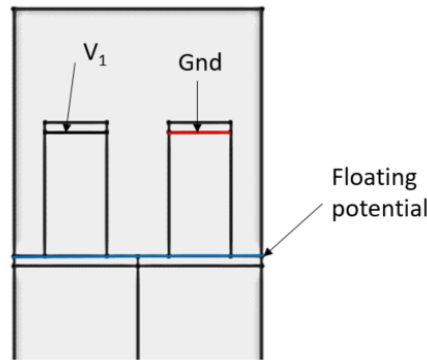
Figure 56: Schematic of the applied electric configuration for the excitation of the pseudo-SAW and the pseudo-BAW modes.

In this configuration, the electric response is calculated as the admittance $Y = I / V$, where V is the voltage applied to one of the top electrodes and I the resulting current flowing through it. Due to the periodic boundary condition, this admittance is therefore to be considered as the self-admittance of one particular transducer considered among the infinity of transducers in the periodic array. In order to distinguish this quantity from the actual admittance of a device, it is called a *harmonic admittance* [99]

The calculation of this harmonic admittance, shown in Figure 57, indicates that only two modes are excited in this configuration. They correspond to the pseudo-SAW and the pseudo-BAW modes introduced in [54]. Their mode shapes and frequencies are the same as the modes 2 and 4 revealed by the dispersion curves of Figure 54.
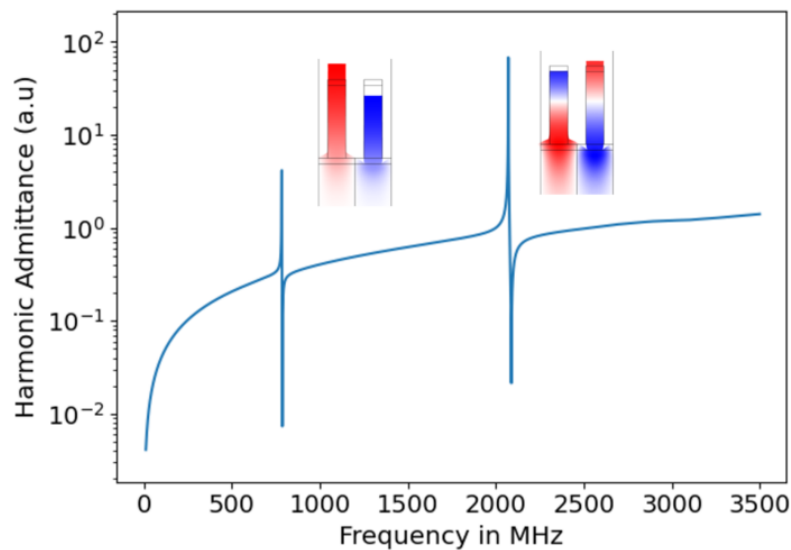
Figure 57: Harmonic admittance calculation for a HSBR with top electrodes alternatingly set to the excitation voltage and to ground, and the common bottom electrode left floating using Mo(150 nm)/AlN(2 μm)/Mo(150 nm). Insets are the modes shapes (colors represent vertical displacements) for the pseudo-SAW and pseudo-BAW modes.

The resonant behavior of the transducer array can be understood by examining these two modes. The pseudo-SAW mode, depicted in Figure 57 (left), is characterized by a rigid translation of the transducer, with a Rayleigh mode propagating on the top surface of the substrate.

It appears at approximately 0.8 GHz. Its effective wave velocity is therefore approximately 1600 m/s, i.e. significantly less than the shear wave or even than the Rayleigh wave velocity in silicon. It

is therefore confined in the vicinity or within the array of transducers. As a result, its propagation losses are very small and it is expected to exhibit high-quality factors (Q).

In contrast, for the pseudo-BAW mode, illustrated in Figure 57 (right), the individual transducers experience a thickness resonance mechanically loaded by the acoustic impedance of the substrate. This mode appears close to 2.2 GHz. Its effective wave velocity is therefore approximately 4400 m/s and can easily reach 5000 m/s for AlN thickness of 1 µm, i.e. close to the Rayleigh wave velocity in silicon [100], but still slower than shear waves in this material (5840 m/s). It remains therefore also confined near the surface of the substrate.

The pseudo-BAW mode is of particular interest due to its operation at high frequency (here 2.2 GHz) and for achieving a large electromechanical coupling factor (k²) up to 6.8% using AlN according to Pashchenko *et al.* [56]. In Figure 57, however, its electromechanical coupling factor is only 2%. The purpose of the next section is therefore to improve this figure appropriately.

Most theoretical studies based on AlN presented in Chapter 1 did not consider the contribution of air around pillars. Our simulations show that while the contribution of air is usually small in most surface or bulk acoustic wave application, this contribution becomes significant due to the large volume fraction of air (50%) included here in between the transducers. The comparison between the performance of pseudo-SAW and pseudo-BAW theoretical performance when air is considered and when it is not considered in presented in Figure 58. The k_t^2 without the consideration of air is close to the results presented in the literature in Table 2.
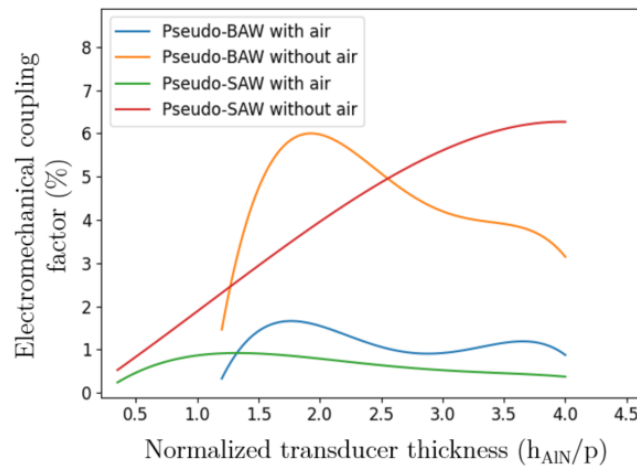
Figure 58: The effect of air consideration on the k^2 of the pseudo-SAW and pseudo-BAW (Mo/AlN/Mo/Si with a/p=0.5, El/p=0.16, etching ratio=1 with straight sidewalls)

2   Design optimization

The HSBR structure is quite sensitive to changes in the geometry, transducer materials or the substrate materials. In this section we optimize these three parameters. We consider a transducer geometry normalized by their pitch so that its frequency can be scaled accordingly based on the end application.

2.1 Transducers thickness

Figure 59: Simplified diagram showing the components of the thickness to pitch ratio and coverage ratio

Figure 59 shows a simplified version of Figure 48 where the parameters 'a' representing the width of the pillar, 'p' representing the periodicity pitch and 'h_{AlN}' representing the height of the AlN pillars are shown clearly. The transducer thickness to pitch ratio (h_{AlN}/p) is the most influential parameter on the performance of the Hybrid SAW/BAW devices. This means that the performance of the HSBR in terms of its resonance frequency at least can be controlled by changing the pitch which in real life is photo-lithographically controlled. Figure 60 provides the dependence of the Pseudo-SAW mode and the Pseudo-BAW mode effective velocities on the thickness to pitch ratio while the immediate electromechaical coupling factors can be seen on Figure 58 with air considered (corresponding line colors).
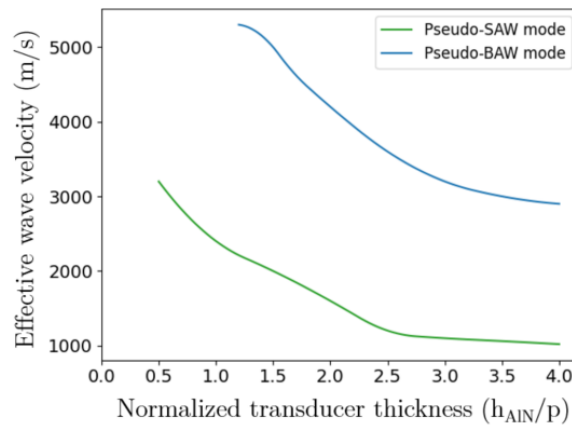
Figure 60: Effective wave velocity (V = 2fp) of the pseudo-SAW and the pseudo-BAW modes versus transducers thickness (Mo/AlN/Mo/Si with a/p=0.5, El/p=0.16, etching ratio=1 with straight sidewalls).

Figure 60 shows that for both modes, thicker transducers decrease the velocity of the waves, in part due to their mass-loading effect. The maximum velocity of the pseudo-SAW mode is approximately 3200 m/s, for a thickness to pitch ratio of 0.5. At this point however, its electromechanical coupling factor approaches 0, as visible in Figure 58. The optimum electromechanical coupling factor is close to $h_{AlN}/p = 1.2$, where it reaches 0.9%, for an effective velocity of 2000 m/s. On the other hand, the pseudo-BAW mode can reach velocities up to 5300 m/s for a thickness to pitch ratio of 1.2, below which its electromechanical coupling factor becomes very small. The maximum electromechanical coupling factor is reached for $h_{AlN}/p = 2$, where it reaches 1.6%. Its effective wave velocity is then about 4200 m/s. It does therefore not radiate in the substrate. This is consistent with other studies from the literature that studied this parameter who found it to have an optimum value for the coupling factor, yet their optimum value was slightly shifted [56], [66].

2.2   Electrodes thickness

The performance of HSBR relies on the transducer structure as a whole. Since the piezoelectric pillars are sandwiched on top and bottom by metal electrodes to establish the electrical contact, these electrodes constitute an integral part of the transducer structure and impact its performance.

The electrode thickness influences the electrical resistance of the electrodes. Thicker electrodes tend to have lower resistance, which can increase electrical losses. The electrode have also a mechanical influence: they affect both the wave velocity and the electromechanical coupling factor and the resonance frequency. Figure 61 shows that the effective wave velocity of the pseudo-SAW mode decreases with increasing the thickness of the top electrode, what can be attributed to increased mass-loading by the electrode. However, we can notice an opposite trend regarding the bottom electrode: increasing its thickness increases slightly the wave velocity. This could be related to the fact that a thicker Mo layer increases the stiffness of the substrate (c_{33} = 440 GPa and c_{44} = 96 GPa for Mo, to be compared to c_{33} = 160 GPa and c_{44} = 80 GPa for Si). The plot of the evolution of the electromechanical coupling factor versus electrode thicknesses highlights that for thin bottom electrodes ($El_{bottom}/p \leq 0.1$), the dependence of k^2 on the top electrode thickness is not monotonous: it exhibits a minimum near $El_{top}/p = 0.13$. For $El_{bottom}/p > 0.16p$, its thickness loses a significant influence, while k^2 increases with the top electrode thickness. k^2 can increase from 0.85 to 1.35% when increasing the top electrode thickness from 0.1p to 0.24p. For a typical pitch of 1 μm, this means an increase from 100 nm to 240 nm. Although this figure can be theoretically extended to El/p up to 2 (an increase to El= 2 μm for a typical p=1 μm) reaching k^2 of 2% where it saturates and remains constant, this would be change the structural problem to be technologically attained and would reduce the effective velocity to 400 m/s.

Figure 61: Evolution of effective wave velocity (a) and k^2 (b) for pseudo-SAW mode versus thickness of the top and bottom electrodes (Mo/AlN/Mo/Si with h/p=2, a/p=0.5, etching ratio=1 with straight sidewalls).

The dependence of the effective velocity and the electromechanical coupling factor of the pseudo-BAW mode are shown in Figure 62. The behavior of this mode is different from the pseudo-BAW mode: the wave velocity decreases with increasing any of the top or bottom electrode thickness, potentially because this mode is less sensitive to the thickness of the substrate than to the frequency of the thickness mode of the transducers which decreases with electrodes thicknesses. Unlike also the pseudo-SAW mode, the electromechanical coupling factor depends on the bottom electrode thickness although the difference accounts only for a 0.2% electromechanical coupling factor increase between a thickness of 0.1 p and 0.24 p. The effect of the top electrode is similar to what was observed for the pseudo-SAW: the thicker the top electrode the better the electromechanical coupling factor.
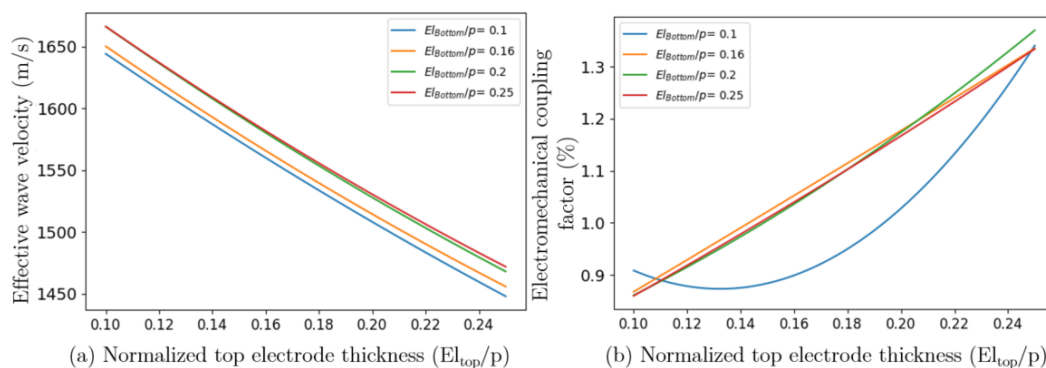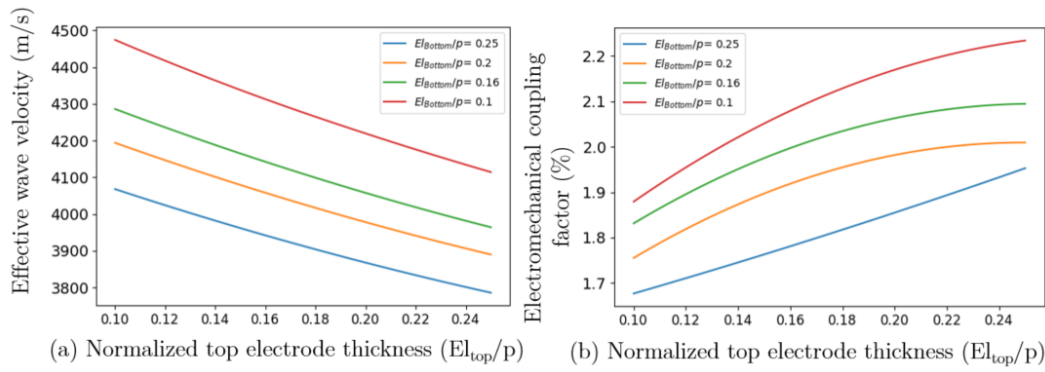
Figure 62: Evolution of (a) effective wave velocity and k^2 (b) for the pseudo-BAW mode versus the thicknesses of the two electrodes. (Mo/AlN/Mo/Si with h/p=2, a/p=0.5, etching ratio=1 with straight sidewalls).

Zhang *et al.* [60] considered this parameter and reached a similar conclusion concerning the pseudo-SAW mode: the increase in the electrode thickness leads to an increase in the coupling factor, but their results were different concerning the pseudo-BAW mode which they found to be harmed by the increase in the thickness of the electrode as shown in Figure 34.

2.3   Electrodes material

The mechanical influence of the electrodes depends not only on their thickness, but also on their stiffness and density. We investigate therefore also the influence of other metals than the molybdenum conventionally employed in the CEA-LETI AlN process. The choice of metal is conditioned by the need for a good electric conductivity, and its compatibility with the fabrication processes used to manufacture the resonator. It should be able to withstand the required deposition techniques, patterning methods, and subsequent processing steps without degradation or damage.

The acoustic impedance of the electrode material is known to contribute to the confinement of acoustic power within the piezoelectric layer in BAW resonators [101]. For this reason, electrodes with a high acoustic impedance lead to improved electromechanical coupling factors in these devices.

Figure 63: The evolution of the effective wave velocity (a) and k^2 (b) for pseudo-SAW with the transducer thickness for different electrode materials (Metal/AlN/Metal/Si with h/p=2, a/p=0.5, El/p=0.16 etching ratio=1 with straight sidewalls).

To investigate if this is also the case for the hybrid SAW/BAW modes, we consider Al (Aluminum), Ru (Ruthenium) and W (Tungsten) as electrode candidates in addition to Mo. Figure 63 and Figure 64 show the evolution of the effective wave velocity and the electromechanical coupling factor of both the pseudo-SAW and the pseudo-BAW modes, respectively.
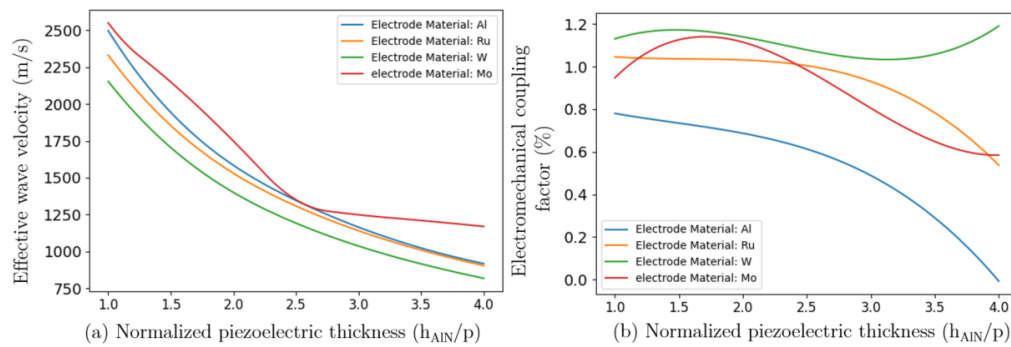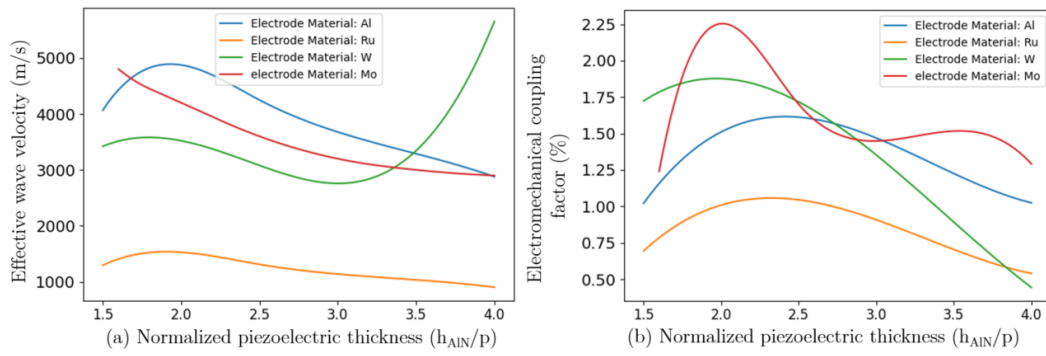
Figure 64: The evolution of the effective wave velocity (a) and k² (b) for pseudo-BAW mode with the transducer thickness for different electrode materials(Metal/AlN/Metal/Si with h/p=2, a/p=0.5, El/p=0.16 etching ratio=1 with straight sidewalls).

The k^2 is affected by the change of electrode material compared to Mo electrodes, and evolve as a function of the ratio between the metal and piezoelectric layer thickness. This is achieved by maintaining the electrodes thicknesses constant ($El_{top}/p = El_{bot}/p = 0.16$), while varying the piezoelectric film thickness. Al electrodes clearly worsens the performance of the pseudo-SAW mode. Ru provides almost similar k^2 to Mo, while W always improves performances. Given that Al has a lower acoustic impedance than Mo, Ru a similar one compared to Mo, and W a larger one, this tends to indicate that electrodes with a high acoustic impedance favor the confinement of the pseudo-SAW mode in the transducers, which improves its electromechanical coupling factor. For the pseudo-BAW mode, the influence of the electrode metal seems less obvious: Mo seems to be the best candidate while Ru performs the worst. W does in this case not provide the best electromechanical coupling factors, indicating that for this mode, what indicates that its behavior is different from the one of conventional thickness modes in BAW resonators. Xu *et al.* [64] consider the thickness and the material of the electrodes shown in Figure 31 but only consider Al and Cu on ZnO/SiC, results are thus difficult to compare.

2.4   Coverage ratio
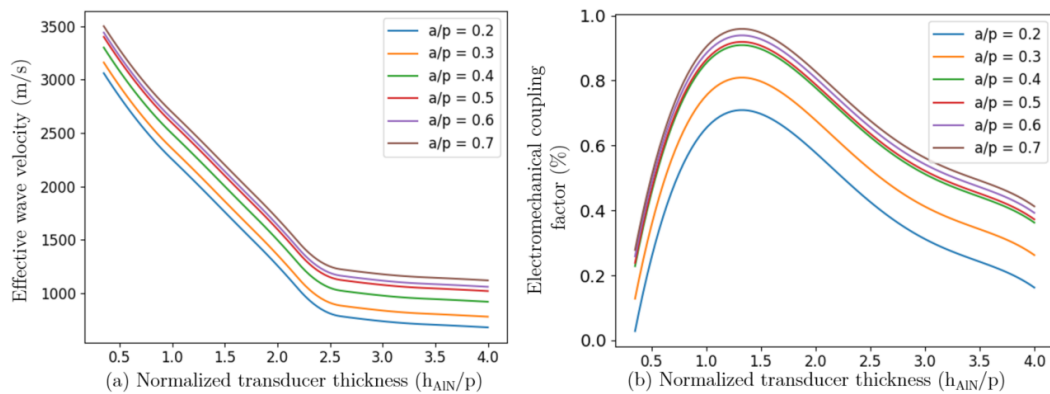
Figure 65: The evolution of the effective wave velocity (a) and k² (b) for pseudo-SAW mode with the transducer thickness to pitch ratio at different coverage ratios (Mo/AlN/Mo/Si with El/p=0.16 etching ratio=1 with straight sidewalls).

The coverage ratio, a/p, is another significant parameter that warrants careful consideration in resonator design. This ratio directly influences the width of the transducers and therefore their interaction with the substrate underneath. It also affects the gap between transducers, and therefore the strength of the electrostatic interaction between neighboring transducers.

Figure 66: The evolution of the effective wave velocity (a) and k² (b) for pseudo-BAW mode with the transducer thickness to pitch ratio at different coverage ratios (Mo/AlN/Mo/Si with El/p=0.16 etching ratio=1 with straight sidewalls).

Figure 65 and Figure 66 illustrate the impact of the coverage ratio on the effective wave velocity and electromechanical coupling factor of the pseudo-SAW and the pseudo-BAW, respectively. They show that, betwe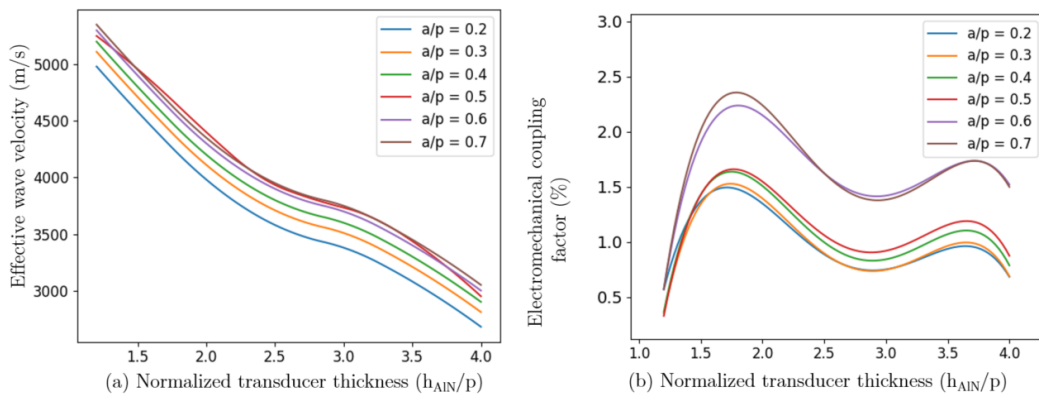en $a/p = 0.2$ and $a/p = 0.7$, the electromechanical coupling factor of both the pseudo-SAW and pseudo-BAW modes increase with a/p and that this parameter is relatively independent of the h_{AlN}/p, so both can be optimized independently. The pseudo-SAW mode can be improved from $k^2 = 0.9\%$ at $h_{AlN}/p = 1.2$ and $a/p = 0.5$ to 0.95% for the same height to pitch ratio and $a/p = 0.7$. Similarly, the pseudo-BAW mode can be improved from $k^2 = 1.6\%$ at $h_{AlN}/p = 1.8$ and $a/p = 0.5$ to 2.4% at $a/p = 0.7$. Technologically, however, the larger a/p, the smaller the width of the trench separating two adjacent transducers, and therefore the more challenging the patterning of the piezo-electric layer is. Because of the relatively low wave velocities of the hybrid SAW/BAW devices, and therefore the small wavelengths when aiming at high frequencies (above 2 GHz) which easily cause the periodicity to approach 1 µm, it seems reasonable to maintain coverage ratios close to 50%, to strike a balance between transducer widths and being able to properly etch narrow trenches to separate the transducers. Lang *et al.* [83] briefly considered the effect of the coverage ratio change of 0.4,0.5,0.6 in their initial study before fixing it to 50% with no trend established.

2.5 Partial etching of the piezoelectric layer
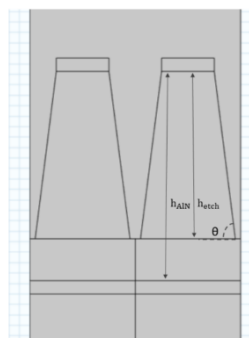
Figure 67: Simplified diagram showing the components of the etching ratio and etching angle

So far, we assumed that the piezoelectric layer was fully etched, with an etching ratio h_{etch}/h_{AlN} assumed to be 100%. The initial assumption was that this would best define the transducers and therefore facilitate their deformation, thus promoting large effective coupling factors. For techno-logical reasons, it may be unavoidable to leave some piezoelectric material at the bottom of the trenches separating transducers. This can be due to etching chemicals having difficulties to reach the bottom of the trenches at high aspect ratios, or on purpose to avoid damaging the bottom elec-trode if the patterning process of the piezoelectric layer lacks enough selectivity with respect to the

metal layer underneath. Leaving a piezoelectric material such as AlN can also be a way of position-ing transducers atop a stiffer substrate, what could potentially increase the wave velocity. This prompted the investigation of the effect of this left over AlN on mode properties.
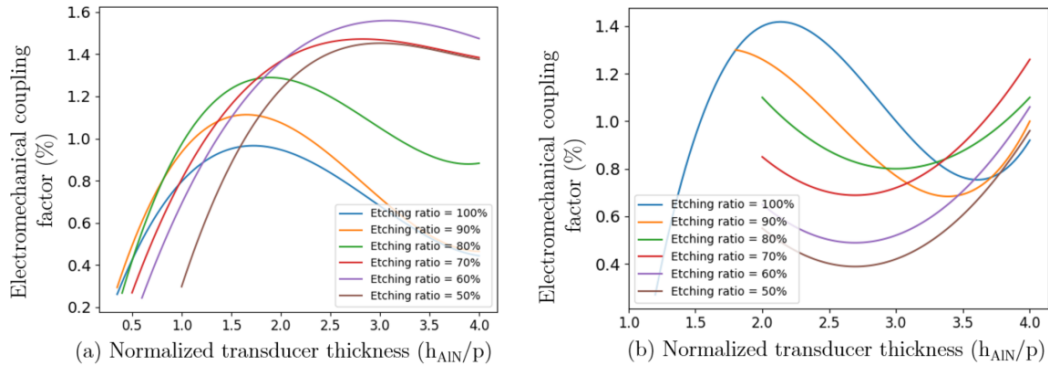
Figure 68: Evolution of the electromechanical coupling factor for the pseudo-SAW (a) and the pseudo-BAW (b) modes with thickness to pitch ratio, at different etching ratios (Mo/AlN/Mo/Si with a/p=0.5, El/p=0.16 with straight sidewalls).

Figure 68 reports the evolution of the electromechanical coupling factor of the pseudo-SAW and the pseudo-BAW modes as a function of the etching ratio. The performance is still being plot against the transducer thickness to pitch ratio since both parameters do not appear to be independent. It appears that an etching ratio of 100% is not optimum for the performance of the pseudo-SAW mode. k^2 can be improved from 0.9% at $h_{AlN}/p = 1.8$ and $h_{etch}/h_{AlN} = 100\%$ to 1.5% for $h_{AlN}/p = 3$ and $h_{etch}/h_{AlN} = 60\%$.

The pseudo-BAW mode displays a different behavior. An etching ratio of 100% seems to be optimum for k^2 except at very high thickness to pitch ratios beyond 3.7. At lower etching ratios and with the increase in the thickness to pitch ratio, the coupling is now hitting a trough before increasing again. A minimum performance point is at and etching ratio of 50% and below. Maximum k^2 of 1.4% is achieved at an etching ratio of 100% and thickness to pitch ratio of 2.

The etching ratio has been studied multiple times in the literature [56], [59] with agreement that an etching ratio of 100% is not always optimal (Figure 19 and Figure 22). The red lines in Figure 19 corresponding to ($h/\lambda=1$) show the optimal etching ratio for the pseudo-SAW mode is between 0.6-0.8 and the optimal point for the pseudo-BAW mode is at 100% etching in agreement with the results presented here.

2.6   Sidewall angle

The sidewall angle θ of the transducers is another parameter related to the geometry of the trans-ducers. The sidewall angle has a maximum of 90° for perfectly vertical transducers, but for slanted pillars the minimum value is not straight forward, as it also depends on the spacing between adjacent transducers and the depth of these trenches, which defines the smallest angle before which the gap between the transducers closes. Figure 69 shows the evolution of the electromechanical coupling factor with the sidewall angle for both pseudo-SAW and pseudo-BAW modes.

Figure 69: Evolution of k^2 for the pseudo-SAW (a) and the pseudo-BAW (b) modes with the sidewall angle for different etching ratios (Mo/AlN/Mo/Si with h/p=2, a/p=0.5, El/p=0.16).
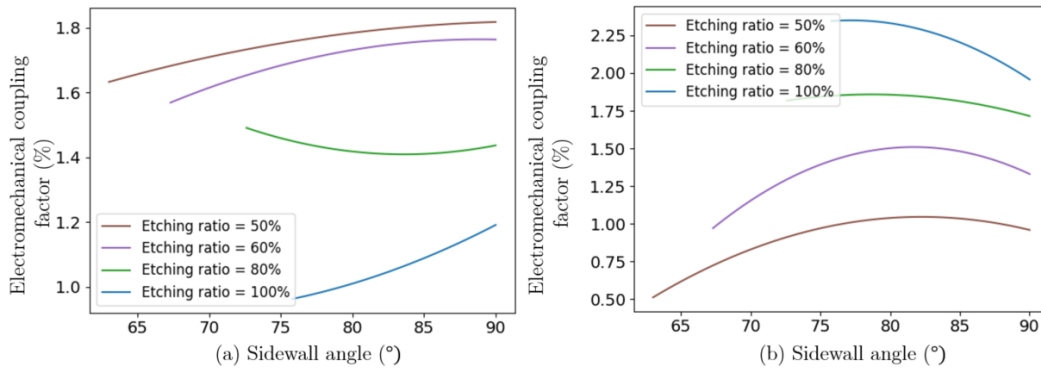
As seen in Figure 69, the sidewall angle has a small effect on the electromechanical coupling factor of both the pseudo-SAW and pseudo-BAW modes, but it is still noticeable. This effect seems however to depend also on other parameter, such as the depth of the trenches separating the transducers. For both pseudo-SAW mode, perfectly vertical sidewalls seem to provide the best electromechanical coupling factors. The one exception is for the pseudo-SAW mode at etching ratio of 80%, where slanted sidewalls near 74° seem to improve the electromechanical coupling factor slightly. For the pseudo-BAW mode, a specific angle seems always to maximize the electromechanical coupling factor. This angle varies with the depth of the trench separating transducers, and seems to decrease with increasing depth down to 75° for a fully etched trench. At this point, the maximum electromechanical coupling factor achieved is 2.3%. The effect of this parameter on HSBR was not really investigated in literature, but the etching of AlN with straight sidewall has been investigated by many like Gorisse *et al.* [84] for example.

2.7   Silicon Dioxide layer

Figure 70: Evolution of the effective wave velocity (a) k^2 (b) for the pseudo-SAW mode with the thickness of the SiO$_2$ layer, at different thickness to pitch ratios (Mo/AlN/Mo/SiO$_2$/Si with a/p=0.5, El/p=0.16, with etching ratio=1 and straight sidewalls).

In the conventional AlN process used at CEA-LETI, Mo / AlN / Mo stacks are deposited on SiO$_2$. This layer of insulating material prevents directly contacting the bottom electrode on silicon, which is not a perfect insulator, even if high resistivity substrates are employed. Figure 70 and Figure 71 present the dependence of the effective wave velocity and the electromechanical coupling factor of both the pseudo-SAW and the pseudo-BAW on SiO$_2$ thickness, for different normalized transducer thicknesses. For the pseudo-SAW, k^2 decreases with increasing SiO$_2$ thickness. The dependence is a little less straightforward for the pseudo-BAW mode. Figure 70(b) that the SiO$_2$ layer improves the electromechanical coupling factor. This behavior is particularly pronounced for a normalized

piezoelectric thickness of $h_{AlN}/p = 1.5$. The electromechanical coupling factor increases almost 0% to 2.5% for SiO$_2$ thicknesses ranging from 0 to 0.7p, before decreasing back to below 1% for h_{SiO2}/p larger than 1.5.

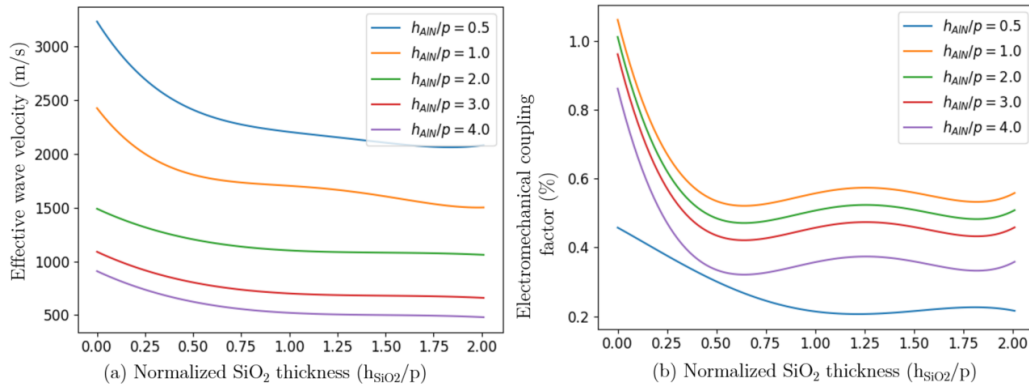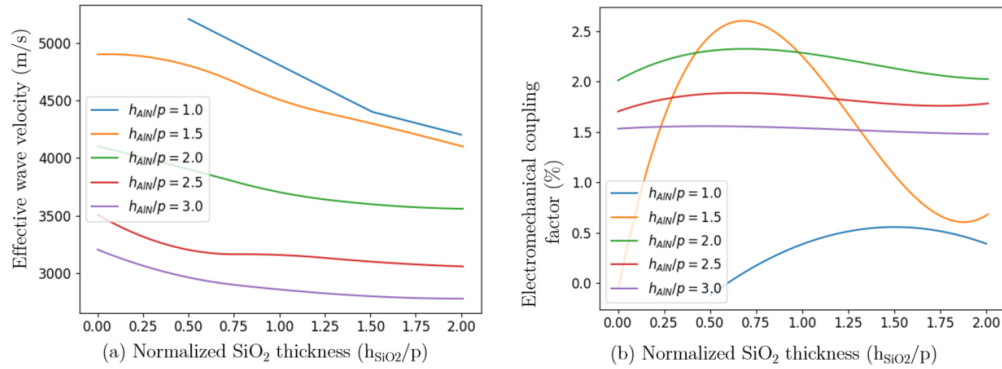
Figure 71: Evolution of the effective wave velocity (a) k2 (b) for the pseudo-BAW mode with the thickness of the SiO$_2$ layer, at different thickness to pitch ratios (Mo/AlN/Mo/SiO$_2$/Si with a/p=0.5, El/p=0.16, with etching ratio=1 and straight sidewalls).

2.8   Substrate material

The analysis of the influence of the previous parameters has highlighted that the velocity of the pseudo-BAW mode can be increased beyond the velocity of shear waves in silicon, what can cause radiation in the substrate, and thus introduce losses. Increasing the acoustic velocity of the pseudo-BAW mode is however necessary if one wants to address high frequency application without exposing sub-micron pitches that would be difficult to implement. To maintain losses low, it may be interesting to replace the Si substrate with a substrate of higher acoustic velocity, such as the ones listed in Table 3.

Table 3: Bulk wave velocities for high velocity substrates.

Substrate	Bulk longitudinal wave velocity (m/s)	Bulk transverse wave velocity (m/s)	Reference
Diamond	18,000	12,000	[102]
Gallium nitride	8,100	4,150	[103]
Sapphire	11,000	6,200	[104]
Silicon	8,430	5,840	[100]

Figure 72: Evolution of effective wave velocity (a) and k^2(b) of pseudo-SAW mode with transducer thickness to pitch ratio for different substrate materials (Mo/AlN/Mo/Substrate with a/p=0.5, El/p=0.16, with etching ratio=1 and straight sidewalls).

Figure 72 presents the impact of using these substrate materials on the pseudo-SAW mode. As expected, since diamond and sapphire substrates are very stiff, they cause an increase in the effective wave velocity from 2600 to 3600 m/s. On the other hand, we notice little variations of the acoustic velocity when considering GaN compared to Si, since its bulk wave velocities are very close to those of silicon. This indicates that the stiffness of the substrate alone is not the In the meantime, the k^2 achieved by the pseudo-SAW mode using a diamond substrate is much higher than with any other substrate material: 3.4% instead of 1.5% when using silicon. Unexpectedly, all other substrate materials seem to decrease the electromechanical coupling factor. The large increase in k^2 observed for diamond is therefore not simply related to the high velocity or high acoustic impedance of the material, and thus to the confinement of the waves in the transducer.

Another interesting observation is that for piezoelectric layer thicknesses larger than 3.2 times p, the nature of the substrate material does no longer influence the effective wave velocity or the electromechanical coupling factor.
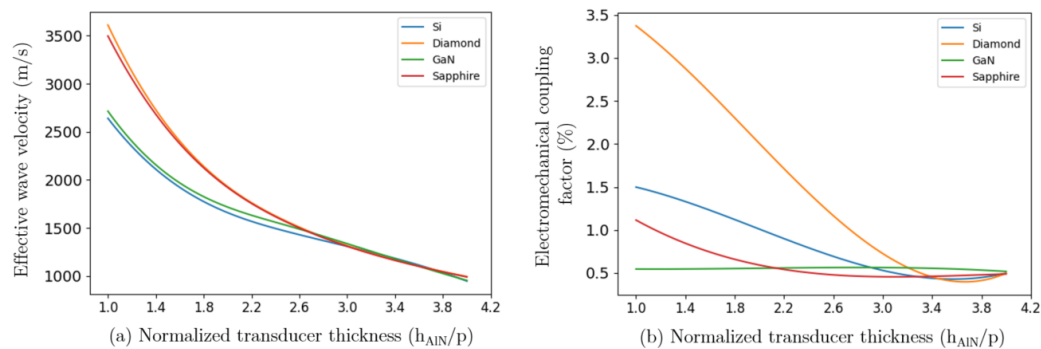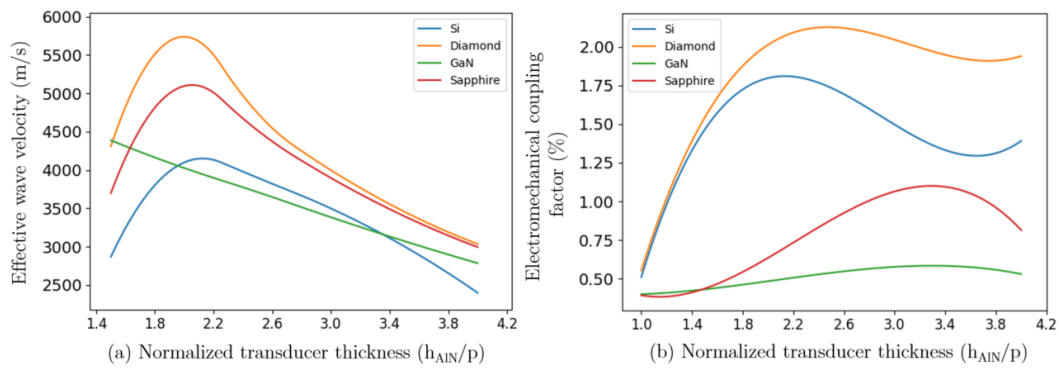

Figure 73: Evolution of the effective wave velocity (a) and k^2 (b) for the pseudo-BAW mode versus piezoelectric film thickness for different substrate materials. Other parameters considered are identical to those of Figure 72.

Figure 73 shows the impact of the substrate material on the pseudo-BAW mode. Again, diamond and sapphire cause a noticeable increase in effective wave velocity compared to silicon, with a maximum wave velocity of 5600 m/s. As for the pseudo-SAW mode, one can notice an increase in k^2 when using a diamond substrate compared to Si, from 1.75 to 2.1%, while the other substrates considered (sapphire and GaN) cause instead a decrease. Contrary to the pseudo-SAW mode, however, the nature of the substrate continue to affect the effective wave velocity or the electromechanical coupling factor when the transducers are relatively thick ($h_{AlN}/p > 3.2$). Again, there is however no direct correlation between k^2 and the acoustic impedance of the substrate, or between the effective velocity and the wave velocity of the substrate, meaning that the interaction between the transducer and the substrate are more complex than a simple mechanical loading.

Liu *et al.* [57] explored the effect of a high velocity acoustic layer insertion demonstrated in Figure 24. Their conclusion are in agreement regarding the superior performance of diamond. As depicted in Figure 24, once the thickness of the layer increases beyond a threshold (one λ), the coupling factor saturates and basically the thickness no longer affects it like an infinite substrate.

3 Conclusions

In this chapter, the focus was on simulating Hybrid SAW/BAW resonators and identifying various resonance modes. These modes arise from the hybridized structure and are highly contingent on structural geometry and material properties. Amid the multitude of modes, a harmonic admittance analysis facilitated the identification of two modes with the strongest coupling, warranting optimization efforts: the pseudo-SAW and pseudo-BAW modes.

Numerous parameters can be independently adjusted to control frequency or enhance the coupling factors of these modes. If these parameters are to be considered together, comprehensive consideration of their dependence and iterative optimization is needed. The result of this iterative process for the pseudo-SAW mode is shown in the harmonic admittance in Figure 74. The pseudo-SAW mode is displaying a k^2 of 3.6% at 1.8 GHz (an effective velocity of 3600 m/s). This is achieved using Mo/AlN/Mo/Diamond with $h_{AlN}/p= 1$, a/p=0.5, El/p=0.08, full etching and straight sidewalls. Despite the improvement of the pseudo-SAW with incomplete etching on Silicon, full etching is optimum on Diamond.

Figure 74: optimum design for the pseudo-SAW mode achieved using Mo/AlN/Mo/Diamond, h/p=1, a/p=0.5, El/p=0.08, etching ratio of 1 and straight sidewalls.

While electromechanical coupling and resonance frequency occasionally respond inversely to parameter variations, a balance can be achieved. This, combined with the challenge of producing a clean peak with no spurious interactions in the vicinity, complicates the problem for the pseudo-BAW mode. Figure 75 illustrates the harmonic admittance analysis for an optimal and clean pseudo-BAW mode design employing a diamond substrate, $h_{AlN}/p = 2.4$, a/p = 0.6 (since higher coverage ratios are practically challenging to attain), an etching ratio of 1, and straight sidewalls. In this configuration, the pseudo-BAW mode demonstrates an effective wave velocity of 5100 m/s and k² of 2.35%, while the pseudo-SAW mode exhibits suboptimal performance with a velocity of 1700 m/s and k² of 1.5%. Notably, variations in the thickness of the top and bottom Mo electrodes exhibit a minimal impact on k² (<0.1%) within this structure.
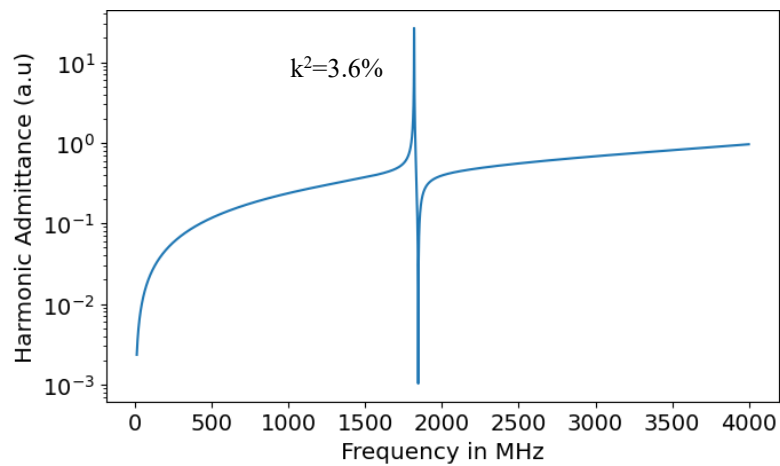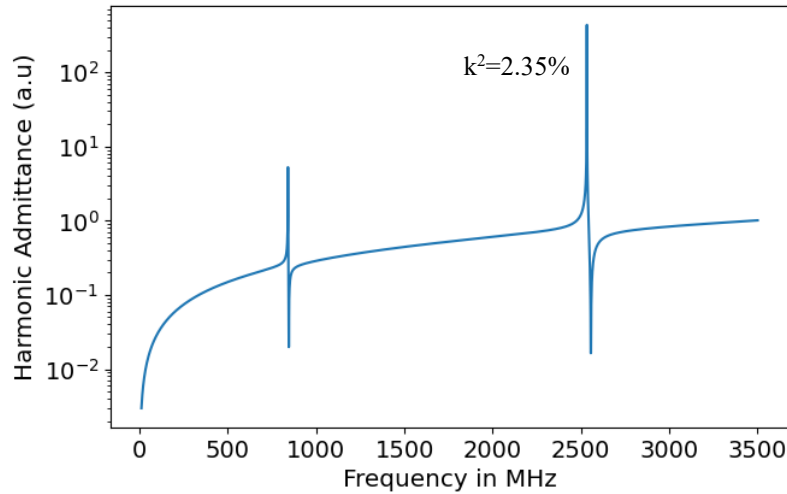
Figure 75: optimum design for the pseudo-BAW mode achieved using Mo/AlN/Mo/Diamond, h/p=2.4, a/p=0.5, El/p=0.16, etching ratio of 1 and straight sidewalls.

On a more realistic note, diamond, while highly desirable for its acoustic properties, it is costly. Maximum achieved coupling factor for the pseudo-SAW mode on a Si substrate is k^2=1.5% at exactly 1 GHz (effective velocity of 2000 m/s) for an etching ratio of 60% and the conditions mentioned in Figure 68. This is about 2% less than the coupling achieved using diamond. While for the pseudo-BAW mode, a coupling factor k^2=2.2% at a velocity of 4200 m/s is achievable after the manipulation of the electrodes thicknesses to have h_{bottom}/p=0.1 and h_{top}/p=0.24 shown in Figure 76. The optimization of the SiO_2 layer could lead a small increase in the coupling factor but with the risk of spurious interactions.
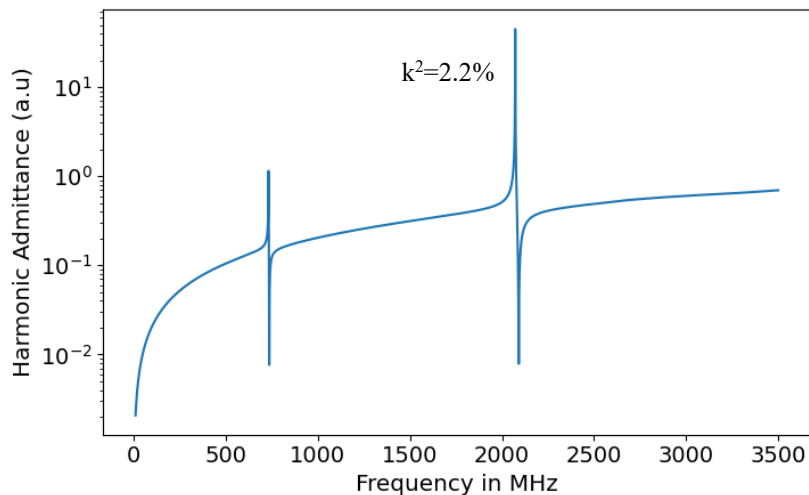
Figure 76: Highest coupling factor for the pseudo-BAW mode on Si substrate is 2.25% at 4200 m/s achieved using Mo/AlN/Mo/Si, h/p=2, a/p=0.5, h_{bottom}/p=0.1 and h_{top}/p=0.24, full etching and sidewall angles

Despite the spurious challenges, this solution is more available since Si and SiO_2 are easier to attain while we focus our manufacturing efforts on the transducer thickness to pitch ratio which remains the most significant parameter in any optimization step. This brings us to chapter 3 where we attempt manufacturing devices with both varying thickness to pitch ratio and SiO_2 layer thickness.

The modest coupling factors achieved in this chapter will be significantly revised using $LiNbO_3$ as the piezoelectric materials in Chapter 4. The question of spurious modes and the different electric configurations that can be used to avoid these interactions will be revisited in Chapter 5.

Chapter 3: Fabrication of AlN-Based HSBR

Introduction

The previous chapter has focused on the modelling and the theoretical analysis of hybrid SAW/BAW devices. We have highlighted that the ratio between the thickness of the transducers and their periodicity has a strong influence on the wave velocity and the electromechanical coupling factor. In this chapter, we focus on the manufacturing efforts to produce hybrid SAW/BAW devices. The goal is to confirm some of the trends we have identified in the previous chapter by implementing devices with varying h_{AlN}/p and h_{SiO2}/p. Our aim is also to complete the study by investigating the influence of parameters that could not be revealed by the periodic models of chapter 2, related to the finite number of electrodes and their electrical connections. Eventually, we also focus on investigating issues related to losses.

In the first section of this chapter, we present the process flow we developed for the fabrication of hybrid SAW/BAW resonators. This process elaborates on the ones presented in Chapter 1, section 3, but also takes into account the specificities of the processes developed for AlN-based acoustic or MEMS devices at CEA-LETI.

In the second section, we present the electric measurement methodology we employed and its adaptation to the various electrical configurations of the devices we characterized. We focus especially on the calculation of the quality factors and how the measurements were adapted to maintain a reasonable level of confidence in their calculations.

We finally confirm experimentally the excitation of both the pseudo-SAW and the pseudo-BAW modes and discuss the conditions to obtain them. We then discuss the experimental dependence of the resonance frequencies, electromechanical coupling factors, and the quality factor results of each mode, as a function of the design parameters varied and compare them to the simulation results from chapter 2 whenever applicable. [105], [106]

1   Fabrication steps of AlN-based resonators

1.1   Process flow

Figure 77 depicts the required arrangement of materials for hybrid SAW/BAW resonators. As discussed in Chapter 1, section 4, the patterning of the transducers constitutes the major fabrication challenge. The analysis of works previously reported in the literature, and previous experiences in the laboratory have shown that photoresist masks are consumed during the patterning of AlN, what leads to the top electrodes to be damaged by the etching process. To avoid this, we employ the process flow developed at CEA-LETI for the thesis work of Marie Gorisse. She introduced a SiO_2 hard mask, which is more resilient than photoresist [84]. This allowed her to etch holes with relatively large aspect ratios and relatively straight sidewalls (less than 10° slope) in AlN films, as shown in Figure 78.
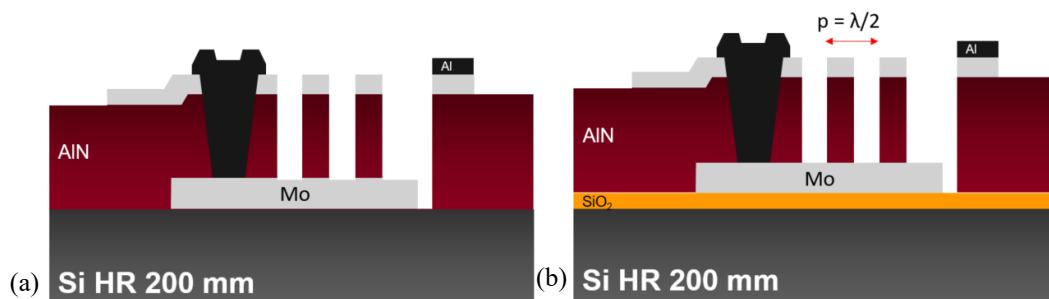
Figure 77: Schematic cross section of an HSBR AlN stack without SiO_2 layer (a) and with SiO_2 layer (b).
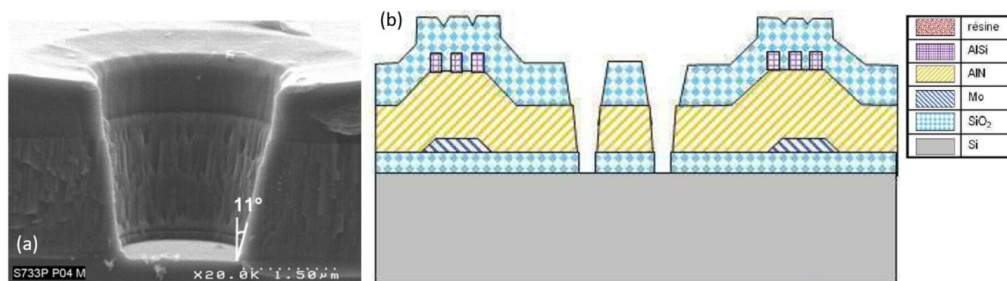
Figure 78: Patterning of AlN using a SiO_2 hard for almost vertical sidewalls [84]: SEM cross section showing resulting AlN sidewalls and the remaining SiO_2 hard mask (a) and the corresponding schematic cross section (b).

In comparison to previous studies, the objective of our work is to achieve smaller dimensions (p = 1 μm, a = 500 nm) and incorporate contacts to the bottom electrodes in the fabricated devices. To accomplish this, the process flow in [84] is modified as follows:

- The Mo/AlN/Mo stack will undergo dry etching using a hard mask to precisely define the transducers. Since the photolithography will have to resolve dimensions down to 500 nm, it is crucial to minimize topographical variations and ensure consistent dimensions in the patterned structures.

- The dry etching process of the AlN layer developed to reach almost vertical sidewalls lacks selectivity with the Mo bottom electrode underneath. In addition, etch rates may depend on the width of the apertures to form. There are therefore risks to damage the bottom electrode, what would prove detrimental for reaching a satisfying electrical contact

on them. For this reason, a different etching process will be carried on to open electrical contacts to the bottom electrode through the AlN film. This will be performed by wet etching of AlN in hot orthophosphoric acid (H_3PO_4). The top Mo layer can be employed as a hard mask, since this process is very selective with respect to Mo. It results in slanted sidewalls, what is also beneficial for later coverage by metal. At this step, relaxed dimensions allow for the use of a thicker photoresist (several micrometers). Therefore, it can occur after the patterning of the transducers, when the wafers exhibit a few microns topology.

- Dry etching of the Mo layer will be conducted to define the top electrodes out of the transducers. The lateral dimensions can be relaxed in this step.
- Mo is a very hard material, on which measurement probes cannot be landed easily. We consider therefore the addition of a third metallic layer (Al) which will be employed to form contact pads, and also to reinforce electrical access lines to decrease their resistivity. To avoid patterning directly Al on Mo and AlN, which could damage these materials, this third layer will be patterned by lift-off.

Based on these considerations, the fabrication process for AlN/Si HSBRs consists in the five masks process flow sketched in Figure 79:

a) Deposition and patterning of a bottom Mo electrode that is common to all transducers.
b) Deposition of the AlN piezoelectric film, the top Mo electrode, and the SiO_2 hard mask. Trenches that separate the transducers are then defined using a combination of UV photolithography and dry-etching of successively SiO_2, Mo and AlN. The etch mask is then removed chemically (HF).
c) The Mo and AlN films are patterned a second time to create electrical contacts towards the bottom electrode using a combination of UV photolithography, dry etching of Mo, and wet etching of AlN.
d) The top Mo electrode is patterned a third time to finalize the geometry of the top electrodes.
e) Finally, Al contact pads are added by lift-offs.
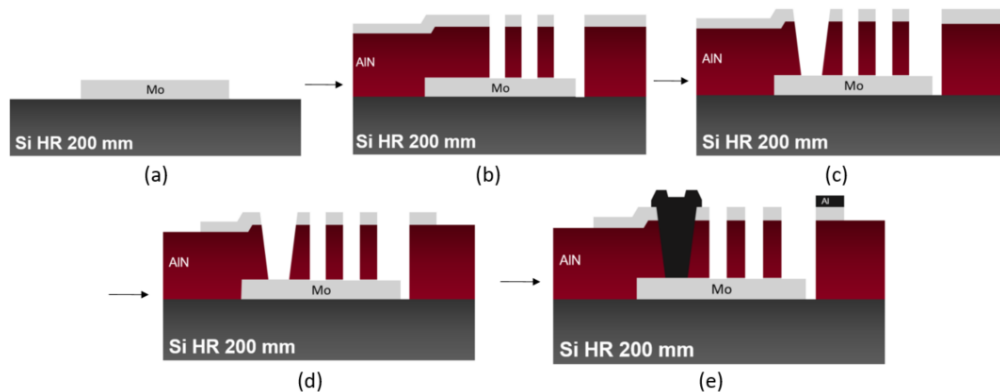
Figure 79: Five masks process flow for the fabrication of AlN hybrid SAW/BAW resonators: a) patterning the bottom electrode, b) patterning of the transducers, c) opening electrical contacts through the AlN layer towards the bottom electrode, d) patterning the top electrode, e) Al pads definition by lift-off.

1.2   Mask layouts

Figure 80 shows a basic resonator is made up of an array of active interdigitated transducers surrounded from the right and left sides by reflectors. Various geometrical and electrical configurations are considered:

- The bottom electrode which is common to all transducers is either floating or grounded,
- The top and bottom electrodes of the reflectors can either be shorted (the top electrodes are electrically connected to the bottom electrode) or open (each top electrode is left floating),
- The number of active transducers is varied,
- Different acoustic apertures are attempted.

In addition, each structure is duplicated with an "Open" structure with identical electrical connections, but disconnected transducers, which allows estimating parasitic capacitances induced by the resonators layout.
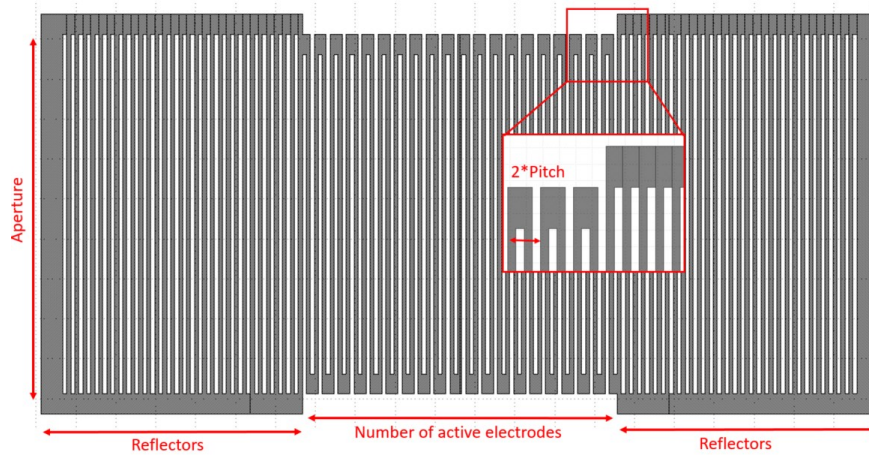
Figure 80: Depiction of the layout of a basic resonator structure.

Because of the need for resolutions down to 500 nm, we rely on a stepper for photolithography steps. Thus, a single field is photo-repeated over a 200 mm wafer. Each field is made up of 576 distinctive devices: $2^3 = 8$ different electrical configurations for 72 different geometric settings: variations in the number of transducers (4), in the acoustic aperture (3) and in wavelengths (6) (4 × 6 × 3 = 72). They are listed in Table 4 and discussed in order afterwards.

Table 4: Different parameters and their attempted. All the possible combinations of these parameters were fabricated.

Functionality	Resonator or Open device
Reflector connections	**Short or Open circuited**
Bottom electrode	**Floating or Grounded**
Number of transducers	**20, 40, 60 or 80**
Transducers periodicity	**1, 1.4, 1.8, 2.2, 2.6 or 3 µm**
Acoustic aperture	**20λ, 30λ or 40λ**

The geometric parameters such as periodicity, number of transducers and acoustic aperture are illustrated in Figure 80 and its inset. It also shows the reflectors surrounding the transducers. Due to size constraints, we opted for a constant number of 30 reflectors for all resonator designs. The assumption was that the thick transducers should provide very large reflection coefficients for the

modes of interest, and that only a small number of reflectors should be sufficient (the partial introduction of the P-matrix in Appendix C suggests a reflection coefficient of 90% per transducer for the pseudo-SAW mode).

For the sake of the masks definition, simplified schematics of the configurations are shown in Figure 81. They show the connections of the transducers as well as left and right reflectors. The top electrodes of the active transducers are connected in an alternating manner to two electrical ports, labelled 1 and 2. The top electrodes of each reflector are either left individually floating like in Figure 81(a) or connected to the common port like in Figure 81(b). All transducers and reflectors have the same bottom electrode in common, which is either left floating or connected to ground.
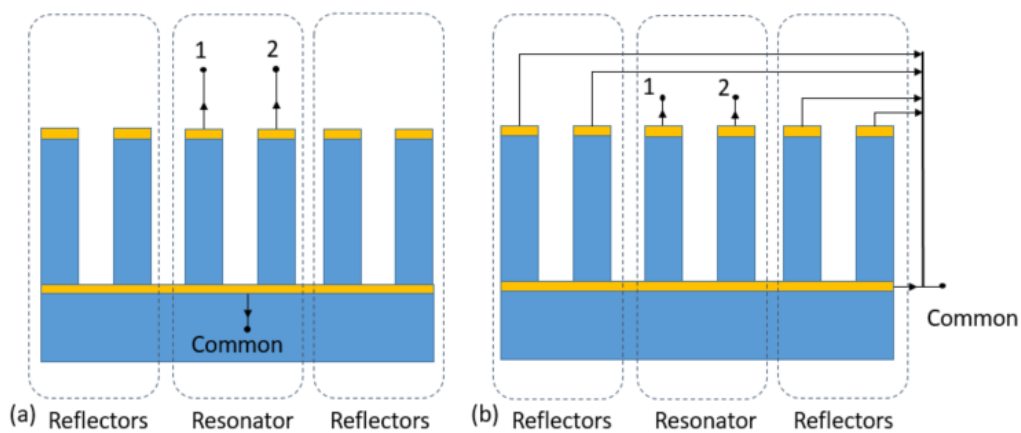
Figure 81: Schematic of a HSBR detailing the connection of a device with open-circuited reflectors (a) and with shorted reflectors (b).

Based on these consideration, we describe in sequence the layouts of the various devices, mask level by mask level. Beginning with the bottom electrode, we can observe the first notable difference between devices with a grounded bottom electrode Figure 82(a) and those with a floating bottom electrode Figure 82(b). The dashed region indicates where the Mo is retained and the white region where it is etched away. In the first case, the bottom electrode reaches the ground loop, while in the second case, the bottom electrode is isolated at the level of the transducers and reflectors to keep it floating.
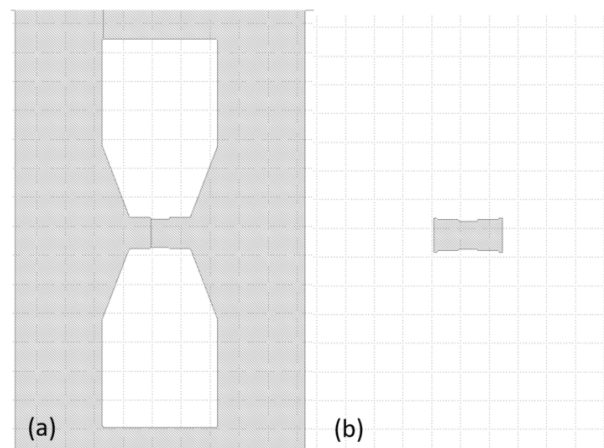
Figure 82: bottom electrode for grounded B.E devices (a), bottom electrode for floating B.E devices (b)

The next step involves depositing AlN, Mo and a SiO$_2$ hard mask. The openings of the AlN at the level of the trenches separating adjacent transducers or reflectors (Figure 79(b)) are shown in Figure 83 in solid black.

Figure 83(a) and (b) shows a view the layout of the trench openings for a device with open reflectors and a grounded bottom electrode. The solid black pattern is fully contained over the bottom Mo in light grey. A trench surrounds the reflectors, effectively severing any electrical connection for their top electrodes. Figure 83(c) shows a magnification for a device with open reflectors and floating bottom electrode. The bottom electrode, which extends out of the transducers array, is not connected to a ground line. Figure 83(d) shows a similar view for a device with shorted reflectors and grounded bottom electrode. This time, the trenches separating reflectors do not cut the metal at the ends of the corresponding transducers, allowing their top electrodes to be connected to the lines that will be defined later. The little squares visible on the layouts, however, are here to induce an extended cut in the top Mo film what will cause subsequent electrode lines to be split. This will disconnect the signal lines from the connections of the top electrodes of the reflectors. Figure 83(e) shows a magnified view for a device with shorted reflectors and a floating bottom electrode. The same principles as for Figure 83(d) have been employed. The only difference is the connection of the bottom electrode.

The second patterning of the top electrode and piezoelectric layer creates openings for establishing electrical contact with the bottom electrode (Figure 79 (c)). The pathway covers a larger etching area and is represented by the dark grey in Figure 83. When the reflectors are shorted, additional openings are added to provide a connection capable of linking the top and bottom electrodes of the reflectors (Figure 83 (d,e)).
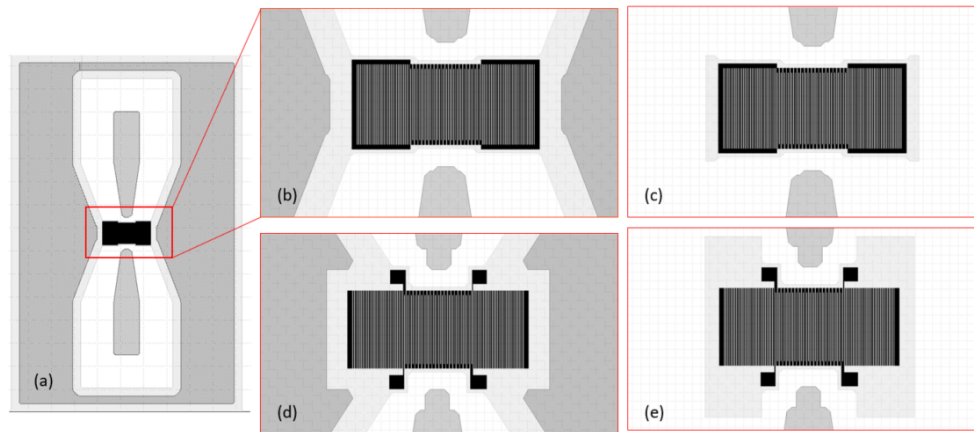
Figure 83: Mask layout for Mo and AlN etching of pillars in solid black and of electrical contact path in dark grey with view of the bottom electrode layout in light grey (a), magnified for open reflectors and grounded bottom electrode (b), magnified for open reflectors and floating bottom electrode (c), magnified for shorted reflectors and grounded bottom electrode (d), and magnified for shorted reflectors and floating bottom electrode (e).

Figure 84 displays the fourth level of the mask (Figure 79 (d)), meant to pattern the top electrode Mo to define the final electrical paths, in red. The previous 3 levels are shown as well. The bottom electrode being the underlying layer is in solid black and AlN trenches are hatched black. The great hatched area around will be later filled with metal pads. The purpose of this step is to separate the signals (middle) and ground lines (side and around).
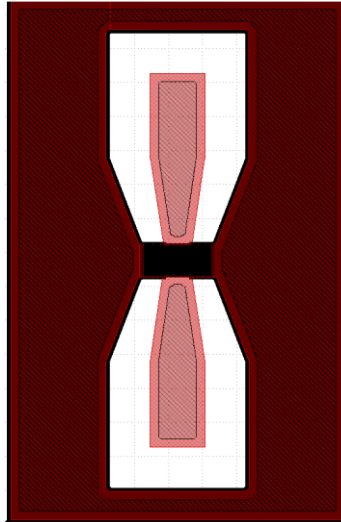
Figure 84: pattern for top electrode in red

In Figure 85 the fifth and final layer is represented in red. The layer represents the deposition and lift-off layout of the Al contact pads. The previous layer for the top electrode is in solid grey. The bottom electrode, and trenches are still in solid and hatched black respectively.
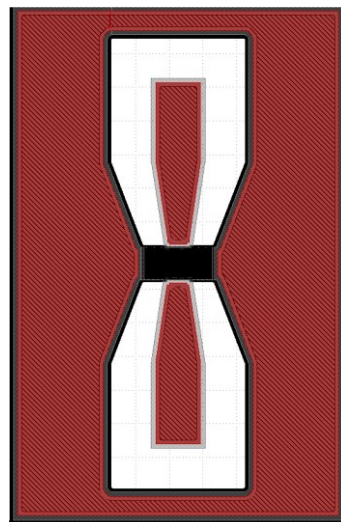
Figure 85: Al lift-off contact pads pattern in red

In the following sub-sections, a detailed description and analysis of each step is provided, highlighting both successful and unsuccessful outcomes.

1.3 Device fabrication

Devices were fabricated with different AlN thicknesses and SiO_2 thickness. To demonstrate the combinations attempts without confusion, the splits are listed in the table below. Each column corresponds to a new stack with different SiO_2, Mo, or AlN thicknesses.

Table 5: Stacks implemented for the first and second rounds of fabrication (all in nm)

SiO_2	0	210	0	210	0	700	1000	0	850	1200	0	1100	1500
Mo		150		150		200			240			320	
AlN		1000		2000		2500			3000			4000	
Mo		150		150		200			240			320	

In chapter 2, we could see in that when the piezoelectric layer is not fully etched, the evolution of the electromechanical coupling factor as a function of the h_{AlN}/p ratio is modified compared to the case where it is fully etched. In particular, Figure 68 shows that the maximum electromechanical coupling factor is reached for normalized AlN thicknesses of $h_{AlN}/p = 2$ for the pseudo-BAW mode when more than 20% of the piezoelectric layer remains in-between the transducers. The pseudo-SAW mode even exhibits a maximum k^2 when $h_{AlN}/p = 3$ and the piezoelectric film is etched over half of its thickness. Consequently we fabricated devices with thickness to pitch ratio of 1 and 2 as a first step, and then we pursued the fabrication of devices with thickness to pitch ratios beyond 2, and pushed the process to more extreme ratios, up to 4. Beyond reaching the optimum point in some specific configuration, the major goal of this experiment is to confirm the trends simulated in Chapter 2 and to investigate what are the limits on the highest transducers aspect ratios that can be realistically fabricated.

In the second round of fabrication, we added focus on the role of the SiO2 layer thickness under the bottom electrode. Figure 70 showed theoretically in Chapter 2 there is a strong effect of the SiO_2 layer on the performance of both the pseudo-SAW and the pseudo-BAW mode. The ratio of the AlN thickness to electrode thickness is kept at $h_{AlN}/h_{Mo}=12.5$ and the thickness of SiO_2 layer is varied to $h_{AlN}/h_{SiO2} = 0, 2.5, 3.5$ which were the optimal Mo and SiO_2 for early simulations.

1. Deposition and patterning of the bottom electrode

We start with high resistivity (HR) 200 mm Silicon wafers. The term "high resistivity" means that the silicon material has a low concentration of dopants. Before beginning the fabrication process, the wafers undergo an initial cleaning process along with protective coating to prepare them for subsequent processing steps. A "Caro" (or Piranha) cleaning step, which utilizes a mixture of diluted hydrogen peroxide and sulfuric acid [107, pp. 311–358], is employed to remove any organic or metallic contaminants present on the substrate surface. Next, an RCA cleaning step is performed, which involves using a combination of ammonia and hydrogen peroxide [107, pp. 311–358] to further remove any remaining impurities from the substrate surface.

For half of the available wafers, silicon dioxide (SiO_2) is deposited using a plasma-enhanced chemical vapor deposition (PECVD) process. PECVD involves introducing a precursor gas into a vacuum chamber and dissociating it by the assistance of a plasma, causing it to react and form a solid thin film on the surface of the substrate [108, p. 511]. A Chemical Mechanical Polishing (CMP) step is then applied to the SiO_2 layer to smooth the surface. The process involves applying a chemical slurry to the surface to be polished and then using a mechanical force to remove a thin layer of material [109]. The thickness of SiO_2 deposited has thus been initially determined so that the residual thickness after polishing is close to 200 nm.

A 150 nm-thick bottom electrode is deposited by sputtering a Mo target with an Ar plasma. The sheet resistance of the films is measured by 4-point probe measurements to determine their thickness, their resistivity having been previously calibrated. These measurements indicate that the Mo films remain within 150±5 nm across all wafers.

The photolithography step to define the bottom electrode is carried out using the first mask level shown in Figure 82. Photolithography involves using light to transfer a pattern from a mask

onto a photosensitive material called a resist. The resist is then developed, leaving a patterned layer that can be used as a template for subsequent processing steps [110], [111]. In our case, this was done using a stepper tool with a 365 nm wavelength ultraviolet light source to photo-repeat patterns across 200 millimeter (mm) substrates.

The Mo is then dry etched using the resist to protect the electrode areas. Dry etching is a process of removing material from a substrate using a plasma containing neutral and reactive species in a vacuum environment [112]. The ions in the plasma are accelerated to the sample by an electric field. The ion bombardment causes matter to be ejected from the sample, while the reactivity of some of the ions initiates some chemical reactions. Both effects contribute to the etching of the material at the surface of the sample. This is followed by stripping, which is the removal of the photo-resist from the surface of the substrate using a commercial stripper solution. Microscope images of patterned bottom electrodes at the fabrication step shown Figure 79 (a) are shown in Figure 86.
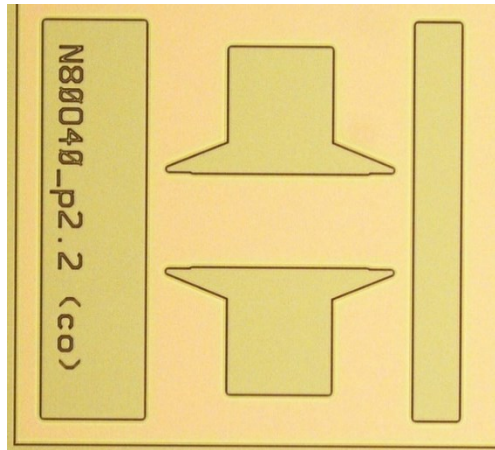
Figure 86: Microscope image of a bottom electrode after patterning.

For the second round of fabrication, the stacks listed in Table 5 demonstrate how different SiO_2 layer thicknesses were attempted. In order to ensure the thickness of this layer is in conformity with target values, reflectometry measurements are carried out and one presented below.

Table 6: SiO_2 thickness measurements for different stacks (in nm).

Target thickness	700	1000	850	1200	1100	1500
Mean thickness	696.5	997.4	848.6	1255.9	1094.4	1485.2
Variation Range	31.6	44.7	35.6	98.8	50.1	69.5

This is followed by the deposition of a Mo layer on the SiO_2 and patterning it using the first layer mask. The thickness was evaluated from the measurements of the square resistance and summarized in Table 7.

Table 7: Mo thickness measurements for different stacks (in nm).

Target thickness	200	240	320
Measured thickness	200±14	240±17	320±23

2. Deposition of AlN and Mo top electrode

In the next step of the fabrication process, AlN is deposited by reactive sputtering of an Al target in an Ar/N_2 plasma. Mo is subsequently deposited by sputtering in a different chamber of the same tool, without intermediate air break. The AlN layer is deposited with a thickness of 1 µm on half of the wafers, while the other half is stacked with 2 µm of AlN. The thickness of the Mo top electrode is 150 nm for all devices. To ensure the quality of the deposition, AFM (Atomic Force Microscopy), XRD (X-Ray Diffraction) and SEM (Scanning Electron Microscopy) techniques are utilized. AFM measures the surface roughness and topography of the deposited layers, while XRD is used to analyze the crystal structure and orientation of the deposited metal layers. SEM is used to obtain high-resolution images of the surface of a sample, providing information on its morphology and topography.

Two control wafers are used to observe the deposition. These wafers have the bottom Mo deposited but not patterned. Control wafer 1 has SiO_2 layer of 210 nm and 1 µm of AlN while control wafer 2 has no SiO_2 and 2 µm of AlN. The XRD 2θ scan, presented in Figure 87, shows distinct peaks of the AlN (002) and the Mo (110) crystal orientation. The rocking curve of the (002) AlN peak complements this measurement by quantifying the amount of disoriented crystalline planes in the diffracting volume sampled. A small rocking curve full width at half maximum indicates a well-defined and highly ordered crystal structure, with minimal defects or strain [113, p. 124]. The rocking curves presented in Figure 87(b) for the AlN shows a full width at half maximum of 1.24° for 1 µm AlN and 1.61° for 2 µm AlN. This is in line with values usually obtained for similar films.
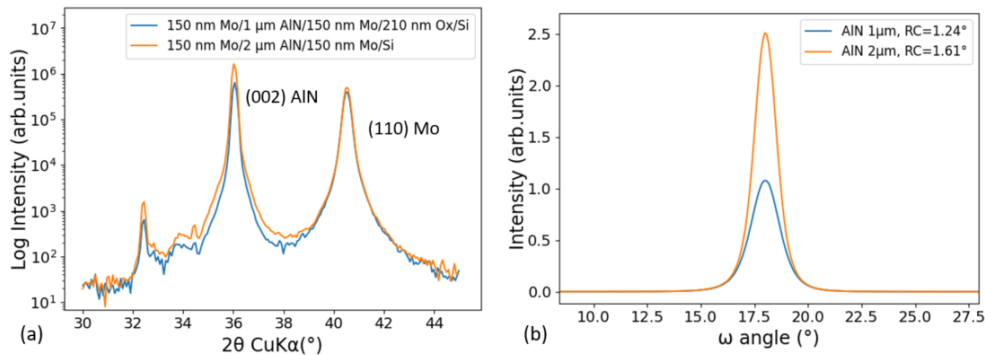
Figure 87: XRD spectra after the deposition of AlN and the top Mo. (a) and rocking curves for the (002) peak of AlN (b).

The Atomic Force Microscopy (AFM) images reveal the presence of a few disoriented grains, as indicated in Figure 88 (a), which shows the AFM image of an AlN film of 1 µm deposited on 210 nm of SiO_2. However, we do not consider them problematic, particularly after analyzing the Root Mean Square (RMS) roughness value, which represents the standard deviation of the height distribution of the surface features on a sample [114]. The roughness obtained from the AFM image presented here is 3.3 nm, which is consistent with values usually obtained for AlN films of similar thickness.
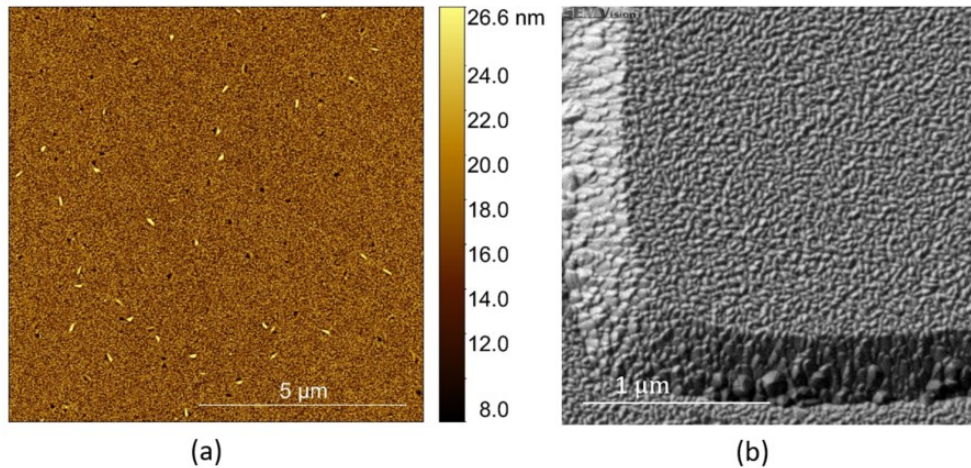
Figure 88: Surface analysis after the deposition of the AlN layer and Mo top electrode on 210 nm of SiO$_2$ AFM (a) and SEM image (b)..

The SEM images provide a highly magnified view of the deposited AlN/Mo surface, revealing a clean surface with no visible defects. The SEM images suggest that the deposition process was successful and the surface is suitable for further processing

AlN and Mo layers are deposited at this step with the perspective thickness listed in Table 5. Figure 89 shows X-Ray diffraction spectra and rocking curves for AlN layers of respectively 2.5, 3 and 4 µm. They are similar to those plotted in Figure 87 for respectively 1 and 2 µm-thick layers. One can even notice that the rocking curve continues to improve with increasing AlN thickness.
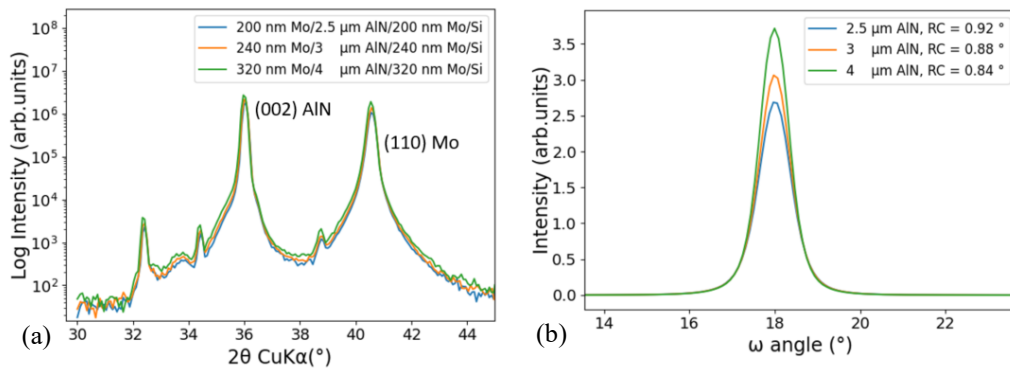
Figure 89: XRD spectra for 2.5, 3 and 4 µm AlN (a) and rocking curves of the corresponding (002) orientation (b).

3. Patterning the top electrode and the AlN film to form the transducers

The next step in the process is the key step of the process flow and it starts with the deposition of a layer of SiO$_2$ by PECVD, which will serve as a hard mask during the etching of the AlN trenches. The thickness of the SiO$_2$ layer is adjusted to be equal to the thickness of the AlN film below.
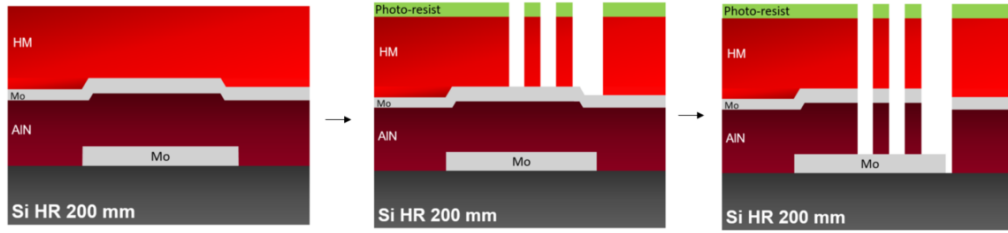
Figure 90: Deposition of the hard mask, patterning the HM with photolithography step and the etching of the Mo/AlN trenches.

During the etching process, the corners of the photoresist mask are etched faster than its top, leading to the increase of the slope of the photoresist sidewalls. This slope, combined with the consumption of the photoresist during etching, resulted in the transfer of a slope (which is different, based on the relative etch rates between the material and the photoresist) onto the etched film. The advantage of using a hard mask is that the slope is transferred to the SiO_2 layer instead of the etched film. When the hard mask has sufficient thickness, the slope does not have enough time to reach the AlN film, thereby maintaining the vertical sidewalls of the AlN layer.

Figure 90 illustrates the process of patterning the deposited hard mask using the IDT pattern discussed earlier in Figure 83. Since the smallest gaps between transducers were 500 nm, we used a relatively thin photoresist layer (1.5 μm). The insulation dose had also to be adjusted. The initial attempt at photolithography resulted in unopened lines for 1 μm AlN, as shown in the left image in Figure 91. This required a rework with adjustments of the exposure dose. The right image shows a successful example of photolithography with a well-defined pattern for 2 μm AlN film.

After ensuring that the expected photoresist mask could be obtained, the hard mask was etched, with the Mo as a stop layer to complete the second step of Figure 90.
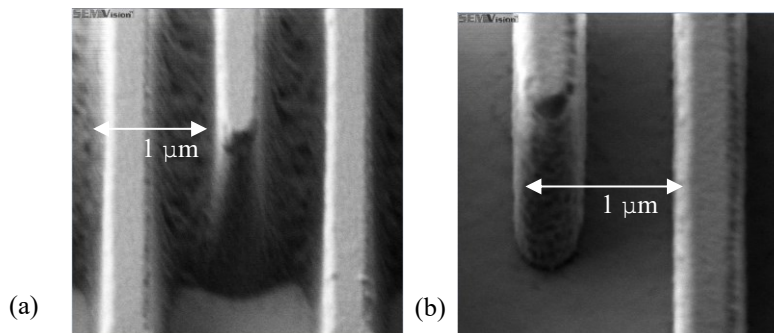
Figure 91: SEM image of the photoresist mask for defining transducers: with the initial insulation dose (a) and after dose adjustment (b).

In the third stage of Figure 90, the Mo/AlN pillars were dry etched, by alternating a reactive ion etching process using fluorine chemistry for the etching of Mo and a process using chlorine chemistry for the etching of AlN. Since the latter is a relatively hard material and we want to achieve sidewalls as vertical as possible, the AlN etching process operates in a regime favoring ion bombardment. It therefore lacks selectivity with respect to the Mo layer on which it has to stop. Care had therefore to be taken to try to etch completely the layer while not etching through the bottom electrode. Since, if this occurs, the chemical etching of the SiO_2 hard mask could also start etching the SiO_2 layer under the bottom electrode on wafers with a SiO_2 layer, we preferred leaving some AlN in the trenches. As a consequence, the etching was stopped as soon as the

endpoint detection of the etching process was reached, without additional over-etch time to ensure that the AlN is fully etched over the whole wafer.
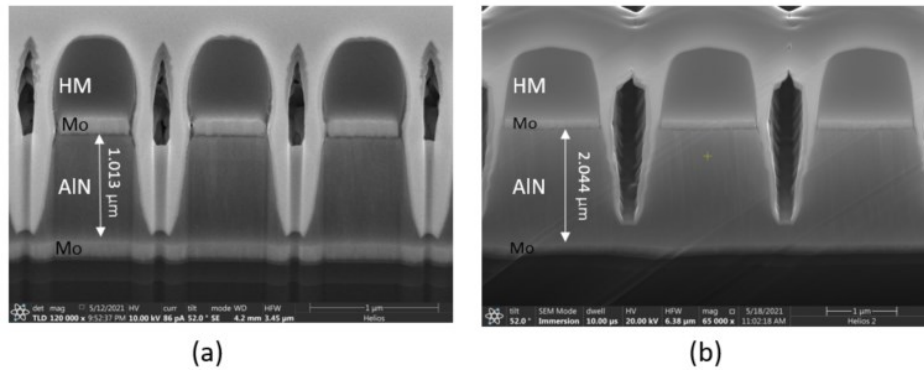
Figure 92: FIB-SEM cross-section view of the final 500 nm-wide transducers spaced by 500 nm for 1 (a) and 2 (b) μm-thick AlN after etching.

To control the patterning process, we etched cross sections using a Focused Ion Beam (FIB) tool, which uses a beam of ions, typically gallium ions, to remove material from the sample surface at a specific location, allowing for the creation of cross-sectional views of the sample without having to cleave it. SEM images of these cross-sections are reproduced Figure 92, corresponding to the last stage of Figure 90 for devices with 1 and with 2 μm AlN. The images reveal that the transducers are well-defined, with almost vertical sidewall angles (80°). The devices were not compromised. The gap between the transducers is well-defined, and the edges of the top electrodes have been adequately protected by the SiO_2 hard mask. The cross-sectional images reveal an etching ratio of nearly 1 for the 1 μm-thick AlN layer, and 0.85 for the 2 μm-thick layer. These findings suggest that the etching process was successful, resulting in accurately defined and robust pillars.

To finalize this fabrication step, the hard mask oxide layer is removed by wet etching. In this case, hydrofluoric acid (HF) is used to remove the hard mask oxide layer, while leaving Mo and AlN unaffected.

For the higher thickness of AlN, we maintain a 1:1 ratio between the thickness of the SiO_2 hard mask and the one of the AlN to be etched. The hard mask was again patterned using photolithography and dry etching. The patterning of the hard mask itself with aspect ratios up to 8 (500 nm trenches in a 4 μm-thick layer) instead of 4 only for the previous run, becomes challenging on its own. The higher aspect ratios make the effect of the ion bombardment less efficient at the bottom of the openings, and the transport of reactive species is also slower. Therefore, to ensure that the hard mask is well opened in the narrowest openings, we allowed for an over-etching duration of 30 seconds after the etching end point detection. Because the photoresist is also largely consumed during the etching of SiO_2, the remaining thickness is not sufficient to withstand the full etching sequence. It is therefore preferable to strip it after the Mo etching, and only rely on the oxide hard mask for the etching of the layers of AlN.

Figure 93 displays a FIB-SEM cross-sectional view of transducers with pitch of 3 μm after etching. As in Figure 92, the transducers exhibit tilted sidewalls. They exhibit effective widths of 1.80 ± 0.05 μm. We also extract geometric ratios from the figure: coverage ratio, etching ratio, and the sidewall angle. Estimations of these values are tabulated in Table 8. It is important to

acknowledge that in some of the SEM images presented, the top edge of the pillars is visible, indicating that the cross-sectional images may not be precisely perpendicular. Consequently, any thickness measurement conducted on these images is subject to inaccuracies due to the degree of image tilt. This mostly affects the evaluation of the sidewall angle, whose calculation depends on the thickness considered. The coverage and etching ratio, being ratios of lengths in the same direction (respectively horizontal and vertical), should not be affected strongly by the tilt angle of the SEM images.
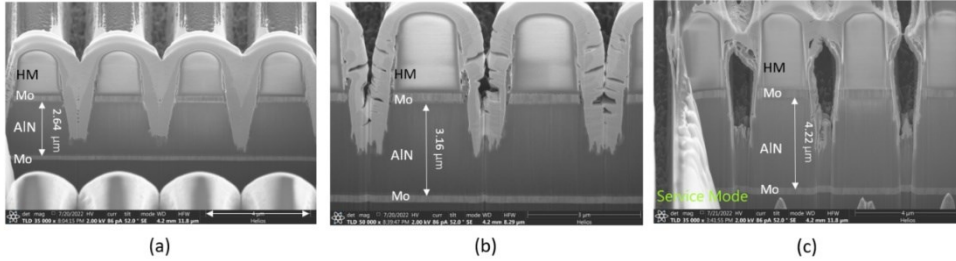
Figure 93: FIB cross section of the etched pillars with 2.5 µm (a) 3 µm (b) and 4 µm (c) of AlN

Table 8: Relevant resulting dimensions for each thickness of AlN attempted

AlN thickness (µm)	1.0	2.0	2.6	3.1	4.2
Coverage ratio			0.63 ± 0.02		
Etching ratio	1	0.85	0.7	0.5	0.4
Sidewall angle	80°	80°	80°	80°	85°

At this point, we could notice that some devices were damaged. During the etching of the trenches, it appears that the adhesion of SiO_2 on the Mo layer is somewhat limited, causing the hard mask to detach at the level of the trenches. The main difference between the first round fabrication (AlN 1 & 2 µm) and the second round (AlN > 2 µm) is the chemicals used for stripping after pillar patterning. The detachment is probably due the high pressure of the chemicals used in the second round but not used in the first round. This is perhaps exacerbated by the residual stress in the relatively thick SiO_2 hard masks.
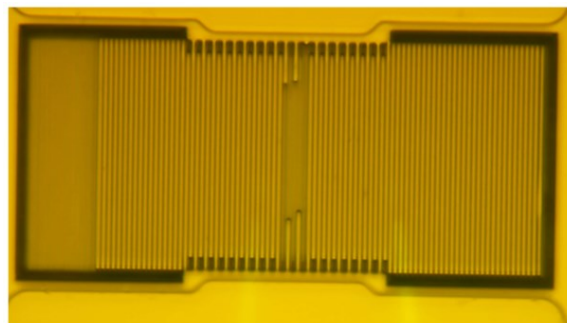
Figure 94: Microscope image showing some pillars were etched away during the etching of the trenches.

The damaged areas appeared to be randomly distributed without any direct correlation to the location on the wafer or with the thickness of the SiO_2 or AlN layers. For instance, the cleanest wafer had the largest thickness of SiO_2, Mo, and AlN, but this did not necessarily mean that it

was less susceptible to damage. However, upon closer examination, it appeared that these delaminations only affected a small portion of the devices. Therefore, we decided to continue the fabrication.

4. AlN openings for electrical contact towards the bottom electrode

The third mask level is utilized to etch a pathway through the AlN and top Mo layer to open electrical contacts to the bottom electrode. These openings have much larger lateral dimensions. Therefore, less photolithography resolution is required. In addition, the depth of the inter-transducer spacing require using a photoresist layer of 2 μm. After the photo-lithography, the Mo top electrode is patterned by dry etching. The Mo layer then serves as a hard mask for the subsequent chemical etching of AlN in hot orthophosphoric acid (H_3PO_4), preventing the lateral over-etch (more than 10 μm) usually seen when only a photoresist mask is used. Since the transducers are protected by the photoresist as this stage, and by their top electrodes, they are not affected by the chemical.

Figure 95 presents microscope images of three devices with increasing AlN thickness at this stage. Openings in the AlN appear as white areas, the Mo top electrode covered with photoresist as darker orange areas, and the trenches filled with photoresist as the darkest lines in the middle.
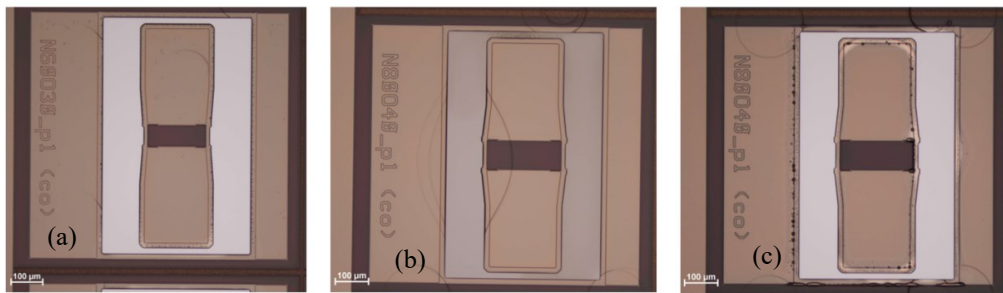
Figure 95: Microscope images after opening the AlN to establish electrical contact with the bottom electrode for 2.5 μm (a) 3 μm (b) and 4 μm (c) of AlN.

5. Patterning the top electrode

In this step, the top electrode is patterned to define the electrical access lines. This process involves photolithography, where the photoresist is patterned with the fourth mask level. Then, dry etching is employed again to etch the top electrode. At this stage, the photoresist protects the exposed bottom electrodes. Once the etching is completed, the photoresist is stripped.

After stripping the photoresist, the resulting AlN layer is revealed as a purple, light grey or dark grey areas in the microscope images for 2.5 μm, 3 μm and 4 μm AlN thicknesses respectively in Figure 96.
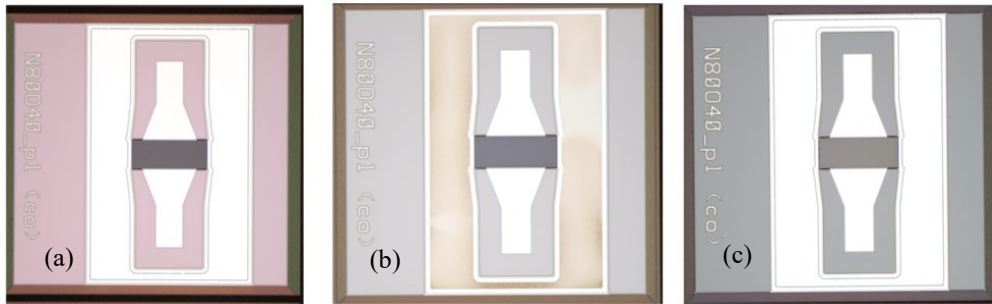
Figure 96: Microscope images after patterning the top electrode for devices with 2.5 µm (a) 3 µm (b) and 4 µm (c) of AlN.

Now that the AlN is exposed, it could be measured by optical reflectometry. The analysis of the spectrum of the reflection coefficient of polarized light at the surface of the sample, in particular the Fabry-Perrot fringes due to the finite thickness of the AlN film, provide a way to evaluate the thickness of the film, its optical indices being known. Mapping such measurements over the wafer area, we could verify that the thicknesses of the piezoelectric films are within 1±0.015 and 2±0.025 µm across all wafers.

6. Al pad deposition using lift-off

Finally, Al pads are patterned on top of the top electrode to establish electrical contact with the bottom electrode lift-off process. This step uses lift-off to pattern aluminum pads over the top electrode and establish electric contacts to the bottom electrode. Lift-off involves depositing a thin layer of a sacrificial material, typically photoresist, on the substrate. A layer of the desired material, such as metal or semiconductor, is then deposited on top of the sacrificial layer. The sacrificial layer is then dissolved using a solvent, leaving the patterned material on the substrate.

At this step, a layer of aluminum with a thickness of 1.3 µm is deposited onto the substrate by evaporation. Evaporation is a physical vapor deposition technique in which a material is evaporated from a source in a vacuum chamber and condensed onto a substrate, forming a thin film [115]. This is followed by the lift-off, using a high pressure stripper spray.

Figure 97 shows SEM images of the final device with Al pads on top. The picture shows signal lines for the two ports on top and bottom, as well as the transducer surrounded by reflectors. The magnified view shows more precisely that the reflectors (left) and transducers with floating top electrodes (right) are well-defined.
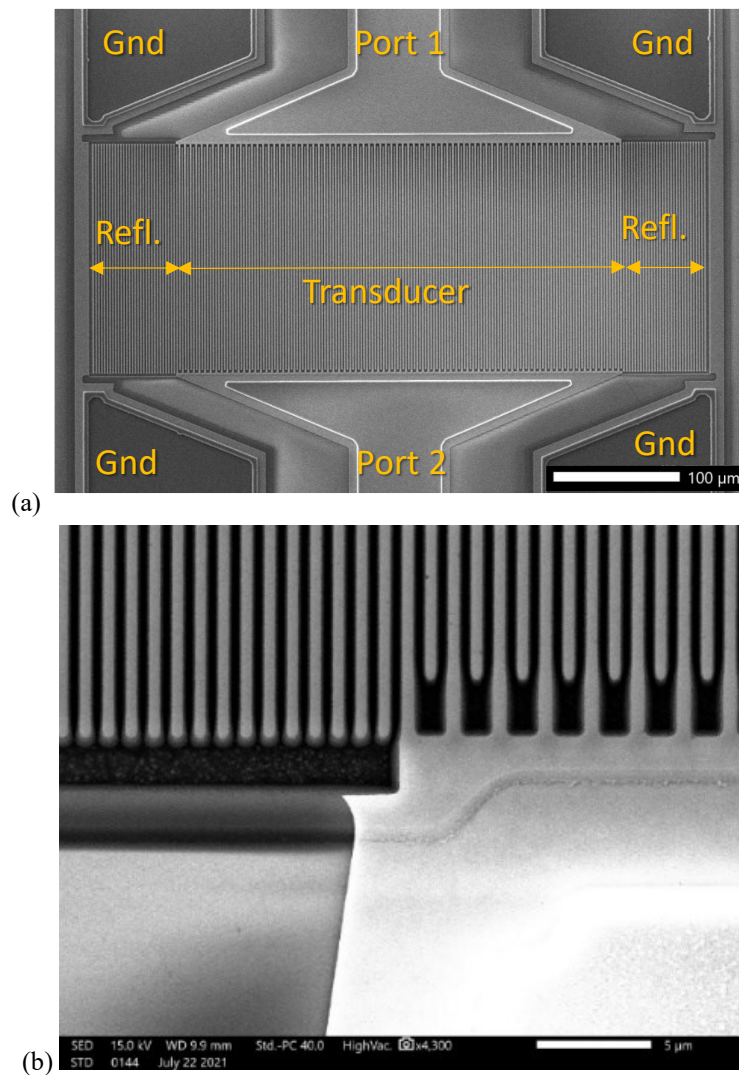
Figure 97: SEM pictures of the final device with Al pads on top: large view of the whole device (a) and magnified view revealing a portion of a reflector and a transducer (b).

At this stage during the second round of fabrication, two types of defects were encountered. The first defect involved the presence of leftover aluminum in the middle of the wafers after the lift-off steps was completed, as shown in Figure 98 (a). This was resolved by repeating the stripping step with a longer duration.

The second defect was observed only on devices with grounded bottom electrodes, where damaged areas appeared at the level of openings towards the bottom electrode. The cause of this defect was likely due to an insufficient etching of AlN in these openings. The damaged devices with grounded bottom electrodes are shown in the red box in Figure 98 (b), while their counterparts with floating bottom electrodes are shown in the green box. These optically damaged devices were found electrically non-functional.

(a)   (b)
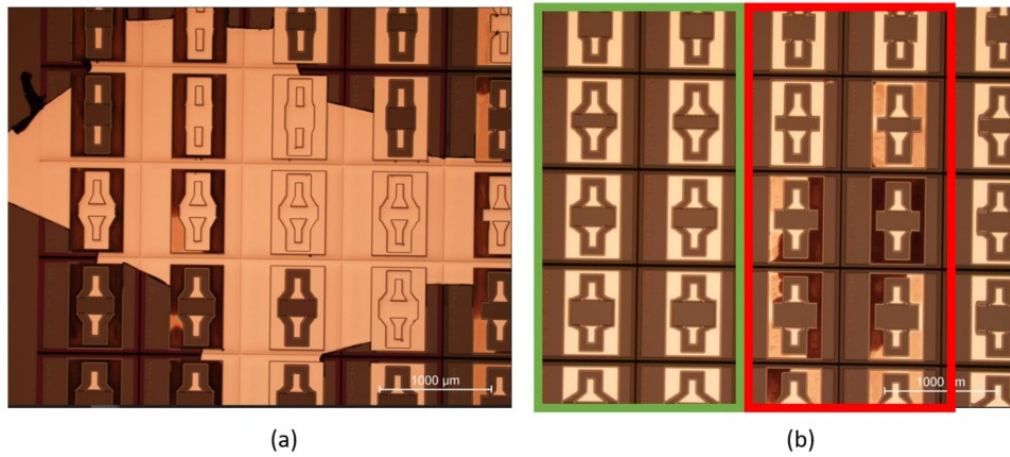
Figure 98: Issues encountered during the lift-off of Al pads: left-over Al at the center of the wafers (a) and damaged devices with grounded bottom electrodes (within the red box) and sound counterparts with floating bottom potential (in green box) (b).

A microscope picture of the final device having 1.5 µm SiO_2 and 4 µm of AlN after the deposition of the Al pads is provided in Figure 99 with a close-up on the trenches with a pitch of 1 µm. This shows a good quality of etching, good definition of pillars and clean fabrication overall and electrical contact on the device.
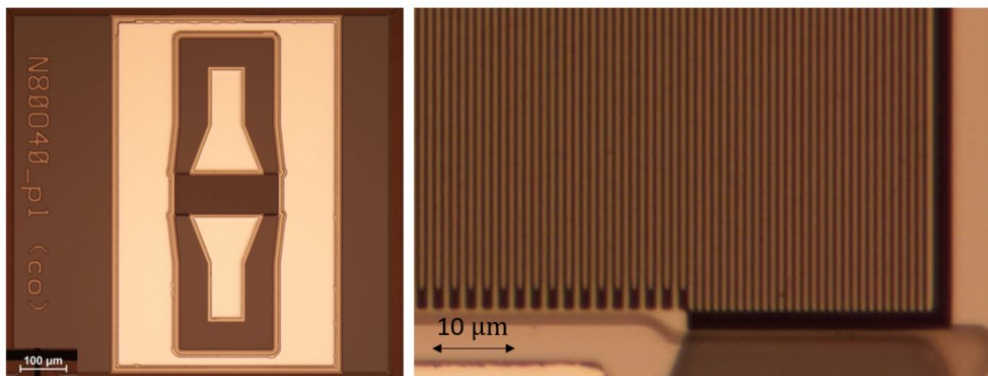
Figure 99: final device after the deposition of Al pads with 4 mm of AlN pillars

2 Electrical characterizations

2.1   Measurement Methodology

All electric measurements were conducted using a Vector Network Analyzer (VNA) to characterize the fabricated devices. A vector network analyzer is a test instrument used to analyze the electrical characteristics of radio frequency (RF) and microwave devices. The VNA operates by measuring the scattering (i.e. reflection and transmission) of electrical power waves send to a device. To do so, it applies power to one port and measures the amount of power reflected back or transmitted to another port [46]. The term "vector" indicates that the equipment characterizes both the magnitude of the scattering parameters and their phase, thus representing them by complex numbers [116], [117]. The VNA returns a so-called the S-parameters matrix to characterize the device under test as a function of frequency.
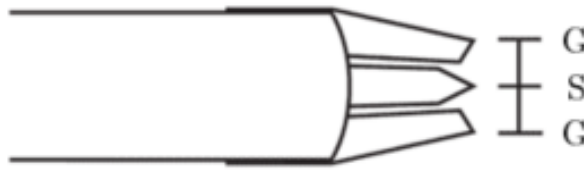
Figure 100: GSG probe [118]

The VNA is connected to GSG (Ground-Signal-Ground) probes (Figure 100) which are designed to make electrical contact with the device under test, allowing for electrical measurements to be made without the need for wiring. The GSG design consists of three contact points: a signal contact flanked by two ground contacts. This configuration introduces a transition between the coaxial cables in which the inner conductor carries the signal while the outer conductor is connected to the ground, and the transmission lines feeding the device to be measured. A prober allows for precise positioning of the probe tip on the device under test.

Because of the influence of the measurement fixture, namely the coaxial cables and the probes used to connect the device under test to the VNA, it is necessary to calibrate the VNA to remove these additional contributions and only calculate the scattering parameters of the device alone. We use a classical SOLT (Short-Open-Load-Thru) calibration, which establishes a reference plane for measurements. In this calibration, short circuits, open circuits, 50 Ω loads and a thru are used to calibrate the system and remove contributions from the test setup [119].

We are rather interested in the description of the electrical response of a device in terms of its admittance, i.e. in the relationships between currents and voltages. The admittance can be calculated from the S-matrix using $\mathbf{Y} = \frac{1}{Z_0}(\mathbf{Id} - \mathbf{S})(\mathbf{Id} + \mathbf{S})^{-1}$, where Y is the admittance matrix, $\mathbf{S}$ the S-parameters matrix, $\mathbf{Id}$ the identity matrix and Z_0 the reference impedance, usually 50 Ω.

The admittance matrix is typically represented as a square matrix, with each element Y_{ij} denoting the value of the current at port i induced by the application of a unit voltage at port j, while maintaining all other ports to 0 V. The diagonal elements represent the input admittance of each port, while the off-diagonal elements represent the mutual admittances between ports.

It is also convenient to derive the impedance matrix ($\mathbf{Z}$), which is the inverse of the admittance matrix. The real part of an admittance ($\mathbf{Y}$) matrix element is the conductance of this element ($\mathbf{G}$). The real part of an impedance ($\mathbf{Z}$) matrix element is the resistance of this element ($\mathbf{R}$).

As discussed before in Chapter 1 section 1.2, a resonance occurs when the energy stored in the resonator is maximized, leading to a peak response in the system. This peak is located at the resonance frequency. On the other hand, the anti-resonance frequency is characterized by a minimum current generation. At this frequency, the impedance becomes very high. In the context of experimental measurements, we evaluate the resonance frequency as the *series resonance frequency* (the maximum of the conductance (G) of the system), and the anti-resonance frequency as the *parallel resonance frequency* (the maximum of the resistance (R)).

Evaluation of quality factors

The definition of the quality factor is mentioned in Chapter 1 on page 14. The quality factor is here calculated by the following equations at resonance and anti-resonance:

$$Q_s = \frac{f_s}{FWHM_s}, \qquad Q_p = \frac{f_p}{FWHM_p} \tag{23}$$

where f_s and f_p are the series and parallel resonance frequencies and $FWHM_s$ and $FWHM_p$ are respectively the full width at half maximum of the conductance and resistance peaks.
The frequency sweep of a VNA has a limited number of points. In our case, it is 20,001. Since we measure the response of our devices between 10 MHz and 10 GHz, a uniform distribution of these points would result in a sampling frequency of 0.5 MHz. Due to this, the evaluation of the full widths at half maximum is made with an uncertainty related to the frequency sampling, which translates into an uncertainty on the quality factors that are evaluated. This is illustrated in Figure 101.
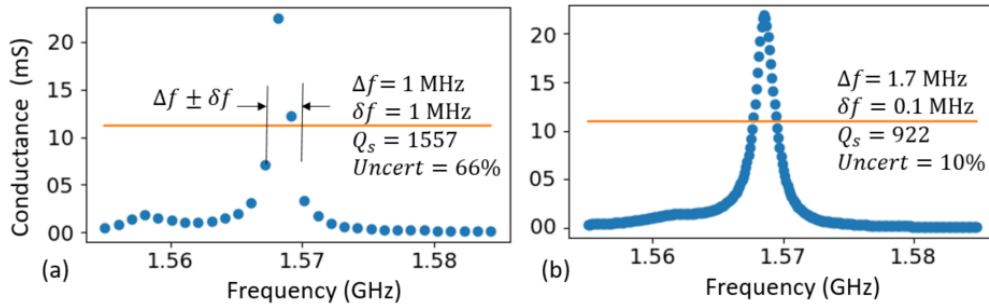
Figure 101: two measurements of the same devices with a low (a) and high (b) frequency resolution. The orange line is the materialization of the half maximum ordinate.

The error on the Q-factor comes from the error in calculating the FWHM from discrete data. While using the first two points above the horizontal line would under-value the width and over-estimate the Q-factor, using the two points below the line will do the opposite. Interpolation at exactly FWHM is a better estimate but is arbitrary since the value will depend on the actual interpolation scheme considered (linear interpolation between points, polynomial, or even fitting the whole peak by a Lorentzian). We define the uncertainty on Q-factors as the difference between the upper and lower estimates divided by the upper estimate.

$$\varepsilon = \frac{\left| Q_{upper} - Q_{lower} \right|}{Q_{upper}} = \left| 1 - \frac{\Delta f}{\Delta f + 2\,\delta f} \right| \tag{24}$$

For instance, the device shown on Figure 101 has a $f_s = 1.568$ GHz and should have a FWHM = 1.7 MHz. Because of the low frequency sampling of 1 MHz shown in (a), Δf is thus measured 1

MHz and this would suggest $Q_s = 1557$. The uncertainty of this Q-factor is however 66%. On the other hand, the good measurement shown in Figure 101 (b) with a frequency sampling of 0.1 MHz, gives $\Delta f = 1.7$ MHz so $Q_s = 922$ with uncertainty about 10%.

To ensure reasonable uncertainties in Q-factor calculations, it is therefore necessary to adopt an inhomogeneous frequency sweep during measurements, which increases the frequency resolution in the vicinity of the resonance and antiresonance frequencies, and decreases in the regions of lower interest.

2.2 Assessment of test BAW resonators

In addition to the fabrication of HSBR, High Overtone Bulk Acoustic Resonators (HBAR) were also implemented. These resonators are implemented by sandwiching the piezoelectric layer between two planar electrodes, as sketched in Figure 102 . Unlike conventional bulk acoustic resonators, they are not isolated from the substrate. Thus, their electric response is made of the many thickness mode resonances of the substrate. However, the envelope of these resonances is characteristic of the electromechanical properties of the piezoelectric film [120].
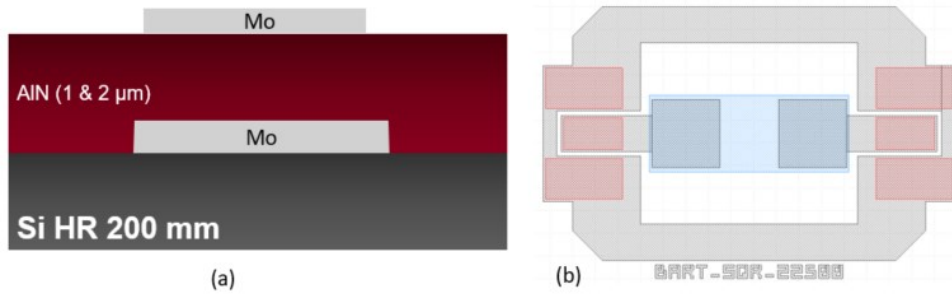
Figure 102: HBAR device stack (a) and top view of the mask (b)

The HBAR device response was fitted with Mason's Model, which is a one-dimensional model used to describe the behavior of acoustic wave resonators. The model considers the wave propagation in multilayers and is capable of calculating the electric response of a resonator as a function of the thicknesses and electromechanical properties of the layers [121]. We considered for this model the thicknesses of the layers as determined by resistivity measurements of the electrodes and ellipsometry for the AlN film at the location closest to the device. Material parameters were taken from [122]. To fit the increasing baseline visible on Figure 103, we also added a series resistance and a series inductance. With only minute changes in layer thicknesses, a satisfying agreement could be obtained. In particular, the electromechanical coupling factor (k_t^2) of longitudinal waves propagating in the AlN layer was kept at 6.5%, which corresponds to the theoretical value. This indicates there were no issues with the deposition of AlN whose piezoelectric properties are as expected.
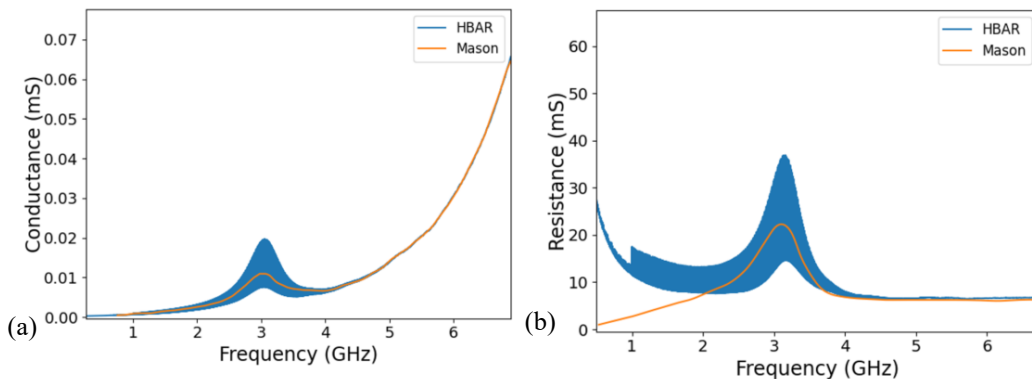
Figure 103: Electric response of a Si/Mo/AlN/Mo HBAR compared to the fitted Mason model: conductance (a) and resistance (b).

2.3 Interpreting the Electrical Response of hybrid SAW/BAW resonators

Electric response of a resonator with a floating bottom electrode
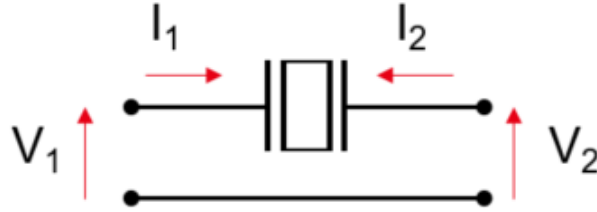
Figure 104: Circuit schematic representation of a hybrid SAW/BAW resonator with a floating bottom electrode as a 2-port device.

As discussed in section 0, hybrid SAW/BAW resonators are implemented as 2-port devices with resonators inserted in series between two ports. Thus, their electrical connections can be represented by the schematic in Figure 104. Hence, their admittance matrix writes.

$$\begin{pmatrix} I_1 \\ I_2 \end{pmatrix} = \begin{pmatrix} Y & -Y \\ -Y & Y \end{pmatrix} \begin{pmatrix} V_1 \\ V_2 \end{pmatrix} \tag{25}$$

with Y being the admittance of the resonator itself. This means that the admittance matrix is symmetric and that all its components are equal, up to a sign change to the off-diagonal components.
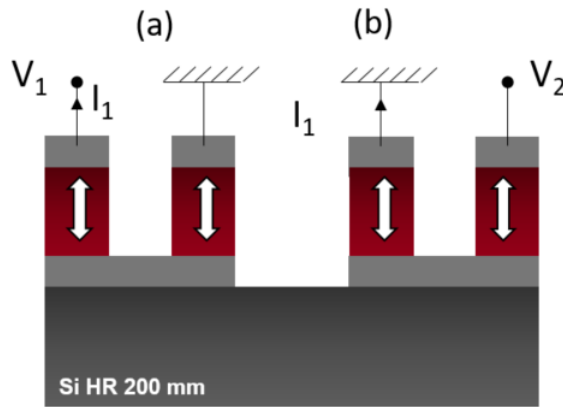
Figure 105: Electrical schematic of the meaning of Y_{11} (a) and Y_{12} (b) representation of a device with floating bottom electrode.

The schematic in Figure 105 shows the physical interpretation of considering $Y_{11} = \left.\frac{I_1}{V_1}\right|_{V_2=0}$ or $Y_{12} = \left.\frac{I_1}{V_2}\right|_{V_1=0}$ for a device with a floating bottom electrode. The two configurations being referred to are expected to have the same behavior in theory, with the only difference being the reversal of the current direction. Therefore, this confirms that the purely electric and purely acoustic analyses are in agreement.
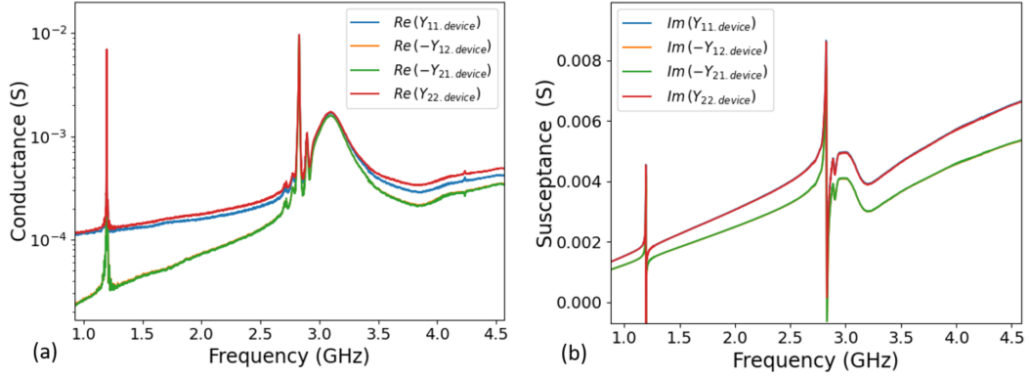
Figure 106: The four components of the admittance matrix (a) real part (conductance) and (b) imaginary part (susceptance).

In practice, it is almost true that the admittance matrix is symmetric. However, there are some factors that can cause slight deviations from perfect symmetry. For instance, the positioning of the probes during measurements may not be perfectly symmetric, and the devices themselves may not exhibit complete symmetry. These factors can contribute to small but measurable deviations from perfect symmetry in the admittance matrix, especially for the conductance, as seen in Figure 106.
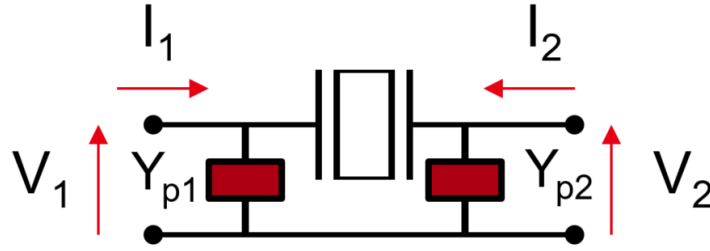
Figure 107: A resonator viewed as a 2-port device with parallel pad capacitances.

In practice, which part of the admittance matrix to consider as the resonator response? While examining the different components of the admittance matrix in Figure 106, it is observed that the off-diagonal elements seem to exhibit a lower static capacitance compared to the diagonal elements. This could be explained by considering the equivalent circuit in Figure 107, in which we introduce the capacitive contributions of the contact pads, modelled as admittances Y_{p1} and Y_{p2} connected in parallel to ports 1 and 2. In this case, the admittance matrix writes:

$$\begin{pmatrix} I_1 \\ I_2 \end{pmatrix} = \begin{pmatrix} Y + Y_{p1} & -Y \\ -Y & Y + Y_{p2} \end{pmatrix} \begin{pmatrix} V_1 \\ V_2 \end{pmatrix}. \qquad (26)$$

This shows that the off-diagonal terms of the admittance matrix are not affected by the spurious contributions of the pad capacitances.

One can also measure directly the parasitic parallel contributions by considering an "open" device, in which the electrodes are disconnected from the signal lines. In this case, the measured response is entirely due to parasitic capacitive contributions. Therefore, the Y_{11} component of the admittance matrix of the "open" device should correspond to the Y_{p1} component of the measurement of the full device. By subtracting it, one can isolate the device's intrinsic response, as shown Figure 108.

The same thing works for the off-diagonal elements. By subtracting the short device from the off-diagonal components, the unwanted feedthrough capacitance between the two ports, which is still included in the Y_{12} term of the resonator measurement, can also be eliminated. In Figure 108, one can notice that now $Y_{11} - Y_{11,open} \cong Y_{12,open} - Y_{12}$, and that this should now correspond to the intrinsic response of the resonator.
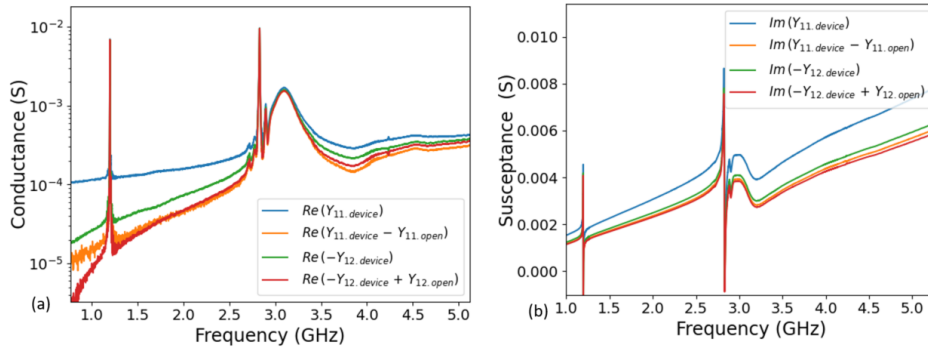
Figure 108: Removing the spurious capacitances by subtracting the "open" device admittance from the admittance of the actual device: conductance (a) and susceptance (b).

Generic analysis scheme

As a consequence, to isolate the electrical response of any resonator in the following section, we use a combination of two calculations:

1. First, the measurement of an "open" device, where the electrodes are disconnected from the signal line, should be subtracted from the measurement of the device under test. This helps to suppress the feedthrough capacitances and provides a more accurate measurement of the resonator response.
2. Second, one of the diagonal elements of the admittance matrix obtained from step (1) should be considered as the intrinsic response of the resonator in order to remove any remaining contributions from the pads.

3 Analysis of resonator responses

3.1 Qualitative analysis
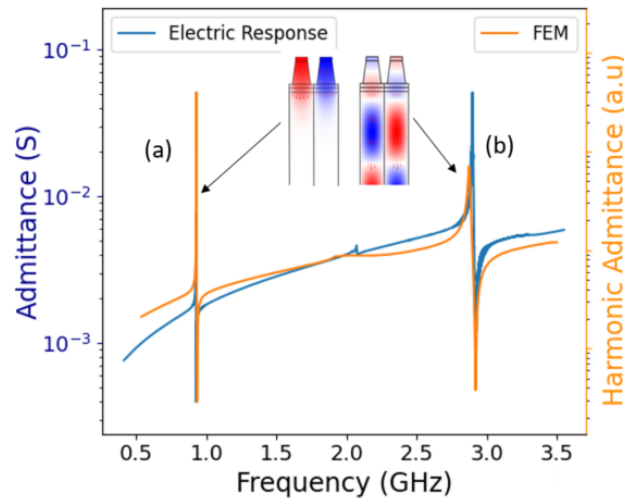
Figure 109: Comparison between the calculated harmonic admittance and the experimental electrical response for a device with 1 µm AlN and 1.4 µm pitch (Other parameters considered for the measured device are 40 electrodes, an aperture of 40λ, a floating bottom electrode and open reflectors.). Insets are the acoustic field representations of the pseudo-SAW (a) and pseudo-BAW (b) modes.

Figure 109 presents a measured electric response for a resonator with $h_{AlN} = 1$ µm, $p = 1.4$ µm. The resonance frequencies of the pseudo-SAW and pseudo-BAW modes are in agreement with the theoretical harmonic admittance, provided the actual geometry is inferred from the experimental results (e.g Figure 92 or Figure 93): a partial etching (h_{etch}/h_{AlN}) of 83% of the original AlN thickness, a sidewall angle of 81°, and a coverage ratio (a/p) of 60%.

Figure 110 expands this comparison to different AlN thicknesses and transducer periodicities for the pseudo-SAW and pseudo-BAW mode. The global evolution of frequencies is in rather good agreement with theoretical expectations, except at a pitch of 1 µm for the two modes. The discrepancy may be due to a lower manufacturing quality at such small trench dimensions. In particular, the effect of slanted walls or of a partial etching of the piezoelectric film in-between transducers may affect frequencies.
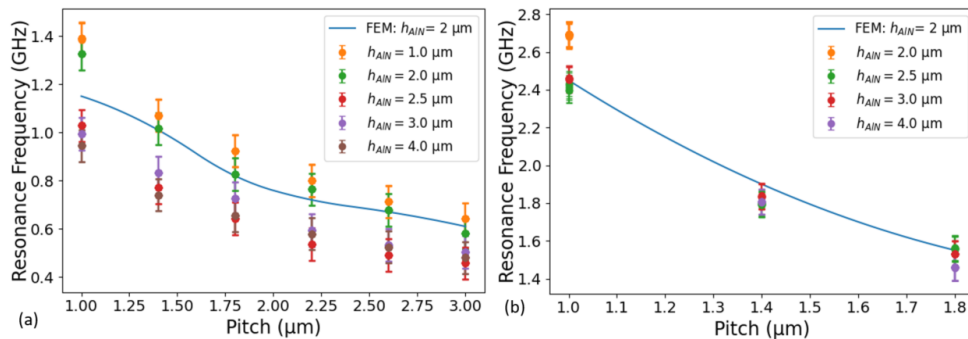
Figure 110: Expanding the comparison of the FEM and Experimental data to different AlN thickness and pitch values for the pseudo-BAW mode (a) and the pseudo-SAW mode (b) in the absence of SiO_2.

Once we subtract the electric measurement of the open devices from the actual devices, 218 distinct device responses are collected. Some of the parameters being varied have little effect on the electric response, while others make a significant difference. The transducers pitch and AlN thickness along with the SiO_2 thickness determine which resonances occur and their frequency location, while the number of electrodes, aperture, and reflectors connection change a little but can affect performance discussed in the next section.

We are narrowing therefore our focus here to three main variables: 1) transducers pitch, 2) AlN thickness, and 3) the SiO_2 layer thickness. Six pitch values ranging from 1 to 3 µm and five AlN thicknesses ranging from 1 to 4 µm were manufactured and tested, with the SiO_2 layer varied as discussed in sections 1.3.

3.2   Condition for the exploitation of the pseudo-SAW and pseudo-BAW modes

The pseudo-SAW mode is clearly and distinctly present in all devices, as illustrated in Figure 111 for transducers with moderate h_{AlN}/p. As demonstrated by Figure 110(a), its frequency varies from 500 MHz. The pseudo-SAW mode presents a peak that goes up to 1.5 GHz at $h_{AlN} = 2$ µm and p= 1 µm, while it can go as low as 500 MHz, as shown in Figure 110. At all thicknesses of AlN, the frequency of the pseudo-SAW mode increases with the reduction in the pitch value.
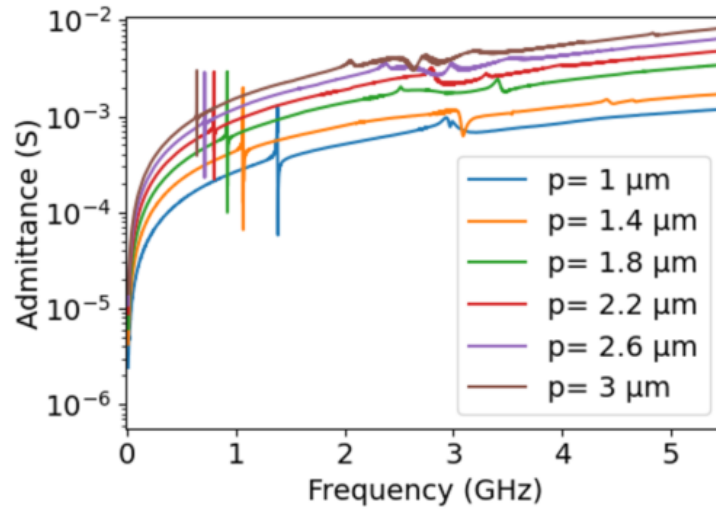
Figure 111: Demonstration of the presence of the Pseudo-SAW peak distinctly for all pitch values, for devices with h_{AlN}=1 um, floating bottom electrode, shorted reflectors, 20 active transducers and an aperture of 20λ.

On the contrary, the pseudo-BAW mode is not well defined for 1 µm-thick AlN in the absence of SiO_2. This is expected from Figure 66(b), which indicates that the condition for the pseudo-BAW mode to appear is for h_{AlN}/p to be higher than 1.2. And its electromechanical coupling factor is expected to increase with h_{AlN}/p. Figure 112 confirms this threshold and shows how the pseudo-BAW mode starts to appear as the normalized height increases.
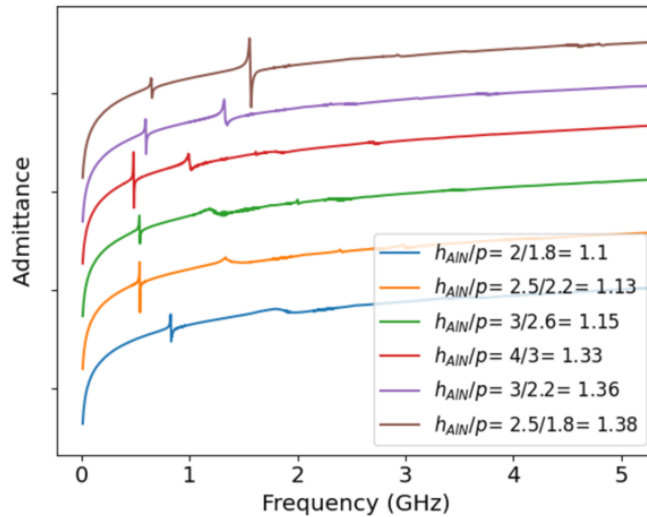
Figure 112: Investigation of the emergence of the pseudo-BAW mode appears with increasing h_{AlN}/p. (Other parameters for the devices are 40 electrodes, an aperture of 40λ, a floating bottom electrode and open-circuited reflectors). The measurements are shifted vertically for clarity.

On the other hand, at h_{AlN}/p larger than 2.8 and above, a new peak appears to accompany the pseudo-BAW mode. It appears experimentally on Figure 113, and is also revealed by the finite element model, despite some discrepancy in its frequency, which can be due to uncertainties in the material constants employed and in the actual geometry of the devices. From the calculated displacement field, this mode could correspond to the hybridization of the second overtone of the thickness mode of the transducers with the surface wave of the substrate.
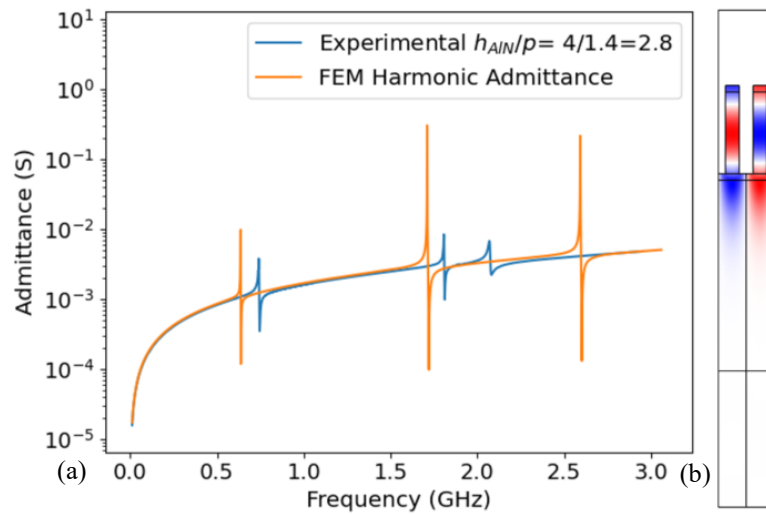
Figure 113: Comparison between the measured electric response of a resonator with $h_{AlN}/p = 2.8$ and the corresponding harmonic admittance calculation (a), revealing the pseudo-SAW, the pseudo-BAW and a higher order mode resulting from the hybridization between the second overtone of the thickness mode of the transducer and the surface wave of the substrate (b).

The introduction of a SiO_2 layer complicates the problem a bit more. Figure 114 compares the electric response of a group of devices with 1 µm of AlN and 210 nm of SiO_2 and varying transducers geometry. As expected, the pseudo-SAW mode always exists. The pseudo-BAW mode only appears for pitch values of 1 µm ($h_{AlN}/p=1$, $h_{SiO2}/p = 0.21$) and 1.4 µm ($h_{AlN}/p=0.7$, $h_{SiO2}/p = 0.15$) at frequencies of respectively 2.8 and 2.1 GHz. For the later periodicity, an additional con-

tribution appears at 2.9 GHz, which could correspond again to the mode resulting from the hybridization between the second order thickness mode in the transducers and the surface wave of the substrate.
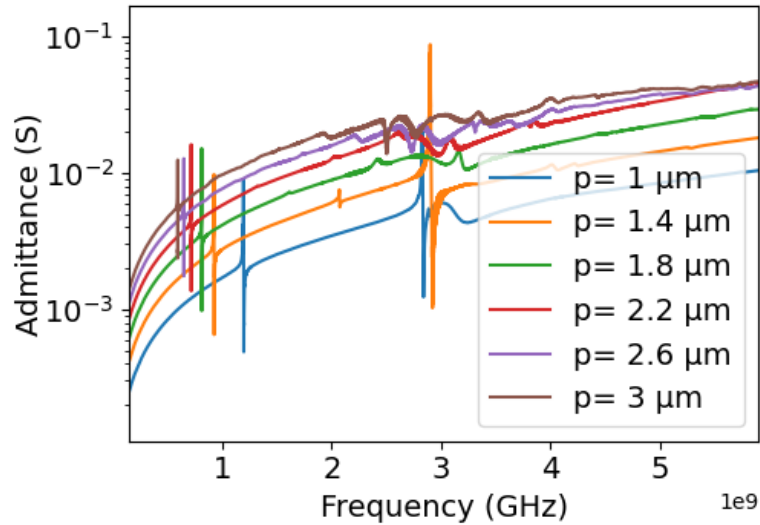
Figure 114: Electrical measurement of devices with SiO_2 underneath (1 µm of AlN, 210 nm of SiO_2, 60 electrodes, aperture of 40λ, open reflectors, and floating bottom electrode).

To reveal only the influence of the SiO_2 layer, independently of periodicity variations, Figure 115 compares the admittances of three identical devices with different SiO_2 layer thicknesses underneath them. All have an AlN thickness of 2.5 µm and a transducers pitch of 1 µm. The pseudo-SAW mode has small change in frequency (as predicted by Figure 70) but lower amplitude, due to decreasing electromechanical coupling factor. Figure 70 (b) expected a decrease of the electromechanical coupling factor of the pseudo-SAW mode from close to 1% down to near 0.45% when increasing h_{SiO2}/p from 0 to 1 at $h_{AlN}/p = 2.5$. On the other hand, the pseudo-BAW frequency varies with SiO_2 thickness (theoretically investigated in Figure 71). We can also notice amplitude variations when varying the SiO2 layer thickness, despite the fact that for this mode, Figure 71(b) would indicate that the electromechanical coupling factor of the pseudo-BAW mode should only vary weakly, from 1.7 to 2.1% at most. This is rather attributed to the evolution of the effective velocity of the mode, which is near 4,800 m/s when $h_{SiO2}/p = 0$ and near 4,200 m/s for $h_{SiO2}/p = 0.7$ or 1. For $h_{SiO2}/p = 0$, the effective wave velocity remains slower than the bulk shear wave velocity in silicon, meaning that the pseudo-BAW mode remains confined close to the surface. For $h_{SiO2}/p = 0.7$ or 1, the wave velocity becomes larger than the bulk shear wave velocity in SiO_2, meaning that acoustic power penetrates in the SiO_2 layer and thus loose confinement.
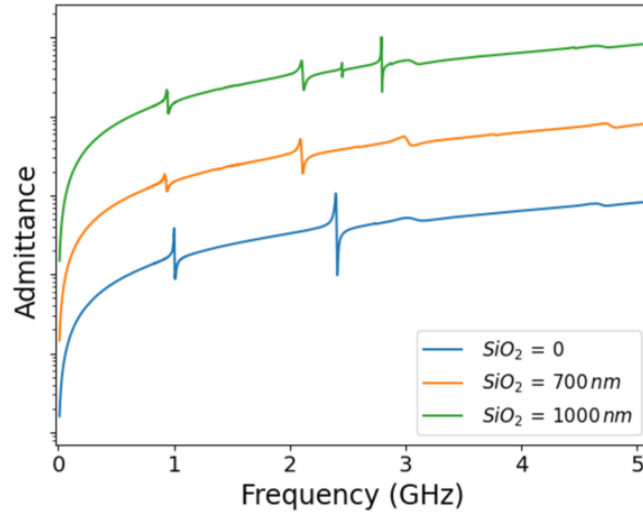
Figure 115: Admittances of identical devices (h_{AlN} = 2.5 µm, p = 1 µm, 80 electrodes, aperture 40λ, open reflectors with floating bottom electrode) with different SiO_2 layer thickness. Responses are offset for clarity.

It is also to be noted that additional contributions start appearing at SiO_2 thicknesses approaching $h_{SiO2}/p = 1$. These contributions are also visible on harmonic admittance calculations, as shown in Figure 116, although further away from the pseudo-BAW mode in the simulations than the experiments. Again, this may be attributed to uncertainties in the material constants employed in the simulation and in the actual device geometry.
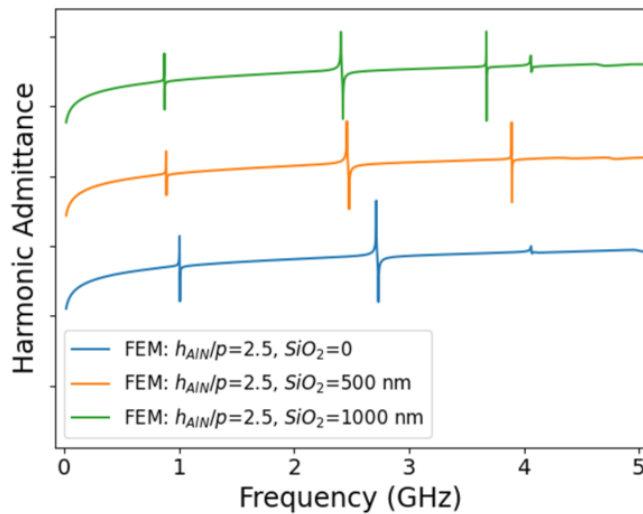
Figure 116: the appearance of the second pseudo-BAW peak with the introduction of SiO_2 according to the FEM

From these observations, it follows that while the pseudo-SAW mode is always excited and well isolated from other modes, the same occurs for the pseudo-BAW mode only for $1.1 < h_{AlN}/p < 2.8$ and $h_{SiO2}/p < 0.7$.

Looking closer to the resonance of the pseudo-SAW mode, one can notice small parasitic interferences whatever the AlN thickness, at p = 1 µm. These parasitic effects almost completely disappear at p = 1.4 µm or higher. The smoothness of the peak keeps improving the higher the

pitch goes, as shown in Figure 117. This could be the result of the difficult etching of the trenches at small pitch values or a higher sensitivity to geometric imperfections for the low pitches.
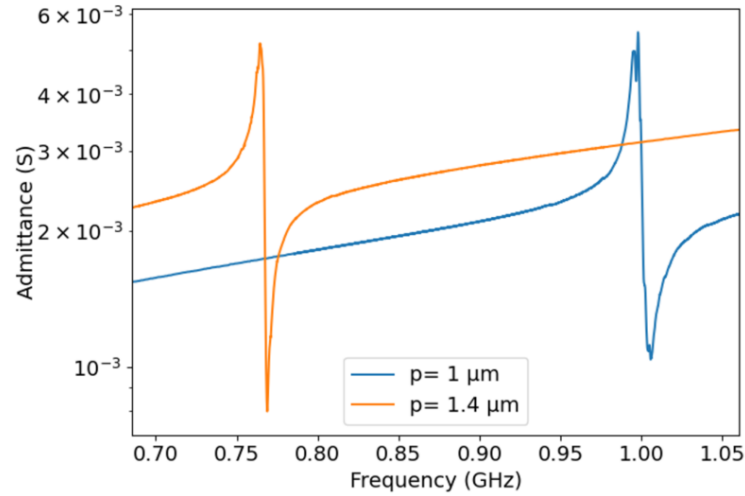
Figure 117: The parasitic interferences at p=1 diminishing with the increase to p=1.4 (h_{AlN} = 2.5 μm, h_{SiO2}=0, 80 electrodes, aperture 40λ, open reflectors with floating bottom electrode)

Figure 118 show the response for a device with p = 3 μm and has Q-factors of 3700 and 3300 at resonance and anti-resonance, respectively.
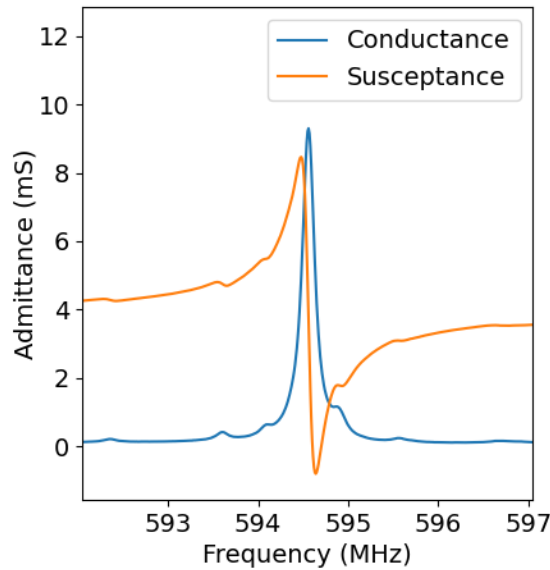
Figure 118: Parasitic-free pseudo-SAW resonance, achieved at h_{AlN} = 1 μm, h_{SiO2} = 210 nm, p = 3 μm, with 40 electrodes, 40λ aperture, floating bottom electrode and open-circuited reflectors.

Similarly, Figure 119 shows one of the most significant electrical measurements of the pseudo-BAW mode, on a wafer with h_{AlN} = 1 μm and h_{SiO2} = 210 nm. It shows little parasitic contributions at 2.8 GHz. The shown response has Q-factors of 1900 and 1700 at resonance and anti-resonance, respectively.
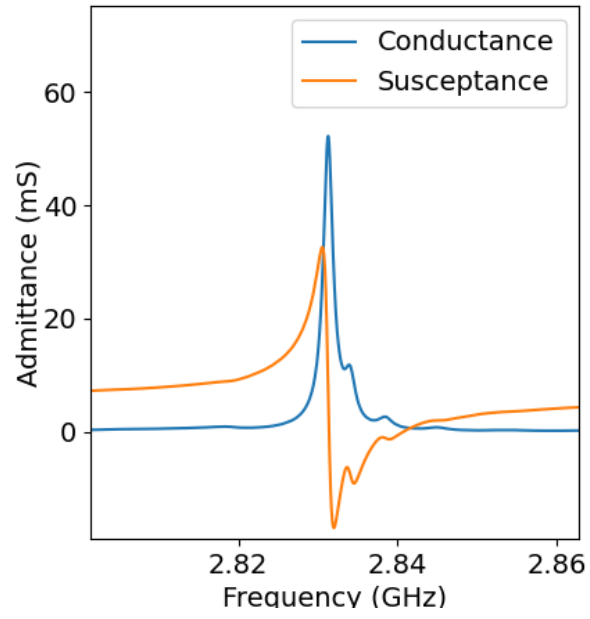
Figure 119: Parasitic-free pseudo-BAW mode resonance achieved at $h_{AlN}=1$ µm, $h_{SiO2} = 210$ nm and p= 3 µm, with 40 electrodes, 40λ aperture, floating bottom electrode and open-circuited reflectors.

3.3   The Pseudo-SAW mode

We discuss here the influence of the most influential geometric parameters on the performances of the pseudo-BAW mode.

Piezoelectric layer thickness

In Chapter 2 section 2.1, the influence of the thickness of the piezoelectric layer was discussed. When hSiO2 = 0, an optimum k² of 0.9% was expected near hAlN/p = 1.8, for a/p = 0.5. Plotting the experimental electromechanical coupling factors as a function of the normalized piezoelectric layer thickness provides a trend which is more difficult to follow. As seen in Figure 120, k_t^2 initially increases with the aspect ratio before it curbs and even slightly decreases. The maximum k_t^2 is about 1.5% at an optimum aspect ratio of h_{AlN}/p = 1.8. This differs from the theoretical expectations (blue curve in Figure 120, which reproduces the curve for a/p = 0.5 of Figure 65 (b)). However, this curve seems to agree well with the distribution of electromechanical coupling factors obtained on devices with 1 μm-thick AlN layers.

It must be noted here that the cross sections shown Figure 92 and Figure 93 indicate that the AlN layers have not been fully etched in between the transducers, with a residual thickness varying from 0 to 40% of the initial layer, depending on the initial thickness and the spacing between transducers. In addition, one can even notice variations in residual thickness from gap to gap even inside the same transducer. As such, it is difficult to precisely evaluate a definite value for the fraction of the piezoelectric layer etched away for a given device. However, plotting also the dependence of k_t^2 on normalized AlN thickness for a minimum value of etching ratio of 60% (dashed green curve in Figure 120), one can notice that the maximum theoretical electromechanical coupling factor is now 1.6% for h_{AlN}/p = 2.4, and that the new curves matches with the distribution of k_t^2 evaluated on devices with 2 μm-thick AlN layers and h_{AlN}/p < 1 (i.e. p = 2.2, 2.6 and 3 μm), or some devices with h_{AlN} = 4 μm. In-between, the plot of the k_t^2 dependence on normalized AlN thickness for an etching ratio of 80% (dashed orange curve in Figure 120) agrees reasonably with the distribution of the electromechanical coupling factors measured for devices with 3 μm-thick AlN. It seems therefore now possible that each experimental point lies on a theoretical k_t^2 vs. transducers aspect ratio curve defined for a specific etching ratio and that the complex dependence of k_t^2 on piezoelectric layer thickness and periodicity results from the difficulty to control consistently the depth of the spacing separating the transducers. These results however also confirm the interest of a partial etching of the piezoelectric layer discussed in Chapter 2 (p. 60), since we would not have been able to reach an electromechanical coupling factor of 1.5% with a complete etching of the AlN layer.
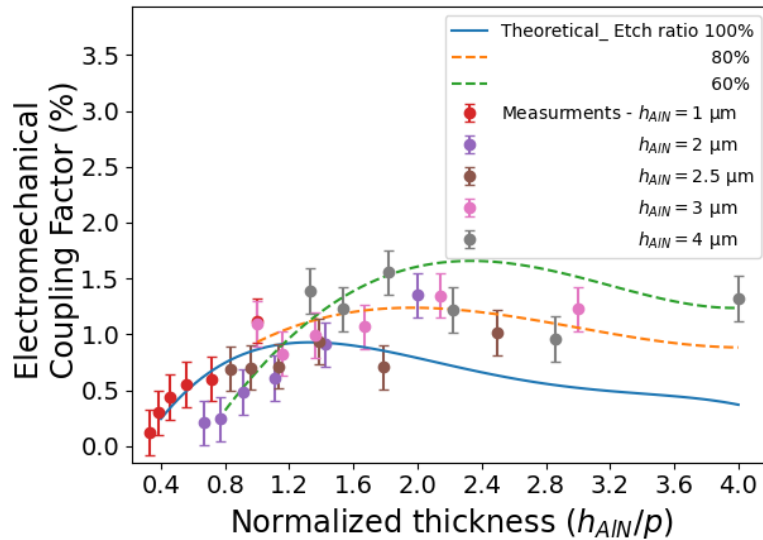
Figure 120: Experimental k_t^2 of pseudo-SAW resonances as a function of the transducers aspect ratios (points), with error bars indicating the spread of experimental values, and comparison with theoretical expectations for fully (solid blue curve) or partially (dashed orange and green curves) etched piezoelectric films in between transducers.

The associated quality factors are reported in Figure 121. Quality factors up to 3,000 at resonance and 7,000 at antiresonance are reached for $h_{AlN} = 1$ µm and no SiO_2. Yet, these values drop suddenly with the thickness of AlN and increase in h_{AlN}/p (i.e. with decrease in periodicity).
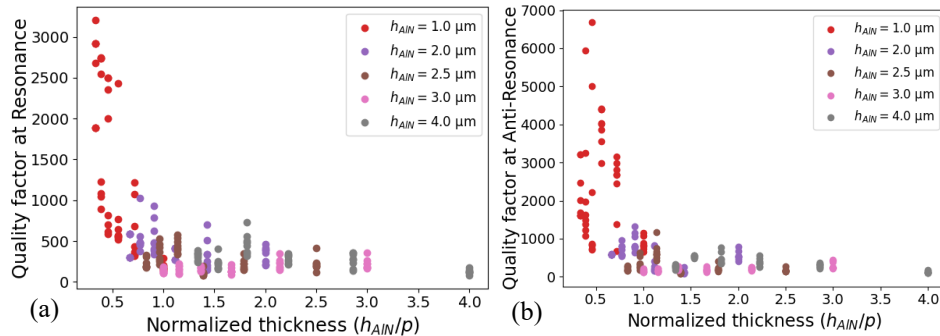
Figure 121: Quality factors of the pseudo-SAW mode as a function of the transducers normalized thickness at resonance (a) and anti-resonance (b).

It must be mentioned that the high quality factors reported are not artifacts caused by spurious resonances or the finite frequency sampling of data that could both affect the calculation of these figures. Figure 122 shows the example of a resonator exhibiting a quality factor at resonance Q_s = 2,900±450 and quality factor at anti-resonance Q_p = 3,200±500.
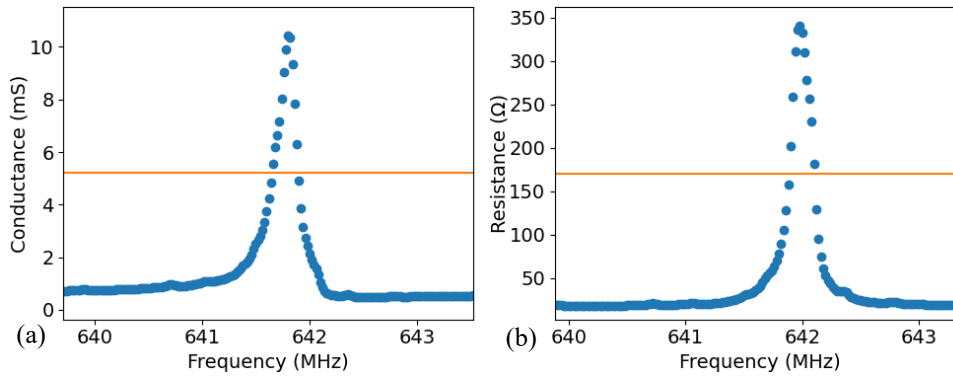
Figure 122: Example of pseudo-SAW resonance (a) and antiresonance (b) with respective quality factors Q_s = 2,900±450 and Q_p = 3,200±500.

The observed fast decrease in quality factors with AlN thickness and with decreasing periodicity seem to originate from two cumulating trends: i) increasing h_{AlN}/p indicate increasing aspect ratios for the trenches etched in the AlN film to pattern the transducer. As discussed previously, this is accompanied by increased sidewall angle, increased AlN remains, but overall a less ideal and reproducible transducers geometry. This ultimately leads to a spread in frequency of the resonance, and thus to reduced quality factors. ii) as discussed in the previous subsection, devices with low pitches exhibit increased spurious resonances content, which also tend to decrease quality factors.

Together, Figure 120 and Figure 121 suggest a compromise between electromechanical coupling factor and quality factor since they behave in opposite trends.

SiO$_2$ layer thickness

In Chapter 2 (p. 62), we have shown that the introduction of a SiO$_2$ layer of a thickness in-between the substrate and the transducers leads to an increase in electromechanical coupling factor of the pseudo-BAW mode for $h_{AlN}/p < 3$, provided h_{SiO2}/p is close to 0.5. It is however expected to have a negative influence on the electromechanical coupling factor of the pseudo-SAW mode. Figure 123(a) shows that this does not seem to be the case experimentally. A closer examination indicates that the theoretical dependence (continuous lines) of k_t^2 on h_{SiO2}/p seems approximately followed for devices implemented with the thinnest AlN layers ($h_{AlN}/p < 2$), but not for devices based on thicker ones ($h_{AlN}/p > 2$). For the later, the residual AlN thickness left in-between the transducers lead to an increase in electromechanical coupling factor, as discussed in the previous paragraph. The amplitude of this effect is sufficient to shadow the influence of the change in silicon dioxide thickness.
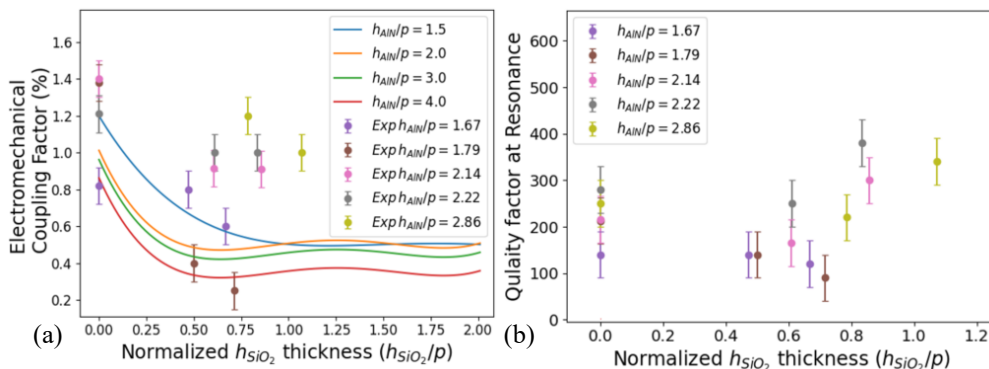
Figure 123: Influence of the SiO$_2$ layer thickness on k_t^2 (a) and Q-factor (b) of the pseudo-SAW mode.

Acoustic aperture

As indicated in section 0, we varied the acoustic aperture of the transducers which is their overlap length between adjacent transducers. In principle, this parameter should only act as a scaling factor for the static capacitance of the resonators, i.e. for their whole electric response. However, Figure 124 indicates that k_t^2 increases with the increase in aperture. This could possibly indicate the existence of some spurious capacitances in-between the end of the transducers and the opposite bus-bar, that could become more prominent as the capacitance of the transducer decreases when the aperture becomes smaller, hence increasing the adverse effect on the electromechanical coupling factor. On the other hand, Figure 124(b) shows that the quality factor decreases with the acoustic aperture. This is a fairly expected effect produced by the increase in electric resistance as the electrodes become longer. In the meantime, a larger aperture leads to an increase of the admittance, hence the decrease of impedance, especially at resonance, which makes the resonator even more sensitive to resistive losses. Therefore, as usual, a compromise has to be struck between the two indices depending on the application.
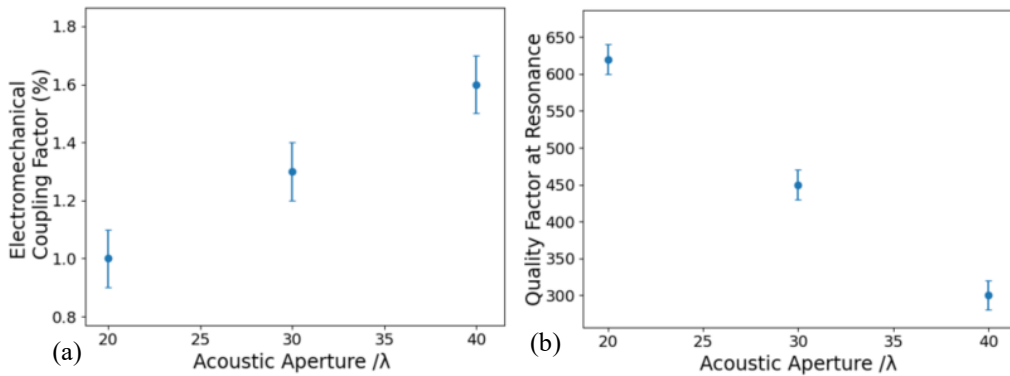
Figure 124: impact of the acoustic aperture on the quality factor (a) and electromechanical coupling factor (b) of the pseudo-SAW mode for devices with 1 µm-thick AlN layer, a 210 nm-thick SiO$_2$ layer, a transducers pitch of 1 µm, 80 electrodes, open reflectors and floating bottom potential.

Reflector connections

The electrical boundary conditions applied to a piezoelectric transducer affect its effective stiffness. Therefore, we may expect that short-circuited and open-circuited reflectors exhibit variations in both the magnitude and phase of their reflection coefficient. Figure 125 depicts the Pseudo-SAW response for a device with short-circuited reflectors and for another with open-circuited reflectors, their geometric parameters being otherwise identical. Although there is a slight frequency shift, both peaks exhibit similar ripples and comparable quality factors (respectively 210±4 in short-circuit condition and 220±3 in open-circuit condition) near the resonance. One can however notice a stronger variation close to the antiresonance, where the quality factors are respectively 270±5 and 140±2. In the open-circuit case, the drop in quality factor is related to a shift in frequency of the spurious resonances located near the antiresonance. At this stage, more investigations are needed to understand the origin of these spurious contributions and whether they are related to the reflectors or not.
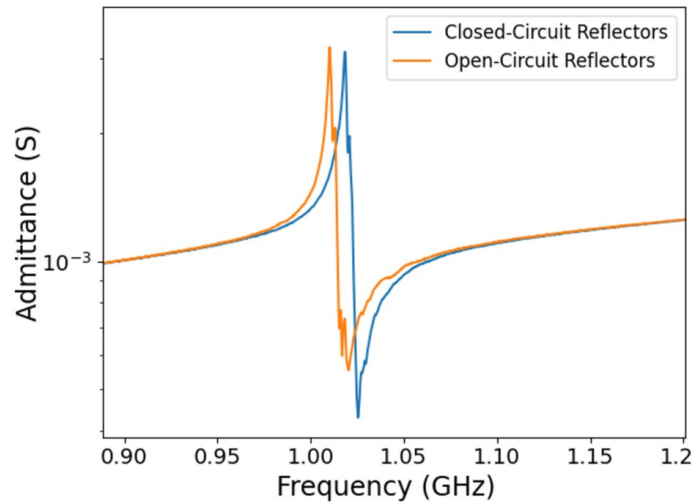
Figure 125: Influence of the electrical connection of reflectors on the pseudo-SAW response.

Conclusions regarding the pseudo-SAW mode

In this section, we presented the electric measurement, coupling factors and quality factors of the pseudo-SAW mode: the first resonance mode of the HSBR appearing at a range of 0.5-1.2 GHz. This mode is undisturbed by other modes in the vicinity. While it is slightly affected by spurious interactions at p=1, these spurious interactions fade the bigger the pitch becomes. This mode is confined and appears at all functional devices with all piezoelectric thicknesses, pitch values and irrelative of the SiO_2 layer.

Best achieved coupling factor was 1.6% on the device demonstrated in Figure 126. It has h_{AlN}=4 μm and p=2.2 μm with 60 electrodes, aperture of 40λ, closed-circuited reflectors and floating bottom potential. The pseudo-SAW mode appears at 0.58 GHz and has quality factors of 370±30 at resonance and 380±25 at anti-resonance. As demonstrated by the SEM pictures in Figure 93, these devices were not completely etched but we conclude this only served towards the increase of their coupling factors.
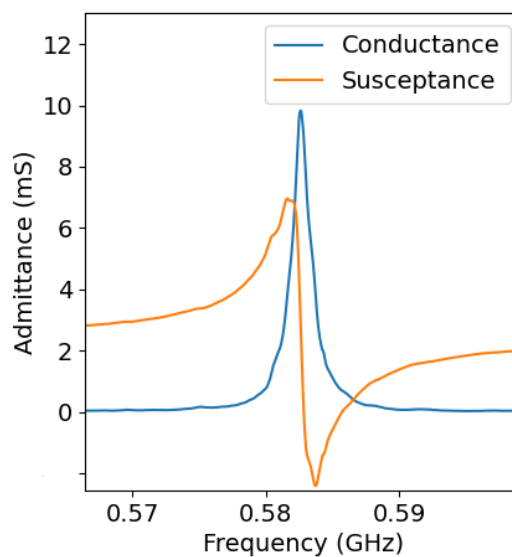
Figure 126: Electric measurement of device with best pseudo-SAW mode coupling factor. (h_{AlN}=4 μm, p=2.2 μm, 60 electrodes, aperture of 40λ, closed-circuit reflector and floating bottom potential).

In terms of quality factors, the pseudo-SAW mode can achieve high quality factors in the order of 4000 as demonstrated in Figure 121. For example, the pseudo-SAW peak presented on Figure 118 with a transducers pitch of 3 µm has a quality factor at resonance of 3700±407 and of 3300±330 at anti-resonance with k^2= 0.1% at 600 MHz. Devices with a small AlN thickness (h_{AlN}=1 µm) had the highest quality factors but have small coupling factors (lower than 0.4%) which motivated us to seek higher AlN thicknesses in the second round of fabrication to attempt improving k^2.

3.4   Pseudo-BAW mode

As we did for the pseudo-SAW mode, we discuss here the impact of the most influential geometric or electrical parameters on the pseudo-SAW mode.

Piezoelectric layer thickness

The conditions for the pseudo-BAW mode to appear and its frequency range are dependent on h_{AlN}/p and were discussed in section 3.2 (p. 94).

In terms of electromechanical coupling factor, the pseudo-BAW mode behaves similar to the pseudo-SAW mode, as shown in Figure 127. k_t^2 is maximum close to $h_{AlN}/p = 1.8$, where k^2=1.7%. The dependency of the electromechanical coupling factor on the AlN thickness follows reasonably the theoretical trends given Figure 66 for a/p = 0.5 or Figure 68(b) for an etching ratio of 100%, the later corresponding to the blue curve added in Figure 127, for AlN thicknesses of 2.5 and 3 µm. Unlike the observations made for the pseudo-SAW mode, the agreement for these thicknesses is reasonably good when considering an etching ratio of 100% for devices with a 2.5 µm-thick AlN layer. According to Figure 68, the points corresponding to a 3 µm-thick AlN layer could rather follow the trend for an etching ratio of 95%. The observed lower k_t^2 values for devices with larger or lower thicknesses could then correspond to lower etching ratios (70% or even lower), especially at high h_{AlN}/p. The inability to accurately determine the etching ratio of the physical devices continues to make the comparison difficult.
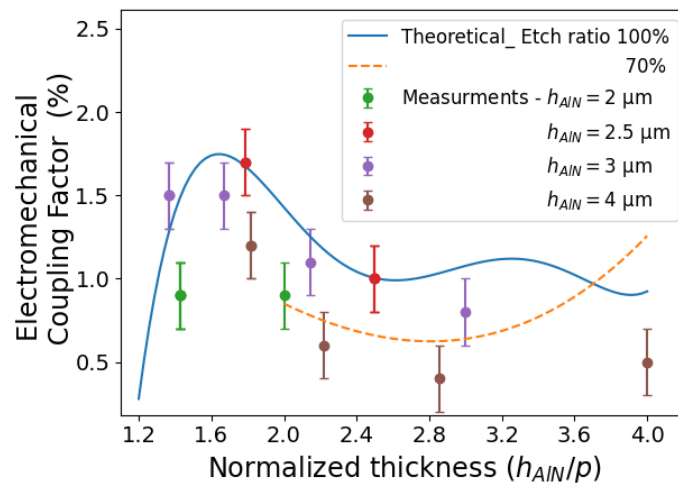
Figure 127: Experimental influence of the transducers aspect ratios on the electromechanical coupling factor of the pseudo-BAW mode (points with error bars indicating the spread of evaluations), along with theoretical expectations when considering an etching ratio of 100% (solid blue line) or 70% (dashed orange line) of the piezoelectric film.

Figure 128 shows that the quality factors of the pseudo-BAW mode increases with the aspect ratio up to approaching 1,000 for the largest aspect ratios. The trend becomes even clearer when viewed with respect to the thickness of the piezoelectric layer only, without normalization by the transducers pitch, as plotted in Figure 129. This seems to indicate that propagation losses, which in principle depend on the ratio h_{AlN}/p, may not be the major contributors to the quality factor. Some other contributions which directly depend on the AlN thickness, such as for example the mechanical damping of the material itself, could limit the quality factors. More investigations would be needed to clarify this.
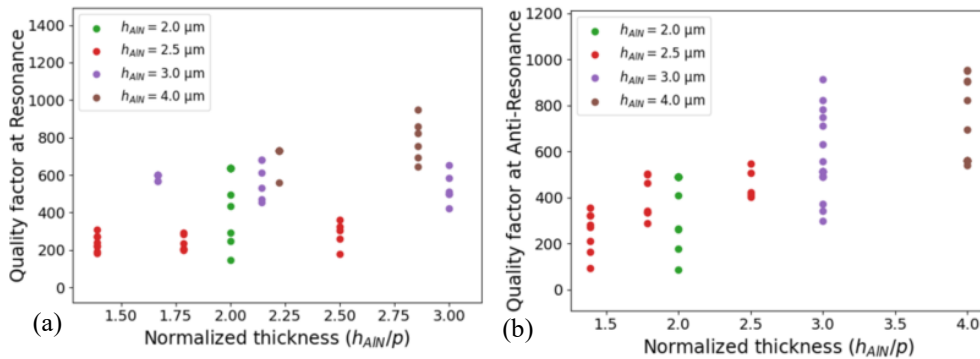
Figure 128: Evolution of the quality factors of the pseudo-BAW mode as a function of the transducers aspect ratio at resonance (a) and anti-resonance (b).
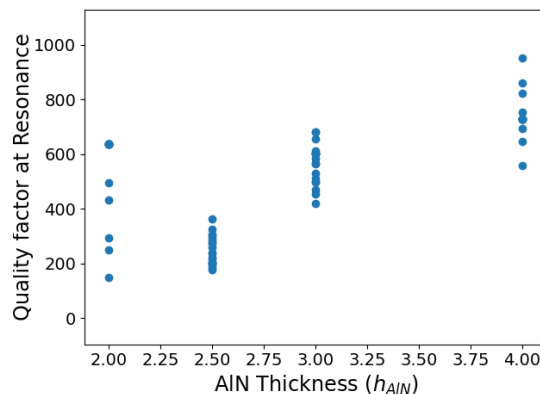
Figure 129: The dependence of the quality factor on the thickness of the piezoelectric layer for the pseudo-BAW mode.

SiO$_2$ layer thickness

The impact we could notice of the SiO$_2$ layer on the performance of the pseudo-BAW mode seems to be less significant than foreseen in the literature, where a large influence of the SiO$_2$ layer thickness was expected [63]. Figure 130(a) shows that, for a given normalized AlN thickness, k_t^2 seems weakly affected by the thickness of the silicon dioxide layer. This is in agreement with Figure 71 given in Chapter 2, which indicated that for $h_{AlN}/p > 1.5$, the electromechanical coupling factor of the pseudo-BAW mode should not vary strongly with the thickness of the SiO$_2$ layer. Therefore, k_t^2 is rather dominated by h_{AlN}/p, whose dependency which we discussed previously is retrieved on these data. Figure 130 (b) also shows that the quality factors (at resonance) are relatively unaffected by the thickness of SiO$_2$, and are mostly dependent on h_{AlN}/p as discussed previously.
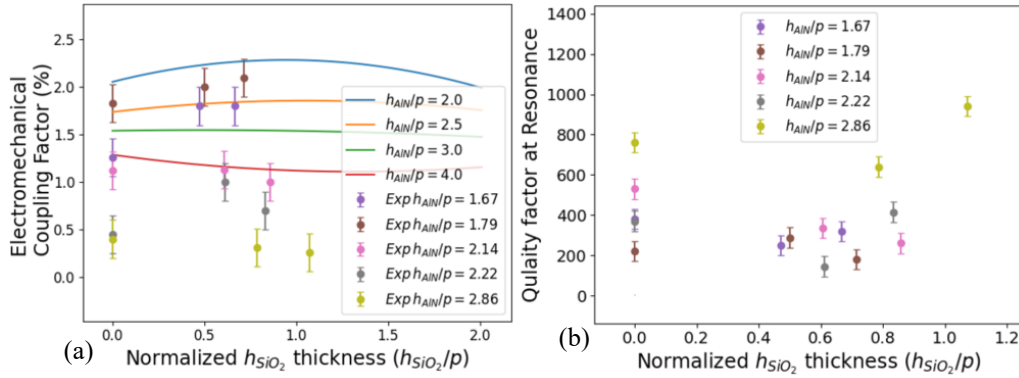
Figure 130: Impact of the SiO$_2$ layer on k$_t^2$ (a) and Q-factor (b) for the pseudo-BAW mode.

Acoustic aperture

The same weak but clear dependence observed for the pseudo-SAW mode is again observed for the pseudo-BAW mode: Figure 131 shows that k$_t^2$ increases with the aperture while the quality factor decreases. As discussed for the pseudo-SAW mode, this could still be related to a decrease of the impedance of the resonator when increasing the aperture and at the same time to an increase of resistive losses in the longer electrodes.
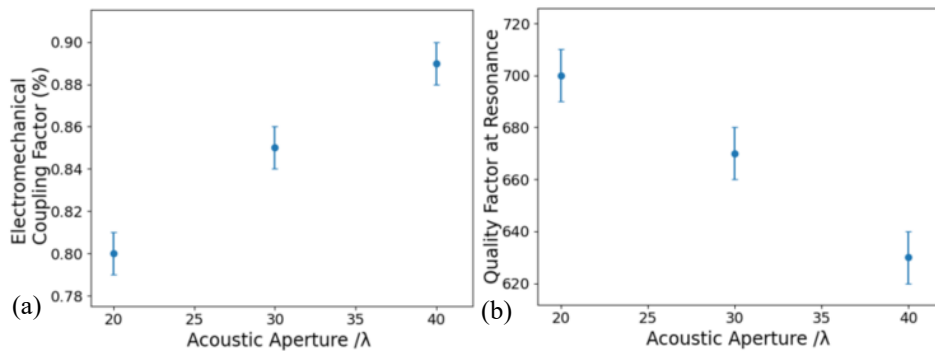
Figure 131: Impact of the acoustic aperture on the k^2 (a) and quality factors (b) of the pseudo-BAW mode for devices with 1 µm of AlN, 210 nm of SiO$_2$ and with a pitch of 1 µm, 80 electrodes, open reflectors and floating bottom potential.

Reflectors connections

Similarly to the pseudo-BAW case, Figure 132, indicates that the resonance with open circuit reflectors is slightly shifted in frequency compared to the one with shorted reflectors. Yet, the short circuit case has a quality factor at resonance of 180±3 and the open circuit case has a quality factor at resonance of 410±12. The quality factor at anti-resonance for the device with short-circuit reflectors is 510±20 and with open circuit reflectors is 370±10. Therefore, while no direct influence of the electrical connections of the reflectors could be determined for the pseudo-SAW mode, we notice an improvement of the Q factor at resonance for the pseudo-BAW mode when considering open circuit reflectors. As for the pseudo-SAW mode, more investigations are needed to clarify the influence of the reflectors at this point.
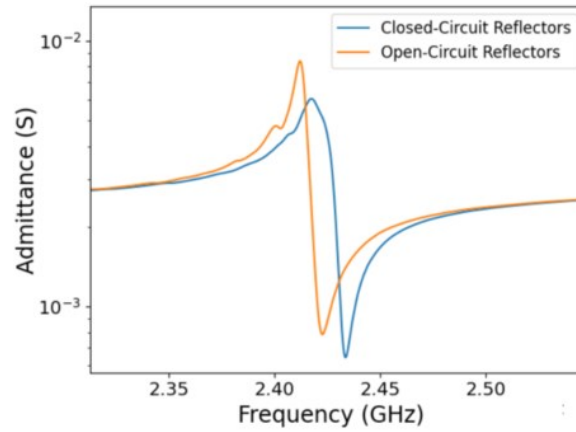
Figure 132: Pseudo-BAW mode admittance for a device with open-circuit reflectors and with closed circuit reflector

Conclusions regarding the pseudo-BAW mode

The coupling factors and the quality factor have inverse proportionality for the pseudo-BAW mode requiring either finding a balance between the two or selecting one over the other as demonstrated in Figure 133. Extra attention needs to be paid to the parasitic contributions interacting with the pseudo-BAW mode in almost completely random manner.
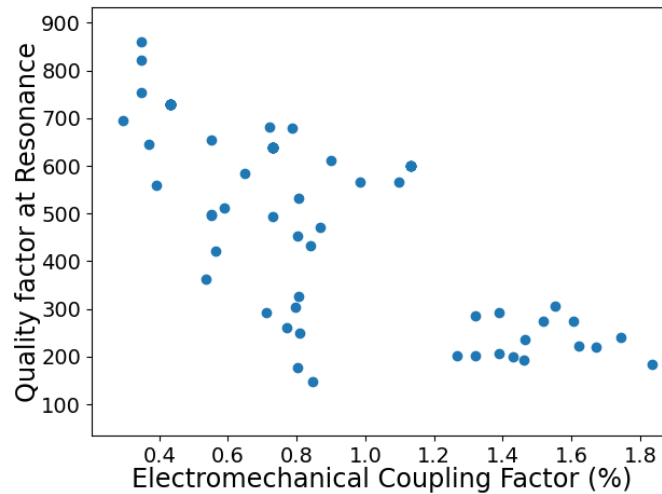
Figure 133: Experimental results showing the inverse proportionality of the coupling factor and the quality factor for the pseudo-BAW mode

Best achieved coupling factor was 1.8% on the device demonstrated in Figure 134. It has h_{AlN}=2.5 μm and p=1.4 μm with 60 electrodes, aperture of 40λ, closed-circuited reflectors and floating bottom potential. The pseudo-BAW mode appears at 1.8 GHz and has quality factors of 200±5 at resonance and 340±10 at anti-resonance. As demonstrated, this device is not disturbed by any spurious interactions or other modes in the vicinity.
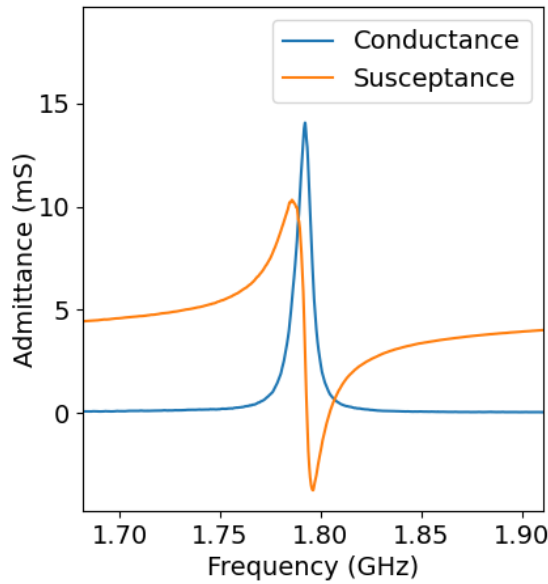
Figure 134: Electric measurement of device with best pseudo-BAW mode coupling factor. (h_{AlN}=2.5 µm, p=1.4 µm, 60 electrodes, aperture of 40λ, closed-circuit reflector and floating bottom potential).

In terms of quality factors, the pseudo-BAW mode can achieve high quality factors in the order of 1000 (much lower than the pseudo-SAW) as demonstrated in Figure 128. While the insertion of the SiO$_2$ seemed to have a little positive effect on the quality factors at high piezoelectric thickness to pitch ratios, the best quality factors observed for the pseudo-BAW were found on a wafer with h_{AlN} = 1 µm and h_{SiO2} = 210 nm shown earlier in Figure 119. It shows little parasitic contributions at 2.8 GHz. The device has Q-factors of 1900±50 and 1700±35 at resonance and anti-resonance, respectively, with k^2 = 0.8%.

4   Towards the fabrication of Scandium-doped Aluminum Nitride HSBR

In order to improve the electromechanical coupling factors of hybrid SAW/BAW resonators, Pashenko *et al.* [81] investigated AlScN as a more promising piezoelectric material than AlN. They determined accurately the piezoelectric coefficients of *c*-axis oriented $Al_{85}Sc_{15}N$ using an interferometer to measure the bending of a test sample under application of an electric field. By comparison with a finite element model to suppress the influence of the electrode size (Figure 135), they could determine effective piezoelectric coefficient of the film.
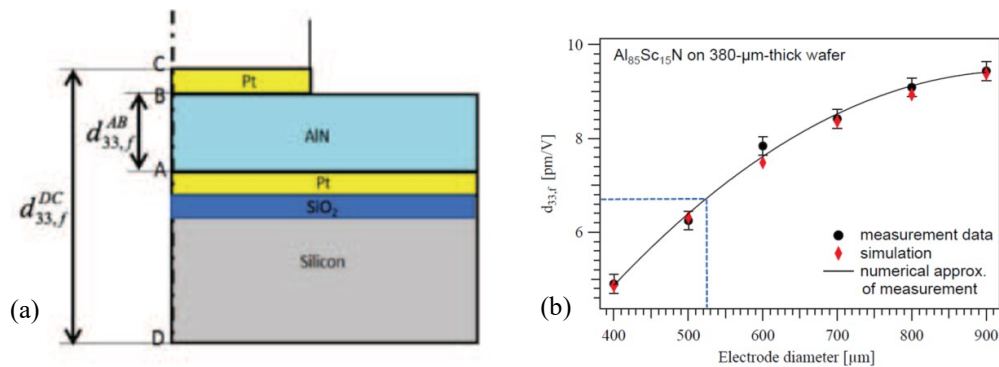
Figure 135: Schematic view of considered device with substrate, Pt top and bottom electrodes, and AlN film (a). Agreement of measured and simulated piezoelectric parameter as a function of the electrode size (b) [81].

The use of scandium doped aluminum nitride (AlScN) instead of pure aluminum nitride (AlN) offers several benefits, including increased piezoelectric properties [58], [73], [74]. This material was introduced relatively recently at CEA-LETI, and is therefore still under development. For this reason, it became available only towards the end of this thesis work.

The effective piezoelectric coefficients of AlScN with varying scandium concentrations were evaluated by measurement of its d_{33} piezoelectric coefficient using a double beam interferometer. The d_{33} parameter quantifies the variation of thickness of the piezoelectric film as a function of the voltage applied to it. Figure 130(a) shows its increase with Sc concentration, in very good agreement with reference values reported in the literature, shown in Figure 130(b).

(a)   (b)
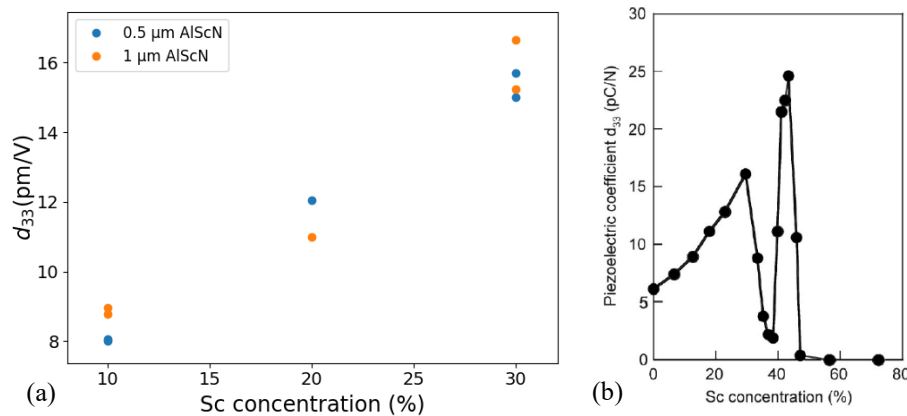
Figure 136: Dependence of the piezoelectric coefficient d_{33} of the AlScN films on Sc doping: measured values (a) and reference values reproduced from [123](b).

We have also started the fabrication of hybrid SAW/BAW resonators using AlScN, using the same process than with AlN to produce a device with similar stack to Figure 77(a). The main technological challenge is the patterning of the AlScN pillars, which is more difficult than for pure AlN [124]

At the point of writing of this work, the deposition of the underlying SiO_2 layer was complete and its thickness confirmed using ellipsometry before and after CMP. The Mo bottom electrode was also deposited and patterned. Figure 137 shows an AFM scan after the deposition of 1 µm of $Sc_{0.1}AlN$ while Figure 138 shows the XRD spectra and rocking curves for all thicknesses and Sc concentrations. The patterning of the transducers is currently under development.
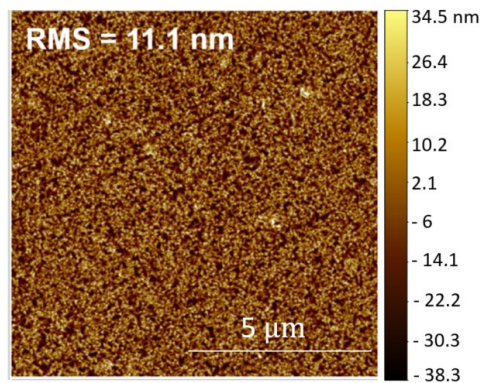
Figure 137: Characterization of AlScN films by AFM
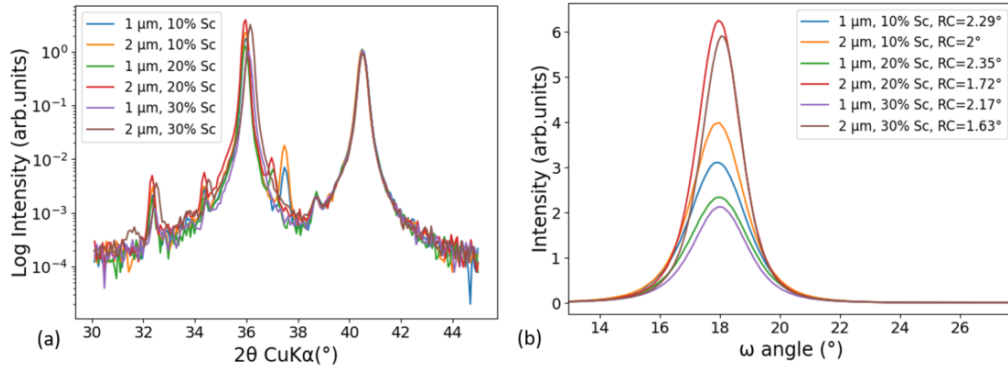
Figure 138: XRD pattern (a) and rocking curves of the (002) peaks of AlScN with different thicknesses and Sc concentrations (b).

5   Conclusions

We have presented in this chapter a process flow for the fabrication of the HSBR using a SiO_2 hard mask and dry etching to define the transducers. This allowed us fabricate resonators with reasonably well defined and well etched at $h_{AlN}/p < 2.5$. For more aggressive features, the trenches between transducers are only etched over 60% of the initial piezoelectric layer. The devices are however functional and compare well with previous attempts at fabricating hybrid SAW/BAW devices reported in the literature (see Chapter 1, section 3).

We then presented the method used for the analysis of the electrical measurements, and especially for the removal of parasitic series resistances and feedthrough capacitances in order to reveal the intrinsic response of the resonators.

Our manufactured devices were functional and exhibited two resonances modes corresponding to the pseudo-SAW and the pseudo-BAW modes. The conditions for the excitation of the pseudo-BAW mode was experimentally found to be $h_{AlN}/p > 1.3$, confirming the theoretical expectations of Chapter 2. We also highlighted that this ratio should remain below $h_{AlN}/p = 2.8$, to prevent a second order thickness mode of the transducer to appear, potentially close to the pseudo-BAW mode.

We then investigated more in detail the dependence of the performances of the two modes on the geometry and electrical configuration of the devices. The pseudo-SAW mode was found to have coupling factors of 1.5% at 600 MHz or near 0.8% at frequencies up to 1.4 GHz. These values agree with the theoretical expectations of Chapter 2. The incomplete etching of the AlN layer has a rather positive influence on the electromechanical coupling factor, as it helps improving it. With the help of the theoretical analysis performed in Chapter 2, we could relate to some extent the experimental electromechanical coupling factors to transducers geometry and to the residual AlN thickness. The pseudo-SAW mode response is in general clean and free of parasitic effects, with quality factors up to $Q_s= 2900\pm450$ and $Q_p = 3200\pm500$ which makes them interesting for timing or sensor applications, where a relatively high quality factor is needed and a moderate electromechanical coupling factor can be employed [125]–[127].

The pseudo-BAW was found to have coupling factors of 1.8% at a frequency of 1.8 GHz, or near 1% at frequencies up to 2.8 GHz. It has quality factors approaching 1000 that can be improved with the introduction of the SiO_2 layer. Here again, these performances are related to the

actual geometry of the transducers. From the theoretical analysis of Chapter 2, the residual AlN remaining in-between the transducers limit the electromechanical coupling factors. For this mode, reaching more ideal geometries would certainly help improving further performances.

Still, we could not measure electromechanical coupling factors beyond 2% with AlN-based resonators, and the theoretical analysis of Chapter 2 seems to confirm that this is the limit that can be reached with this material. To reach higher electromechanical coupling factors, it is necessary to change the piezoelectric materials. We have presented at the end of the chapter future plans to reapply the same process flow to Sc doped AlN. The process adjustments needed for this, especially the patterning of AlScN, is currently under development. In Chapter 4, we propose an alternative approach based on lithium niobate ($LiNbO_3$) a material also known for its superior piezoelectric properties compared to AlN.

The frequency range achieved so far (below 1.4 GHz for the pseudo-SAW mode and between 2 and 3 GHz for the pseudo-BAW mode) is well covered by existing industrial solutions with already impressive performances. New applications would require operation at higher frequencies. This will be covered in chapter 5, where we propose a different configuration which allows a new high frequency mode to be exploited beyond 4 GHz.

Chapter 4: Lithium niobate based HSBR

Introduction

The previous two chapter have focused on the use of AlN as the piezoelectric material for hybrid SAW/BAW resonators. However, lithium niobate (LiNO$_3$ or LNO) offers distinct advantages over Aluminum Nitride (AlN) as a material for various MEMS applications. LNO exhibits high electromechanical coupling coefficients, and low mechanical losses [39]. Therefore, in this chapter, we investigate hybrid SAW/BAW resonators based on lithium niobate thin films. This material exhibits a different crystal symmetry than AlN, AlScN or ZnO. In particular, it is well suited to the excitation of thickness shear waves, which is supposed to lead to the appearance of new modes resulting from the interaction of LNO thickness modes with a substrate.

In section 1, we present briefly modifications of the finite element model we presented in Chapter 2 to deal with the peculiarities of lithium niobate: the possibility to vary the crystal orientation of the piezoelectric layer, which offers a new design parameter to investigate, and the need to account for shear horizontal waves that were not considered in the 2D model used for AlN.

In section 2, we then investigate the dependence of the wave velocity and electromechanical coupling factor for the modes of interest on crystal orientation in order to define the crystal cut and propagation direction of highest potential to favor a high operation frequency and high electromechanical coupling factors.

In section 3, for the two modes of interest we retained in section 2, a paramedic analysis is conducted, similar to the ones performed in Chapter 2 for the pseudo-SAW and pseudo-BAW mode in AlN-based devices, in order to refine the design.

In section 4, we address the fabrication of lithium niobate-based devices. We discuss the modifications required by the fact that lithium niobate cannot be deposited and is only available in thin-film form through layer transfer techniques, which add their own constraints and present some preliminary experimental results of the first steps.

1   Finite Element Model

The crystal symmetries of lithium niobate being more complicated than those of AlN, there are a few differences to apply to the model described in Chapter 2. The general layout description and assumptions described previously apply, with the exception of the differences listed here.

1.1   Adaptations of the finite element model
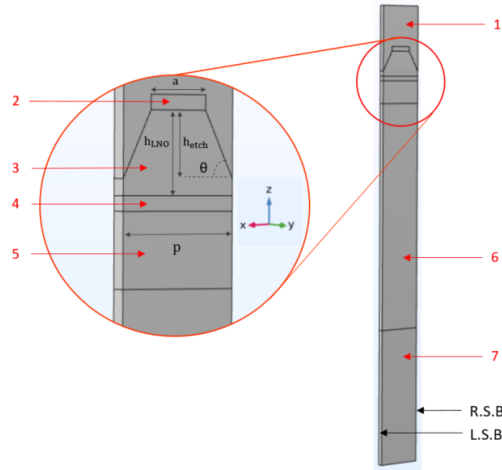
Figure 139: Periodic unit for a LNO-based HSBR.

Figure 139 shows an edited version of Figure 48, where the unit cell is a slice made up of one transducer. Compared to the 2D model of Chapter 2, we refer to new axis directions: x is the propagation direction of the wave, z is the thickness direction and the y is the depth, oriented along the pillar length. The differences between this model and the AlN-based model are as follows:

1-   The model is now 3-dimensional instead of 2-dimensional. In Comsol Multiphysics, this first allows for the freedom to specify the crystal orientation of LNO, through the definition of the geometric transformation leading from the geometric frame (x, y, z) to the crystal orientation frame (X, Y, Z), which was much more constraint in 2D. This transformation is in practice a rotation, described using Euler's angles (α, β, γ), following a Z-X-Z convention. The transformation and the definition of the rotation angles is depicted in Figure 140.
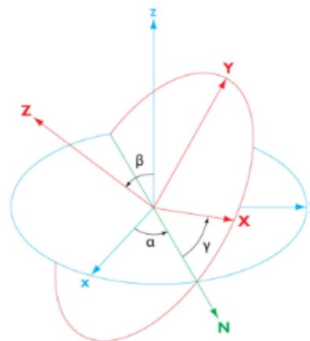
Figure 140: Definition of a rotated coordinate system though Euler's angles [128].

The move to a three-dimensional model also allow the software to consider out of plane displacements (along the y direction), that are necessary to consider shear horizontal modes, but which were not available in the previous two-dimensional model.

2- While the geometry is mostly the same as before, we will always consider a SiO_2 layer underneath the bottom electrode here. This layer is necessary for fabrication purposes. Figure 139 shows therefore 7 domains: domains 1 and 2 correspond to the vacuum and the top electrode; domain 3 is the piezoelectric pillar, whose geometry is defined as a function of the etching ratio and the etching angle; domain 4 is the bottom electrode on top of the SiO_2 layer, which constitutes domain 5; domains 6 and 7 represent the substrate material, typically Si, and the PML layer.

3- In the HSBR structure, the pillars are designed with significantly higher aperture compared to the pitch, which supports the validity of assuming plain strain conditions in the two-dimensional model. In order to incorporate the same assumption into a three-dimensional model, a periodic boundary condition is introduced to ensure that the mechanical displacements and the electric potential are the same on both sides along the y-direction of the slab we model. Provided the depth of this slab is small enough, this constraints the field to exhibit no dependence on the depth coordinate (y). By implementing this continuity boundary condition, the simulation follows the same assumptions of the two-dimensional model of Chapter 2, while benefiting from more freedom to specify the crystal orientation and to be able to simulate shear horizontal modes.

4- To save computational power, the periodic unit cell is composed of one transducer instead of two. As we still represent an alternating excitation applied to the top electrodes, we consider that each transducer is 180° out of phase with its successor. Therefore, periodic conditions with Floquet conditions $k_p = \pi/p$ are applied on the opposite faces along the x direction. In this case, the piezoelectric layer is encompassed between a top electrode set to a 1 V voltage. The electric boundary conditions will thus implicitly consider that the neighboring transducers will have their top electrodes set to -1 V. So we ground the bottom electrode in order to provide an electrical boundary condition compatible with the Floquet condition considered. This could be equivalent to assuming that the bottom electrode is left floating, as the only floating electric potential solution of the problem would be 0 V.

1.2   Hybrid SAW/BAW modes with lithium niobate transducers

Figure 141(a) shows the calculation of the harmonic admittance of a hybrid SAW/BAW structure based on lithium niobate (Y-cut, propagation along the X crystalline axis i.e. Euler angles (0°, 90°, 0°)). Figure 141(b) shows the calculation of dispersion curves in the same structure. By comparison with respectively Figure 54, these calculations show that in the general case, the lithium niobate hybrid SAW/BAW structures support more modes than the AlN-based ones. In particular, we identify the first 7 modes, labelled on Figure 141, and whose displacement fields are shown in Figure 142.
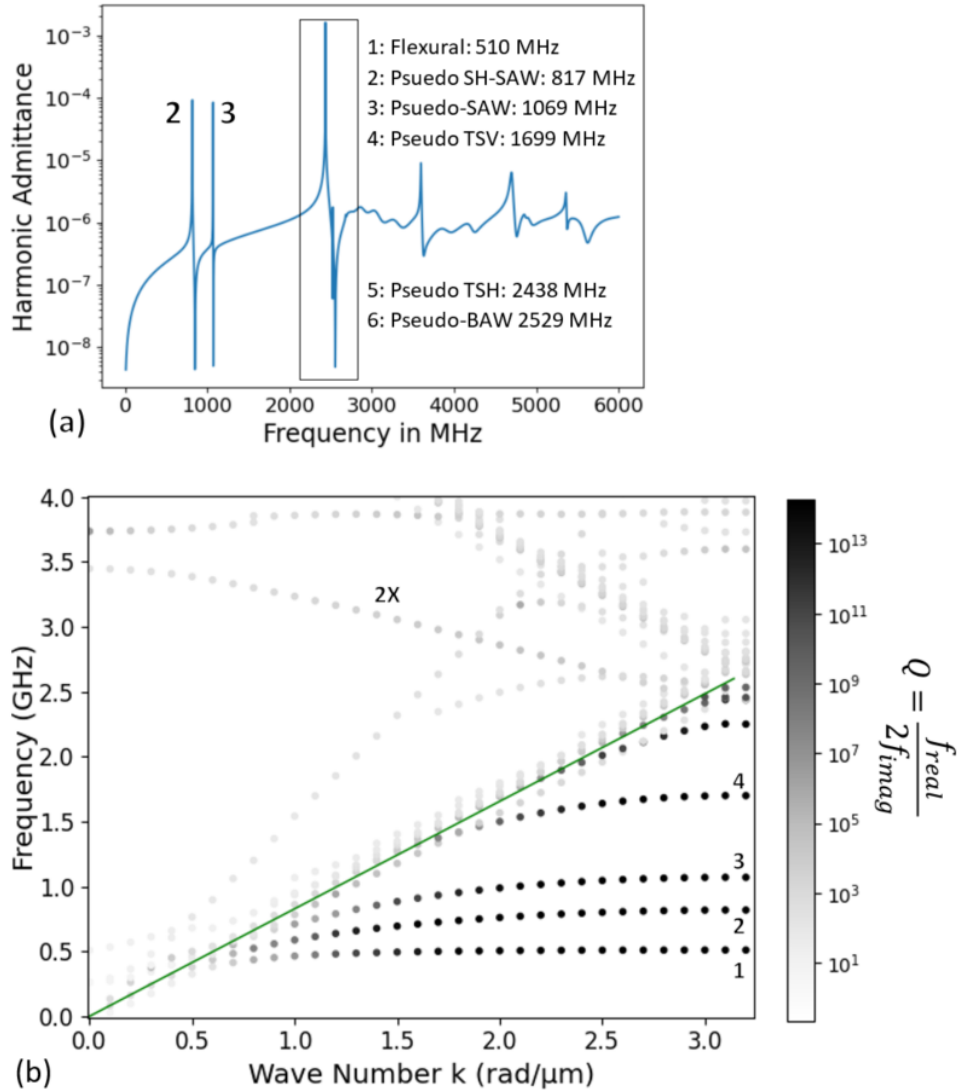
Figure 141: Harmonic admittance calculated for k=3.14 1/um (a) and dispersion curve (b) for a structure based on Y-cut lithium niobate, propagation along the X-axis. (Al/LNO/Al/SiO$_2$/Si, h$_{LNO}$/p=0.55, a/p=0.5, El/p=0.1, h$_{SiO2}$/p=0.5) Green line is the substrate wave velocity.

- The **Flexural Mode** (Figure 142 (a)): the displacements are primarily along the x direction: this corresponds thus to shear deformations of the transducers. The mode shape corresponds to the thickness shear mode of the pillar, where the top and bottom surfaces move in opposite directions along the x-axis. Since the bottom edge is attached to the substrate, the bottom of the transducer is almost clamped while to top experiences maximum displacement. As with AlN devices, this mode does not appear on the harmonic admittance, since its electromechanical coupling factor is zero.

- **The pseudo-SAW mode** (Figure 142 (b)), which is identical to the mode visible on AlN devices. The branch labelled "2" corresponds to the dispersion branch of this mode where the maximum displacement coincides with the center of the pillar. This mode reaches the end of the Brillouin zone at a frequency of 817 MHz, above which it is no longer excited since the periodicity of the transducers induce a stop-band for this mode. It reappears above 2.457 GHz, along the dispersion branch labelled "2X", where it is spatially shifted so that the transducers are located now on its nodal points.

- **The pseudo shear horizontal (SH) SAW mode** (Figure 142 (c)) is the analogous of the flexural mode, but with displacements primarily along the transverse (y) direction. The mode shape represents lateral shearing of the pillar's surface in the y direction, with particles oscillating horizontally. Similar to the pseudo-SAW mode, the wave is travelling on the surface of the substrate, which indicates a coupling between the mode of the transducer and the shear horizontal surface wave. This mode certainly existed only in AlN devices, but could not be revealed by the 2D model employed to simulate them. Here, with lithium niobate, this mode even has a contribution on the harmonic admittance, indicating that it has piezoelectric coupling. Its vicinity with the pseudo-SAW mode means that care should be taken to try to excite only one of those two modes at a time, so that they do not disturb each other.

- **The pseudo thickness shear (vertical) (TSV) mode** (Figure 142 (d)), which corresponds to the coupling between the bulk shear mode (thickness shear mode) of the piezoelectric pillar and the surface wave of the substrate. It involves shear motion predominantly along the x-direction. The pseudo TSV mode and the flexural mode are the least coupled modes of all 6 modes.

- **The pseudo-BAW mode** (Figure 142 (e)), similar to the same mode excited in AlN resonators. It is the pseudo thickness extensional mode.

- **The pseudo thickness shear horizontal mode (TSH)** (Figure 142 (f)) results from the coupling between the thickness shear horizontal mode of the transducer, where shear motion is polarized predominantly along the y-axis, and the shear horizontal surface wave.
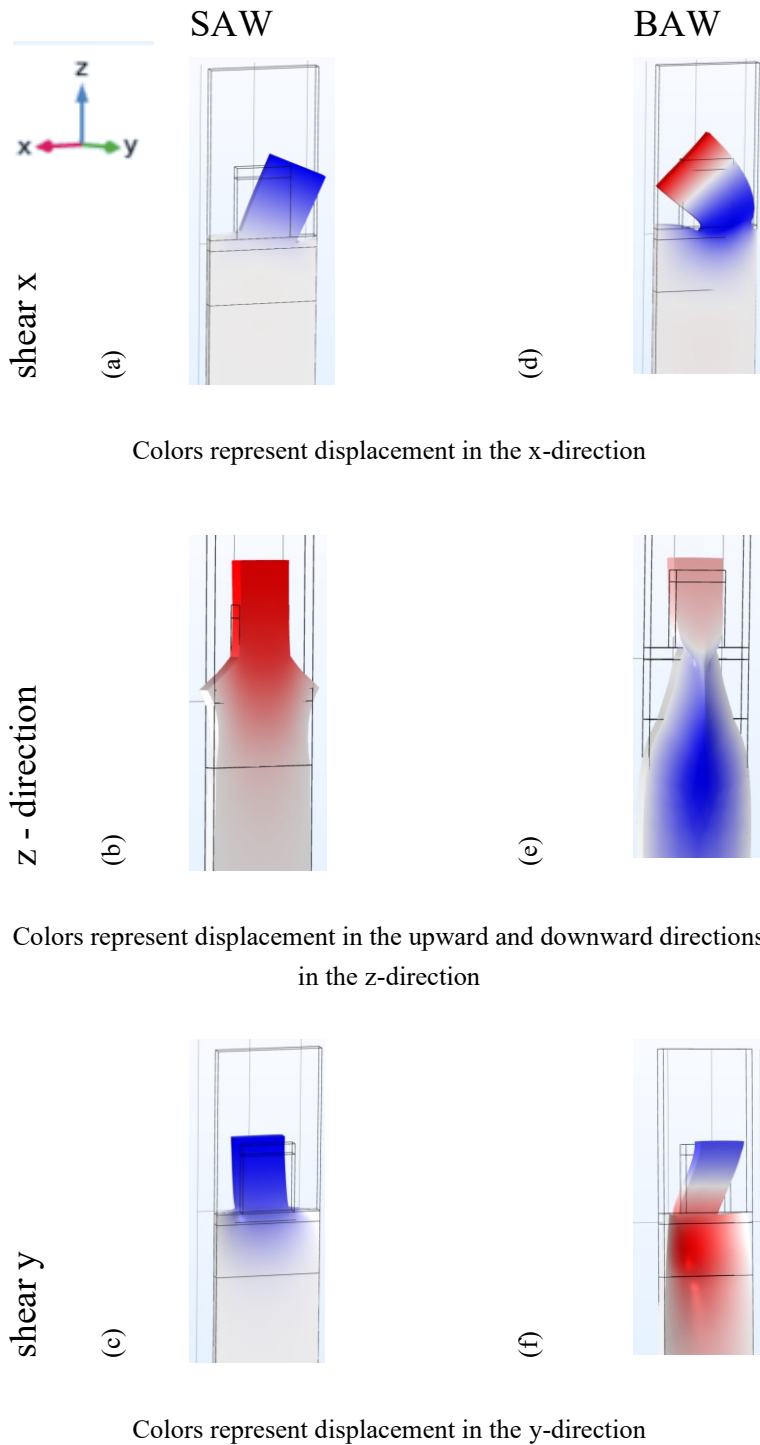
Figure 142: Modes supported by a LNO hybrid SAW/BAW structure, represented at k = π/p and same structural parameters as Figure 141 (a) flexural mode, (b) pseudo-SAW mode, (c) pseudo shear horizontal surface wave mode, (d) pseudo thickness shear vertical mode, (e) pseudo BAW mode, (f) pseudo thickness shear horizontal mode.

2   Lithium Niobate crystal orientation

LNO exhibits strong anisotropic properties. Therefore, the behavior of the acoustic wave within the hybrid SAW/BAW structure is intricately tied to both the crystalline orientation of the lithium niobate film and the propagation direction of the wave, affecting factors such as the mode of propagation, its wave velocity, and its electromechanical coupling.

Although all orientations can be theoretically analyzed, practical considerations often limit the options to orientations that are readily accessible. Lithium niobate thin films are either obtained by growth or layer transfer methods. In the first case, the crystal orientation of the material results from the crystalline structure on the substrate on which the layer is grown and from the deposition process. In principle, films with orientations (0001) or Z-cut, (01-12) or Y+33°, (10-10) or Y-cut and X (11-20) may be grown, but on very specific substrates [129]. Layer transfer methods offer more versatility, since the film is obtained by thinning or splitting a bulk lithium niobate wafer. In this case, for easier fabrication and practical implementation, devices are based on commercially available crystal orientations. These orientations are thus given more attention here. We consider aluminum (Al) as the electrode material, as it is the material used at CEA-LETI for the electrodes of SAW or BAW devices [40], [130], instead of the Mo considered in the previous chapters. The investigations are conducted while keeping geometrical parameters fixed to the values given in Table 9.

Table 9: geometrical parameters considered during the investigation of the influence of the LNO crystal orientation.

Periodicity (p)	1 µm
Piezoelectric layer thickness (h_{LNO}/p)	0.7
Bottom and top electrode thicknesses (h_{Al}/p)	0.1
SiO_2 thickness (h_{SiO2}/p)	0.5
Etching Ratio (h_{etch}/h_{LNO})	100%
Coverage ratio (a/p)	0.7
Sidewall angle	90 °

2.1   Rotated Y-cut

A majority of available substrates or grown layers exhibit a crystal orientation described as a *rotated Y*-cut. This means that the thickness of the layer is oriented by an angle θ from the Y-axis of the crystal, in the YZ plane, as sketched in the inset of Figure 143. We consider in the meanwhile the X-axis as the propagation direction, with the crystalline axes X, Y and Z defined as specified in [10] Several specific cases are identified as the θ goes from 0 to 360:

1) $\theta=0°$ corresponds to the Y-cut, whose harmonic admittance is shown in Figure 141(a)

2) $\theta=90°$ corresponds to the Z-cut

3) $\theta=36°$, 41°, 64°, 128° and 163° are the orientations available commercially. The Y+36° and Y+163° cuts are usually considered for BAW applications as they favor the excitation of respectively bulk longitudinal and bulk shear waves [131]. The other orientations are usually considered for SAW applications, with the Y+41° favoring the excitation of a shear horizontal SAW mode.

Figure 143 shows the dependence of the electromechanical coupling factor of the four modes that are excited on the crystal orientation: the pseudo SH-SAW, the pseudo-SAW mode, the pseudo TSH and the pseudo-BAW mode. It is interesting to note that the pseudo-SAW and the

pseudo-BAW modes on one hand and the pseudo-SH-SAW and the pseudo TSH modes on the other hand exhibit the same dependence. This is an indication that they both result from the hybridization of either the thickness longitudinal or the thickness shear vibrations of the transducers with surface modes.   The pseudo-BAW mode exhibits a maximum k^2 of 1.2% at about θ=40° cut, while the pseudo-SAW mode has a maximum k^2 of 4.8% at about θ=30°. This is higher than what could be achieved with AlN-based devices. Both modes also exhibit a minimum electromechanical coupling factor for θ=90°, which was the equivalent of the crystal orientation of c-axis AlN considered in chapters 2 and 3, which proves that both piezoelectric materials have very different piezoelectric tensors. Modes with higher coupling factors are the pseudo SH-SAW, with a maximum k^2= 11% for θ=0°, and the pseudo TSH mode with a maximum k^2 of 17.5%, also for θ=0°. However, as seen Figure 143, since the electromechanical coupling factor of the pseudo-BAW mode does not reach exactly 0 (k^2=0.04%) for θ=0°, the pseudo TSH mode and the pseudo-BAW modes are overlapping in this configuration.
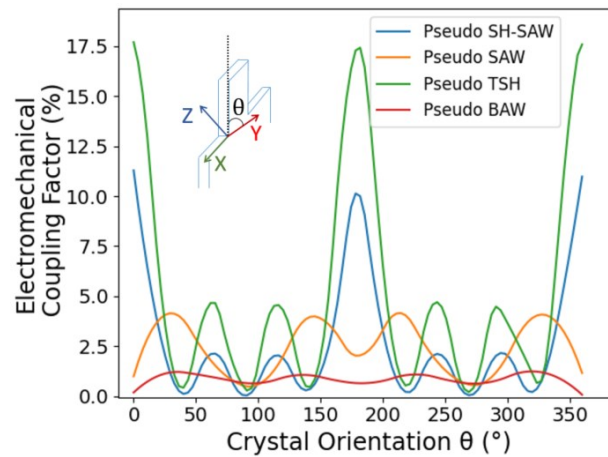
Figure 143: Variation of electromechanical coupling factor of the modes of interest with crystal orientation.

As the Y-cut seems to show the highest potential for reaching large electromechanical coupling factors, we now investigate the influence of the propagation direction φ in this plane, as shown in Figure 144. The change in in-plane propagation direction does not seem to affect the pseudo-SAW mode, which maintains an almost constant electromechanical coupling factor of k^2=1.3%. Both the SH-SAW and the SH-BAW have a maximum electromechanical coupling factor at φ=0°, which drop significantly to near zero as φ reaches 90°. Clearly, when using the Y-cut, propagation along the X-crystalline axis is the best choice.
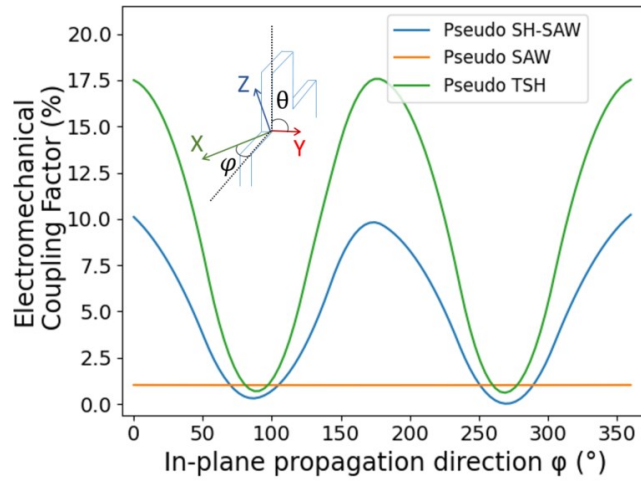
Figure 144: Variation of electromechanical coupling factor with in-plane orientation for Y-cut piezoelectric films (where θ=0).

2.2   Rotated X-cut

Although rotated X-cuts are not commercially available, we investigated the dependence of the electromechanical coupling factors of the various modes also on the crystal orientation for such potential cuts. We consider the thickness direction to be inclined by an angle θ off the X-cut in the XZ plane, with the Y-axis being the propagation direction, as shown in Figure 145. For such orientations, the flexural mode, the pseudo-SH-SAW mode, the pseudo TSV mode and the pseudo TSH mode appear distinctly on the harmonic admittance and are electromechanically coupled. The pseudo-SAW mode appears at the exit of its stop-band rather than at the entrance as in the case of AlN. Again, as for rotated Y-cuts, a similar dependence of k^2 upon θ is seen for the pseudo SH-SAW and the pseudo TSV modes, indicating that they originate from the same deformation of the transducers. Maximum electromechanical coupling factors are respectively $k^2=1.75\%$ at $\theta=0°$ for the flexural mode, $k^2=0.45\%$ at $\theta=0°$ for the pseudo TSV mode and $k^2=1\%$ at θ=30° for the pseudo-SAW mode. The most significant modes in terms of coupling factors are again the pseudo-SH-SAW mode with a maximum k^2 of 11% and the pseudo TSH mode with a maximum k^2 of 22% at exactly θ=0°. Therefore, the X-cut appears to lead to higher electromechanical coupling factors than any Y-cut configuration for the pseudo-SH-SAW and the pseudo TSH modes.
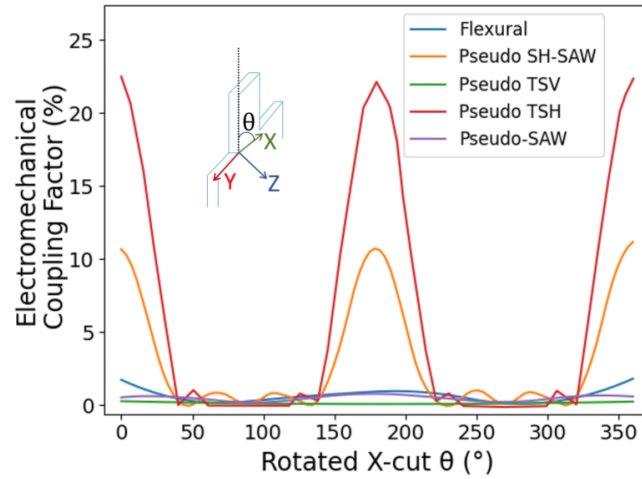
Figure 145: Variation of the electromechanical coupling factors of the modes of interest with crystal orientation for rotated X-cuts.

Considering an X-cut film, we investigate the influence of the in-plane propagation direction φ (Figure 146). The pseudo TSV and the flexural modes have maximum k^2 equal to 1.4% and 5.2% respectively at φ=70°. The electromechanical coupling factor of the pseudo SH-SAW mode is also improved by varying the propagation direction and reaches 15% at φ=150°. The coupling factor of the TSH mode is improved in the same way and reaches 25% for the same propagation direction.
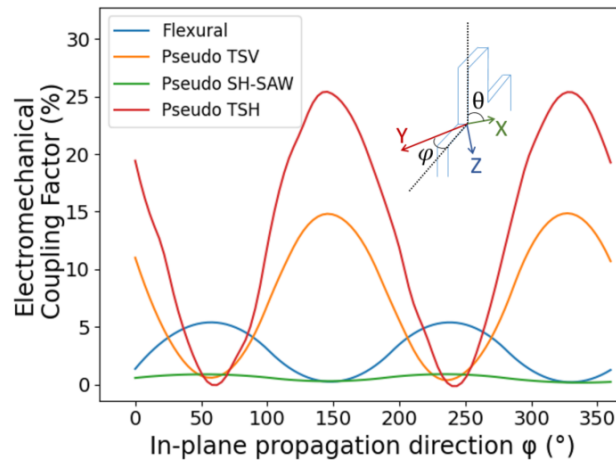
Figure 146: Variation of electromechanical coupling factor with in-plane propagation direction for X-cut lithium niobate films.

Two main conclusions may be drawn from this section: first, the two shear horizontal modes, i.e. the pseudo SH-SAW and the pseudo TSH modes, display much higher electromechanical coupling factors than the other modes, not to write about the modes excited in AlN-based hybrid SAW/BAW devices. The most favorable crystal orientation for these modes is X-cut, propagation Y+150°. It is interesting to note that this combination of crystal orientation and propagation direction is close to the X-cut, propagation Y+170° that maximizes the electromechanical coupling factor for shear horizontal plate waves in suspended LNO membranes [132]

In the following section, we will consider this particular orientation and will investigate the influence of the other geometrical parameters to further improve the performances of these modes.

3   Optimization of geometrical parameters

The parameters considered for optimization are the thickness of the LNO film (h_{LNO}/p), the coverage ratio (a/p), the etching ratio, the sidewall angle, the thickness of the bottom and top electrodes, the electrode material and the thickness of the SiO_2 layer. As mentioned before, the $SiO_{2\ layer}$ is needed for the bonding of the LNO layer onto the substrate.

3.1   Pseudo SH-SAW mode

SiO_2 layer thickness

Figure 147 shows the influence of the SiO_2 layer thickness on the electromechanical coupling factor of the SH-SAW mode. An increase in the thickness of this layer induces a decrease of the electromechanical coupling factor of at most about 2%. As this decrease remains limited, and for technological reasons, we continue considering in the following a SiO_2 thickness of 0.5 p under the bottom electrode.
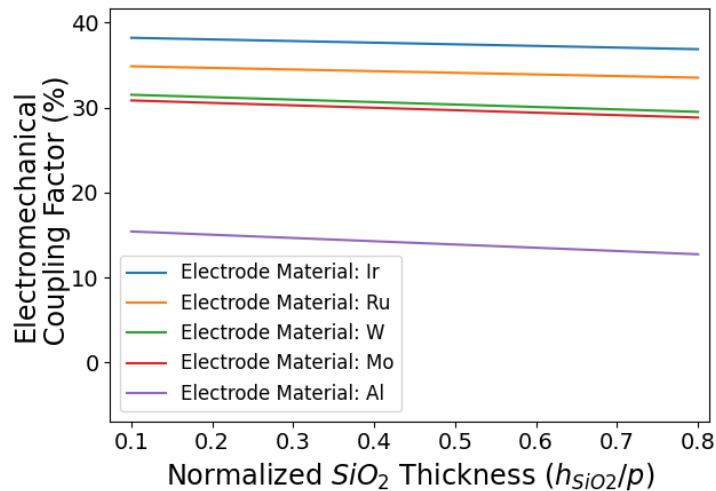
Figure 147: Influence of the SiO_2 layer thickness and the electrode material on the electromechanical coupling factor of the pseudo-SH-SAW mode.

Electrodes material

We then consider various electrode materials, as shown in Figure 147. The maximum electromechanical coupling factor determined in the previous section was 11% for the pseudo SH-SAW mode when using aluminum electrodes. However, as discussed in Chapter 2, section 2.3, this material has elastic properties approaching those of silicon dioxide, which results in a lack of confinement of waves in the transducers. When replacing aluminum by molybdenum or tungsten, the electromechanical increases up to about 30%, as shown Figure 147. Ruthenium or iridium electrodes allow even reaching electromechanical coupling factors of respectively 35% and 38%.

Top and bottom electrodes thicknesses

Considering iridium, we plot in Figure 148 the dependence of the electromechanical coupling factor on the respective thicknesses of the top and bottom electrodes. Trends are clear for both parameters: the thicker the top and the bottom electrodes the higher the coupling factor. It is worth

noting that this change is quite small and adds only about 2 to 3% electromechanical coupling factor. The maximum electromechanical coupling factor achieved is 38.3% for top and bottom electrode thicknesses of 0.25p.
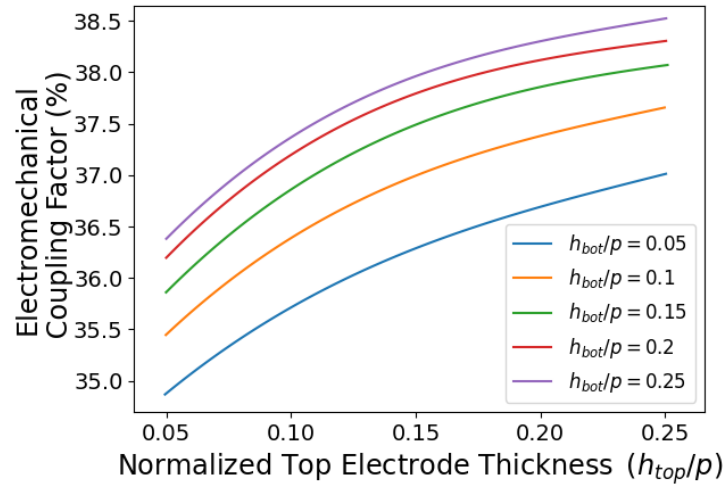
Figure 148: Impact of top and bottom electrodes thicknesses on the electromechanical coupling factor of the pseudo-SH-SAW mode.

Lithium niobate thickness

Considering iridium electrodes of thicknesses equal to 0.25p, we investigate the influence of the thickness of the piezoelectric material. Figure 149 shows that the electromechanical coupling factor of the pseudo-SH mode increases with piezoelectric layer thickness. The best k^2 is achieved at the highest normalized thickness considered, of 0.7. Theoretically, the thickness could be increased further but this appears technologically unrealistic since this would correspond to a thickness of 700 nm for a periodicity of 1 μm. 700 nm already corresponds to the maximum thickness that can be achieved with techniques such as the Smart Cut[TM] process [39], while pitches of 1 μm approach the photolithography resolution limit beyond which advanced lithography tools such as e-beam become necessary.

Coverage ratio

Figure 149 shows the electromechanical coupling factor decreases with increasing coverage ratio. This effect seems to be rather small and the drop in coupling factor seems to be minimal. For the thickness to pitch ratio of 0.5, a change in coverage ratio from 0.3 to 0.7 takes the coupling factor from 35% to 32%. We however consider a coverage ratio of 0.3 for the remainder of the optimization process.
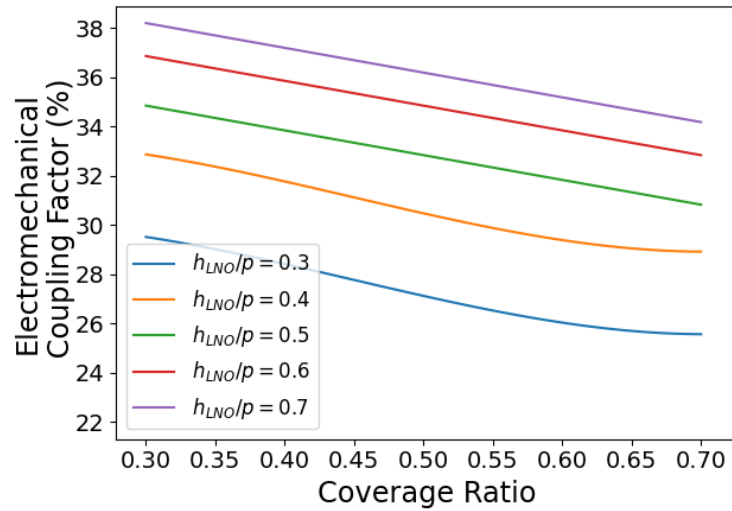
Figure 149: Impact of piezoelectric layer thickness and coverage ratio on the electromechanical coupling factor of the SH-SAW mode.

Etching ratio

As we did in Chapter 2, section 2.5, we consider in Figure 150 the influence of a partial etching of the piezoelectric layer in-between transducers. It appears that the pseudo-SH-SAW mode does not behave like the pseudo-SAW in AlN structures, but rather like the pseudo-BAW mode: the thicker the residual piezoelectric later, the higher the electromechanical coupling factor. Full patterning of the pillar can lead to a k² of 38% while only etching the piezoelectric layer over half of its thickness leads to electromechanical coupling factors of more than 46%.

Sidewall angle

The overall effect of the sidewall angle is to decrease the effective electromechanical coupling factor, which however shows a minimum. The change in electromechanical coupling factor is about 2-3% between optimal and minimal points, so this effect is not dramatic. However, it appears that it is still interesting to try to achieve sidewalls as vertical as possible.
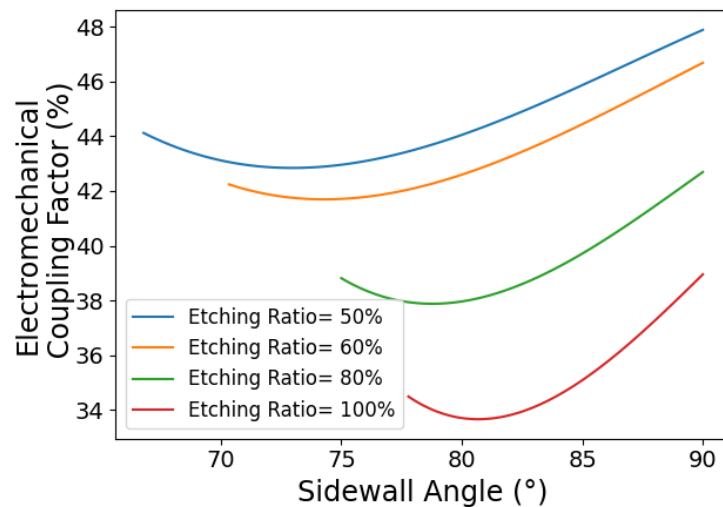
Figure 150: Impact of etching ratio and sidewall angle on the electromechanical coupling factor of the pseudo-SH-SAW mode.

Figure 151 shows an example of the harmonic admittance calculation of a device with coupling factor $k^2= 47.7\%$ for the pseudo SH-SAW mode at effective wave velocity of 1300 m/s. This represents the best coupling factor achieved. Unfortunately, designs with partial etching of the piezoelectric layer cause the pseudo-SAW mode to be a little coupled at 1.2 GHz. Due to the presence of the pseudo-SAW mode, we prefer the cleaner response achieved with 100% etching presented in the following conclusion section.
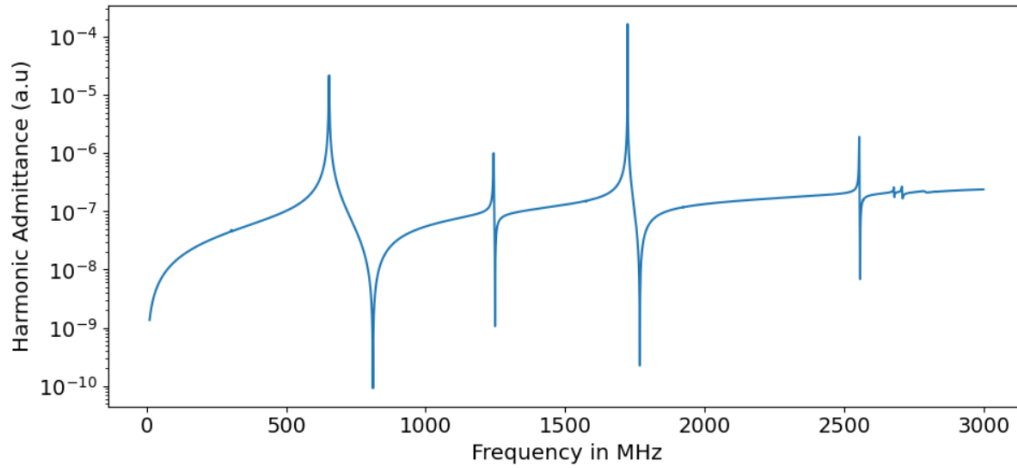
Figure 151: Harmonic admittance for LNO HSBR with the highest $k^2=47\%$ using the pseudo SH-SAW mode (X-cut, propagation Y+150, Ir/LNO/Ir/SiO$_2$/Si, h_{LNO}/p=0.7, a.p=0.3, etching ratio=50%, straight side-walls and El/p=0.25, h_{SiO2}/p=0.5)

Conclusions concerning the pseudo SH-SAW

Table 10 lists the design parameters corresponding to the configuration offering the optimum electromechanical coupling factor for a clean pseudo SH-SAW mode: 38%.

Table 10: Optimum design for LNO HSBR using the SH-SAW mode ($k^2=38\%$)

Crystal orientation	X-cut, propagation Y+150°
Substrate	Silicon
h_{LNO}/p	0.7
Coverage ratio (a/p)	0.3
Etching ratio	100%
Sidewall angle	90°
Electrode Material	Ir
Bottom electrode thickness (h_{bottom}/p)	0.25
Top zlectrode thickness (h_{top}/p)	0.25
h_{SiO2}/p	0.5

The harmonic admittance corresponding to these parameters, with a pitch of 1 μm, is shown in Figure 152. The pseudo-SH-SAW mode, whose resonance is located at 500 MHz, exhibits a clean response up to 1.5 GHz, when the contribution of the pseudo thickness shear horizontal mode appears. Despite its extremely high $k^2=38\%$ this mode has only a wave velocity of about 1,000 m/s, and is therefore not adapted to high frequency applications.
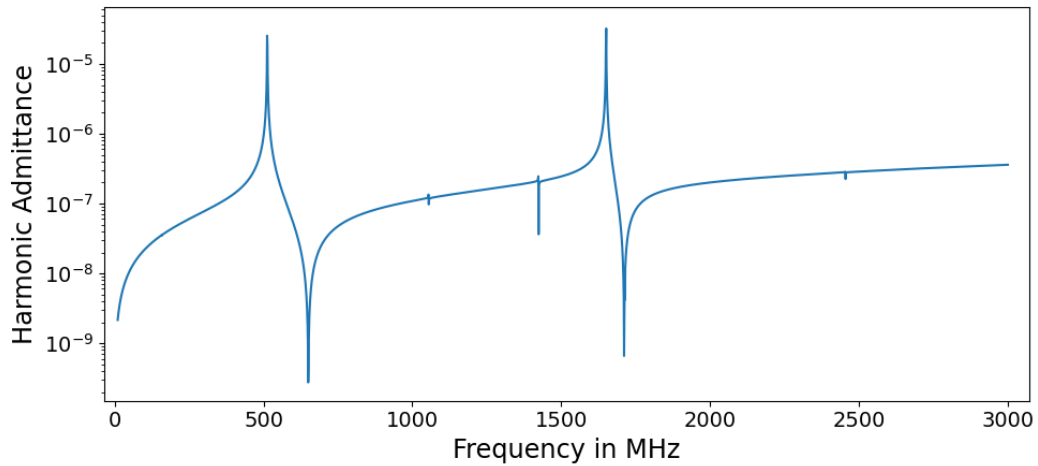
Figure 152: Harmonic admittance for Optimum design for LNO HSBR using the SH-SAW mode.

3.2   Pseudo thickness shear horizontal mode

The main advantage of the pseudo thickness shear horizontal mode compared to the pseudo SH-SAW mode is that its effective velocity is larger, over 3,000 m/s for the case of Figure 152, allowing to reach resonance frequencies up to 1.5-2 GHz.

Electrode material

Motivated by the huge influence of the electrode material on the pseudo SH-SAW mode, we explore its effect on the SH-BAW mode first. The influence of the electrode material is shown Figure 153. By comparison with the pseudo SH-SAW mode, where replacing aluminum electrodes by iridium lead nearly to increasing the electromechanical coupling factor by a factor 2, the influence of the electrode material on the pseudo thickness shear horizontal mode is not as significant. Yet, k^2 increases from 25% with Al electrodes to 28% with Ir. Surprisingly, and unlike the other modes investigated so far, tungsten seems not to favor a very strong electromechanical coupling factor, as Figure 153 shows that some configurations based on aluminum electrodes perform as well. In the following of the investigations, we will consider iridium electrodes, unless stated otherwise.

SiO$_2$ layer thickness

The thickness SiO$_2$ layer seems to exhibit a far more important influence on the electromechanical coupling factor than modifying the electrode material. Variations in SiO$_2$ layer thickness could lead to changes in the electromechanical coupling factor up to 9%.As was observed for the pseudo-BAW mode in AlN HSB structures in Chapter 2, Figure 71, the electromechanical coupling factor is maximized for an optimum thickness, which depends on the electrode material. The maximum coupling factor for Al electrodes is obtained for a SiO$_2$ layer thickness of 0.5 µm which was the default value considered so far (see section 2). This maximum is slightly shifted down for higher acoustic impedance electrode materials, for which it becomes closer to 0.4 µm. This is the SiO$_2$ thickness we consider in the following.
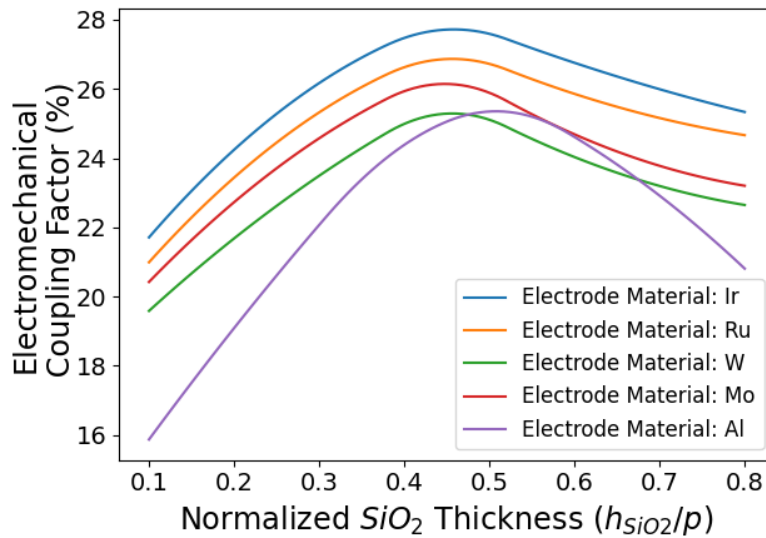
Figure 153: Influence of the electrode material and the thickness of the SiO₂ layer on the electromechanical coupling factor of the SH-BAW mode.

Piezoelectric layer thickness

Similar to the pseudo-BAW mode in AlN structures, for the thickness shear horizontal mode, the thickness of the piezoelectric layer has a very high impact on the electromechanical coupling factor, as shown Figure 154. Due to the limitation in piezoelectric layer thickness, one remains in a range where k^2 increases monotonously with h_{LNO}/p. The best achievable coupling factors are therefore obtained for $h_{LNO}/p = 0.7$. The sensitivity to the layer thickness is quite high, since a 100 nm drop of LNO thickness leads to a 10% drop of k^2 for a periodicity of 1 µm.

Coverage ratio

As for the pseudo-BAW mode in AlN structures, the electromechanical coupling factor increases monotonously with coverage ratio when $h_{LNO}/p > 0.4$. So we consider in the following a coverage ratio a/p of 70%.
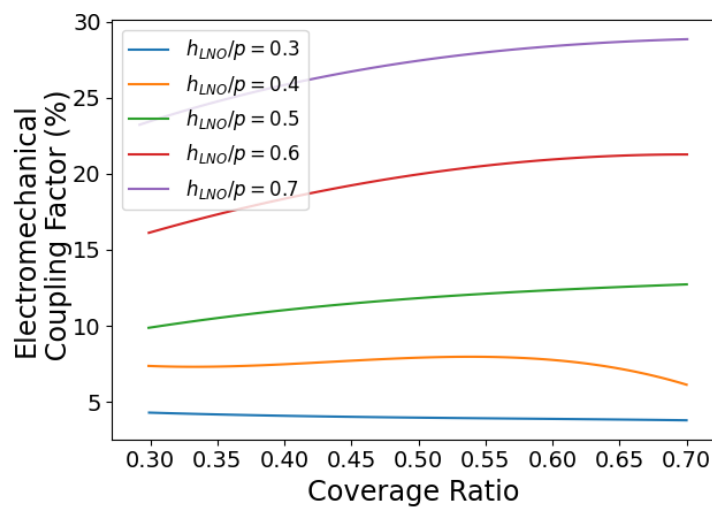
Figure 154: Influence of the thickness of the piezoelectric layer and the coverage ratio on the electromechanical coupling factor of the pseudo thickness shear horizontal mode.

Etching Ratio

As for the pseudo-BAW mode of AlN based hybrid SAW/BAW structures (Chapter 2 section 2.5), the pseudo thickness shear horizontal mode of LNO-based structures reaches its highest coupling factor when the piezoelectric layer is fully etched in between the transducers, as visible Figure 155. At low etching ratios of 50-60%, the electromechanical coupling is 10% lower than the coupling factor at 100% etching. This is why, unlike the optimization of the pseudo SH-SAW mode, we will consider fully etched piezoelectric layers in what follows.

Sidewall angle

The steepness of the transducers sidewalls has the most effect on the electromechanical coupling factor when the piezoelectric layer is fully etched. Perfectly vertical sidewalls favor the highest electromechanical coupling factor, close to 28%, but this can drop down to 24% for slanted sidewalls approaching 80°. Anyway, the effect of the sidewall angle is much smaller than the effect of the etching ratio.
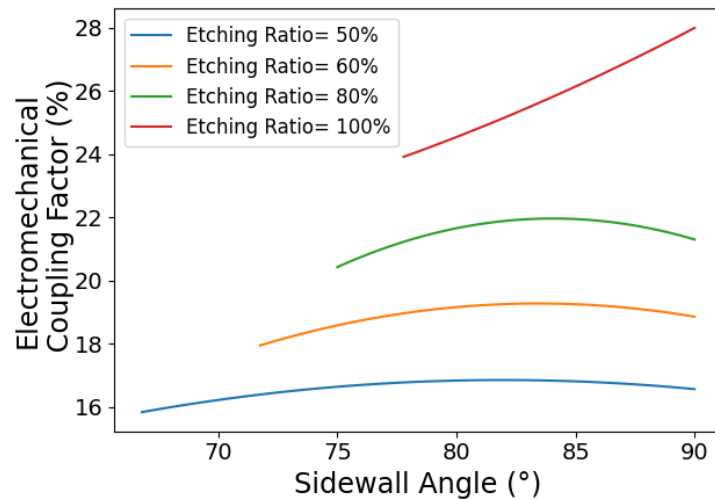
Figure 155: Influence of etching ratio and sidewall angle on the electromechanical coupling factor of the pseudo thickness shear horizontal mode.

Electrodes thicknesses and spurious modes suppression

The optimization of the thickness shear horizontal mode is finalized considering the effect of electrodes thicknesses. Figure 156 shows how the thicknesses of top and bottom electrodes affect the electromechanical coupling factor. As for the pseudo-BAW mode considered in Chapter 2, section 2.2, k^2 decreases with the normalized thickness of both top and bottom electrodes. The highest electromechanical coupling factor achieved can reach 32% with a $h_{bot}/p=0.1$ and h_{top}/p of 0.05. Figure 157 shows the calculated harmonic admittance for a $h_{bot}/p=0.15$ and a $h_{top}/p=$ of 0.05. It shows the appearance of a spurious contribution near 1850 MHz in between the resonance and antiresonance, which corresponds to the pseudo TSV mode. Additional contributions from the pseudo-SAW mode (at the exit of its stopband) and the pseudo-BAW mode should appear also in the vicinity of the frequencies of interest. Fortunately, they are both uncoupled for the crystal orientation (X-cut, propagation at Y+150°) considered (Figure 146). Therefore, only the interaction between the pseudo TSH and the pseudo TSV modes needs to be addressed.
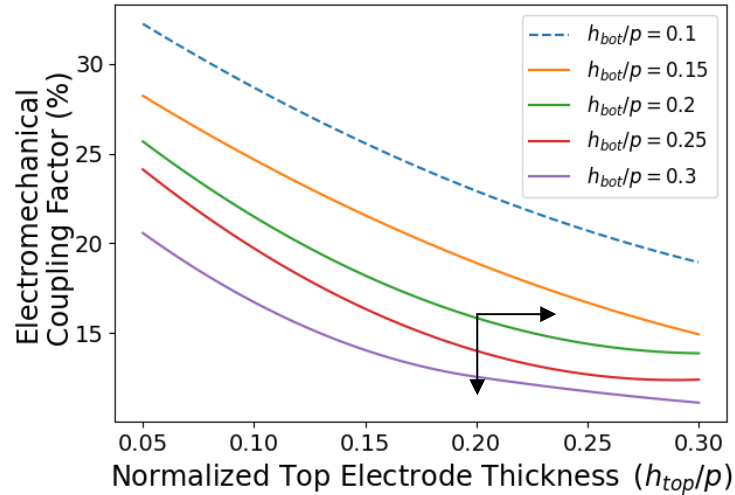
Figure 156: Impact of bottom and top electrodes thicknesses on the coupling factor of SH-BAW mode

Considering the evolution of the harmonic admittance along the plots of Figure 156, it appears that for thin electrodes, the pseudo thickness shear horizontal and the pseudo thickness shear modes get so close in frequency that their responses cannot be distinguished. However, increasing the thicknesses of both electrodes increases their spacing, at the expense of the electromechanical coupling factor. As an example, Figure 157 (a) corresponds to the calculation of the harmonic admittance for a $h_{bot}/p=0.15$ and a $h_{top}/p=$ of 0.05: the pseudo thickness shear horizontal mode exhibits an electromechanical coupling factor of 28%, with a strong interaction with the pseudo TSV mode shown in the inset. The pseudo thickness shear horizontal mode recovers a spurious resonance-free harmonic admittance when both the top and bottom electrodes are thicker than $El/p = 0.2$. Figure 157(b) shows the harmonic admittance of the pseudo thickness shear horizontal BAW mode with $El/p = 0.25$. Its electromechanical coupling factor is now 14%, without sign of spurious contributions.
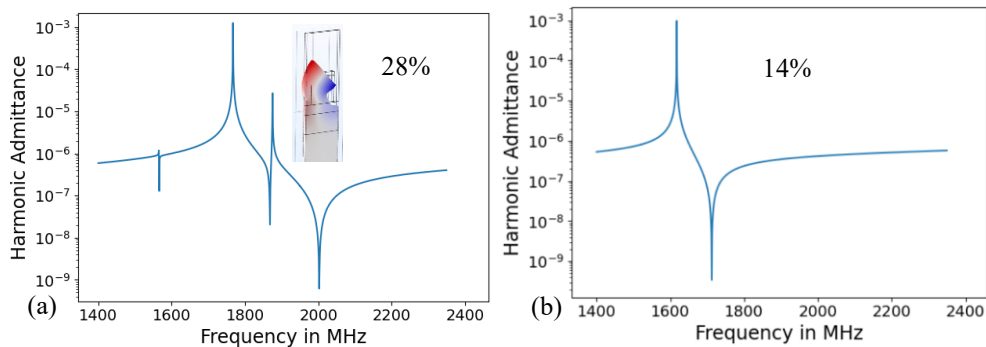
Figure 157: Harmonic admittance of the SH-BAW mode displaying high coupling and high interaction for 150 nm bottom electrode and 50 nm top electrode (a) and smaller coupling factor without interaction for 250 nm top and bottom electrodes (b)

The geometrical parameters associated with optimal pseudo TSH mode shown in Figure 157 (b) are listed in Table 11.

Table 11: Optimum design for LNO hybrid SAW/BAW structures favoring the pseudo thickness shear horizontal mode with $k^2=14\%$.

Crystal orientation	X-cut, propagation Y+150°
Piezoelectric layer thickness (h_{LNO}/p)	0.7
Coverage ratio (a/p)	0.7
Etching Ratio	100%
Sidewall Angle	90°
Electrode Material	Ir
Bottom Electrode thickness (h_{bottom}/p)	0.25
Top Electrode thickness (h_{top}/p)	0.25
SiO$_2$ thickness (h_{SiO2}/p)	0.4

4   Process Flow based on lithium niobate
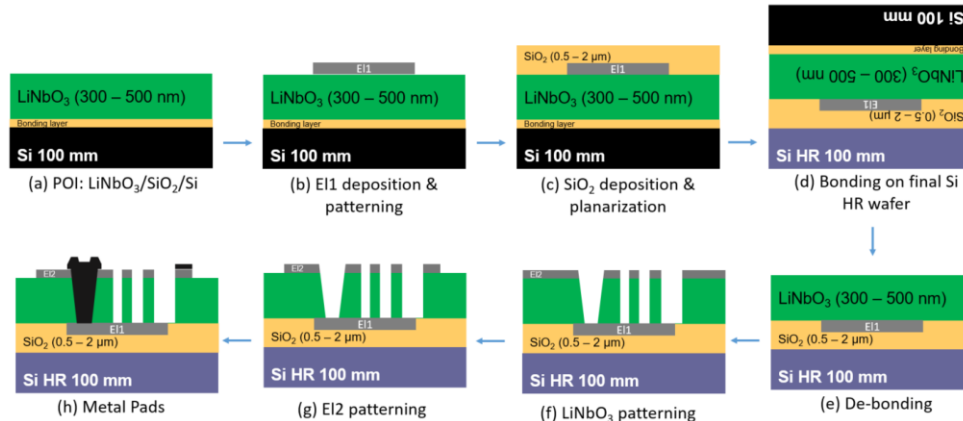
Figure 158: Simplified scheme of process flow for LiNbO₃ HBSR fabrication

As seen in the previous section, LNO based HSBR have the potential of achieving high coupling factors up to 38% at low frequencies and up to 14% at 1.5 GHz. Yet, for the fabrication of HSB devices using LNO, it is not procedural to deposit LNO on top of the electrode material [46]. The proposed process (shown in Figure 158), is inspired from the process flows for the fabrication of LNO BAW resonators [130] and of thin film SAW resonators exploiting electrodes inserted inside the piezoelectric film [133].

The process starts with a Piezoelectric On Insulator (POI) substrate consisting of a LNO layer on a SiO_2 bonding layer, on top of a Si substrate (a). The first electrode is deposited and patterned (b). Among the materials that can be used for the electrodes including Al, Mo, Ru, W and Ir, Al is the most established in terms of manufacturing processes (examples in [40], [134]). The bottom electrode is then covered with a SiO_2 layer and planarized using Chemical-Mechanical-Polishing (CMP) (c). This layer is used for bonding the POI wafer on the final Si high-resistance carrier wafer (d), using direct hydrophilic bonding. A debonding step is required to detach the SiO_2/metal/LNO stack from the initial substrate onto the final one (e).

A layer of metal is then deposited on the LNO as a top electrode. Unlike the process flow developed for AlN resonators, the patterning of the trenches forming the transducer pillars and the opening of electrical contacts to the bottom electrode are performed in the same sequence of photolithography and dry etching (f). This is made possible by the fact that LNO is etched by ion beam etching, which is little sensitive to features such as size of the openings and density of the mask. After that, the top electrode is patterned to define the access lines (g). Eventually, metal pads and electrical contacts allowing to connect the top and bottom electrodes together (for example to implement short-circuited reflectors) are formed by lift-off of an additional aluminum layer (h).

The new process flow requires changes in the design of photolithography masks, to consider that some steps are merged. The new mask was redrawn with the following breakdown:
1.   Bottom electrodes patterning
2.   Engraving of trenches between transducers and opening of electrical contacts to the bottom electrode
3.   Top electrodes
4.   Metal overload

While AlN devices were fabricated on 200 mm wafers, LNO films will be fabricated on 100 mm wafers. This means the new process will not exclusively operate on the CMOS 200 mm line of CEA-LETI. Instead, the process will be split between the MEMS 200 mm facility of CEA-LETI, and the Plateforme Technologique Amont (PTA) de Grenoble for most of the patterning steps. Due to the need for sub-micron resolution for the photolithography when patterning the LNO film, this particular step will use the stepper available at frec|n|sys in Besançon, FR.

At the time of writing, this process has been started relatively late, with only the fabrication of LNO POI wafers, shown in Figure 159, achieved
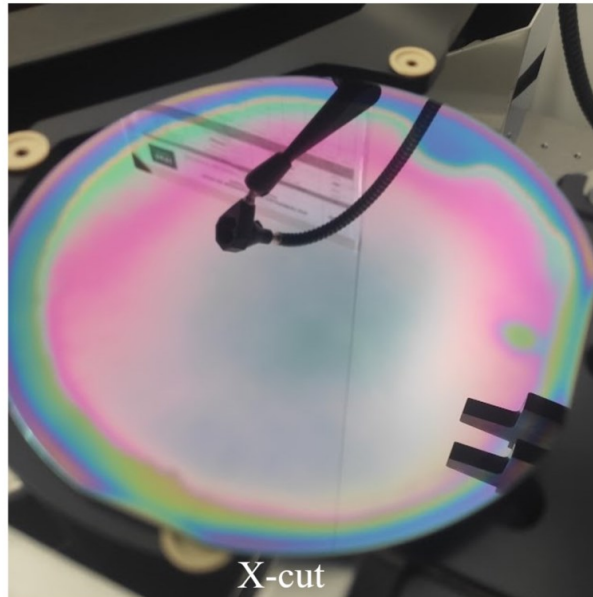
Figure 159: Initial POI substrate.

5 Conclusions

In this chapter, we delved into the investigation of Lithium Niobate (LNO)-based hybrid SAW/BAW resonators. The exploration revealed an array of resonance modes, in addition to their AlN counterparts. Alongside the pseudo-SAW and pseudo-BAW modes found in AlN devices, the introduction of LNO gave rise to shear modes, encompassing shear horizontal and shear vertical modes. These modes exhibited a diverse nature, appearing either as predominantly surface waves, exemplified by the pseudo SH-SAW mode, or as bulk waves, such as the pseudo TSV and pseudo TSH modes. Significantly, it was evident that these LNO-based modes could achieve higher coupling factors compared to AlN resonators.

To facilitate a comprehensive understanding of these resonators, we adapted our finite element model to simulate these newfound modes effectively. Through thorough investigation, we identified the optimal crystalline orientation and in-plane propagation direction, which proved essential for exploiting these modes. Specifically, the X-cut crystal orientation emerged as the prime choice for promoting the largest coupling factor, while the Y+150° propagation direction was found to be optimal.

We further embarked on the journey of optimizing the pseudo SH-SAW mode and pseudo TSH mode. Notably, the former demonstrated the potential to reach a remarkable k^2 of 38%, particularly when employing Ir electrodes, despite its limitation to approximately 500 MHz due to its lower velocity. In contrast, the latter achieved a k^2 of 14% resulting in an operational frequency of around 1.5 GHz. The concluded best coupling factors are lower than the optimal 47% and 28% for the pseudo SH-SAW and the pseudo TSH modes respectively primarily because addressing spurious resonances or avoiding the coupling of other modes necessitated a non-optimal configuration.

However, the quest for operating at even higher frequencies while exciting a single mode remains unfulfilled. These paramount objectives will be addressed in the final chapter of this study.

Chapter 5: High Frequency HSB devices

Introduction

In chapter 1, we introduced the need for acoustic resonators with high electromechanical coupling at high frequencies, and with possibly low losses. AlN based Hybrid SAW/BAW resonators investigated theoretically in Chapter 2 and experimentally in Chapter 3 exhibit two resonance: the pseudo-SAW and the pseudo-BAW modes. The effective velocity of these modes does not exceed 3,500 m/s, what limits their operation frequency. In addition, neither of these modes achieves high electromechanical coupling factors. The litterature addresses the issue of the electromechanical coupling factor with the replacement of AlN by AlScN. In Chapter 4, we provided an alternative solution based on lithium niobate, which offers very promising perspectives. However, the modes investigated in chapter 4 do not appear faster than those studied in AlN structures. So the increase in frequency remains an open issue. To answer it, we introduce in this chapter a new mode that is capable of reaching high frequencies, with a significantly better electromechanical coupling factor than the pseudo-SAW and the pseudo-BAW modes.

In section 1, we present how this mode was first revealed on the electrical measurements of the AlN devices fabricated in Chapter 3. We investigate its origin and present some experimental evaluations of this mode

Then, in section 2, we investigate how to properly excite it and how to optimize its performance by investigating the influence of different design parameters, as we did in Chapters 2 and 4 for the classical hybrid SAW/BAW modes in AlN or LNO structures. We start by investigating its capabilities in AlN structures. In section 3, we continue the analysis of this mode, but this time in LNO structures.

1 Analysis of AlN-based HSBR with grounded bottom electrodes
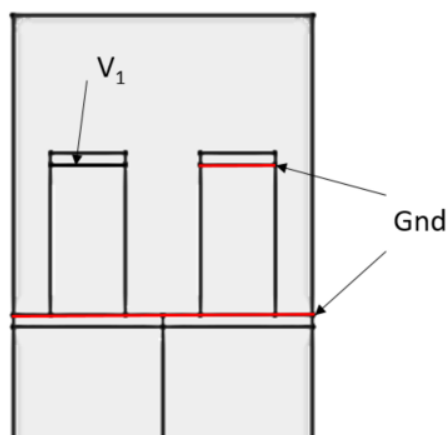
Figure 160: electric configuration for the calculation of the Y_{11} admittance term of devices with grounded bottom electrodes.

In chapter 3, we evaluated the electric response of AlN hybrid SAW/BAW resonators. We however only considered in the analysis devices with a floating bottom electrode, while we indicated that some devices had their bottom electrode connected to ground. The former case was the

simplest to analyze, as we could consider in our finite element model that if one transducer top electrode is excited with a voltage of 1 V, the neighboring transducers have their top electrodes connected to ground, as shown Figure 105. The floating bottom electrode common to all transducers is then assumed to position itself to an intermediate electric potential of 0.5 V if the device has an even number of transducers. This is confirmed by Figure 49 in Chapter 2 when considering the electrostatic behavior of an infinitely long resonator.

When the bottom electrode is grounded, the behavior becomes different. The analysis of the terms of the admittance matrix given Equation (25) is still valid and we still have

$$Y_{11} = \frac{I_1}{V_1}\bigg|_{V_2=0} \quad \text{or} \quad Y_{12} = \frac{I_1}{V_2}\bigg|_{V_1=0}$$

In this case, however, the theoretical configuration corresponding for example to Y_{11} is shown in Figure 160. In this configuration, one can notice that one every two transducers is shorted, and only the other transducer is actually excited. In principle, one expects that this configuration is detrimental to the electromechanical coupling factor of the mode, since only half of the transducers are exploited. We nevertheless investigated it theoretically and experimentally.

1.1   Theoretical analysis
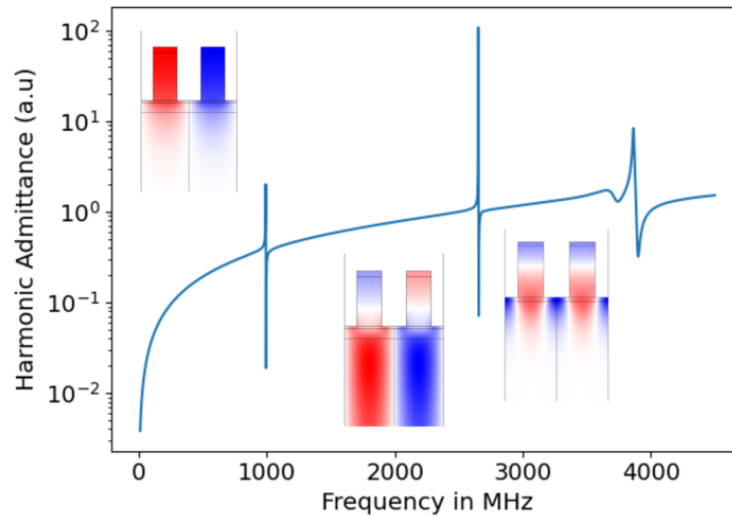
Figure 161: harmonic admittance calculation for a HSBR when considering the electrical boundary conditions given in Figure 160, and corresponding vertical displacements calculated for the Pseudo-SAW mode at 1 GHz, for the Pseudo-BAW mode at 2.6 GHz, and for the resonance at 4.2 GHz in the insets. Red corresponds to upwards displacement, while blue corresponds to downwards displacement. (Mo/AlN/Mo/Si, h_{AlN}/p=1, a/p=0.5, El/p=0.08, Full etching and straight sidewalls).

Figure 161 shows the harmonic admittance calculated given the electric configuration of Figure 160. The pseudo-SAW mode appears at 1 GHz and the pseudo-BAW mode appears at 2.6 GHz, as confirmed by the displacement profile shown in Figure 161 insets while near 3.9 GHz, a new contribution appears. This mode appears relatively similar to the pseudo-BAW mode, except that adjacent transducers seem to vibrate in phase as one wavelength of the mode corresponds to one transducer. By comparison, one wavelength of the pseudo-SAW and pseudo-BAW mode correspond to two transducers.

In other words, this new mode seems to correspond to the hybridization of the thickness longitudinal (or thickness extensional) mode of the transducers and the second overtone of the Rayleigh wave (for which $\lambda=p$). As such, we could describe this mode as the $TE_{2,1}$ mode, where *2* stands for the overtone number, or the number of nodes in the horizontal direction, of the surface wave, and 1 for the overtone number of the bulk wave (i.e. the number of nodes in the vertical direction). Using the same rationale, the pseudo-BAW mode would correspond to the hybridization of the fundamental thickness extensional mode of the transducers with the fundamental Rayleigh wave (for which $\lambda=2p$) and could thus write $TE_{1,1}$. The pseudo-SAW mode would then correspond similarly to the $TE_{1,0}$ mode.

Table 12: number of nodes in the horizontal and vertical direction experienced by each mode.

	Horizontal	Vertical
Pseudo-SAW mode	1	0
Pseudo-BAW mode	1	1
New mode	2	1

 The $TE_{2,1}$ mode did not contribute to the admittance of devices with a floating bottom electrode, as the mechanical and electrical periodicities are not aligned, leading to a cancelation of the currents induced when adjacent transducers are excited with opposite phase. However, when only one every two transducers is actually excited, this cancellation between neighboring transducers does not occur, resulting in the appearance of this new mode.

The two keys observations about this mode are:

1. Due to its shorter horizontal wavelength, it appears at nearly twice the frequency of the pseudo-SAW or pseudo-BAW modes

2. Despite its high frequency, it is properly confined near the surface of the substrate. This is because its effective velocity remains lower than the bulk shear wave velocity in the substrate (5,600 m/s), with $V = f \lambda = f\, p = 4.2$ GHz $\times$ 1 μm = 4,200 m/s. This is faster than the velocity of the pseudo-SAW mode:
    $(V = f \lambda = 2\, f\, p = 2 \times 1.2$ GHz $\times$ 1 μm = 2,400 m/s)
    but remains even lower than the velocity of the pseudo-BAW mode:
    $(V = f \lambda = 2\, f\, p = 2 \times 2.7$ GHz $\times$ 1 μm = 5,400 m/s).
    This means that this mode benefits from an even better confinement than the pseudo-BAW mode, unlike what its frequency would indicate at first sight.

1.2   Experimental observation of the new mode

Analyzing the electric response of devices with a grounded bottom electrode

In Chapter 3, devices with floating bottom potential were presented as components inserted in series in between the two electrical ports, as sketched in Figure 104 or Figure 107. In order to isolate the electrical response of these floating bottom potential resonators the measurement of an "open" device, where the electrodes are disconnected from the signal line, was subtracted from

the measurement of the device under test. And then the diagonal elements of the admittance matrix were considered as the intrinsic response of the resonator in order to remove any remaining contributions from the pads.

It is important to note that the above mentioned method does only apply if the device under consideration has a grounded bottom electrode. Devices with grounded bottom electrodes are instead represented by the generic schematic for an electric quadrupole shown Figure 162. Equation (25) or Equation (26) do therefore no longer hold, and circuit theory does in principle not provide specific relationships between the diagonal and off-diagonal elements of the admittance matrix.
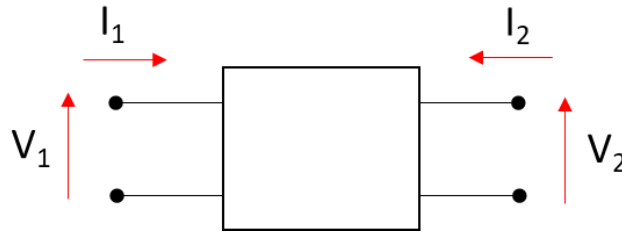
Figure 162 : Schematic of the classical representation for an electric quadrupole.

The acoustic interpretation of Y_{11} and Y_{21} in the case of a grounded bottom electrode is depicted in Figure 163. The first is similar to the theoretical scheme sketched Figure 160.
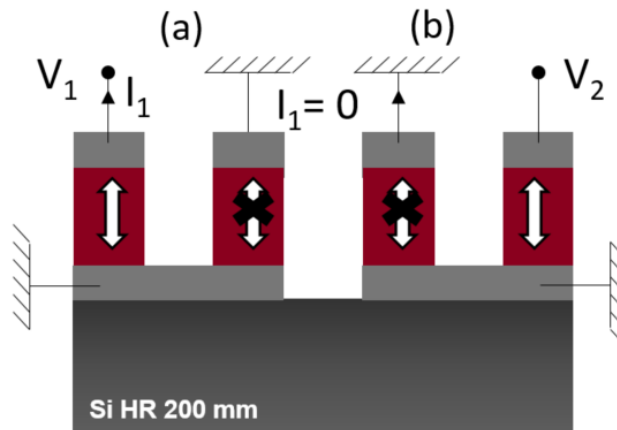
Figure 163: Electrical piezoelectric schematic of Y_{11} (a) and Y_{12} (b) representation of a device with grounded bottom electrode.

In this configuration, Y_{11} includes the sum of the capacitive contribution from the transducer to which the voltage V_1 is applied and from the piezoelectric contribution when the transducer is in mechanical motion. Conversely, Y_{12} does not include a capacitive contribution since the transducer connected to port 1 is effectively shorted in this configuration. It does however still include a piezoelectric contribution when the transducer is in motion. Therefore, Y_{12} is in practice negligible compared to $Y_{11,}$ as shown Figure 164.
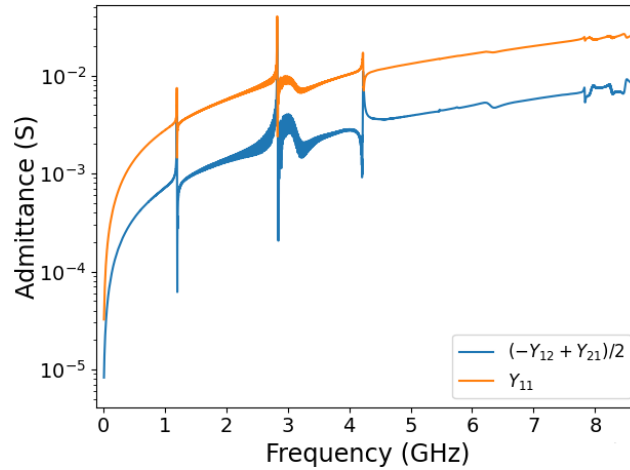
Figure 164 : Electric measurement example with same structure as Figure 161. Comparison of the Y_{11} and Y_{12} admittance matrix components for a resonator with a grounded bottom electrode. (h_{AlN}=1 μm, p=1 μm, h_{SiO2}=210 nm, 60 reflectors, aperture 40λ, close-circuited reflectors, and grounded bottom electrode)

When considering Y_{11} in Figure 164, the contributions of the pseudo-SAW mode at 1.1 GHz, the pseudo-BAW mode at 2.8 and the new $TE_{2,1}$ mode at 4.2 GHz are clearly visible. This is comparable to Figure 161 that bears the same structure theoratically.

Analysis of the $TE_{2,1}$ mode

In the absence of SiO_2, things look slightly different but the coupling factors remain almost the same.
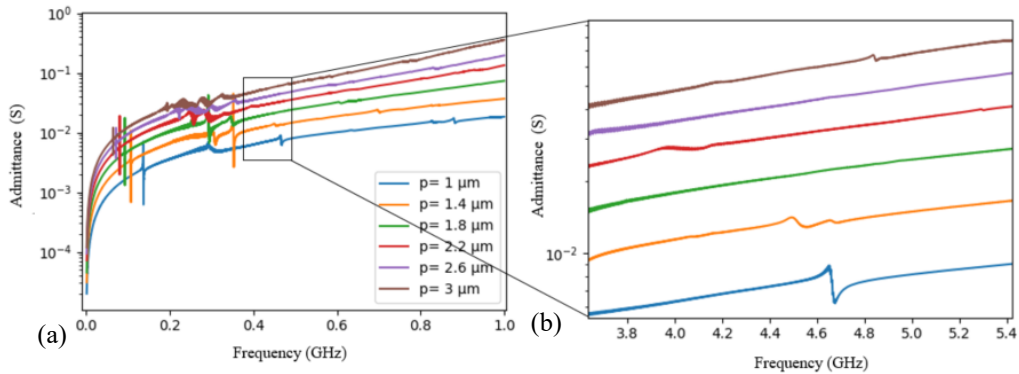
Figure 165: Input admittance for devices with 1 μm of AlN, without SiO_2 and a grounded bottom electrode.(h_{AlN}=1 μm, p=1 μm, no SiO_2, 60 reflectors, aperture 40λ, close-circuited reflectors, and grounded bottom electrode).

Figure 165 shows the electric response of devices with a grounded bottom electrode, 1 μm of AlN and no SiO_2 underneath. The new mode appears for p = 1 μm located at 4.6 GHz.
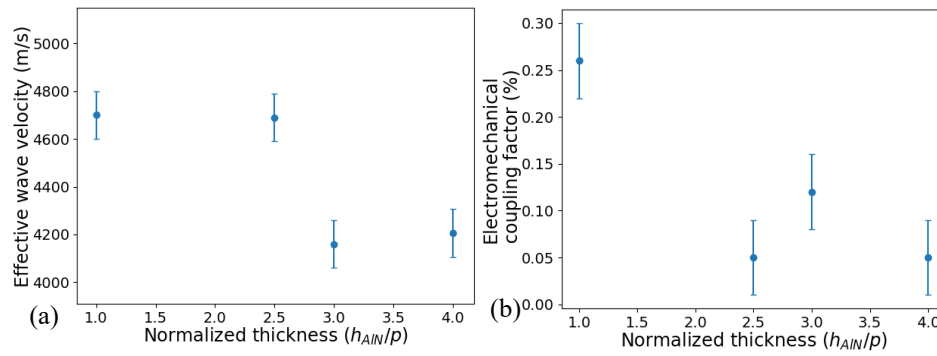
Figure 166: Effective wave velocity (a) and electromechanical coupling factor (b) of the $TE_{2,1}$ mode as a function of the AlN thickness.

The $TE_{2,1}$ appears for most AlN thickness but only for the lowest pitches of 1 µm. It can be found between 4.1 GHz and 4.8 GHz, as shown Figure 166 (a). Its respective electromechanical coupling factors are shown Figure 166 (b) and remain below 0.3%. Looking at Figure 166 (b), the electromechanical coupling factor decreases with increasing piezoelectric layer thickness.

Figure 167 shows the evaluations of the quality factors of the $TE_{2,1}$ for various AlN thicknesses. The values range up to 250.
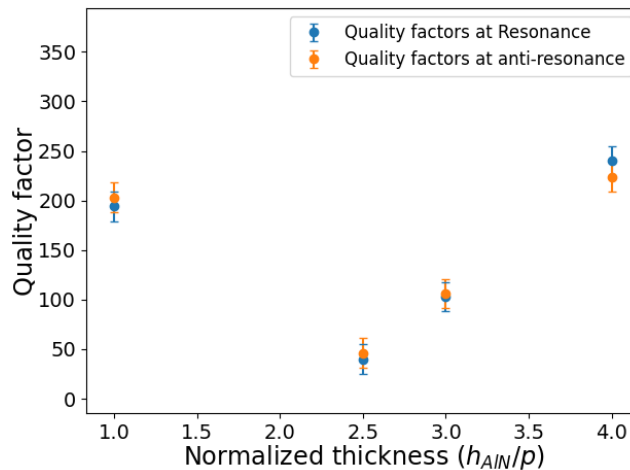
Figure 167: Quality factors of the $TE_{2,1}$ as a function of the normalized thickness ratio.

2   Optimization of the TE$_{2,1}$ mode based on AlN
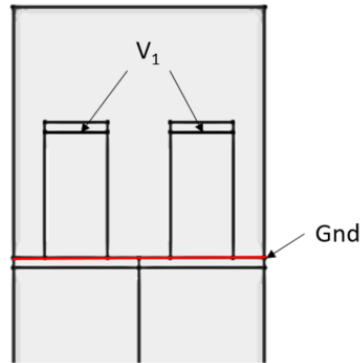
Figure 168: electric configuration for the in-phase excitation of the TE$_{2,1}$ mode

In order to efficiently excite the TE$_{2,1}$ mode, the electrical periodicity must match its wavelength. This is achieved through the electric configuration represented in Figure 168: the same electric potential is applied on the top electrodes, while the common bottom electrode remains grounded. This makes all transducers electrically identical as all the pillars are now connected in series to the two electric ports.
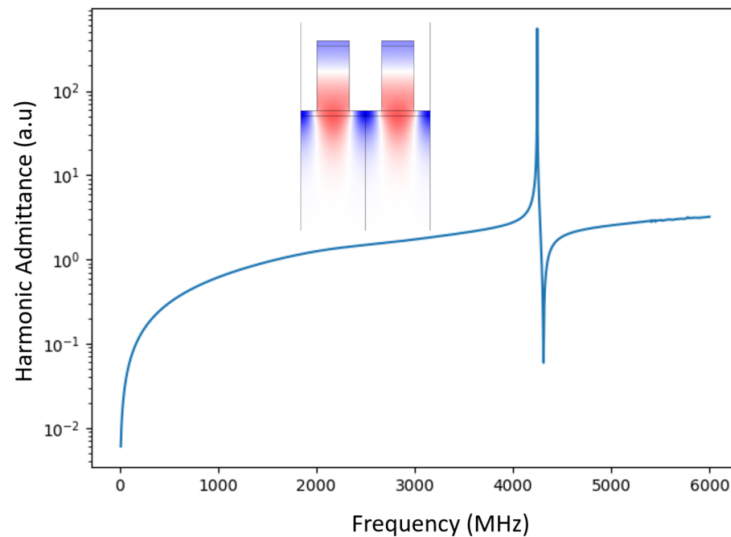
Figure 169: harmonic admittance calculation for an in-phase excitation of the top electrodes and a grounded bottom electrode and vertical displacement field calculated at resonance in the inset. Red colors correspond to upwards vertical displacement while blue corresponds to downwards displacement. Same Geometry as Figure 161

As demonstrated in Figure 169 (a), this configuration results in the isolation of the TE$_{2,1}$ mode and the suppression of all other modes including the Pseudo-SAW and Pseudo-BAW modes. The single mode response is achieved while even increasing the electromechanical coupling factor compared to Figure 161 is notable here.

Effect of the piezoelectric layer thickness and coverage ratio

Quantitatively, Figure 170 shows the evolution of the wave velocity and the electromechanical coupling factors of the TE$_{2,1}$ mode as a function of the piezoelectric layer thickness and of the coverage ratio. Figure 170 (b) confirms the qualitative guess that the electromechanical coupling

factor is considerably improved, as it can reach up to 5% for a coverage ratio of 0.5 and a normalized thickness of $h_{AlN}/p = 0.7$. The corresponding velocity is about 4,750 m/s. At first, it may appear that the optimum k^2 is reached for a small AlN thickness compared to the pseudo-SAW and the Pseudo-BAW modes, whose k^2 were maximized for respectively $h_{AlN}/p = 1.3$ and $h_{AlN}/p = 1.7$. One has to remind here that in the former case $\lambda = 2p$ while now $\lambda = p$, which means that the k^2 is in practice maximized for $h_{AlN}/\lambda = 0.65$, 0.85 and 0.7 for respectively the pseudo-SAW, the pseudo-BAW and the TE2,1 modes. So the electromechanical coupling factor is in fact maximized for the same range of piezoelectric layer thickness compared to the wavelength of the mode.
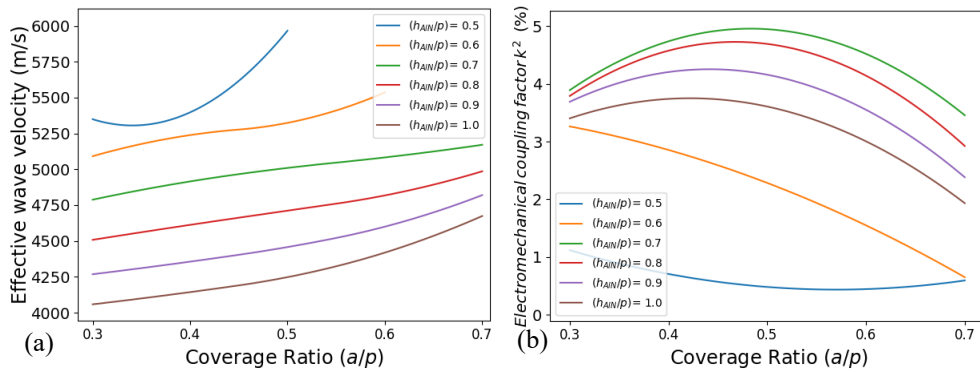
Figure 170: evolution of k^2 (a) and wave velocity (b) of the TE$_{2,1}$ mode with the transducer thickness to pitch ratio and coverage ratio. (Mo/AlN/Mo/SiO$_2$/Si, etching ratio=1, straight sidewalls, h_{bottom}/p=0.1, h_{top}/p=0.1, h_{SiO2}/p=0.5)

Figure 170(a) shows that the effective wave velocity increases significantly with a decrease in the piezoelectric layer thickness. It varies from 4,000 m/s at $h_{AlN}/p = 1$ to 5,500 m/s at $h_{AlN}/p = 0.5$.

Effect of the etching ratio and sidewall angle
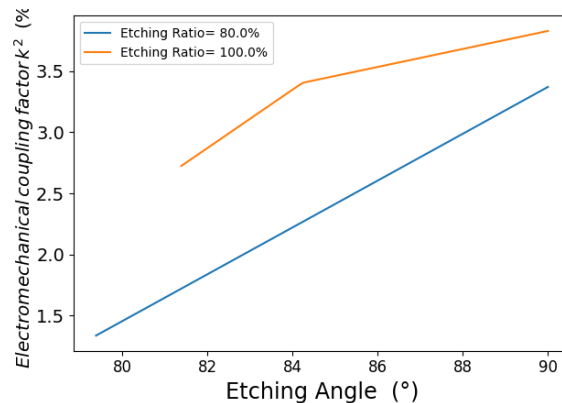
Figure 171: Evolution of k^2 for the TE$_{2,1}$ mode with sidewall angle at different etching ratios (Mo/AlN/Mo/SiO$_2$/Si, h_{AlN}/p=1, a/p=0.5, h_{bottom}/p=0.1, h_{top}/p=0.1, h_{SiO2}/p=0.5)

The TE$_{2,1}$ mode appears to be very sensitive to the sidewall angle of the transducers. Figure 171 shows that the TE$_{2,1}$ coupling factor more than doubles from 1.4% to over 3.2% when the sidewall angle goes from 80° to 90° at an etching ratio of 80%. An etching ratio of 100% leads to a much higher electromechanical coupling factor than an etching ratio of 80%. At lower etching ratios below 80%, spurious modes appear in addition of the weakness of the TE$_{2,1}$, making it difficult to have a recognizable clean peak as seen in Figure 172. However, at 80% and above, the TE$_{2,1}$ resonance remains clean.
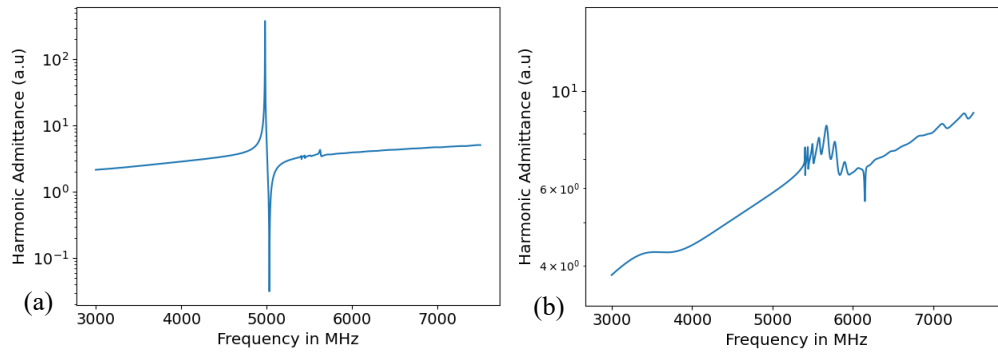
Figure 172: The TE$_{2,1}$ mode as observed on HSBR device with 80% etching ratio (a) and 50% etching ratio (b) (Mo/AlN/Mo/SiO$_2$/Si, h$_{AlN}$/p=1, a/p=0.5, h$_{bottom}$/p=0.1, h$_{top}$/p=0.1, h$_{SiO2}$/p=0.5, straight sidewalls)

Effect of top and bottom electrode thicknesses

Since working with Mo electrodes is the most established process for HSBR based on AlN and since it provides configurations with a clean response, the only motive for changing the electrode material would be to increase the coupling factor. Other electrode materials did however not provide better coupling factors than Mo. For example the TE$_{2,1}$ mode has a coupling factor of 3.8% using Ir electrodes but at a resonance frequency of only 3.4 GHz.

The thickness of the Mo top and bottom electrodes affect the coupling factor and the resonance frequency of the TE$_{2,1}$ mode as shown in Figure 173. While the wave velocity remains relatively insensitive to the top electrode thickness, the thickness of the bottom electrode can increase the resonance frequency from 3,900 to 4,400 m/s. The highest wave velocity is close to 4,600 m/s, achieved with thinnest bottom electrode of 50 nm and a top electrode thickness of 120 nm.

The effect of the electrodes' thicknesses on the coupling factor is opposite each other as well. The increase in the bottom electrode thickness leads to an increase in the electromechanical coupling, while the increase in the top electrode thickness leads to a decrease. It is worth noting that these effects are opposite to the effect on the wave velocity meaning that the highest wave velocity is associated with the lowest electromechanical coupling factor. The maximum electromechanical coupling factor is 4.2%, and is obtained with h$_{Mo,top}$/p = 0.05 and h$_{Mo,bottom}$/p = 0.12.
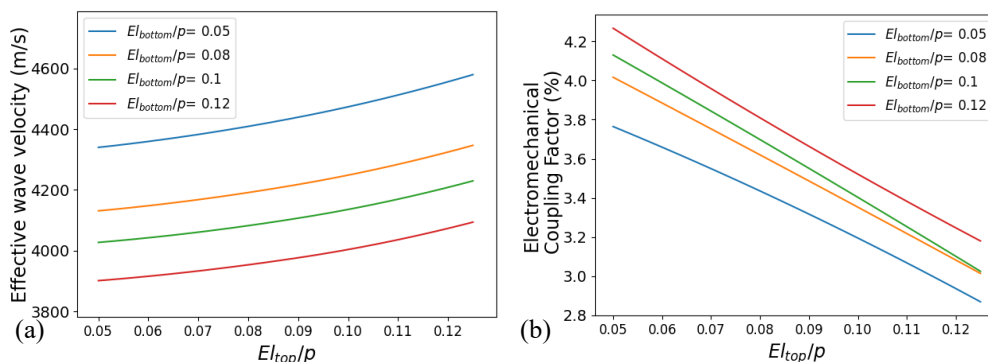
Figure 173: Influence of the top and bottom electrode thicknesses on the electromechanical coupling factor (a) and the effective wave velocity (b) of the TE$_{2,1}$ mode in AlN devices. (Mo/AlN/Mo/SiO$_2$/Si, h$_{AlN}$/p=1, a/p=0.5, etching ratio=1, straight sidewalls, h$_{SiO2}$/p=0.5)

Effect of the SiO$_2$ layer thickness

The thickness of the SiO$_2$ layer also has a significant effect on the performance of the TE$_{2,1}$ mode. Figure 174 shows how the coupling factor varies with the increase of the SiO$_2$ thickness.

Figure 174: impact of the SiO$_2$ layer thickness on the effective wave velocity (a) and coupling factor (b) of the TE$_{2,1}$ mode in AlN devices. (Mo/AlN/Mo/SiO$_2$/Si, h$_{AlN}$/p=0.7, a/p=0.5, etching ratio=1, straight sidewalls, h$_{bottom}$/p=0.12, h$_{top}$/p=0.05)

The figure demonstrates there is an optimum point at a SiO$_2$ thickness of 0.4 p, where the maximum k^2 achieved is 6.7%. The coupling factor decreases beyond this point and saturates at about 5.5%. It is worth noting that not hitting the optimum point but erring on the side of more SiO$_2$ is still better than no SiO$_2$ layer at all. In the case of absence of SiO$_2$, the electromechanical coupling factor falls to about 4.2%, as we have seen before.

Conclusions

Table 13 summarizes of parameters representing the configuration leading the the highest electromechanical coupling factor (6.5%) for the TE$_{2,1}$ mode using AlN.

Table 13: Geometric parameters leading to the highest possible TE$_{2,1}$ mode based on AlN with k^2=6.5%.

Pitch (p)	1 µm
h$_{AlN}$/p	0.7
Coverage ratio (a/p)	0.5
Etching Ratio	100%
Sidewall Angle	90 °
Electrode Material	Mo
Bottom Electrode (h$_{Mo,bottom}$/p)	0.12
Top Electrode(h$_{Mo,top}$/p)	0.05
SiO$_2$ thickness (h$_{SiO2}$/p)	0.4

3   TE$_{2,1}$ mode based on LNO

3.1   TE$_{2,1}$ mode in LNO

The TE$_{2,1}$ can be excited in LNO structures using the same electric configuration based on an in-phase excitation of the transducers. Figure 175 shows that the mode appears also around 4GHz, for a pitch of 1 μm and geometric parameters summarized in Table 14, with an even higher electromechanical coupling factor (16%) than AlN. However, unlike the case of AlN, the TE$_{2,1}$ mode is not the only mode that is excited in this electric configuration. There is therefore an additional difficulty when optimizing structures exploiting this mode, in that one does not only try to increase the electromechanical coupling factor, but also to suppress the other modes.
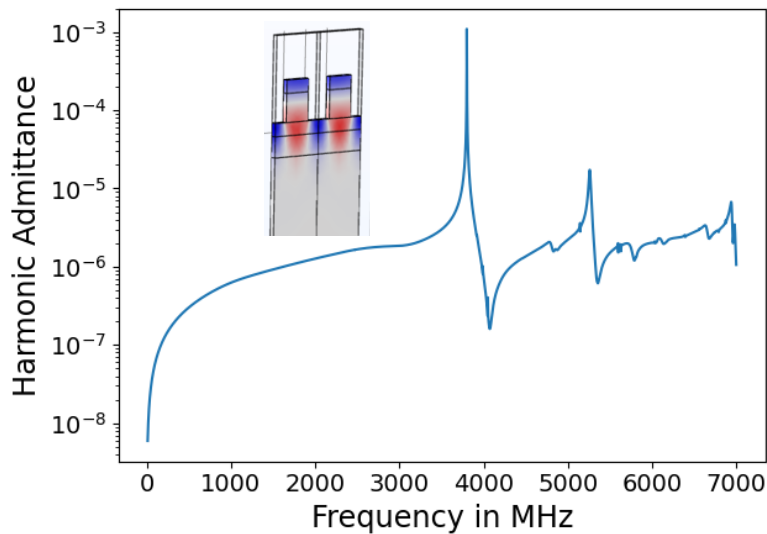
Figure 175: harmonic admittance calculation for a LNO HSBR with all top electrodes connected to the same port and the bottom electrode grounded, and vertical displacement field the TE$_{2,1}$ mode near 4 GHz (inset). Red and blue correspond respectively to positive (upwards) and negative (downwards) vertical displacements. The structure considered is summarized in Table 14.

In the same manner the pseudo-SAW and pseudo-BAW modes were optimized in Chapter 4, there are material orientation and geometrical parameters optimizations to be made. We start by considering the parameters listed in Table 14. We consider in particular the Y+30° crystal cut, as it is the one which promotes the highest electromechanical coupling factor for bulk longitudinal waves in lithium niobate [135].

Table 14: Optimum parameters for the optimization of the TE$_{2,1}$ mode based on LNO (k^2=16%)

LiNbO$_3$ crystal orientation	Y+30°, propagation X
Pitch (p)	1 μm
h$_{LNO}$/p	0.55
Coverage ratio (a/p)	0.5
Etching Ratio	100%
Sidewall Angle	90 °
Electrode Material	Al
Bottom Electrode (h$_{bottom}$/p)	0.25
Top Electrode (h$_{top}$/p)	0.25
SiO$_2$ thickness (h$_{SiO2}$/p)	0.5

3.2   Optimization of LNO crystal orientation

As we have seen in Chapter 4, the electromechanical coupling factor of the various modes is strongly dependent on the crystal orientation. For the $TE_{2,1}$ mode, this is also the case, and its dependence on the crystal orientation is shown in Figure 176. The electromechanical coupling factor is maximum (16.7%) for the Y+30° cut, and can almost disappear near Y+100°.
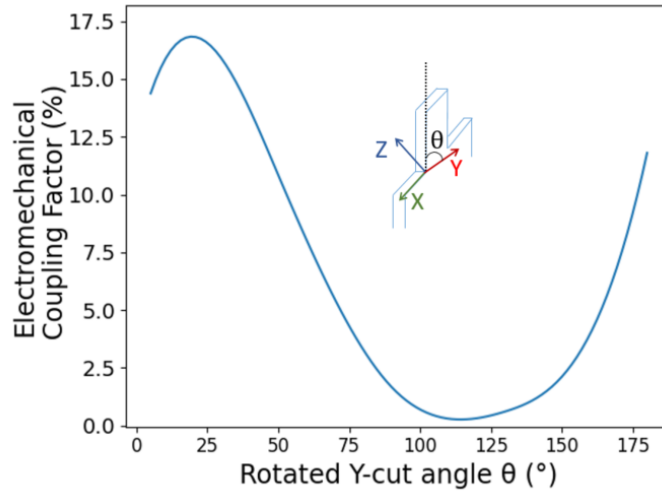
Figure 176: Dependence of the electromechanical coupling factor of the $TE_{2,1}$ mode as a function of the cut angle for rotated Y orientations. Other parameters correspond to those listed in Table 14.

Setting the crystal orientation to the Y+30° cut, we investigate the influence of the in-plane orientation of the transducers in Figure 177. The electromechanical coupling factor is maximum when the propagation direction is X (k^2 = 16.7%) and decreases down to 9% for a propagation along the X+90° (Z') direction.
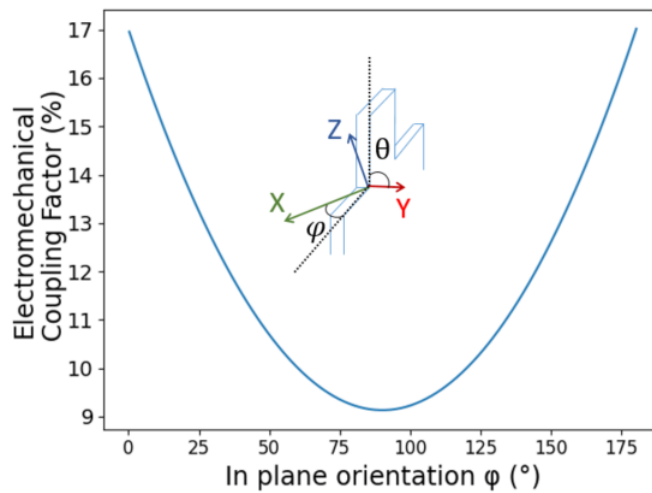
Figure 177: variation of the electromechanical coupling factor of the $TE_{2,1}$ mode with in-plane orientation φ (for $\theta = 30°$). Other parameters correspond to those listed in Table 14.

3.3   Optimization of geometrical parameters

Thickness to pitch ratio and coverage ratio

Figure 178 shows the effect of the piezoelectric layer thickness and the coverage ratio on the electromechanical coupling factor and the effective wave velocity of the $TE_{2,1}$ mode in LNO Y+30°, propagation X.
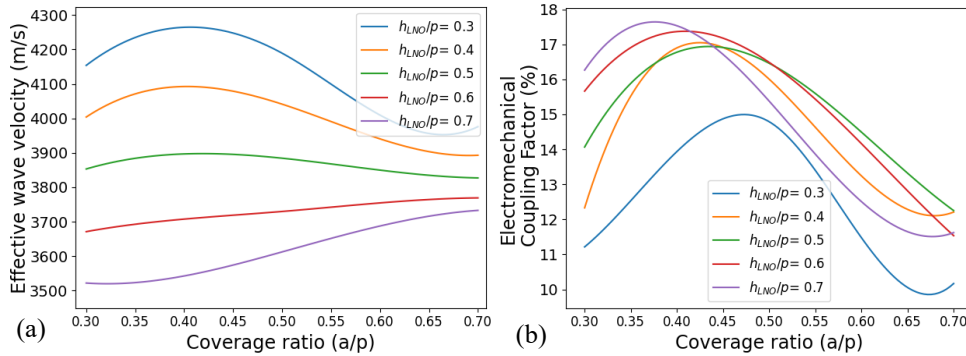
Figure 178: Impact of the piezoelectric layer thickness and the coverage ratio on the effective wave velocity (a) and electromechanical coupling factor (b) of the $TE_{2,1}$ mode using LNO. Other parameters correspond to those listed in Table 14

First, the increase in the piezoelectric layer thickness leads to a decrease in the effective wave velocity, possibly due to an increase in the mass-loading of the transducers. The difference is significant, as the velocity ranges from 4,200 m/s for $h_{LNO}/p = 0.3$ to 3,500 m/s for $h_{LNO}/p=0.7$. The effect of the coverage ratio is less clear: an increase in coverage ratio increases the velocity for piezoelectric layer thicknesses larger than 0.6, but on the contrary decreases the velocity for thicknesses lower than 0.6.

The electromechanical coupling factor is also highly dependent on the thickness of the piezo-electric layer and the coverage ratio. The maximum k^2 achieved is 17.5% at $h_{LNO}/p=0.7$ and a/p=0.4 which is not too far from the default set of parameters selected in Table 14. A decrease in the thickness to 0.3 p can bring the maximum coupling factor down to 14%. The effect of the coverage ratio is more significant and this parameter has therefore to be kept close to 0.4. A high or a small coverage ratio can lead to a drop in k² of about 5%.

Etching ratio and sidewall angle

The dependence of the electromechanical coupling factor of the $TE_{2,1}$ mode on the geometry of the transducers, shown in Figure 179, is more complex than what we could observe for the pseudo-SAW and pseudo-BAW modes in AlN, or for the pseudo-SH-SAW and pseudo thickness shear horizontal mode in LNO. For straight sidewalls, the best coupling factor is achieved when the piezoelectric layer is fully etched. The electromechanical coupling factor drops significantly from 16% to 11% or 9% at etching ratios of 80% and 60%. Unlike the previously studied modes, here we see an optimum sidewall angle that maximizes the electromechanical coupling factor. This optimum point differs depending on the etching ratio. At etching ratio of 100%, the optimum sidewall angle is 80° and leads to a k² of 16.5%. For an etching ratio of 80%, the optimum coupling is 17% at a sidewall angle of 65°; and at an etching ratio of 60%, the optimum coupling is about 15% at an etch angle of 60°. It appears therefore that slanted sidewalls are not necessary a bad thing, provided the depth of the trenches separating the transducers is adjusted accordingly.
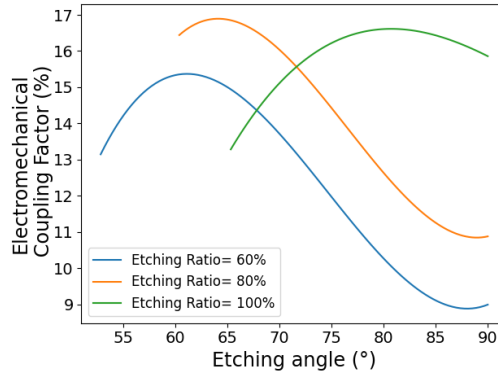
Figure 179: The evolution of k^2 for the TE$_{2,1}$ mode with the etching angle at different etching ratios for $h_{LNO}/p=0.55$. Other parameters correspond to those listed in Table 14

Top and bottom electrode thicknesses

Focusing on Al electrodes, Figure 180 shows the effect of the thicknesses of the top and bottom electrodes on the electromechanical coupling factor and the velocity of the TE$_{2,1}$ mode using LNO. The effect of the bottom electrode thickness on the wave velocity is small and varies within the range of 4,000 to 4,200 m/s. In contrast, the top electrode thickness has a much higher influenced and causes velocity variations between 3,600 and 4,200 m/s. The highest velocity is 4,200 m/s, for a bottom electrode thickness of 0.1 p and a top electrode thickness of 0.1 p.
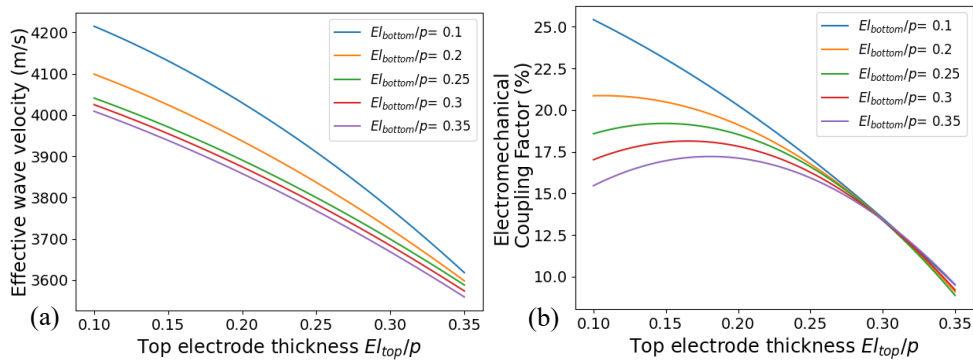
Figure 180: impact of the top and bottom electrode thicknesses on the electromechanical coupling factor (a) and the effective wave velocity (b) of the TE$_{2,1}$ mode using LNO Y+30°, propagation X. Other parameters correspond to those listed in Table 14

The electromechanical coupling factor follows similar trends than the resonance frequency. The largest electromechanical coupling factor achieved is as high as 25% at the same optimal parameters as for resonance frequency: a bottom electrode thickness of 0.1 p and a top electrode thickness of 0.1p. Unfortunately, the thicknesses of the top and bottom electrodes have a large effect on the spurious resonances appearing in the vicinity of the mode of interest. It appears that the smaller the thicknesses of the electrodes the less clean the resonance is, so we opt rather for top and bottom electrode thicknesses of 250 nm, where the coupling factor is unfortunately only 16%.

SiO$_2$ layer thickness

Unlike AlN, the presence of the SiO$_2$ layer is mandatory for designs based on LNO since it is used for bonding of the piezoelectric layer on the substrate during the fabrication process. Figure 181 shows the dependence of the electromechanical coupling factor on the SiO$_2$ layer thickness.

An optimum point appears. For $h_{LNO}/p=0.55$, the optimum SiO_2 thickness is at $0.3p$, which provides a coupling factor above 17%. For larger thicknesses, k^2 drops significantly, down to 13% for example for $h_{SiO2}/p = 0.7$.
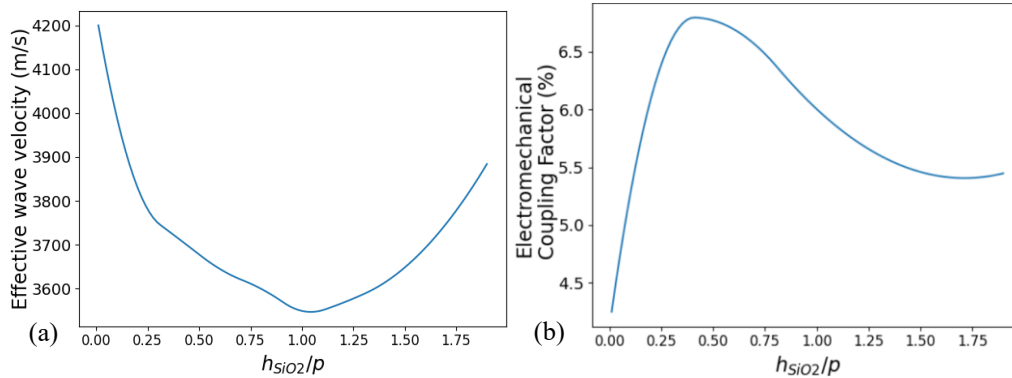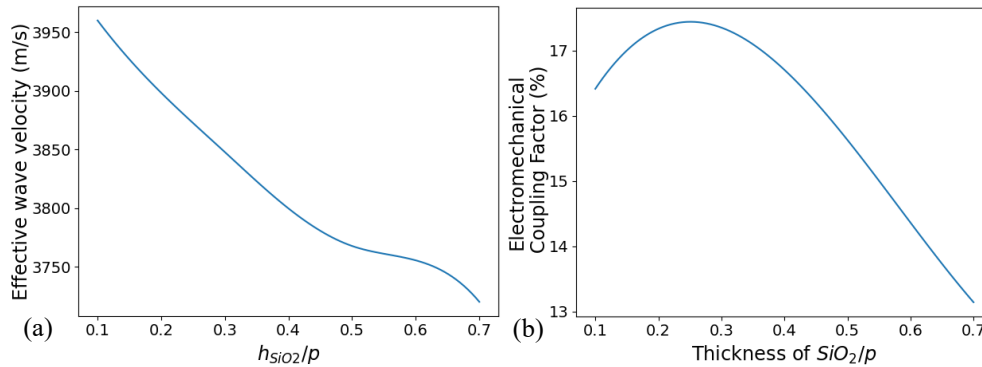

Figure 181: The impact of the SiO_2 layer thickness on the effective wave velocity (a) the coupling factor (b) of the $TE_{2,1}$ mode using LNO. Other parameters correspond to those listed in Table 14

3.4   HSBR Filter design

The configurations exploiting the $TE_{2,1}$ mode provide single mode operation, at high frequency and with large electromechanical coupling factors. They appear therefore suitable for the implementation of filters. To illustrate this, an example filter was designed used a simple ladder circuit, to visualize the kind of band-pass filter that can be built with HSBR. The mode exploited is the $TE_{2,1}$, with an in-phase excitation of a LNO Y+36 cut transducers oriented perpendicularly to the X-crystalline axis. We use parameters similar to those mentioned in Table 14 with the exception of slightly different cut angle and $h_{SiO2}/p=0.5$ to reduce the parasitic interactions slightly. The harmonic admittance of this resonator resulting from a FEM simulation is shown in Figure 182. The simulated resonator has a resonance frequency of $f_s= 3.96$ GHz, an anti-resonance frequency $f_p= 4.19$ GHz, and $k^2= 14\%$.
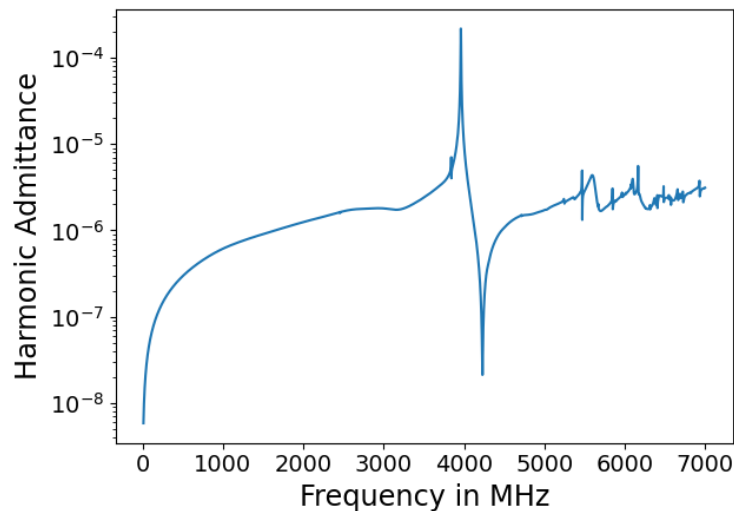
Figure 182: Harmonic admittance of a HSBR using the $TE_{2,1}$ mode in LNO Y+36°, propagation X.

A ladder filter consists of multiple resonators connected in parallel and in series. For a first evaluation, we consider a "T" circuit made of one parallel and two series resonators. A schematic is shown in Figure 183.
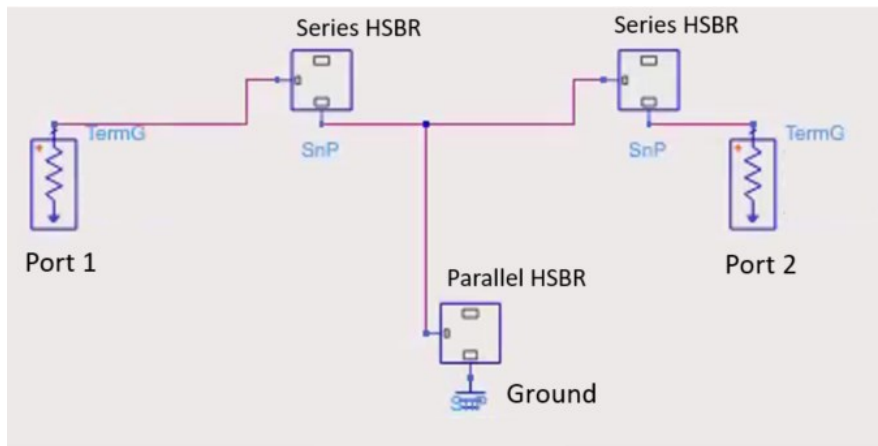
Figure 183: Circuit schematic of a "T" ladder filter utilizing HSBR.

The parallel resonator has an anti-resonance frequency (where its admittance is minimum) matched to the center frequency of the filter. At this frequency, the impedance is maximum, and the signal is therefore constraint to remain in the series path.

At the resonance of the parallel resonator, the signal is shunted to ground and is therefore prevented to reach the output of the circuit. At the antiresonance of the series resonators, the signal is instead blocked, and again prevented to reach the output. The combination of these behaviors induce a band-pass type transmission.

We first design a circuit with ideal BVD components having the same resonance, anti-resonance and coupling factors as the HSBR. By tuning the parameters of the BVD blocks, i.e. the resonance frequencies and the static capacitances of the resonators, the filter can be designed to have desired bandwidth, center frequency, and selectivity.

- Parallel resonator: f_s= 3.828 GHz, f_p= 4.05 GHz
- Series resonator: f_s= 4.235 GHz, f_p= 4.52 GHz

.
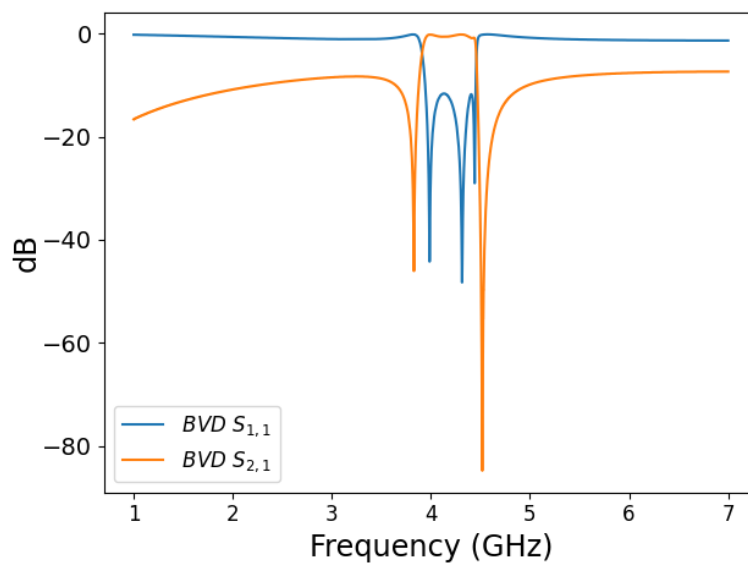
Figure 184: ideal filter response using BVD components

The ideal filter response simulated using BVD components is shown in Figure 184. We then scale the harmonic admittance to have their static capacitance equal to the one of the BVD components. In practice, this would be achieved by designing resonators with given numbers of electrodes and adjusting their aperture. The frequencies of the parallel resonator are artificially shifted from the calculated series resonator response. Figure 185 then shows the simulated filter based on the finite element simulations of the hybrid SAW/BAW resonators, and compares them with the ideal filter response calculated using BVD components. The designed filter has the following characteristics:

- Passband (the range of frequencies for which the filter transmission is higher than -3 dB): 3.95 GHz to 4.45 GHz
- Insertion loss (the minimum attenuation of the signal in the passband): 1.5 dB
- Rejection (the attenuation of the signal outside of the passband): 6 dB
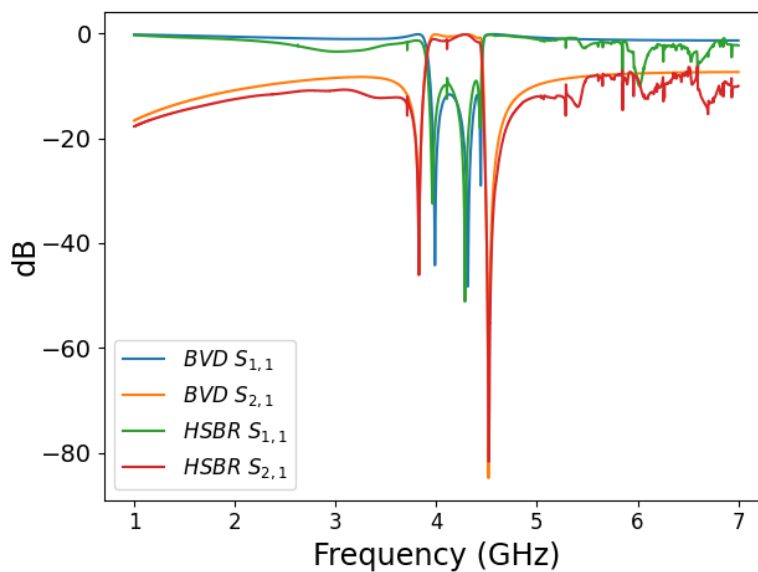
Figure 185: comparison between ideal filter response using BVD components and using FEM HSBR admittance

With a passband of nearly 500 MHz near 4 GHz, such a filter approaches the specifications for the 5G telecommunication band n78 (3.3 – 3.8 GHz). With a bit more optimizations, it could approach also the 600 MHz required for band n79 (4.4 – 5 GHz), although this would also require more aggressive geometric dimensions (p = 0.9 μm) due to the need to increase the center frequency of the filter.

So far, these filters remain challenging to implement with conventional AlScN BAW filters. A demonstration of an n78 band filter has been proposed very recently in the literature, based on SAW devices made of LNO on an SiC substrate [136]. It requires similar electrode periodicities than in our case. However, the need for SiC substrates instead of Si as for our structure, makes the solution we propose competitive.

n79 filters have been also proposed, based on XBAR devices, *i.e.* laterally-excited bulk wave resonators implemented in suspended LNO membranes [137], or in LNO films isolated from the substrate using an acoustic Bragg mirror [138]. LNO BAW filters have also been demonstrated for this band [85]. Each solution having its own pros and cons, none of these technologies has

fully emerged on the filter market yet. LNO Hybrid SAW/BAW devices exploiting the $TE_{2,1}$ mode remain therefore a potential solution worth continuing exploring.

4   Conclusions

In this chapter we have shown the potential of the HSBR to achieve single mode and high frequency operation using a new mode that we called the $TE_{2,1}$ mode. This mode results from the hybridization between the second order surface wave propagating on the substrate and the fundamental thickness mode of the transducers. Despite a smaller wave velocity than the pseudo-BAW or the pseudo thickness shear horizontal mode (about 4,200 m/s in AlN/Si structures), its smaller wavelength (λ=p instead of λ=2p as for the other modes considered in this manuscript) makes it appear at frequencies near 4 GHz. This mode was first noticed on the experimental response of devices fabricated in Chapter 3, with grounded bottom electrode, although these devices were not optimized for its exploitation. This resulted in relatively small electromechanical coupling factors (k^2= 0.3% at most).

We have investigated the best ways to exploit the $TE_{2,1}$ mode, first in AlN hybrid SAW/BAW resonators. Provided all the transducers are excited in-phase through, the $TE_{2,1}$ is solely excited, while the pseudo-SAW and pseudo-BAW modes studied in chapters 2 and 3 are completely cancelled. Its electromechanical coupling factor can be optimized up to 6.5% with conventional AlN piezoelectric films, i.e. up to the electromechanical coupling factor of BAW devices.

We also considered similar structures based on LNO. We determined the most interesting crystal orientation and geometry to exploit it and reach clean electric responses. Actually, a compromise had to be established between these two goals, which resulted in structures promoting an electromechanical coupling factor of 16% with the least spurious resonances possible. We considered this structure to design a simple ladder filter which exhibits a bandwidth of 500 MHz at 4.2 GHz, , insertion loss of 1.5 dB and a rejection of 6 dB for a simple "T" circuit. These performances compete well with alternative solutions based on LNO/SiC SAW devices, LNO BAW devices, or XBARs and demonstrate that LNO hybrid SAW/BAW resonators exploiting this new mode show a great potential.

General Conclusions and Perspectives

This thesis has focused on the exploration of Hybrid SAW/BAW structures, with the aim of investigating their applicability for RF filtering applications. Our goal was to investigate what performances, in terms of frequency, electromechanical coupling factor and quality factor can be achieved in practice. These structures have revealed supporting several modes, each influenced differently by design parameters, leading to a rich landscape for exploration. Our approach has therefore be explore theoretically this design space, while in the parallel developing fabrication processes for the implementation of such structures.

A first part of our work aimed at building the periodic finite element models used consistently throughout this thesis to evaluate the propagation properties (wave velocity, possible radiation losses) and the electromechanical coupling of the hybrid SAW/BAW modes. Our first investigations revealed the importance of considering the electrostatic contribution of the vacuum medium surrounding the transducers, since it makes up 50% of the structure and affects therefore largely the electric field distribution in the piezoelectric transducers, which causes a decrease in the electromechanical coupling factor. We then investigated the dependence of the electromechanical properties of the so-called pseudo-SAW and pseudo-BAW modes on the geometry of the hybrid SAW/BAW structure. An optimization to maximize the coupling factor of AlN-based transducers yielded modest electromechanical coupling factors 3.6% at an effective velocity of 3600 m/s for the pseudo-SAW mode using diamond substrate. On a Silicon substrate, the pseudo-SAW mode has a maximum 1.5% at 2000 m/s and the pseudo-BAW mode has a maximum of 2.2% at 4200 m/s.

Experimentally, we developed a process flow to fabricate HSB devices with well-defined AlN transducers on Si and SiO_2/Si substrates. We worked in particular on the patterning of the piezoelectric transducers with relatively high thickness to width or thickness to gap aspect ratios, up to 8:1. Even with sidewall angles better than 80°, we could notice that the etching stops for the most aggressive aspect ratios ($h_{AlN}/p > 2.5$), leaving about 40% of the initial piezoelectric layer between the transducers. This did however not prevent the devices from being functional. The pseudo-SAW mode exhibits experimental electromechanical coupling factor of 1.5% at 600 MHz or near 0.8% at frequencies up to 1.4 GHz, with quality factors up to $Q_s = 2900 \pm 450$ and $Q_p = 3200 \pm 500$, which makes it interesting for timing or sensor applications.. The pseudo-BAW mode was found to have a maximum electromechanical coupling factor of 1.8% at a frequency of 1.8 GHz, or near 1% at frequencies up to 2.8 GHz, with quality factors approaching 1000, improved with the introduction of the SiO_2 layer. Although modest, these performances are in-line with the expected mode properties and near the theoretical limit.

A second part of this thesis aimed at improving the performances of hybrid SAW/BAW resonators. At first, our goal was to increase the electromechanical coupling factors beyond the limit of 2% for AlN. While other groups investigated AlScN as the piezoelectric material, we shifted our focus on $LiNbO_3$ instead. This was motivated by the available expertise at CEA-LETI and frec|n|sys in developing acoustic devices based on this material. The more complex crystal symmetries of LNO compared to AlN, coupled to the possibility to select specific crystal orientations, make new modes appear, with shear vertical or shear horizontal polarizations. Due to the larger piezoelectric coefficients of LNO compared to AlN, one can reach higher electromechanical coupling factors in general, however at the expense of stronger spurious modes content in the electric response. We identified two modes to be of special interest: the pseudo shear horizontal SAW

mode and the pseudo thickness shear horizontal mode. They were found to have the highest electromechanical coupling factor in X-cut LNO, when the propagation direction is 150° off the Y crystalline axis. The pseudo-SH-SAW mode, whose resonance is located at 500 MHz, exhibits a clean response and high coupling factor. Despite its particularly high k^2 up to 38%, this mode has only a wave velocity of about 1,000 m/s, and is therefore not adapted to high frequency applications. The pseudo TSH mode operates at a higher effective velocity of 3200 m/s but with an electromechanical coupling factor of 14%. These k^2 represent a vast step forward beyond what AlN offers but are still low in frequency.

To answer the need for increasing frequency, a third part of this thesis focused on a new mode, which originally appeared in AlN devices at a resonance frequency of about 4.2 GHz. This mode, which results from the hybridization between the second overtone of the surface wave in the substrate and the fundamental thickness mode of the transducer, and that we therefore call the $TE_{2,1}$ mode, is efficiently excited when all transducers are excited in phase (*i.e.* not with an alternating electric field as the other modes considered so far). The advantage of this excitation scheme is not only the increase in frequency, but also the complete suppression of all other modes (in particular the pseudo-SAW and pseudo-BAW modes), leading to a single mode response. Such an electric configuration also leads to the augmentation of the electromechanical coupling of the $TE_{2,1}$ mode, which can be optimized to reach 6.5% at frequency of 3.7 GHz for a transducer periodicity of 1 μm, using $AlN/SiO_2/Si$.

We were able to excite the same mode using $LiNbO_3$ which again provided higher piezoelectric coupling but with spurious contributions to be considered. The $TE_{2,1}$ mode reached a k^2 of 16% at a frequency of 4 GHz, still for a transducer periodicity of 1 μm, using $LNO/SiO_2/Si$ with a minimal amount of spurious contributions. Using the later configuration, we designed a simple ladder filter which exhibits a bandwidth of 500 MHz at 4.2 GHz, insertion loss of 1.5 dB and a rejection of 6 dB for a simple "T" circuit. This evaluation shows that hybrid SAW/BAW devices based on LNO and exploiting the $TE_{2,1}$ mode could, in principle, address the n78 and n79 5G frequency bands, which are currently knowingly difficult to implement with classical SAW or BAW solutions.

In Figure 186, we update Figure 47 that summarized in chapter 1 the electromechanical coupling factors reported so far for HSB resonators in the literature. This highlights the interest of LNO-based HSB structures either the pseudo-SH-SAW mode on the low-frequency side, or the new $TE_{2,1}$ mode on the high frequency side.
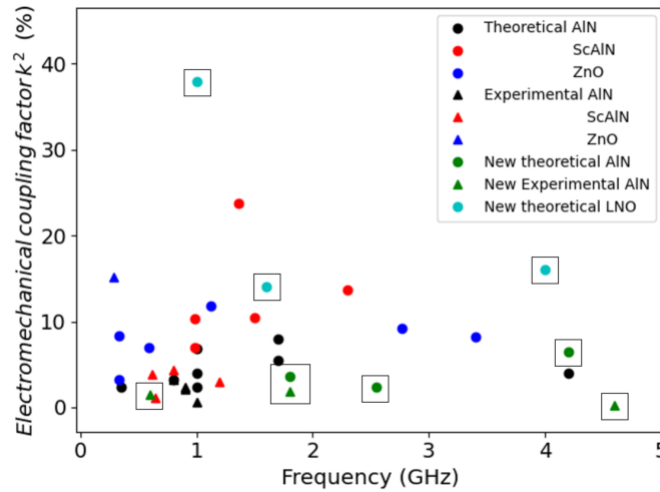
Figure 186: Comparison of the theoretical (circles) and experimental (triangles) electromechanical coupling factors reported in the literature for hybrid SAW/BAW devices based on AlN (black), AlScN(red), ZnO(blue) with the new results based on AlN (green) and LNO (cyan).

Due to time constraints, not all investigations have reached their end. First, regarding the improvements of the electromechanical coupling factors of the hybrid SAW/BAW resonators, we mentioned briefly at the end of Chapter 3 that we had starting investigating the AlScN-based devices. During the writing of the manuscript, some structures based on this material and optimized to reach electromechanical coupling factors of 23% at a frequency of 1.4 GHz have been proposed [66]. They have yet to be demonstrated experimentally. There are therefore high expectations for finishing the fabrication of AlScN resonators and characterizing them.

In Chapter 4, we considered instead LNO-based structures. We mentioned also that their fabrication had started, but remain at the time of writing far from being completed. Even if these devices use the same designs as for the AlN-based resonators, there are high expectations for these structures as well.

Finally, the $TE_{2,1}$ mode investigated in Chapter 5 could not be efficiently exploited given the designs implemented so far. Designing a new mask-set providing devices with grounded bottom electrodes and top electrodes all connected to the same electrical port would allow for the experimental investigation of $TE_{2,1}$ mode, and a confirmation of the theoretical study performed in this manuscript.

Further explorations of HSBR should aim at increasing the confinement of the waves in the vicinity of the transducers, in order to improve the electromechanical coupling factors and reduce losses. We exploited the guidance of slow waves near the surface of the substrate. However, this mechanism ultimately limits the velocity of the modes we can exploit. We have investigated in Chapter 2 other substrates than Si to mitigate this issue, but the need to rely on diamond or sapphire substrates makes this solution relatively difficult to industrialize on the long term. The introduction of artificial confinement structures, such as a Bragg Mirror, or on the contrary suspending the transducers appear in principle as more realistic to implement. Such structures would in principle converge towards approaches for solidly mounted Lamb wave devices [139], or thickness shear horizontal Lamb wave devices (also called YBAR) [53], which have already demonstrated promising performances.

If hybrid SAW/BAW resonators keep up their promises experimentally, there remain many challenges to solve to mature this technology before exploiting it in real applications. In particular, we did not consider so far issues such as the temperature stability of these devices. Performing electric measurements as a function of temperature on one hand to determine the temperature coefficient of frequency would be necessary. Updating the models to be able to include this parameter in designs, and potentially to optimize the structures also for temperature stability, would be also needed. Other issues such as power handling or reliability may also require some extensive work. In particular, the devices we fabricated are not passivated, so the molybdenum electrodes may easily oxidize if the resonators heat too much when exposed to high input power. Improving these issues will require a combination of process adjustments (how to passivate properly these structures with high aspect ratios), acoustic design (what is the impact of an added passivation layer and how to mitigate it), and even thermal design (how well can the heat spread out of the resonators).

Beyond technological challenges, there is also the need to develop design tools devoted to hybrid SAW/BAW resonators. Most of the investigations, either in this manuscript or in the literature, rely on periodic finite element simulations. A proper design of resonators would need models capable of considering a finite number of transducers, with the associated effects, such as the P-matrix [140], [141] or the Coupling-Of-Modes (COM) [142] which are widely employed to design SAW devices. The adaptation of these models requires considering two levels of electrodes instead of only one for SAW, and potentially multiple modes depending on the level of detail one wants to be able to consider.

Bibliography

[1] R. A. Galván. Conception de nouveaux composants RF agiles à ondes acoustiques de surface. Micro et nanotechnologies/Microélectronique. Thèse de doctorat de l'Université de Lille, 2022.

[2] Y. Liu and Z. Zhang, "Forming Low-Impedance MEMS Bandpass Filters," Microwaves&RF. March, 2017

[3] N. Popoff, and C.Malaquin, "RF Front-End for Mobile 2023; Yole Group, 2023."

[4] R. Aigner, "Tunable Filters? Reality Check Foreseeable Trends in System Architecture for Tunable RF Filters," *IEEE Microw. Mag.*, vol. 16, no. 7, pp. 82–88, Aug. 2015, doi: 10.1109/MMM.2015.2428439.

[5] A. F. Ulitko, "Theory of electromechanical energy conversion in nonuniformly deformable piezoceramics," *Sov. Appl. Mech.*, vol. 13, no. 10, pp. 1055–1062, Oct. 1977, doi: 10.1007/BF00883190.

[6] B. Aronov, "On the optimization of the effective electromechanical coupling coefficients of a piezoelectric body," *J. Acoust. Soc. Am.*, vol. 114, no. 2, pp. 792–800, Aug. 2003, doi: 10.1121/1.1592163.

[7] H. Campanella, *Acoustic Wave and Electromechanical Resonators: Concept to Key Applications*. in Artech House integrated microsystems series. Artech House, 2010. [Online]. Available: https://books.google.fr/books?id=ps64Hun17wcC

[8] Q. Chen and Q.-M. Wang, "The effective electromechanical coupling coefficient of piezoelectric thin-film resonators," *Appl. Phys. Lett.*, vol. 86, no. 2, p. 22904, Jan. 2005, doi: 10.1063/1.1850615.

[9] P. Muralt, J. Antifakos, M. Cantoni, R. Lanz, and F. Martin, "Is there a better material for thin film BAW applications than A1N?," Proceedings of the *IEEE Ultrasonics Symposium, 2005.*, pp. 315–320. doi: 10.1109/ULTSYM.2005.1602858.

[10] "IEEE Standard on Piezoelectricity," in ANSI/IEEE Std 176-1987, 1988, doi: 10.1109/IEEESTD.1988.79638.

[11] J. M. L. Miller, A. Ansari, D. B. Heinz, Y. Chen, I. B. Flader, D. D. Shin, L. G. Villanueva, T. W. Kenny; Effective quality factor tuning mechanisms in micromechanical resonators. Appl. Phys. Rev. 1 December 2018; 5 (4): 041307. https://doi.org/10.1063/1.5027850

[12] RF Filter Technology For Dummies®, Qorvo Special Edition, 2022 by John Wiley & Sons, Inc.

[13] J. M. Carcione, "Viscoelasticity and wave propagation," in *Wave Fields in Real Media*, Elsevier, 2022, pp. 63–133. doi: 10.1016/B978-0-32-398343-3.00011-8.

[14] F. Wudy, C. Stock, and H. J. Gores, "MEASUREMENT METHODS | Electrochemical: Quartz Microbalance," in *Encyclopedia of Electrochemical Power Sources*, Elsevier, 2009, pp. 660–672. doi: 10.1016/B978-044452745-5.00079-4.

[15] K. M. Lakin and J. S. Wang, "UHF Composite Bulk Wave Resonators," in *1980 Ultrasonics Symposium*, 1980, pp. 834–837. doi: 10.1109/ULTSYM.1980.197515.

[16] Lord Rayleigh, "On Waves Propagated along the Plane Surface of an Elastic Solid," *Proc. Lond. Math. Soc.*, vol. s1-17, no. 1, pp. 4–11, Nov. 1885, doi: 10.1112/plms/s1-17.1.4.

[17] R. Banu Priya, T. Venkatesan, G. Pandiyarajan, H. M. Pandya "A Short Review of SAW Sensors," *J. Environ. Nanotechnol.*, vol. 4, no. 4, pp. 15–22, Dec. 2015, doi: 10.13074/jent.2015.12.154171.

[18] D. Royer and E. Dieulesaint, *Ondes élastiques dans les solides*. Masson, 1996.

[19] M. A. Pelissier, H. Hoeber, N. van de Coevering, and I. F. Jones, Eds., *Classics of Elastic Wave Theory*. Society of Exploration Geophysicists, 2007. doi: 10.1190/1.9781560801931.

[20] R. M. White and F. W. Voltmer, "DIRECT PIEZOELECTRIC COUPLING TO SURFACE ELASTIC WAVES," *Appl. Phys. Lett.*, vol. 7, no. 12, pp. 314–316, Dec. 1965, doi: 10.1063/1.1754276.

[21] P. V. Wright, "A review of SAW resonator filter technology," Proceedings of the *IEEE 1992 Ultrasonics Symposium Proceedings*, 1992, pp. 29–38. doi: 10.1109/ULTSYM.1992.276068.

[22] V. L. Strashilov and V. M. Yantchev, "Surface transverse waves: properties, devices, and analysis," Proceedings of the *IEEE Trans. Ultrason. Ferroelectr. Freq. Control*, vol. 52, no. 5, pp. 812–821, May 2005, doi: 10.1109/TUFFC.2005.1503967.

[23] M. I. Gaso Rocha, Y. Jimenez, F. A., and A. Arnau, 'Love Wave Biosensors: A Review', State of the Art in Biosensors - General Aspects. InTech, Mar. 13, 2013. doi: 10.5772/53077.

[24] V. R. Pagan, "Aluminum nitride deposition/characterization for MEMs/SAW device simulation/fabrication," MS, West Virginia University Libraries, 2009. doi: 10.33915/etd.2012.

[25] F. Engelmark, "AlN and High-k Thin Films for IC and Electroacoustic Applications," Ph.D Dissertation , Uppsala, Sweden, 2002.

[26] K. M. Lakin, "Thin film resonator technology," in *IEEE International Frequency Control Sympposium and PDA Exhibition Jointly with the 17th European Frequency and Time Forum, 2003.* pp. 765–778. doi: 10.1109/FREQ.2003.1275190.

[27] T. Makkonen, T. Pensala, J. Vartiainen, J. V. Knuuttila, J. Kaitila, and M. M. Salomaa, "Estimating materials parameters in thin-film BAW resonators using measured dispersion curves," *IEEE Trans. Ultrason. Ferroelectr. Freq. Control*, vol. 51, no. 1, pp. 42–51, Jan. 2004, doi: 10.1109/TUFFC.2004.1268466.

[28] M. Dubois, C. Billard, C. Muller, G. Parat, and P. Vincent, "Integration of high-Q BAW resonators and filters above IC," in *Digest of Technical Papers of the 2005 Solid-State Circuits Conference*, pp. 392–394. doi: 10.1109/ISSCC.2005.1494034.

[29] G. Piazza, V. Felmetsger, P. Muralt, R. H. Olsson III, and R. Ruby, "Piezoelectric aluminum nitride thin films for microelectromechanical systems," *MRS Bull.*, vol. 37, no. 11, pp. 1051–1061, Nov. 2012, doi: 10.1557/mrs.2012.268.

[30] K. M. Lakin, G. R. Kline, and K. T. McCarron, "Development of miniature filters for wireless applications," *IEEE Trans. Microw. Theory Tech.*, vol. 43, no. 12, pp. 2933–2939, Dec. 1995, doi: 10.1109/22.475658.

[31] C. C. W. Ruppel, "Acoustic Wave Filter Technology–A Review," *IEEE Trans. Ultrason. Ferroelectr. Freq. Control*, vol. 64, no. 9, pp. 1390–1400, Sep. 2017, doi: 10.1109/TUFFC.2017.2690905.

[32] Y. Zou, Y. Zou, C. Gao, J. Zhou, Y. Liu, Q. Xu, Y. Qu, W. Liu, J. B. W. Soon, Y. Cai & C. Sun, "Aluminum scandium nitride thin-film bulk acoustic resonators for 5G wideband applications," *Microsyst. Nanoeng.*, vol. 8, no. 1, p. 124, Nov. 2022, doi: 10.1038/s41378-022-00457-0.

[33] Y. Satoh, T. Nishihara, T. Yokoyama, M. Ueda, and T. Miyashita, "Development of Piezoelectric Thin Film Resonator and Its Impact on Future Wireless Communication Systems," *Jpn. J. Appl. Phys.*, vol. 44, no. 5, p. 2883, May 2005, doi: 10.1143/JJAP.44.2883.

[34] Y. Liu, Y. Cai, Y. Zhang, A. Tovstopyat, S. Liu, and C. Sun, "Materials, Design, and Characteristics of Bulk Acoustic Wave Resonator: A Review," *Micromachines*, vol. 11, no. 7, p. 630, Jun. 2020, doi: 10.3390/mi11070630.

[35] Y. Yang, C. Dejous, and H. Hallil, "Trends and Applications of Surface and Bulk Acoustic Wave Devices: A Review," *Micromachines*, vol. 14, no. 1, p. 43, Dec. 2022, doi: 10.3390/mi14010043.

[36] S. Elisabeth, C. Malaquin, System Plus Consulting, Yole, "Intensifying Technology Competition in the Acoustic Wave Filter Market," Microwave Journal. https://shorturl.at/gDKP7

[37] Q. Xiao, C. Dong, X. Ji, P. Cai, and J. Chen, "Investigation of incredible high performance surface acoustic wave properties with a structure of IDT/ (Θ 0) YX-LiTaO3/SiO2/AlN/Silicon," in *2017 Symposium on Piezoelectricity, Acoustic Waves, and Device Applications (SPAWDA)*, 2017, pp. 197–201. doi: 10.1109/SPAWDA.2017.8340321.

[38] R. Vetury, M. D. Hodge, and J. B. Shealy, "High Power, Wideband Single Crystal XBAW Technology for sub-6 GHz Micro RF Filter Applications," in *2018 IEEE International Ultrasonics Symposium (IUS)*, 2018, pp. 206–212. doi: 10.1109/ULTSYM.2018.8580045.

[39] A. Reinhardt, L.Benaissa, J. David; N. Lamard; V. Kovacova; N. Boudou; E. Defaÿ., "Acoustic filters based on thin single crystal LiNbO3 films: Status and prospects," in *2014 IEEE International Ultrasonics Symposium*, Sep. 2014, pp. 773–781. doi: 10.1109/ULTSYM.2014.0191.

[40] M. Bousquet, P. Perreau, C. Maeder-Pachurka and A. Joulie, F. Delaguillaumie, J. Delprato, G. Enyedi, G. Castellan, C. Eleouet, T. Farjot, C. Billard, A. Reinhardt "Lithium niobate film bulk acoustic wave resonator for sub-6 GHz filters," Proceedings of the *2020 IEEE International Ultrasonics Symposium (IUS)* doi: 10.1109/IUS46767.2020.9251654.

[41] R. Lu, Y. Yang, S. Link, and S. Gong, "A1 Resonators in 128° Y-cut Lithium Niobate with Electromechanical Coupling of 46.4%," *J. Microelectromechanical Syst.*, vol. 29, no. 3, pp. 313–319, Jun. 2020, doi: 10.1109/JMEMS.2020.2982775.

[42] Y. Yang, A. Gao, R. Lu, and S. Gong, "5 Ghz lithium niobate MEMS resonators with high FoM of 153," in *2017 IEEE 30th International Conference on Micro Electro Mechanical Systems (MEMS)*, Jan. 2017, pp. 942–945. doi: 10.1109/MEMSYS.2017.7863565.

[43] Y. Yang, R. Lu, T. Manzaneque, and S. Gong, "1.7 GHz Y-Cut Lithium Niobate MEMS Resonators with FoM of 336 and f.Q of $9.15{\times}10^{12}$," in *2018 IEEE/MTT-S International Microwave Symposium - IMS,* Jun. 2018, pp. 563–566. doi: 10.1109/MWSYM.2018.8439516.

[44] Y. Yang, R. Lu, L. Gao, and S. Gong, "4.5 GHz Lithium Niobate MEMS Filters With 10% Fractional Bandwidth for 5G Front-Ends," *J. Microelectromechanical Syst.*, vol. 28, no. 4, pp. 575–577, Aug. 2019, doi: 10.1109/JMEMS.2019.2922935.

[45] S. Gong and G. Piazza, "Design and Analysis of Lithium–Niobate-Based High Electromechanical Coupling RF-MEMS Resonators for Wideband Filtering," *IEEE Trans. Microw. Theory Tech.*, vol. 61, no. 1, pp. 403–414, Jan. 2013, doi: 10.1109/TMTT.2012.2228671.

[46] M. Gorisse, L. Dours, P. Perreau, A. Ravix, R. Lefebvre, G. Castellan, C. Maeder-Pachurka, M. Bousquet, A. Reinhardt, R. Bauder, H.J. Timme, H. P. Friedrich, "High Frequency LiNbO $_3$ Bulk Wave Resonator," in *2019 Joint Conference of the IEEE International Frequency Control Symposium and European Frequency and Time Forum (EFTF/IFC),* doi: 10.1109/FCS.2019.8856017.

[47] X. Bai, Y. Shuai, L. Lv, Y. Xing, J. Zhao, W. Luo, C. Wu, T. Yang, W. Zhang, "The thin film bulk acoustic wave resonator based on single-crystalline 43 Y-cut lithium niobate thin films," *AIP Adv.*, vol. 10, no. 7, p. 075002, Jul. 2020, doi: 10.1063/1.5143550.

[48] K. Matsumoto, M. Kadota, and S. Tanaka, "High frequency thickness expansion mode bulk acoustic wave resonator using LN single crystal thin plate," *Jpn. J. Appl. Phys.*, vol. 59, no. 3, p. 36506, Mar. 2020, doi: 10.35848/1347-4065/ab7861.

[49] S. Zhang, R. Lu, H. Zhou, S. Link, Y. Yang, Z. Li, K. Huang, X. Ou, S. Gong, "Surface Acoustic Wave Devices Using Lithium Niobate on Silicon Carbide," *IEEE Trans. Microw. Theory Tech.*, vol. 68, no. 9, pp. 3653–3666, Sep. 2020, doi: 10.1109/TMTT.2020.3006294.

[50] P. Chen, G. Li, and Z. Zhu, "Development and Application of SAW Filter," *Micromachines*, vol. 13, no. 5, p. 656, Apr. 2022, doi: 10.3390/mi13050656.

[51] K.-Y. Hashimoto, M. Yamaguchi, S. Mineyoshi, O. Kawachi, M. Ueda, and G. Endoh, "Optimum leaky-SAW cut of LiTaO/sub 3/ for minimised insertion loss devices," in *1997 IEEE Ultrasonics Symposium Proceedings. An International Symposium*, 1997, pp. 245–254. doi: 10.1109/ULTSYM.1997.663019.

[52] T. Takai, H. Iwamoto, Y. Takamine, H. Yamazaki, T. Fuyutsume, H. Kyoya, T. Nakao, H. Kando, M. Hiramoto, T. Toi, M. Koshino, N. Nakajima, "Incredible high performance SAW resonator on novel multi-layerd substrate," in *2016 IEEE International Ultrasonics Symposium (IUS)*, Sep. 2016 doi: 10.1109/ULTSYM.2016.7728455.

[53] V. P. Plessky, J. Koskela, and S. Yandrapalli, "Crystalline Y-cut Lithium Niobate Layers for the Bulk Acoustic Wave Resonator (YBAR)," in *2020 IEEE International Ultrasonics Symposium (IUS)*, Sep. 2020 doi: 10.1109/IUS46767.2020.9251647.

[54] V. Plessky, S. Ballandras, V. Grigorievsky, and V. Yantchev, "3rd type of FBARs?," in *2013 IEEE International Ultrasonics Symposium (IUS)* Jul. 2013, pp. 239–242. doi: 10.1109/ULTSYM.2013.0062.

[55] R. Rouffaud, F. Levassort, and A.-C. Hlady-Hennion, "Unified model for the electromechanical coupling factor of orthorhombic piezoelectric rectangular bar with arbitrary aspect ratio," *AIP Adv.*, vol. 7, p. 25302, Feb. 2017, doi: 10.1063/1.4976298.

[56] V. Pashchenko, R. Matloub, F. Parsapourkolour, P. Muralt, S. Ballandras, and K. Haffner, "Hybrid BAW/SAW AlN and AlScN thin film resonator," in *2016 IEEE International Ultrasonics Symposium (IUS)*, doi: 10.1109/ULTSYM.2016.7728649.

[57] K. Liu, J. Liang, and T. Wu, "AlN Hybrid-Coupled Resonators With High Acoustic Velocity Layer," in *2020 IEEE International Ultrasonics Symposium proceedings.* doi: 10.1109/IUS46767.2020.9251778.

[58] V. Pashchenko, F. Parsapour, S. Ballandras, K. Haffner, and P. Muralt, "Effective SAW excitation on non-piezoelectric substrate using AlScN piezoelectric thin film BAW/SAW hybrid transducer," *Proceedings of the 2017 IEEE International Ultrasonics Symposium (IUS)* doi: 10.1109/ULTSYM.2017.8091929.

[59] A. Qamar and M. Rais-Zadeh, "Coupled BAW/SAW Resonators Using AlN/Mo/Si and AlN/Mo/GaN Layered Structures," *IEEE Electron Device Lett.*, vol. 40, no. 2, pp. 321–324, Feb. 2019, doi: 10.1109/LED.2018.2890755.

[60] Y. Zhang, Y. Zhang, J. Zhou, Y. Xie, C. Tang, Y. Zou, A. Tovstopyat, H. Yu, C. Sun, "Dual-Mode Hybrid Quasi-SAW/BAW Resonators With High Effective Coupling Coefficient," *IEEE Trans. Ultrason. Ferroelectr. Freq. Control*, vol. 67, no. 9, pp. 1916–1921, Sep. 2020, doi: 10.1109/TUFFC.2020.2985983.

[61] K. Liu, Y. Wang, and T. Wu, "AlN Hybrid-Coupled Resonator With Phononic Crystal Reflector," in *2021 IEEE 16th International Conference on Nano/Micro Engineered and Molecular Systems (NEMS),* Apr. 2021, pp. 1517–1520. doi: 10.1109/NEMS51815.2021.9451325.

[62] G. Sai Krishna Santosh and H. B. Nemade, "Investigation of properties of surface acoustic waves generated by periodically patterned ZnO on silicon substrate," *Ultrasonics*, vol. 59, pp. 40–44, May 2015, doi: 10.1016/j.ultras.2015.01.008.

[63] S. K. Santosh Gollapudi and H. B. Nemade, "Design and Fabrication of SAW Resonators on Silicon Substrate Employing Transverse BAW in Patterned ZnO," in *2019 IEEE International Ultrasonics Symposium (IUS)*, Oct. 2019, pp. 695–698. doi: 10.1109/ULTSYM.2019.8925645.

[64] H. Xu, S. Fu, R. Su, J. Shen, F. Zeng, C. Song and F. Pan , "Enhanced Coupling Coefficient in Dual-Mode ZnO/SiC Surface Acoustic Wave Devices with Partially Etched Piezoelectric Layer," *Appl. Sci.*, vol. 11, no. 14, p. 6383, Jul. 2021, doi: 10.3390/app11146383.

[65] X. Han, F. Wang, K. Zhang, D. Kong, K. Hu, L. Qian, L. Li, W. Nie, and Z. Yang, "Effect on coupling coefficient of diamond-based surface acoustic wave devices using two layers of piezoelectric materials of different widths," *Diam. Relat. Mater.*, vol. 125, p. 109041, May 2022, doi: 10.1016/j.diamond.2022.109041.

[66] G. Lang, S. Yandrapalli, and G. Villanueva, "Study on the Performances of AlScN based SAW/BAW Hybrid Resonators : A Parametric Analysis of Acoustic Wave Resonators with Large Figure of Merit," in *2021 Joint Conference of the European Frequency and Time Forum and IEEE International Frequency Control Symposium (EFTF/IFCS)*, Jul. 2021,. doi: 10.1109/EFTF/IFCS52194.2021.9604342.

[67] S. Yandrapalli, S. K. Eroglu, J. Mateu, C. Collado, V. Plessky, and L. G. Villanueva, "Toward Band n78 Shear Bulk Acoustic Resonators Using Crystalline Y-Cut Lithium Niobate Films With Spurious Suppression," *J. Microelectromechanical Syst.*, vol. 32, no. 4, pp. 327–334, Aug. 2023, doi: 10.1109/JMEMS.2023.3282024.

[68] G. Chen and M. Rinaldi, "Aluminum Nitride Combined Overtone Resonators for the 5G High Frequency Bands," *J. Microelectromechanical Syst.*, vol. 29, no. 2, pp. 148–159, Apr. 2020, doi: 10.1109/JMEMS.2020.2975557.

[69] I. Koné, F. Domingue, A. Reinhardt, H. Jacquinot, M. Borel, M. Gorisse, G. Parat, F. Casset, D. Pellissier-Tanon, J. F. Carpentier, L. Buchaillot, B. Dubus, "Guided acoustic wave resonators using an acoustic Bragg mirror," *Appl. Phys. Lett.*, vol. 96, no. 22, p. 223504, Jun. 2010, doi: 10.1063/1.3440370.

[70] M. Clement, E. Iborra, J.Olivares, N. Rimmer, S. Giraud, S. Bila, and A. Reinhardt, "DCS Tx filters using AlN resonators with iridium electrodes," *IEEE Trans. Ultrason. Ferroelectr. Freq. Control*, vol. 57, no. 3, pp. 518–523, 2010, doi: 10.1109/TUFFC.2010.1442.

[71] G. Pillai and S.-S. Li, "Piezoelectric MEMS Resonators: A Review," *IEEE Sens. J.*, vol. 21, no. 11, pp. 12589–12605, Jun. 2021, doi: 10.1109/JSEN.2020.3039052.

[72] G. Pillai, A. A. Zope, and S.-S. Li, "A novel transducer design to enable high-performance piezoelectric MEMS resonators and oscillators," in *2018 IEEE Micro Electro Mechanical Systems (MEMS)*, Belfast: IEEE, Jan. 2018, pp. 166–169. doi: 10.1109/MEMSYS.2018.8346510.

[73] S. Mishin and Y. Oshmyansky, "Magnetron Deposition of AlN and ScAlN for Mass-production for BAW Devices and MEMS," in *2019 IEEE International Ultrasonics Symposium* pp. 891–893. doi: 10.1109/ULTSYM.2019.8925969.

[74] A. Lozzi, M. Liffredo, E. T.-T. Yen, J. Segovia-Fernandez, and L. G. Villanueva, "Evidence of Smaller 1/F Noise in AlScN-Based Oscillators Compared to AlN-Based Oscillators," *J. Microelectromechanical Syst.*, vol. 29, no. 3, pp. 306–312, 2020, doi: 10.1109/JMEMS.2020.2988354.

[75] S. Shahraini, H. Mansoorzare, A. Mahigir, and R. Abdolvand, "Thickness-Lamé Thin-Film Piezoelectric-on-Silicon Resonators," *J. Microelectromechanical Syst.*, vol. 29, no. 3, pp. 296–305, Jun. 2020, doi: 10.1109/JMEMS.2020.2972779.

[76] K. Choy, "Chemical vapour deposition of coatings," *Prog. Mater. Sci.*, vol. 48, no. 2, pp. 57–170, 2003, doi: 10.1016/S0079-6425(01)00009-3.

[77] J. R. Mileham, S. J. Pearton, C. R. Abernathy, J. D. MacKenzie, R. J. Shul, and S. P. Kilcoyne, "Wet chemical etching of AlN," *Appl. Phys. Lett.*, vol. 67, no. 8, pp. 1119–1121, Aug. 1995, doi: 10.1063/1.114980.

[78] D. Zhuang and J. H. Edgar, "Wet etching of GaN, AlN, and SiC: a review," *Mater. Sci. Eng. R Rep.*, vol. 48, no. 1, pp. 1–46, Jan. 2005, doi: 10.1016/j.mser.2004.11.002.

[79] Z. Luo, S. Shao, and T. Wu, "Characterization of AlN and AlScN film ICP etching for micro/nano fabrication," *Microelectron. Eng.*, vol. 242–243, p. 111530, Apr. 2021, doi: 10.1016/j.mee.2021.111530.

[80] S. I. Cho, H. K. Park, S. An, and S. J. Hong, "Plasma Ion Bombardment Induced Heat Flux on the Wafer Surface in Inductively Coupled Plasma Reactive Ion Etch," *Appl. Sci.*, vol. 13, no. 17, 2023, doi: 10.3390/app13179533.

[81] V. Pashchenko, S. Mertin, F. Parsapour, J. Li, P. Muralt, and S. Ballandras, "Properties of AlScN thin films for hybrid BAW/SAW resonator fabrication," in *2017 Joint Conference of the European Frequency and Time Forum and IEEE International Frequency Control Symposium (EFTF/IFC)*, Jul. 2017, pp. 565–566. doi: 10.1109/FCS.2017.8088958.

[82] B. Xie, F. Ding, H. Shang, D. Huang, Q. Zou, C. Li, and H. Gu, "Fabrication and characterization of hybrid bulk and surface acoustic wave resonators with Ag/patterned-AlN/Mo/diamond/Si layered structure," *Diam. Relat. Mater.*, vol. 134, p. 109769, Apr. 2023, doi: 10.1016/j.diamond.2023.109769.

[83] G. Lang, G. Villanueva, "Aluminum Scandium Nitride as Piezoelectric Material for SAW/BAW Hybrid Resonators with Large Figure of Merit," Advanced NEMS lab, EPFL, Lausanne, Switzerland, Master Thesis, Jan. 2021.

[84] M. Gorisse, "Réalisation de filtres RF à base de cristaux phononiques," Thèse Universite de Grenoble, 2011. [Online]. Available: https://theses.hal.science/tel-00716818

[85] M. Bousquet, P. Perreau, J. Delprato, M. Sansa, G. Enyedi, E. Soulat, G. Lima, H. Dahmani, G. Castellan, C. Eleouet, J. Guerrero, Y. Lamy, A. Reinhardt, 'Single crystal LiNbO3 and

LiTaO3 bulk acoustic wave resonator', Proceedings of the 2023 IEEE International Ultrasonics Symposium

[86] H. L. Liu, Q. Z. Zhang, X. Y. Zhao, S. L. Fu, and W. B. Wang, "High Performance Coupled BAW/SAW Resonator Using ScAlN/AlN Thin Film Hetero Acoustic Layered (HAL) Structure," in *2021 IEEE International Ultrasonics Symposium (IUS)*Sep. 2021 doi: 10.1109/IUS52206.2021.9593811.

[87] *COMSOL Multiphysics® v. 6.1. www.comsol.com. COMSOL AB, Stockholm, Sweden.*

[88] V. Plessky, "XBAR," in *2022 IEEE International Ultrasonics Symposium (IUS),* Oct. 2022. doi: 10.1109/IUS54386.2022.9957805.

[89] J. Ransley and N. Elabbasi, "Modeling MEMS Gyroscopes with COMSOL Multiphysics®," presented at the COMSOL Conference North America, 2020. Accessed: Sep. 24, 2023. [Online]. Available: https://shorturl.at/nJNPR

[90] B. Uppalapati, G. Koley, and A. Kota, "Finite Element Modeling of an AlGaN/GaN Based VOC Sensor Using COMSOL®," presented at the COMSOL Conference North America, 2020. Accessed: Sep. 24, 2023. [Online]. Available: https://shorturl.at/kBEHL

[91] S. B. McGrayne, E. E. Suckling, E. Kashy, F. Neville and H. Robinson, "Deriving electric field from potential," *Encyclopedia Britannica*. in Electricity. 2023. [Online]. https://www.britannica.com/science/electricity

[92] COMSOL multiphysics®, "COMSOL multiphysics® Reference Manual, version 5.5: Generalized Plane Strain," doc.comsol.com. Accessed: Sep. 07, 2023. [Online]. Available: https://doc.comsol.com/6.1/doc/com.comsol.help.sme/sme_ug_theory.06.015.html

[93] COMSOL multiphysics®, "COMSOL multiphysics® Reference Manual, version 5.4: Structural Mechanics Module," doc.comsol.com. Accessed: Sep. 07, 2023. [Online]. https://doc.comsol.com/5.4/doc/com.comsol.help.sme/StructuralMechanicsModuleUsersGuide.pdf

[94] COMSOL multiphysics®, "COMSOL multiphysics® Reference Manual, version 5.6: Thin-Film BAW Composite Resonator," doc.comsol.com. Accessed: Sep. 07, 2023. [Online]. https://doc.comsol.com/5.6/doc/com.comsol.help.models.mems.thin_film_baw_resonator/models.mems.thin_film_baw_resonator.pdf

[95] COMSOL multiphysics®, "COMSOL multiphysics® Reference Manual, version 5.5: Perfectly Matched Layers (PMLs)," doc.comsol.com. Accessed: Sep. 07, 2023. [Online]. https://doc.comsol.com/5.5/doc/com.comsol.help.aco/aco_ug_pressure.05.106.html

[96] Y.V. Komlenko, "Floquet theory," *Encyclopedia of Mathematics.* [Online]. Available: https://encyclopediaofmath.org/index.php?title=Floquet_theory&oldid=18199

[97] M. J. S. Lowe, "WAVE PROPAGATION | Guided Waves in Structures," in *Encyclopedia of Vibration*, S. Braun, Ed., Oxford: Elsevier, 2001, pp. 1551–1559. doi: https://doi.org/10.1006/rwvb.2001.0173.

[98] A. Khelif, A. Choujaa, S. Benchabane, B. Djafari-Rouhani, and V. Laude, "Guiding and bending of acoustic waves in highly confined phononic crystal waveguides," *Appl. Phys. Lett.*, vol. 84, no. 22, pp. 4400–4402, May 2004, doi: 10.1063/1.1757642.

[99] V. P. Plessky, S. V. Biryukov, and J. Koskela, "Harmonic admittance and dispersion equations - the theorem," in *2000 IEEE Ultrasonics Symposium. Proceedings. An International Symposium*, 2000, pp. 159–162 vol.1. doi: 10.1109/ULTSYM.2000.922530.

[100] A. Tarasenko, R. Čtvrtlík, and R. Kudělka, "Theoretical and experimental revision of surface acoustic waves on the (100) plane of silicon," *Sci. Rep.*, vol. 11, no. 1, p. 2845, Feb. 2021, doi: 10.1038/s41598-021-82211-6.

[101] A. Reinhardt, V. Laude, T. Pastureaud, and S. Ballandras, "Numerical simulation and comparison of membrane and solidly mounted FBAR's," in *2002 IEEE Ultrasonics Symposium, 2002. Proceedings.*, 2002, pp. 497–500 vol.1. doi: 10.1109/ULTSYM.2002.1193450.

[102] P. Djemia, C. Dugautier, T. Chauveau, E. Dogheche, M. I. De Barros, and L. Vandenbulcke, "Mechanical properties of diamond films: A comparative study of polycrystalline and smooth fine-grained diamonds by Brillouin light scattering," *J. Appl. Phys.*, vol. 90, no. 8, pp. 3771–3779, Oct. 2001, doi: 10.1063/1.1402667.

[103] R. J. Jiménez Riobóo; E. Rodríguez-Cañas; M. Vila; C. Prieto; F. Calle; T. Palacios; M. A. Sánchez; F. Omnès; O. Ambacher; B. Assouar; O. Elmazria., "Hypersonic characterization of sound propagation velocity in AlxGa1−xN thin films," *J. Appl. Phys.*, vol. 92, no. 11, pp. 6868–6874, Nov. 2002, doi: 10.1063/1.1517728.

[104] J. Pedrós , F. Calle , J. Grajal , R.J. Jiménez Riobóo , C. Prieto , J.L. Pau , J. Pereiro , M. Hermann , M. Eickhoff , Z. Bougrioua , "Anisotropic propagation of surface acoustic waves on nitride layers," *Superlattices Microstruct.*, vol. 36, no. 4, pp. 815–823, 2004, doi: https://doi.org/10.1016/j.spmi.2004.09.044.

[105] S. Barsoum, C. Hellion, E. Vermandé, J. M. Quemper, M. Bousquet, A. Reinhardt, T. Laroche, S. Ballandras, B. Dubus, "High Quality Factor Hybrid SAW/BAW Resonators," in *2022 Joint Conference of the European Frequency and Time Forum and IEEE International Frequency Control Symposium (EFTF/IFCS)*, 2022,. doi: 10.1109/EFTF/IFCS54560.2022.9850764.

[106] S. Barsoum, A. Schembri, M. Bernard, A. Lefevre, M. Bousquet, A. Reinhardt, T. Laroche, S. Ballandras, B. Dubus, "Impact of Transducer Aspect Ratio on the Performance of AlN Hybrid SAW/BAW Resonators," in *2023 IEEE International Ultrasonics Symposium*,

[107] A. Stapf, C. Gondek, E. Kroke, and G. Roewer, "Wafer Cleaning, Etching, and Texturization," in *Handbook of Photovoltaic Silicon*, D. Yang, Ed., 2019, pp. 311–358. doi: 10.1007/978-3-662-56472-1_17.

[108] A. C. Jones and M. L. Hitchman, *Chemical vapour deposition: precursors, processes and applications*. Cambridge, UK: Royal Society of Chemistry, 2009.

[109] K. C. Cadien and L. Nolan, "Chemical Mechanical Polishing Method and Practice," in *Handbook of Thin Film Deposition*, Elsevier, 2018, pp. 317–357. doi: 10.1016/B978-0-12-812311-9.00010-4.

[110] J. del Barrio and C. Sánchez-Somolinos, "Light to Shape the Future: From Photolithography to 4D Printing," *Adv. Opt. Mater.*, vol. 7, no. 16, p. 1900598, Aug. 2019, doi: 10.1002/adom.201900598.

[111] J. Liu, H. Weng, A. A. Afridi, J. Li, J. Dai, X. Ma, H. Long, Y. Zhang, Q. Lu, J. F. Donegan, and W. Guo, "Photolithography allows high-Q AlN microresonators for near octave-spanning frequency comb and harmonic generation," *Opt. Express*, vol. 28, no. 13, p. 19270, Jun. 2020, doi: 10.1364/OE.395013.

[112] S. J. Pearton, R. J. Shul, and F. Ren, "A Review of Dry Etching of GaN and Related Materials," *MRS Internet J. Nitride Semicond. Res.*, vol. 5, no. 1, p. 11, 2000, doi: 10.1557/S1092578300000119.

[113] Y. Waseda, E. Matsubara, and K. Shinoda, *X-Ray diffraction crystallography: introduction, examples and solved problems*. Springer, 2011.

[114] B. R. Kumar and T. S. Rao, "AFM studies on surface morphology, topography and texture of nanostructured zinc aluminum oxide thin films" *Dig. J. Nanomater. Biostructures*, vol. 7, no. 4, pp. 1881–1889, Oct. 2012.

[115] S. I. Shah, G. H. Jaffari, E. Yassitepe, and B. Ali, "Evaporation," in *Handbook of Deposition Technologies for Films and Coatings*, Elsevier, 2010, pp. 135–252. doi: 10.1016/B978-0-8155-2031-3.00004-1.

[116] H. Zhang, S. Krooswyk, and J. Ou, "Measurement and data acquisition techniques," in *High Speed Digital Design*, Elsevier, 2015, pp. 199–219. doi: 10.1016/B978-0-12-418663-7.00005-8.

[117] A. Zaidi, F. Athley, J. Medbo, U. Gustavsson, G. Durisi, and X. Chen, "Propagation & Channel Modeling," in *5G Physical Layer*, Elsevier, 2018, pp. 35–85. doi: 10.1016/B978-0-12-814578-4.00008-4.

[118] "GSG Microwave Probes," lakeshore.com. [Online]. Available: https://www.lakeshore.com/products/product-detail/cryogenic-probe-stations/gsg-microwave-probes

[119]   J. Wilde, L. Reindl, and C. Stewart, "Testing, Calibration and Compensation," in *Comprehensive Microsystems*, Elsevier, 2008, pp. 495–538. doi: 10.1016/B978-044452190-3.00026-4.

[120]   K. S. Sharma, S. Enjamuri, and K. C. James Raju, "Effect of change in piezoelectric layer thickness in high-overtone bulk acoustic resonator," in *2013 Annual International Conference on Emerging Research Areas and 2013 International Conference on Microelectronics, Communications and Renewable Energy.* doi: 10.1109/AICERA-ICMiCR.2013.6576023.

[121]   C. Zhou, W. Pang, Q. Li, H. Yu, X. Hu, and H. Zhang, "Extracting the electromechanical coupling constant of piezoelectric thin film by the high-tone bulk acoustic resonator technique," *IEEE Trans. Ultrason. Ferroelectr. Freq. Control*, vol. 59, no. 5, pp. 958–962, May 2012, doi: 10.1109/TUFFC.2012.2280.

[122] D. Petit, "Caractérisation et modélisation thermique des résonateurs BAW en vue de leur intégration dans des architectures d'oscillateurs à fréquence stable," Thèse de doctorat de l'Institut National des Sciences Appliquées de Lyon, 2010

[123]   M. Akiyama, T. Kamohara, K. Kano, A. Teshigahara, Y. Takeuchi, and N. Kawahara, "Enhancement of Piezoelectric Response in Scandium Aluminum Nitride Alloy Thin Films Prepared by Dual Reactive Cosputtering," *Adv. Mater.*, vol. 21, no. 5, pp. 593–596, Feb. 2009, doi: 10.1002/adma.200802611.

[124]   A. S. M. Z. Shifat, I. Stricklin, R. K. Chityala, A. Aryal, G. Esteves, A. Siddiqui and T. Busani., "Vertical Etching of Scandium Aluminum Nitride Thin Films Using TMAH Solution," *Nanomaterials*, vol. 13, no. 2, p. 274, Jan. 2023, doi: 10.3390/nano13020274.

[125] M. Ueda, T. Nishihara, J. Tsutsumi, S. Taniguchi, T. Yokoyama, S. Inoue, T. Miyashita, Y. Satoh, "High-Q Resonators using FBAR/SAW Technology and their Applications," in *IEEE MTT-S International Microwave Symposium Digest,* pp. 209–212, 2005. doi: 10.1109/MWSYM.2005.1516561.

[126]   W. Xu, X. Zhang, S. Choi, and J. Chae, "A High-Quality-Factor Film Bulk Acoustic Resonator in Liquid for Biosensing Applications," *J. Microelectromechanical Syst.*, vol. 20, no. 1, pp. 213–220, Feb. 2011, doi: 10.1109/JMEMS.2010.2093568.

[127]   S. Bing, K. Chawang, and J.-C. Chiao, "A Self-Tuned Method for Impedance-Matching of Planar-Loop Resonators in Conformable Wearables," *Electronics*, vol. 11, no. 17, p. 2784, Sep. 2022, doi: 10.3390/electronics11172784.

[128]   COMSOL multiphysics®, "COMSOL multiphysics® Reference Manual, version 5.5," doc.comsol.com.

[129]   A. Bartasyte, S. Margueron, T. Baron, S. Oliveri, and P. Boulet, "Toward High-Quality Epitaxial LiNbO3 and LiTaO3 Thin Films for Acoustic and Optical Applications," *Adv. Mater. Interfaces*, vol. 4, no. 8, p. 1600998, Apr. 2017, doi: 10.1002/admi.201600998.

[130] M. Bousquet, A. Joulie, C. Hellion, M. Sansa, J. Delprato, P. Perreau, G. Enyedi, G. Lima, J. Guerrero, G. Castellan, A. Tantet, S. Chevallet, T. Monniez, A. Reinhardt, "200 mm Surface and Bulk Acoustic Wave devices based on POI substrate for 5G," presented at the 2023 Joint Conference of the European Frequency and Time Forum and IEEE International Frequency Control Symposium (EFTF/IFCS)

[131] A. Reinhardt, M. Bousquet, A. Joulie, C. . -L. Hsu, F. Delaguillaumie, C. Maeder-Pachurka, G. Enyedi, P. Perreau, G. Castellan, J. Lugo., "Lithium Niobate Film Bulk Longitudinal Wave Resonator," in *2021 Joint Conference of the European Frequency and Time Forum and IEEE International Frequency Control Symposium (EFTF/IFCS)*, 2021. doi: 10.1109/EFTF/IFCS52194.2021.9604280.

[132]   I. E. Kuznetsova, B. D. Zaitsev, S. G. Joshi, and I. A. Borodina, "Investigation of acoustic waves in thin plates of lithium niobate and lithium tantalate," *IEEE Trans. Ultrason. Ferroelectr. Freq. Control*, vol. 48, no. 1, pp. 322–328, 2001, doi: 10.1109/58.896145.

[133]   A. Clairet, T. Laroche, E. Michoulier, S. N. Diaye, F. Bernard, and S. Ballandras, "Electrode Confined Acoustic Wave (ECAW) devices for Ultra High Band applications," Proceedings of the 2023 IEEE International Ultrasonics Symposium 2023.

[134] S. Huang, Y. Shuai, L. Lv, Z. Wei, W. Fan, Y. Wang, D. Zhu, X. Pan, W. Luo, C. Wu and W. Zhang, "LiNbO3 Surface Acoustic Wave Resonators with Large Effective Electromechanical Coupling," *Electronics*, vol. 12, no. 13, p. 2964, Jul. 2023, doi: 10.3390/electronics12132964.

[135] M. Pijolat, "Etude de résonateurs acoustiques à couches minces piézoélectriques monocristallines," Thèse de doctorat, l'Université de Franche-Comté, 2010.

[136] H. Xu, S. Fu, R. Su, P. Liu, S. Zhang, Z. Lu AU, B. Xiao, R. Wang, C. Song, F. Zeng, W. Wang, F. Pan, "SAW Filters on LiNbO3/SiC Heterostructure for 5G n77 and n78 Band Applications," *IEEE Trans. Ultrason. Ferroelectr. Freq. Control*, vol. 70, no. 9, pp. 1157–1169, 2023, doi: 10.1109/TUFFC.2023.3299635.

[137] P.J. Turner, B. Garcia, V. Yantchev, G. Dyer, S. Yandrapalli, L.G. Villanueva, R.B. Hammond, V. Plessky, "5 GHz Band n79 wideband microacoustic filter using thin lithium niobate membrane," *Electron. Lett.*, vol. 55, no. 17, pp. 942–944, Aug. 2019, doi: 10.1049/el.2019.1658.

[138] B. Peng, N. Hu, B. Jia, and H. Wang, "A novel N79 filter using solid-mounted A1-mode resonator for 5G applications," in *2021 IEEE International Ultrasonics Symposium (IUS)*, 2021. doi: 10.1109/IUS52206.2021.9593414.

[139] M. Solal; T. Daniel; P. Rath; J. McGann; C. Huck; S. Inoue; H. Henry; C. Hella; and D. Allen, "A 4.5 GHz surface excitation solidly mounted microacoustic resonator with 20% coupling," in *2022 IEEE International Ultrasonics Symposium (IUS)*, 2022. doi: 10.1109/IUS54386.2022.9957465.

[140] M. Solal, "A P-matrix-based model for the analysis of SAW transversely coupled resonator filters, including guided modes and a continuum of radiated waves," *IEEE Trans. Ultrason. Ferroelectr. Freq. Control*, vol. 50, no. 12, pp. 1729–1741, Dec. 2003, doi: 10.1109/TUFFC.2003.1256314.

[141] M. Mayer, S. Ammann, M. Pernpeintner, J. Johnson, T. Ebner, and K. Wagner, "Multi-Mode P-Matrix Models for the Description of Interacting Modes in TCSAWand LSAW Devices," in *2018 IEEE International Ultrasonics Symposium (IUS)*, Oct. 2018. doi: 10.1109/ULTSYM.2018.8579681.

[142] V. Plessky and J. Koskela, "COUPLING-OF-MODES ANALYSIS OF SAW DEVICES," *Int. J. High Speed Electron. Syst.*, vol. 19, no. 4, pp. 867–947, 2000.

[143] Curie, P.; Curie, J., "Bulletin de Minéralogie. 1880, 90."

[144] Curie, P.; Curie, J., "Contractions et Dilatations Produites Par Des Tensions Électriques Dans Les Cristaux Hémièdres à Face Inclinées. Compte rendus de l'Académie des Sciences 1881, XCIII, 1137."

[145] S. O. Kasap, *Principles of electronic materials and devices*, 3rd ed. Boston: McGraw-Hill, 2006.

[146] K. Lefki and G. J. M. Dormans, "Measurement of piezoelectric coefficients of ferroelectric thin films," *J. Appl. Phys.*, vol. 76, no. 3, pp. 1764–1767, Aug. 1994, doi: 10.1063/1.357693.

[147] P. Muralt, A. Kholkin, M. Kohli, and T. Maeder, "Piezoelectric actuation of PZT thin-film diaphragms at static and resonant conditions," *Sens. Actuators Phys.*, vol. 53, no. 1–3, pp. 398–404, May 1996, doi: 10.1016/0924-4247(96)01139-9.

[148] D. J. Bryzek, "Roadmap to a $ Trillion MEMS Market," https://api.semanticscholar.org/CorpusID:19422852

[149] S.-S. Li, "CMOS-MEMS resonators and their applications," in *2013 Joint European Frequency and Time Forum & International Frequency Control Symposium (EFTF/IFC)*, 2013, pp. 915–921. doi: 10.1109/EFTF-IFC.2013.6702098.

[150] S. Tanifuji, Y. Aota, S. Kameda, T. Takagi, and K. Tsubouchi, "Discussion of millimeter wave FBAR with very thin AlN film fabricated using MOCVD method," in *2009 IEEE International Ultrasonics Symposium*, Sep. 2009, pp. 2170–2173. doi: 10.1109/ULTSYM.2009.5441657.

[151] J. B. Shealy, R. Vetury, S. R. Gibb, M. D. Hodge, P. Patel, M. A. McLain, A. Y. Feldman, M. D. Boomgarden, M. P. Lewis, B. Hosse, R. Holden, "Low loss, 3.7GHz wideband BAW

filters, using high power single crystal AlN-on-SiC resonators," in *2017 IEEE MTT-S International Microwave Symposium (IMS)* Jun. 2017, pp. 1476–1479. doi: 10.1109/MWSYM.2017.8058901.

[152] R. Ding, W. Xuan, Shurong Dong, B. Zhang, F. Gao, G. Liu, Z. Zhang, H. Jin and J. Luo, "The 3.4 GHz BAW RF Filter Based on Single Crystal AlN Resonator for 5G Application," *Nanomaterials*, vol. 12, no. 17, p. 3082, Sep. 2022, doi: 10.3390/nano12173082.

[153] Y. Zhu, N. Wang, G. Chua, C. Sun, N. Singh, and Y. Gu, "ScAlN-Based LCAT Mode Resonators Above 2 GHz With High FOM and Reduced Fabrication Complexity," *IEEE Electron Device Lett.*, vol. 38, no. 10, pp. 1481–1484, Oct. 2017, doi: 10.1109/LED.2017.2747089.

[154] M. A. Caro, S. Zhang, M. Ylilammi, T. Riekkinen, M. A. Moram, O. Lopez-Acevedo, J. Molarius and T. Laurila., "Erratum: Piezoelectric coefficients and spontaneous polarization of ScAlN (2015 *J. Phys. Condens. Matter* 27 245901)," *J. Phys. Condens. Matter*, vol. 27, no. 27, p. 279602, Jul. 2015, doi: 10.1088/0953-8984/27/27/279602.

[155] G. Wingqvist, F. Tasnádi, A. Zukauskaite, J. Birch, H. Arwin, and L. Hultman, "Increased electromechanical coupling in w−ScxAl1−xN," *Appl. Phys. Lett.*, vol. 97, no. 11, p. 112902, Sep. 2010, doi: 10.1063/1.3489939.

[156] R. Aigner, G. Fattinger, M. Schaefer, K. Karnati, R. Rothemund, and F. Dumont, "BAW Filters for 5G Bands," in *2018 IEEE International Electron Devices Meeting (IEDM)*, Dec. 2018, pp. 14.5(1-4). doi: 10.1109/IEDM.2018.8614564.

[157] M. Moreira, J. Bjurström, I. Katardjev, and V. Yantchev, "Aluminum scandium nitride thin-film bulk acoustic resonators for wide band applications," *Vacuum*, vol. 86, no. 1, pp. 23–26, Jul. 2011, doi: 10.1016/j.vacuum.2011.03.026.

[158] T. Yanagitani and M. Suzuki, "Electromechanical coupling and gigahertz elastic properties of ScAlN films near phase boundary," *Appl. Phys. Lett.*, vol. 105, no. 12, p. 122907, Sep. 2014, doi: 10.1063/1.4896262.

[159] M. Schneider, M. DeMiguel-Ramos, A. J. Flewitt, E. Iborra, and U. Schmid, "Scandium Aluminium Nitride-Based Film Bulk Acoustic Resonators," in *Proceedings of Eurosensors 2017, 2017*, MDPI, Aug. 2017, p. 305. doi: 10.3390/proceedings1040305.

[160] H. Bhugra, *Piezoelectric mems resonators*. New York, NY: Springer Science Business Media, 2016.

[161] A. Arora, A. Arora, V. K. Dwivedi, P. J. George, K. Sreenivas, and V. Gupta, "Zinc oxide thin film-based MEMS acoustic sensor with tunnel for pressure compensation," *Sens. Actuators Phys.*, vol. 141, no. 2, pp. 256–261, 2008, doi: https://doi.org/10.1016/j.sna.2007.09.016.

[162] H. Pandya, S. Chandra, and A. Vyas, "A Novel Sensor for VOCs Using Nanostructured ZnO and MEMS Technologies," *Sens. Transducers*, vol. 14, pp. 244–252, Mar. 2012.

[163] Y. Yuan , K. S. Chow , H. Du, P. Wang , M. Zhang , S. Yu & B. Liu, "A ZnO thin-film driven microcantilever for nanoscale actuation and sensing," *Int. J. Smart Nano Mater.*, vol. 4, no. 2, pp. 128–141, Jun. 2013, doi: 10.1080/19475411.2012.749959.

[164] O. Mortada, A. H. Zahr, J.-C. Orlianges, A. Crunteanu, M. Chatras, and P. Blondy, "Analysis and optimization of acoustic wave micro-resonators integrating piezoelectric zinc oxide layers," *J. Appl. Phys.*, vol. 121, no. 7, p. 74504, Feb. 2017, doi: 10.1063/1.4976063.

[165] A. Zaman, A. Alsolami, I. F. Rivera, and J. Wang, "Thin-Piezo on Single-Crystal Silicon Reactive Etched RF MEMS Resonators," *IEEE Access*, vol. 8, pp. 139266–139273, 2020, doi: 10.1109/ACCESS.2020.3012520.

[166] O. Mortada, P. Blondy, J.-C. Orlianges, M. Chatras, and A. Crunteanu, "Quality factor optimization of composite piezoelectric single-crystal silicon MEMS resonators," in *2015 IEEE MTT-S International Microwave Symposium*, May 2015. doi: 10.1109/MWSYM.2015.7166968.

[167] P. Muralt, "AlN Thin Film Processing and Basic Properties," in *Piezoelectric MEMS Resonators*, H. Bhugra and G. Piazza, Eds., in Microsystems and Nanosystems. , Cham: Springer International Publishing, 2017, pp. 3–37. doi: 10.1007/978-3-319-28688-4_1.

[168]   C.-Y. Chung, Y.-C. Chen, Y.-C. Chen, K.-S. Kao, and Y.-C. Chang, "Fabrication of a 3.5-GHz Solidly Mounted Resonator by Using an AlScN Piezoelectric Thin Film," *Coatings*, vol. 11, no. 10, p. 1151, Sep. 2021, doi: 10.3390/coatings11101151.

[169]   S. Yandrapalli, V. Plessky, J. Koskela, V. Yantchev, P. Turner, and L. G. Villanueva, "Analysis of XBAR resonance and higher order spurious modes," in *2019 IEEE International Ultrasonics Symposium (IUS)*, Oct. 2019, pp. 185–188. doi: 10.1109/ULTSYM.2019.8925993.

[170]   N. Setter; D. Damjanovic; L. Eng; G. Fox; S. Gevorgian; S. Hong; A. Kingon; H. Kohlstedt; N. Y. Park; G. B. Stephenson; I. Stolitchnov; A. K. Taganstev; D. V. Taylor; T. Yamada; S. Streiffer, "Ferroelectric thin films: Review of materials, properties, and applications," *J. Appl. Phys.*, vol. 100, no. 5, p. 51606, Sep. 2006, doi: 10.1063/1.2336999.

[171]   G. H. Haertling, "Ferroelectric Ceramics: History and Technology," *J. Am. Ceram. Soc.*, vol. 82, no. 4, pp. 797–818, Apr. 1999, doi: 10.1111/j.1151-2916.1999.tb01840.x.

[172]   Y. Masuda and A. Baba, "D.C Bias and Frequency Dependence of the Dielectric Constant PZT Family ferroelectric Ceramics," *Jpn. J. Appl. Phys.*, vol. 24, no. S3, p. 113, Jan. 1985, doi: 10.7567/JJAPS.24S3.113.

[173] S. S. Bedair, J. S. Pulskamp, R. G. Polcawich, D. Judy, A. Gillon, S. Bhave, B. Morgan, "Low loss micromachined lead zirconate titanate, contour mode resonator with 50 (Ohm) termination," in *2012 IEEE 25th International Conference on Micro Electro Mechanical Systems (MEMS)*, Jan. 2012, pp. 708–712. doi: 10.1109/MEMSYS.2012.6170285.

[174]   M.Szalewski, "Relations Between Losses In Piezoelectric Ceramic And The Magnitude Of Its Vibration Level ," *Arch. Acoust.*, vol. 25, no. 2, pp. 235–249, 2000.

[175] X. Zhao, O. Kaya, M. Pirro, M. Assylbekova, L. Colombo, P. Simeoni, C. Cassella, "A 5.3 GHz Al$_{0.76}$Sc$_{0.24}$N Two-Dimensional Resonant Rods Resonator With a k$_t^2$ of 23.9%," *J. Microelectromechanical Syst.*, vol. 31, no. 4, pp. 561–570, Aug. 2022, doi: 10.1109/JMEMS.2022.3178978.

[176]   G. Tobolka, "Mixed Matrix Representation of SAW Transducers," *IEEE Trans. Sonics Ultrason.*, vol. 26, no. 6, pp. 426–427, 1979, doi: 10.1109/T-SU.1979.31128.

[177]   D. P. Morgan, Surface acoustic wave filters: with applications to electronic communications and signal processing, 2nd ed. Academic Press, 2007.

[178]   P. Warder and A. Link, "Golden Age for Filter Design: Innovative and Proven Approaches for Acoustic Filter, Duplexer, and Multiplexer Design," IEEE Microw. Mag., vol. 16, no. 7, pp. 60–72, Aug. 2015, doi: 10.1109/MMM.2015.2431236

[179]   S. Ballandras, and T. Laroche, " Dispositif d'onde acoustique de surface sur substrat composite", FR3079668B1, March 29th, 2018, Current Patent Assigne: Soitec SA.

Appendices

Appendix A   Piezoelectricity

Piezoelectricity describes the ability of some materials to generate an electric charge in response to mechanical stress or pressure applied to them. This unique property arises due to the asymmetry of the crystal lattice structure in these materials, which results in the displacement of positive and negative charges within the lattice when subjected to mechanical deformation. This effect was first observed by Pierre and Jacques Curie in 1880 when they discovered that applying mechanical pressure to crystals like quartz and tourmaline generated an electric potential across the material [143], [144].

Piezoelectricity manifests through two reciprocal effects: direct and converse. Direct piezoelectricity refers to the generation of an electric polarization when mechanical stress is applied to the material as in Figure 187(b). In this case, the mechanical deformation causes a shift in the equilibrium positions of the charged atoms in the crystal lattice, leading to the separation of charges and the appearance of electric dipoles, which result in charges accumulating at the surface of the crystal. On the other hand, inverse piezoelectricity refers to the phenomenon where the application of an external electric field induces mechanical deformation in the material as in Figure 187(c, d). In this case, the electric field causes the charged atoms to move away from their equilibrium position, resulting in a change in the shape or dimensions of the material [145].
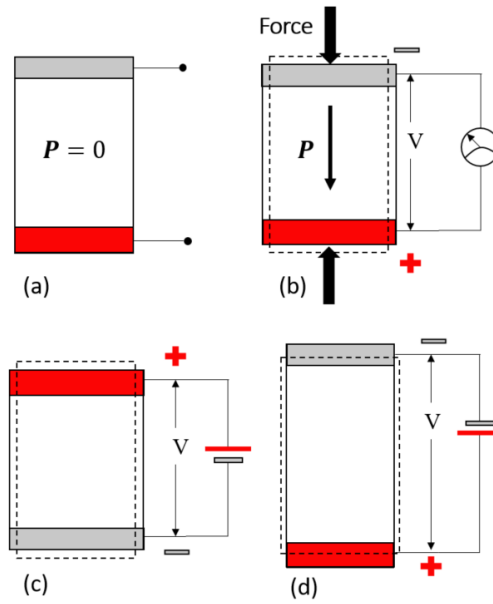
Figure 187: piezoelectricity. A crystal at rest (a), an applied force induces polarization and generated charge (b) and an applied field causes the crystal to become strained (c and d)

The mathematical representation of piezoelectricity involves the use of constitutive equations that relate mechanical stress and electric field to the corresponding strains and electric displacement in the material. These equations depend on the crystal symmetry and the type of piezoelectric material being considered. The piezoelectric effect is commonly described using the piezoelectric tensor, which captures the linear relationship between the mechanical and electrical quantities.

There are two groups of piezoelectric equations, written in tensor form, describing the coupled set of mechanical-electrical equations. Assuming linear piezoelectricity, the "ANSI/IEEE Standard on Piezoelectricity" [10] describes the constitutive equations (using Einstein's convention for implicit summation of repeated indices) in one of four alternative forms listed below. The physical meaning of these quantities and their units is listed in Table 15.

$$
\begin{aligned}
T_i &= c_{ij}^E S_j - e_{ki} E_k & S_i &= s_{ij}^E T_j + d_{ki} E_k \\
D_k &= e_{ki} S_i + \varepsilon_{lk}^S E_k & D_k &= d_{ki} T_i + \varepsilon_{lk}^T E_k \\[1em]
S_i &= s_{ij}^D T_j + g_{ki} D_k & T_i &= c_{ij}^D S_j - h_{ki} D_k \qquad (27) \\
E_k &= -g_{ki} T_i + \beta_{lk}^T D_k & E_k &= -h_{ki} S_i + \beta_{lk}^S D_k \\
k,l &= 1 \rightarrow 3 \\
i,j &= 1 \rightarrow 6
\end{aligned}
$$

The first group of equations relates the stress (T) and strain (S) using the stiffness (c) or compliance (s) defined by Hooke's law and then adds the electric contribution using the piezoelectric tensor to translate the mechanical effect of applying an electric field (E) or of inducing an electric displacement (D). The second group of equations relates conversely the electric field (E) and the electric displacement (D) via the electric permittivity (ε) or electric impermeability (β) and then adds an electrical contribution resulting from the application of a stress (T) or a strain (S) to the material. The piezoelectric constants are related to each other in the following way.

$$d_{mi} = \varepsilon_{mn}^T g_{ni} = e_{mj} c_{ji}^E \qquad\qquad g_{mi} = \beta_{mn}^T d_{ni} = h_{mj} s_{ji}^D$$

$$e_{mi} = \varepsilon_{mn}^T h_{ni} = d_{mj} c_{ji}^E \qquad\qquad h_{mi} = \beta_{mn}^T e_{ni} = g_{mj} s_{ji}^D$$

$$m, n = 1 \rightarrow 3$$

$$i, j = 1 \rightarrow 6 \tag{28}$$

Table 15: quantities and coefficients used to describe piezoelectricity. **Superscripts signify a constant quantity (e.g c_{ij}^E is the elastic stiffness matrix at a constant electric field E)**

Physical parameter	Symbol	Unit	Dimensionality
Electric displacement	D	$C.m^{-2}$	3x1
Electric field	E	$V.m^{-1}$	3x1
Stress	T	$N.m^{-2}$	6x1
Mechanical strain	S	/	6x1
Dielectric permittivity	ε	$F.m^{-1}$	3x3
Dielectric impermeability	β	$m.F^{-1}$	3x3
Elastic stiffness	c	$N.m^{-2}$	6x6
Elastic compliance	s	$m^2.N^{-1}$	6x6
Piezoelectric strain constant	d	$m.V^{-1}$	3x6
Piezoelectric stress constant	e	$C.m^{-2}$	3x6
Piezoelectric stress constant	h	$V.m^{-1}$	3x6
Piezoelectric strain constant	g	$m^2.C^{-1}$	3x6

When a piezoelectric material is in thin film form, it is typically deposited on a substrate, which can impose strains on the thin film. These strains can modify the crystal structure and alter the piezoelectric constants, leading to different effective piezoelectric properties compared to the bulk material [146], [147, pp. 398–404].

The effective piezoelectric coefficient is a term used to describe the effective or apparent piezoelectric constant in thin films, which takes into account the substrate-induced strain effects. It is used to characterize the piezoelectric response of the thin film, accounting for both the intrinsic piezoelectric constants of the material and the strain-induced modifications due to the substrate. In this thesis, it is assumed that the effective piezoelectric constants are used whenever these coefficients are mentioned

Piezoelectric materials

Multiple piezoelectric materials are available for the manufacturing of piezoelectric resonators including AlN, AlScN, ZnO, LiNbO$_3$, LiTaO$_3$, and PZT.

AlN has a wurtzite crystalline structure and several desirable properties, such as high phase velocity (~10,000 m/s), high stiffness coefficients (340-400 GPa), and relatively low dielectric constant (ε_{33} = 95 pF/m) [148], [149]. AlN exhibits piezoelectric properties up to 1150°C which is high compared to other conventional piezoelectric materials like ZnO and BaTiO$_3$ that are limited to temperatures of 400-450°K. These temperatures make those material unsuitable for harsh environment applications despite their high coupling coefficients. AlN exhibits coupling factors up to 7% and quality factors up to 2000 and is fairly well established in terms of manufacturability [150]–[152].

Scandium-doped AlN (AlScN) is a newly emerging material that has been widely studied in bulk acoustic wave resonators because of its high k_t^2 [153] Its piezoelectric coefficients d_{33} and d_{11} are improved greatly when the Sc-doping ratio increases and reaches a maximum at 43% [123], [154], [155]. On the other hand, Sc doping can be detrimental to the quality factor [156]. Typical resonators using $Sc_{0.12}Al_{0.88}N$ have coupling factors of 14% and quality factors up to 650 [4], [157]–[159].

Wurtzite Zinc Oxide (ZnO) is a piezoelectric material with the highest piezoelectric coefficients in comparison with the other tetrahedral coordinated materials [160], making it a suitable option for sensors and actuators [161]–[163]. ZnO has a higher electromechanical coupling factor k^2 than AlN, but a lower longitudinal acoustic wave velocity. Pure ZnO-based resonators suffer from low quality factor. This is overcome by using low defect materials such as silicon as the main device layer [164]–[166]. ZnO is not most suited for high-frequency applications due to its acoustical leakage problems at high frequencies, yet it has been widely used in various applications [160]. ZnO resonators have k^2 of 9% and quality factors of 1770 [34], [167] which is much lower than AlN. Both AlN and ZnO are excellent piezoelectric materials but the current trend shows AlN attracting more attention than ZnO [168].

The crystal lattice of $LiNO_3$ consists of corner-sharing octahedra formed by the niobium and oxygen atoms, creating a framework of oxygen ions. Within this structure, lithium ions occupy octahedral sites, surrounded by six oxygen ions, giving rise to a non-centrosymmetric arrangement. The asymmetric arrangement of ions leads to the manifestation of piezoelectric and pyroelectric effects, making lithium niobate an excellent material for various electro-optic, acousto-optic, and photonic applications [39], [41]–[44]. There are reports of resonators with LNO or LTO reaching coupling factors of 20% with quality factors up to 1000 but are not commercialized [40], [169].

Another potential piezoelectric material used in MEMS is Lead Zirconate Titanate (PZT). PZT is a ferroelectric material whose properties vary with orientation, grain size, and material defects [170]–[172]. The large dielectric coefficients of PZT enable the design of resonators and filters with low termination impedances, which minimizes impedance mismatch loss in the system [173]. However, at high frequencies (> 500 MHz), PZT exhibits high electrical and mechanical losses [174], and its low acoustic velocity and large dielectric constant pose design challenges [71]. PZT resonators have coupling factors of 9.6% and quality factors 237 [34], [167].

Appendix B   HSBR Literature attempts beyond January 2021

1. Novel theoretical investigations

Liu *et al.* [86] also considered AlScN. They optimized the thickness of a SiO$_2$ layer inserted between the Si substrate, as shown in Figure 188, and the bottom electrode, and considered several electrode materials, differing by their acoustic impedance layers. They indicate that high acoustic impedance electrodes such as Mo, Pt or W contribute to improving the effective electromechanical coupling factor, by contributing to the wave confinement in the transducers. When the thicknesses of top and bottom electrodes correspond to h$_e$/λ =0.04 and the silicon dioxide layer is set to h$_{SiO2}$/λ=0.3, respectively, the pseudo-BAW mode is considerably slowed down to 5100 m/s, i.e. below the velocity of the bulk shear wave mode in the silicon substrate (5680 m/s).

This structure provides in theory a remarkable theoretical coupling factor of 21% with quality factors reaching 3458 at a resonance frequency of 4.83 GHz, an 1348 at anti-resonance frequency of 5.32 GHz. It is to be noted that to reach such high frequencies, the periodicity of the transducers should be only about 500 nm, which is extremely challenging.
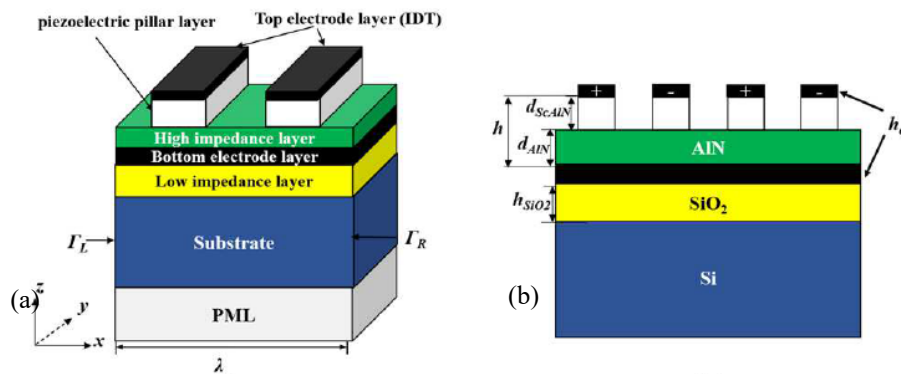
Figure 188: schematic view of the coupled SAW/BAW resonator proposed by Liu *et al.* in 3D (a) and cross section material and electrical details (b) [86].

Further theoretical analysis were mentioned briefly by Plessky in his 2022 XBAR review [88] and were discussed in details in [67], they included further simulations of the YBAR (Figure 189). The simulated response had a resonance to anti-resonance ratio of 16% which translates into k^2 of 39%.
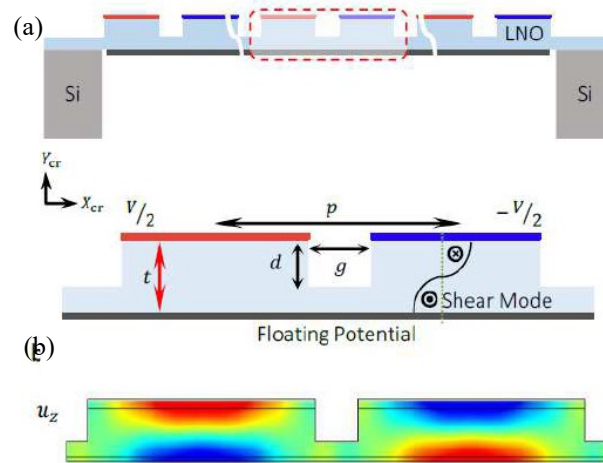
Figure 189: periodic system of shear wave resonators, Y-cut, 400nm LN membrane, with etched 250 nm deep tranches (a), FEM simulation of displacements (perpendicular to the page) (b).

The 2DRR prototype achieves k²$_t$ of 23.9% (Figure 190). This result was obtained by optimizing the acoustic engineering of the 2DRR's unit-cell to maximize the piezo-generated mechanical energy within each rod and minimize the transduction of spurious modes around resonance.

2. Novel experimental realizations
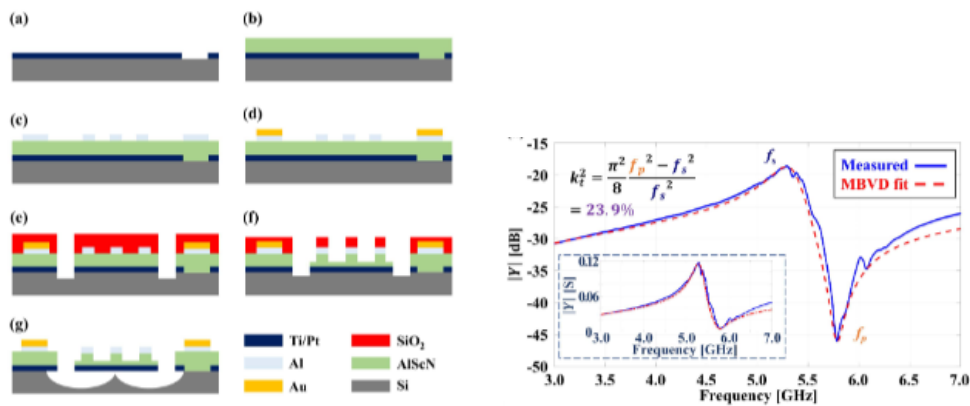
Figure 190: Fabrication process flow (left) and electric response (right) by Zhao *et al.* [175]

Using AlN, a hard mask technique was used by Zhao *et al.* [175] to fabricate a 2DRR on a low resistivity silicon wafer by using the process flow described in Figure 190. The fabrication flow consists of the following steps: (a) Deposition of Ti/Pt and patterning through ICP RIE. (b) Reactive co-sputtering of Al and Sc in a N_2 atmosphere, to form an $Sc_{0.24}Al_{0.76}N$ film. (c) Sputtering and patterning of Al to form the top electrodes. (d) Deposition of a layer of Au to cover the contact pads and routing. (e) Creation of release pits on the 2DRR's sides by deposition and patterning of a 2 μm-thick PECVD SiO2 hard mask and dry etching. (f) Second patterning of the SiO_2 layer for AlScN partial-etch required to form the rods. (g) Removal of the remaining SiO_2 by fluorine-based ICP-RIE and release of the device through a XeF_2 isotropic etch.

While not directly hybrid SAW/BAW devices, the YBAR structures based on LNO bear some similarities to hybrid SAW/BAW devices. Yandrapalli *et al.* [67] presented a process flow for their implementation, reproduced in Figure 191. The process starts by evaporating a Cr (5 nm)/Al (100 nm) layer on an LNOI wafer. Subsequently, the top electrodes and the $LiNbO_3$ layer are

patterned by e-beam lithography and ion beam etching. Argon ions from an ICP source are employed to physically etch the substrate. Following this, the chip's surface is first cleaned and then a protective covering and structural support in the form of a photoresist layer with a thickness of 5 μm is applied. To enable the backside etching stage, the chip is securely attached to a wafer utilizing a hot melt adhesive. Subsequently, a backside photolithography is carried out by coating a 5-μm-thick photoresist layer, followed by direct laser inscription on the chip to define the backside release. Cavities are then etched using a Bosch process to achieve vertical sidewalls for these cavities. The creation of the bottom metal plate, serving as the bottom electrode, involves the evaporation of Cr/Al (5nm/25nm). Finally, the structural support provided by the photoresist is removed, thereby completing the release of the resonators.
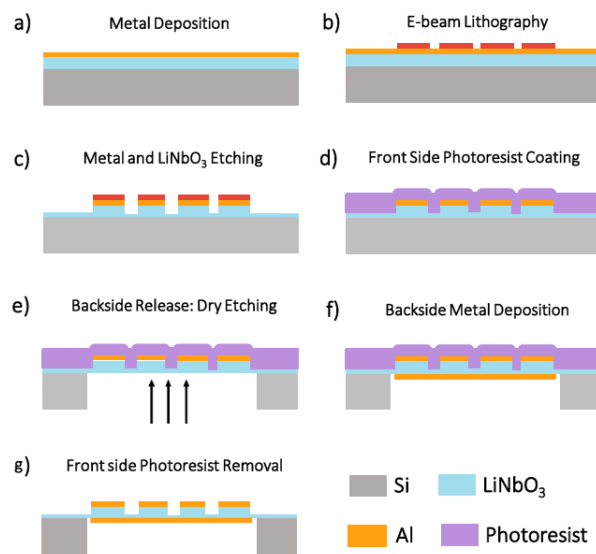
Figure 191: Process flow for YBAR [67] (a) Cr/Al evaporation (b) E-beam lithography with ZEP 520A (c) Ion beam etching of the metal and LiNbO$_3$ (partially) (d) Photoresist coating as a surface protection layer (e) Silicon DRIE (f) Cr/Al evaporation for bottom electrode (g) Removal of front side photoresist layer by remover 1165.

Their experimental response is shown in Figure 192. It exhibits Q factors of 110 and 230 at resonance and anti-resonance respectively, and a resonance to anti-resonance ratio of 16.3% which translates to k²=40.2%
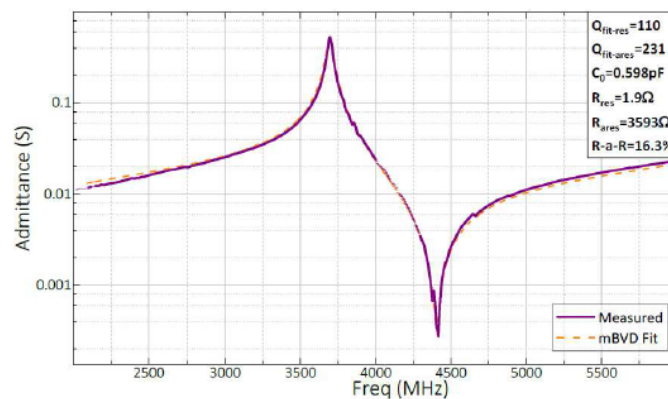
Figure 192: Electric response of an YBAR based on LiNbO$_3$ [88].

Appendix C   Modeling finite size hybrid SAW/BAW devices

The periodic model considered in chapter 2 is suitable to analyze the propagation characteristics of the hybrid SAW/BAW modes in an infinite array of transducers. Actual devices are however only composed of a finite number of transducers, what needs to consider more precisely the influence of the ends of the array of transducers, their respective interactions, and their electrical connections. This could be modelled by a finite element model taking into account several tens of transducers. However, that would lead to models with a large number of degrees of freedom. This situation is in practice the same as the one encountered with SAW devices, which are composed of several tens or hundreds of individual electrodes located atop a semi-infinite substrate. To ease the design of SAW devices, simplified one dimensional models such as the Coupling of Modes (COM) [142] or the P-matrix [176] models have been proposed. They rely on a one-dimensional analysis of the propagation of acoustic waves whose characteristics are simply described by a few parameters which encompass the very nature of these waves or their propagation medium. Here we focus on the P-matrix model.

1. General Description of the P-Matrix

While extensive derivations can be found in [177], a summarized version of the formulation is presented here. Adaptations to the case of hybrid SAW/BAW resonators will be described in the next section.

Admittance of an acoustic device

In linear circuit theory, the admittance of an n-port device relates to the current following through each conductor to the voltage applied to each electrode through

$$I = Y V \tag{29}$$

where I is the vector of the currents flowing through each conductor and V the vector of the voltages applied to each conductor, relative to an arbitrary reference voltage.

When conductors are employed to stimulate electromechanical waves within a piezoelectric medium, the admittance can be interpreted as the combination of two distinct components: a purely electrostatic contribution and an acoustic contribution:

$$Y = Y_C + Y_A \tag{30}$$

The electrostatic contribution writes usually $Y_C = j\,C\,\omega$, where C is the matrix of the mutual capacitances between conductors. The P-Matrix is used to compute the acoustic component.

The definition of the p-matrix

The P-matrix describes the scattering of acoustic waves by an arbitrary structure and its interaction with electric ports. Figure 193 shows a schematic of the possible interactions.
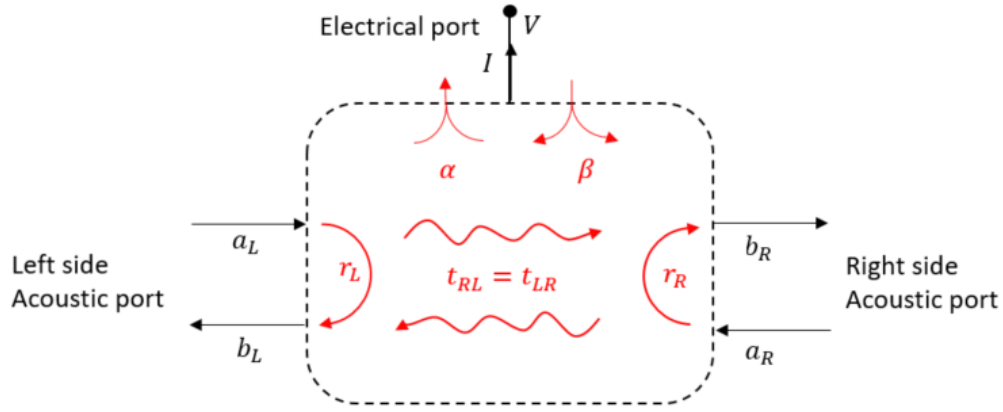
Figure 193: Electrical and acoustic components of the p-matrix

The electric signal is represented by current and voltage vectors. An acoustic wave travelling in opposite directions has a right side and left side incident wave amplitude noted a_R and a_L respectively. These incident waves can be either reflected and their reflections accounted for by reflection coefficient r_{LL} and r_{RR} or transmitted through the structure, with a transmission accounted for by the transmission coefficients t_{LR} and t_{RL}. The piezoelectric transduction is represented by vectors α and β which respectively describe mechano-electric and electro-mechanical transduction occurring in the structure. The resulting outgoing waves on both the right and left side are represented by the amplitudes b_L and b_R.

The p-matrix representing this cell would write as follows

$$\begin{pmatrix} b \\ I \end{pmatrix} = \begin{pmatrix} S & \alpha^t \\ \beta & Y_A \end{pmatrix} \begin{pmatrix} a \\ V \end{pmatrix} \tag{31}$$

where S stands for the acoustic scattering matrix, α^t the electro-acoustic transduction vector, β the acousto-electric transduction vector and Y_A the acoustic contribution to the admittance matrix. This can be expanded using the scattering parameters as follows

$$\begin{pmatrix} b_L \\ b_R \\ I \end{pmatrix} = \begin{pmatrix} r_L & t_{RL} & \alpha_L^t \\ t_{LR} & r_R & \alpha_R^t \\ \beta_L & \beta_R & Y_A \end{pmatrix} \begin{pmatrix} a_L \\ a_R \\ V \end{pmatrix} \tag{32}$$

Accordingly the P-matrix is fully represented by $(n + 2)^2$ components, where n is the number of electrical ports considered.

Assumptions and validity

We assume that the behavior of a transducer is independent of its environment and the behavior of the entire structure may be reconstructed from the behavior of each individual transducers. The admittance in the P-matrix directly represents the acoustic contribution to the overall admittance.

The P-matrix described by (18) is valid for single-mode structures. For multi-mode structures, the P-matrix becomes more complex, requiring several acoustic ports to account for each elastic mode [140], [141]. However, quantifying the couplings between these modes remains a challenge.

Since the pseudo-SAW and the pseudo-BAW modes are well separated in frequency, we can consider a different model for each of them.

Internal relationships

The reciprocal nature of piezoelectricity implies that when we apply to an electrode the same voltage as the one that would be generated in this same electrode when a wave reaches this electrode, it will excite a wave with the same amplitude as the originally incident wave. Reciprocity also dictates that a wave traveling in the backward direction will have the same effect as a wave traveling in the forward direction. These conditions are satisfied if:

$$\begin{cases} t_{LR} = t_{RL} = t \\ \beta_L = -\alpha_L \\ \beta_R = -\alpha_R \\ Y = Y^t \end{cases} \tag{33}$$

From these conditions, the P-matrix of a reciprocal structure writes

$$\begin{pmatrix} b_L \\ b_R \\ I \end{pmatrix} = \begin{pmatrix} r_L & t & \boldsymbol{\alpha_L^t} \\ t & r_R & \boldsymbol{\alpha_R^t} \\ -\boldsymbol{\alpha_L} & -\boldsymbol{\alpha_R} & \boldsymbol{Y} \end{pmatrix} \begin{pmatrix} a_L \\ a_R \\ V \end{pmatrix} \tag{34}$$

In the case of lossless structures, the power supplied by one branch must be balanced by the power exiting the structure through the other branches. One can demonstrate that the consequence is that three independent parameters can be used to describe the scattering components

$$t = \cos \Delta \, e^{-j\psi}$$
$$r_L = -j \sin \Delta \, e^{-j \, (\psi + \psi_r)} \tag{35}$$
$$r_R = -j \sin \Delta \, e^{-j \, (\psi - \psi_r)}$$

Furthermore, the purely electrical and acousto-electric terms can be represented mathematically by utilizing a set of three initially independent vectors.

$$\boldsymbol{\alpha_L} = \left(j \sqrt{\boldsymbol{G_s}} \, e^{-j\frac{\Delta}{2}} + j \sqrt{\boldsymbol{G_a}} \, e^{-j\frac{\Delta}{2}} \right) e^{-j\frac{(\psi + \psi_r)}{2}}$$
$$\boldsymbol{\alpha_R} = \left(j \sqrt{\boldsymbol{G_s}} \, e^{-j\frac{\Delta}{2}} - j \sqrt{\boldsymbol{G_a}} \, e^{-j\frac{\Delta}{2}} \right) e^{-j\frac{(\psi - \psi_r)}{2}} \tag{36}$$
$$G_{A,ij} = Re(Y_{ij}) = \sqrt{G_{s_i} G_{s_j}} + \sqrt{G_{a_i} G_{a_j}}$$

The energy conservation and forces to write components of the P-matrix as a function of only six independent real parameters, each of which holds a physical interpretation:

1- $sin\ \Delta$: represents the modulus of the reflection coefficient for waves interacting with the considered structure. It characterizes the extent to which waves are reflected by the structure, ranging from complete reflection ($sin\ \Delta = 1$) to complete transmission ($sin\ \Delta = 0$).
2- ψ: is phase shift experienced by the wave when it propagates through the structure.

$$\psi = \frac{\omega l}{V} \left(1 - j \frac{\alpha \log 10}{40 \, \pi} \right) \tag{37}$$

where ω is the angular frequency, l the length of the structure considered, V the wave velocity and α its attenuation (in dB/λ).

3- ψ_r: It represents the phase shift between the centers of transduction and reflection.

4- α_L and α_R: denote the electro-acoustic couplings. They quantify the conversion of acoustic waves to electric signals and vice versa. α_L and α_R describe the acoustic/electric and electric/acoustic conversion towards the left and the right directions respectively.

5- G_s and G_a: These vectors represent the radiation conductance from the viewpoint of the electrical ports. They quantify how much electrical energy is lost through the excitation of acoustic waves. These two radiation conductances can be expressed by relating them through a unique radiation conductance vector **G** and a parameter called directivity δ:

$$\begin{aligned} \boldsymbol{G_s} &= \boldsymbol{G}\cos(\delta)^2 \\ \boldsymbol{G_a} &= \boldsymbol{G}\sin(\delta)^2 \end{aligned} \tag{38}$$

Eventually, we can formulate an expression for the susceptance (**B**)

$$\boldsymbol{B_A} = \frac{(\boldsymbol{G_s}+\boldsymbol{G_a})\sin\psi - (\boldsymbol{G_s}-\boldsymbol{G_a})\sin\Delta}{\cos\Delta - \cos\psi} \tag{39}$$

This permits us to calculate the acoustic admittance $\boldsymbol{Y_A} = \boldsymbol{G_A} + \boldsymbol{B_A}j$

At a given frequency, an elementary P-matrix can thus be built for the following geometrical and wave parameters:

1- l: length of the structure
2- C_o: Static capacitance
3- V: wave velocity
4- α: attenuation
5- Δ: arcsin of the magnitude of the reflection coefficient
6- G: radiation conductance
7- δ: directivity
8- ψ_r: offset between reflection and transduction centers

Cascading P-matrices

In practice, these parameters are usually considered for the simplest structure: usually a single electrode for a SAW device. In our case, we assume these parameters are determined for a single transducer. The behavior of the whole structure is then reconstructed by assembling each unit P-matrix into a global matrix. This is achieved by considering the following two cascading conditions:

1- The wave escaping the left structure ("L") from the right is the wave entering the right section ("R") from the left:

$$a_{L,R} = b_{R,L} \tag{40}$$

2- The wave escaping the right structure from the left is the wave entering the left section from the right:

$$a_{R,L} = b_{L,R} \tag{41}$$

Mathematically, if we consider two P-matrix representing a "left" structure and a "right" one:

$$P_L = \begin{pmatrix} r_{LL} & t_L & \alpha_{LL}^t \\ t_L & r_{RL} & \alpha_{RL}^t \\ -\alpha_{LL} & -\alpha_{RL} & Y_L \end{pmatrix}$$
$$P_R = \begin{pmatrix} r_{LR} & t_R & \alpha_{LR}^t \\ t_R & r_{RR} & \alpha_{RR}^t \\ -\alpha_{LR} & -\alpha_{RR} & Y_R \end{pmatrix} \tag{42}$$

These two matrices would be cascaded into a new matrix

$$P = \begin{pmatrix} r_L & t & \alpha_L^t \\ t & r_R & \alpha_R^t \\ -\alpha_L & -\alpha_R & Y_A \end{pmatrix} \tag{43}$$

The components of the new matrix can be computed as follows

$$r_L = r_{LL} + \frac{r_{LR}\, t_L^2}{\Delta_r}$$

$$r_R = r_{RR} + \frac{r_{RL}\, t_R^2}{\Delta_r}$$

$$t = \frac{t_L\, t_R}{\Delta_r}$$

$$\alpha_L = \begin{pmatrix} \alpha_{LL} + \dfrac{t_L\, r_{LR}}{\Delta_r}\, \alpha_{RL} \\ \dfrac{t_L}{\Delta_r}\, \alpha_{LR} \end{pmatrix}$$

$$\alpha_R = \begin{pmatrix} \dfrac{t_R}{\Delta_r}\, \alpha_{RL} \\ \alpha_{RR} + \dfrac{t_R\, r_{RL}}{\Delta_r}\, \alpha_{LR} \end{pmatrix} \tag{44}$$

$$Y_A = \begin{pmatrix} Y_L - \dfrac{r_{LR}}{\Delta_r}\, \alpha_{RL}\alpha_{RL}^t & -\dfrac{1}{\Delta_r}\, \alpha_{RL}\alpha_{LR}^t \\ -\dfrac{1}{\Delta_r}\, \alpha_{LR}\alpha_{RL}^t & Y_R - \dfrac{r_{RL}}{\Delta_r}\, \alpha_{LR}\alpha_{LR}^t \end{pmatrix}$$

$$with\ \Delta_r = 1 - r_{LR}r_{RL}$$
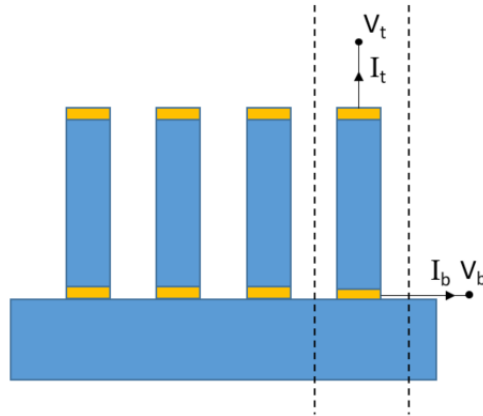
2. P-Matrix for Hybrid SAW/BAW resonators

Figure 194: schematic of a hybrid SAW/BAW resonators, with illustration of a unit cell with two electrical ports

A typical hybrid SAW/BAW device is sketched in Figure 194. The unit cell for such a structure is a single transducer, which has two separate electrodes. Consequently, instead of dealing with just one voltage and one current as in SAW devices where the unit cell is a single electrode, the analysis necessitates here handling two electric potentials, V_t and V_b for the top and bottom electrodes respectively, as well as two corresponding currents (I_t and I_b). The system can thus theoretically have 2n different ports where n is the number of transducers each having a separate voltage and current.

We make the assumption that the piezoelectric excitation only results from potential difference $(V_t - V_b)$ applied between the two electrodes of the transducer. This means we neglect the influence of the electrostatic coupling between adjacent transducers, such as the one revealed by Figure 49, on the piezoelectric excitation. We similarly assume that only a single current $I = I_t = -I_b$ flows through each pillar. This is motivated by the current considered in the P-matrix results only from the acoustic contribution. Electrostatic couplings between the transducers may be considered in the Yc contribution that is not considered directly in the P-matrix model.

The classic P-matrix previously introduced thus writes for a single transducer

$$\begin{pmatrix} b_L \\ b_R \\ I \end{pmatrix} = \begin{pmatrix} r_L & t_{RL} & \alpha_L \\ t_{LR} & r_R & \alpha_R \\ -\alpha_L & -\alpha_R & Y_A \end{pmatrix} \begin{pmatrix} a_L \\ a_R \\ V_t - V_b \end{pmatrix} \tag{45}$$

To allow for possible independent top and bottom potentials, we expand the matrix elements without introducing any new parameters.

$$\begin{pmatrix} b_L \\ b_R \\ I_t \\ I_b \end{pmatrix} = \begin{pmatrix} r_L & t_{RL} & \alpha_L & -\alpha_L \\ t_{LR} & r_R & \alpha_R & -\alpha_R \\ -\alpha_L & -\alpha_R & Y_A & -Y_A \\ \alpha_L & \alpha_R & -Y_A & Y_A \end{pmatrix} \begin{pmatrix} a_L \\ a_R \\ V_t \\ V_b \end{pmatrix} \tag{46}$$
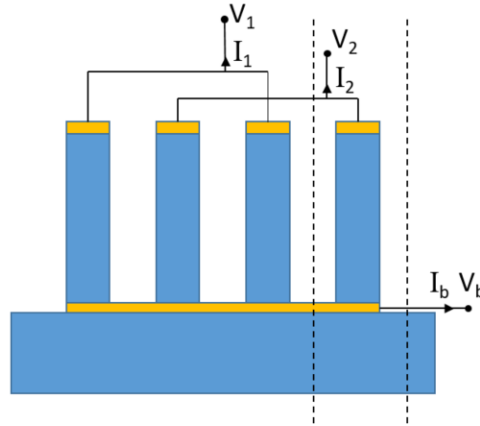
Figure 195: simplified diagram of a hybrid SAW/BAW resonators: alternating top ports with a common bottom port

Figure 195 displays HSBR with top electrodes forming sets of interdigitated electrodes and a bottom electrode common to all transducers. This means three ports are assumed:

$$V_{t,n} = \begin{cases} V_1 & \text{if n is even} \\ V_2 & \text{if is odd} \end{cases}, \tag{47}$$

while V_b is always the potential of the bottom electrode. It is possible for the individual unit P-matrix to be re-written in terms of all three potentials and all three currents although only one of the top two potentials is valid for each transducer. In this case, the parameter components of the $I_{1,n}$ are equal to 0 if n is even and the parameter components of the $I_{2,n}$ are equal to 0 if n is odd.

$$\begin{pmatrix} b_L \\ b_R \\ I_1 \\ I_2 \\ I_3 \end{pmatrix} = P \begin{pmatrix} a_L \\ a_R \\ V_1 \\ V_2 \\ V_3 \end{pmatrix} \tag{48}$$

$$P = \begin{cases} \begin{pmatrix} r_L & t & \alpha_L & 0 & -\alpha_L \\ t & r_R & \alpha_R & 0 & -\alpha_R \\ -\alpha_L & -\alpha_R & Y & 0 & -Y \\ 0 & 0 & 0 & 0 & 0 \\ \alpha_L & \alpha_R & -Y & 0 & Y \end{pmatrix} & \text{if n is even} \\ \begin{pmatrix} r_L & t & 0 & \alpha_L & -\alpha_L \\ t & r_R & 0 & \alpha_R & -\alpha_R \\ 0 & 0 & 0 & 0 & 0 \\ -\alpha_L & -\alpha_R & 0 & Y & -Y \\ \alpha_L & \alpha_R & 0 & -Y & Y \end{pmatrix} & \text{if n is odd} \end{cases} \tag{49}$$

Using these simplified P-matrices and the definition of the parameters from the previous section, an elementary P-matrix can be built for each transducer. These matrices are then cascaded iteratively:
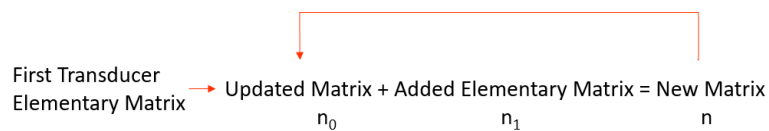
n_0 stands for initial matrix at each step, n_1 stands for the elementary matrix of the following transducer and n stands for the resulting general P-matrix representing n transducers.

If we start with transducer number 0 with P_{n_0}, an even-type elementary matrix is added as the updated matrix. Then the updated matrix P_{n_0} and the elementary matrix of the following transducer P_{n_1} are cascaded to build a new matrix. The resulting matrix P_n becomes the new updated matrix before another one is cascaded. To add a new transducer, we update $P_{n_0} = P_n$

$$P_n = \begin{pmatrix} r_{L,n} & t_n & \alpha_{L1,n} & \alpha_{L2,n} & \alpha_{L3,n} \\ t_n & r_{R,n} & \alpha_{R1,n} & \alpha_{R2,n} & \alpha_{R3,n} \\ -\alpha_{L1,n} & -\alpha_{R1,n} & Y_{11,n} & Y_{12,n} & Y_{13,n} \\ -\alpha_{L2,n} & -\alpha_{R1,n} & Y_{21,n} & Y_{22,n} & Y_{23,n} \\ -\alpha_{L3,n} & -\alpha_{R3,n} & Y_{31,n} & Y_{32,n} & Y_{33,n} \end{pmatrix} \tag{50}$$

1- The wave escaping section n_0 from the right is the wave entering section n_{0+1} in the left:
   $a_{L,n_{0+1}} = b_{R,n_0}$ (updated notation of cascading condition 1: Equation (40))
2- The wave escaping section n_{0+1} from the left is the wave entering section n_0 in the right:
   $a_{R,n_0} = b_{L,n_{0+1}}$ (updated notation of cascading condition 2: Equation (41))
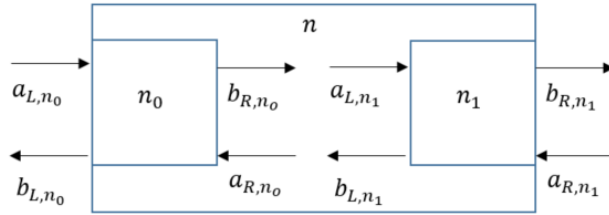

Figure 196: simplified visualization for conditions 1 and 2

In addition:

3- The voltages considered for each port are independent of the section considered (the same potential is applied to all electrodes connected to the same electric port)
4- The contribution from each cell to the current ports add up (the net current flowing through one port results from the sum of the currents flowing through each electrode connected to this port). The P_n matrix resulting from the cascading of matrices P_{n0} and P_{n1} therefore writes

$$\begin{pmatrix} b_{L,n_0} \\ b_{R,n_1} \\ I_{1,n} \\ I_{2,n} \\ I_{3,n} \end{pmatrix} = p_n \begin{pmatrix} a_{L,n_0} \\ a_{R,n_1} \\ V_1 \\ V_2 \\ V_3 \end{pmatrix} \tag{51}$$

From cascading condition 1:
$$\begin{aligned} b_{L,,n_1} &= r_{L,n_1} a_{L,n_1} + t_{n_1} a_{R,n_1} + \alpha_{L1,n_1} V_1 + \alpha_{L2,n_1} V_2 + \alpha_{L3,n_1} V_3 \\ &= r_{L,n_1} b_{R,n_0} + t_{n_1} a_{R,n_1} + \alpha_{L1,n_1} V_1 + \alpha_{L2,n_1} V_2 + \alpha_{L3,n_1} V_3 \\ &= r_{L,n_1} (t_{n_0} a_{L,n_0} + r_{R,n_0} a_{R,n_0} + \alpha_{R1,n_0} V_1 + \alpha_{R2,n_0} V_2 + \alpha_{R3,n_0} V_3) + \\ & t_{n_1} a_{R,n_1} + \alpha_{L1,n_1} V_1 + \alpha_{L2,n_1} V_2 + \alpha_{L3,n_1} V_3 \end{aligned} \tag{52}$$

Inserting condition 2:

$$
\begin{aligned}
b_{L,n_1} = a_{R,n_0} = \big(& r_{L,n_1} t_{n_0} a_{L,n_0} + t_{n_1} a_{R,n_1} + \big(r_{L,n_1}\alpha_{R1,n_0} + \alpha_{L1,n_1}\big)V_1 \\
& + \big(r_{L,n_1}\alpha_{R2,n_0} + \alpha_{L2,n_1}\big)V_2 + \big(r_{L,n_1}\alpha_{R3,n_0} + \alpha_{L3,n_1}\big)V_3 \big) \\
& /\big(1 - r_{L,n_1} r_{R,n_0}\big)
\end{aligned}
\tag{53}
$$

Similarly cascading condition 2 results in:

$$
\begin{aligned}
b_{R,n_1} &= t_{n_0} a_{L,n_0} + r_{R,n_0} a_{R,n_0} + \alpha_{R1,n_0} V_1 + \alpha_{R2,n_0} V_2 + \alpha_{R3,n_0} V_3 \\
&= t_{n_0} a_{L,n_0} + r_{R,n_0} b_{L,n_1} + \alpha_{R1,n_0} V_1 + \alpha_{R2,n_0} V_2 + \alpha_{R3,n_1} V_3 \\
&= t_{n_0} a_{L,n_0} + r_{R,n_0}\big(t_{n_1} a_{R,n_1} + r_{L,n_1} a_{L,n_1} + \alpha_{L1,n_1} V_1 + \alpha_{L2,n_1} V_2 + \alpha_{L3,n_1} V_3\big) \\
&\quad + \alpha_{R1,n_0} V_1 + \alpha_{R2,n_0} V_2 + \alpha_{R3,n_0} V_3
\end{aligned}
\tag{54}
$$

Inserting cascading condition 1:

$$
\begin{aligned}
a_{L,n_1} = b_{R,n_0} = \big(& t_{n_0} a_{L,n_0} + r_{R,n_0} t_{n_1} a_{R,n_1} + \big(r_{R,n_0}\alpha_{L1,n_1} + \alpha_{R1,n_0}\big)V_1 \\
& + \big(r_{R,n_0}\alpha_{L2,n_1} + \alpha_{R2,n_0}\big)V_2 + \big(r_{R,n_0}\alpha_{L3,n_1} + \alpha_{R3,n_0}\big)V_3 \big) \\
& /\big(1 - r_{R,n_0} r_{L,n_1}\big)
\end{aligned}
\tag{55}
$$

Using these expressions, the elements of the new p-matrix P_n can written

$$
b_{L,n_0} = r_{L,n_0} a_{L,n_0} + t_{n_0} a_{R,n_0} + \alpha_{L1,n_0} V_1 + \alpha_{L2,n_0} V_2 + \alpha_{L3,n_0} V_3
\tag{56}
$$

$$
\begin{aligned}
b_{L,n_0} = &\left(r_{L,n_o} + \frac{r_{L,n_1} t_{n_0}^2}{\big(1 - r_{L,n_1} r_{R,n_0}\big)}\right) a_{L,n_0} + \left(\frac{t_{n_0} t_{n_1}}{1 - r_{L,n_1} r_{R,n_0}}\right) a_{R,n_1} \\
& + \left(\alpha_{L1,n_0} + \frac{t_{n_0}\big(r_{L,n_1}\alpha_{R1,n_0} + \alpha_{L1,n_1}\big)}{\big(1 - r_{L,n_1} r_{R,n_0}\big)}\right) V_1 \\
& + \left(\alpha_{L2,n_0} + \frac{t_{n_0}\big(r_{L,n_1}\alpha_{R2,n_0} + \alpha_{L2,n_1}\big)}{\big(1 - r_{L,n_1} r_{R,n_0}\big)}\right) V_2 \\
& + \left(\alpha_{L3,n_0} + \frac{t_{n_0}\big(r_{L,n_1}\alpha_{R3,n_0} + \alpha_{L3,n_1}\big)}{\big(1 - r_{L,n_1} r_{R,n_0}\big)}\right) V_3
\end{aligned}
\tag{57}
$$

This allows us to identify:

- The new reflection coefficient on the left hand side:

$$
r_{L,n} = r_{L,n_0} + \frac{r_{L,n_1} + t_{n_o}^2}{\big(1 - r_{L,n_1} r_{R,n_0}\big)}
\tag{58}
$$

- The new transmission coefficient

$$
t_n = \frac{t_{n_0} t_{n_1}}{\big(1 - r_{L,n_1} r_{R,n_0}\big)}
\tag{59}
$$

- The new transduction vector on the left hand side:

$$\overrightarrow{\alpha_{L,n}} = \begin{pmatrix} \alpha_{L1,n} \\ \alpha_{L2,n} \\ \alpha_{L3,n} \end{pmatrix} = \begin{pmatrix} \alpha_{L1,n_0} \\ \alpha_{L2,n_0} \\ \alpha_{L3,n_0} \end{pmatrix} + \frac{t_{n_0} r_{L,n_1}}{(1 - r_{L,n_1} r_{R,n_0})} \begin{pmatrix} \alpha_{R1,n_0} \\ \alpha_{R2,n_0} \\ \alpha_{R3,n_0} \end{pmatrix} \\ + \frac{t_{n_0}}{(1 - r_{L,n_1} r_{R,n_0})} \begin{pmatrix} \alpha_{L1,n_1} \\ \alpha_{L2,,n_1} \\ \alpha_{L3,,n_1} \end{pmatrix}$$

(60)

While equations (58) and (59) are similar to equations (44), equation (60) is slightly modified compared to the generic P-matrix cascading. This is because we expressed the P-matrix is expressed for each individual cell as a function of the electrical ports instead of the electric potentials of each electrode considered individually.

Considering now the P-matrix of cell n_1 and writing the expression for b_{R,n_1}

$$b_{R,n_1} = t_{n_1} a_{L,n_1} + r_{R,n_1} a_{R,n_1} + \alpha_{R1,n_1} V_1 + \alpha_{R2,n_1} V_2 + \alpha_{R3,n_1} V_3$$

(61)

Equation (55) is inserted to eliminate a_{L,n_1}:

$$b_{R,n_1} = \left(\frac{t_{n_0} t_{n_1}}{(1 - r_{L,n_1} r_{R,n_0})} \right) a_{L,n_0} + \left(r_{R,n_1} + \frac{r_{R,n_0} t_{n_1}^2}{1 - r_{L,n_1} r_{R,n_0}} \right) a_{R,n_1} \\ + \left(\alpha_{R1,n_1} + \frac{t_{n_1} (r_{R,n_0} \alpha_{L1,n_1} + \alpha_{R1,n_0})}{(1 - r_{R,n_0} r_{L,n_1})} \right) V_1 \\ + \left(\alpha_{R2,n_1} + \frac{t_{n_1} (r_{R,n_0} \alpha_{L2,n_1} + \alpha_{R2,n_0})}{(1 - r_{L,n_1} r_{R,n_0})} \right) V_2 \\ + \left(\alpha_{R3,n_1} + \frac{t_{n_1} (r_{L,n_0} \alpha_{L3,n_1} + \alpha_{R3,n_0})}{(1 - r_{L,n_1} r_{R,n_0})} \right) V_3$$

(62)

The first term in this equation confirms the transmission coefficient given in Equation (59). The other terms give:

- The new reflection coefficient on the right hand side

$$r_{R,n} = r_{R,n_1} + \frac{r_{R,n_0} t_{n_1}^2}{(1 - r_{L,n_1} r_{R,n_0})}$$

(63)

- The new transduction vector on the right hand side:

$$\boldsymbol{\alpha_{R,n}} = \begin{pmatrix} \alpha_{R1,n} \\ \alpha_{R2,n} \\ \alpha_{R3,n} \end{pmatrix} = \begin{pmatrix} \alpha_{R1,n_1} \\ \alpha_{R2,n_1} \\ \alpha_{R3,n_1} \end{pmatrix} + \frac{t_{n_1} r_{R,n_0}}{(1 - r_{L,n_1} r_{R,n_0})} \begin{pmatrix} \alpha_{L1,n_1} \\ \alpha_{L2,n_1} \\ \alpha_{L3,n_1} \end{pmatrix} \\ + \frac{t_{n_1}}{(1 - r_{L,n_1} r_{R,n_0})} \begin{pmatrix} \alpha_{R1,n_0} \\ \alpha_{R2,,n_0} \\ \alpha_{R3,,n_0} \end{pmatrix}$$

(64)

Equation (63) is identical to the one provided in (44) but equation (64) is slightly modified to express directly the P-matrices as a function of the port voltages.

From condition on the currents above, the contributions of the two cells to the electrical port currents add up. Hence, the expression for the cumulated contribution of the two cells to the current of port i is written as

$$I_{i,n} = I_{i,n_0} + I_{i,n_1}$$

$$= -\alpha_{Li,n_0}a_{L,n_0} - \alpha_{Ri,n_0}a_{R,n_0} - \alpha_{Li,n_1}a_{L,n_1} - \alpha_{Ri,n_1}a_{R,n_1} + (Y_{i1,n_0} \quad (65)$$

$$+ Y_{i1,n_1)}V_1 + (Y_{i2,n_0} + Y_{i2,n_1})V_2 + (Y_{i3,n_0} + Y_{i3,n_1)}V_3$$

Inserting Equations (53) and (55) to eliminate $a_{R,n}$ and a_{L,n_1}:

$$
\begin{aligned}
I_{i,n} = & -\left(\alpha_{Li,n_0} + \frac{r_{L,n_1}t_{n_0}}{(1 - r_{L,n_1}r_{R,n_0})}\alpha_{Ri,n_0} + \frac{t_{n_0}}{(1 - r_{L,n_1}r_{R,n_0})}\alpha_{Li,n_1} \right) a_{L,n_0} \\
& -\left(\alpha_{Ri,n_1} + \frac{t_{n_1}}{(1 - r_{L,n_1}r_{R,n_0})}\alpha_{Ri,n_0} + \frac{r_{R,n_0}t_{n_1}}{(1 - r_{R,n_0}r_{L,n_1})}\alpha_{Li,n_1} \right) a_{R,n_1} \\
& +\left(Y_{i1,n_0} + Y_{i1,n_1} - \alpha_{Ri,n_0}\frac{r_{L,n_1}\alpha_{R1,n_0} + \alpha_{L1,n_1}}{(1 - r_{R,n_0}r_{L,n_1})} \right. \\
& \qquad \left. - \alpha_{Li,n_1}\frac{r_{R,n_0}\alpha_{L1,n_1} + \alpha_{R1,n_0}}{(1 - r_{R,n_0}r_{L,n_1})} \right) V_1 \\
& +\left(Y_{i2,n_0} + Y_{i2,n_1} - \alpha_{Ri,n_0}\frac{r_{L,n_1}\alpha_{R2,n_0} + \alpha_{L2,n_1}}{(1 - r_{L,n_0}r_{R,n_0})} \right. \\
& \qquad \left. - \alpha_{Li,n_1}\frac{r_{R,n_0}\alpha_{L2,n_1} + \alpha_{R2,n_0}}{(1 - r_{R,n_0}r_{L,n_1})} \right) V_2 \\
& +\left(Y_{i3,n_0} + Y_{i3,n_1} - \alpha_{Ri,n_0}\frac{r_{L,n_1}\alpha_{R3,n_0} + \alpha_{L3,n_1}}{(1 - r_{R,n_0}r_{L,n_1})} \right. \\
& \qquad \left. - \alpha_{Li,n_1}\frac{r_{R,n_0}\alpha_{L3,n_1} + \alpha_{R3,n_0}}{(1 - r_{R,n_0}r_{L,n_1})} \right) V_3
\end{aligned}
\quad (66)
$$

The first two terms of this equation confirm the new expressions of transduction given in Equation (60) and (64). The other terms make up the admittance matrix:

$$Y_n = \begin{pmatrix} Y_{11,n} & Y_{12,n} & Y_{13,n} \\ Y_{21,n} & Y_{22,n} & Y_{23,n} \\ Y_{31,n} & Y_{32,n} & Y_{33,n} \end{pmatrix}, \quad (67)$$

where the individual components write

$$
\begin{aligned}
Y_{ij,n} = & Y_{ij,n_0} + Y_{ij,n_1} - \frac{1}{(1 - r_{R,n_0}r_{L,n_1})}\left(\alpha_{Ri,n_0}\alpha_{Lj,n_1} + \alpha_{Li,n_1}\alpha_{Rj,n} \right) \\
& - \frac{r_{L,n_1}}{(1 - r_{R,n_0}r_{L,n_1})}\alpha_{Ri,n_0}\alpha_{Rj,n_0} \\
& - \frac{r_{R,n_0}}{(1 - r_{R,n_0}r_{L,n_1})}\alpha_{Li,n_0}\alpha_{Lj,n_0}
\end{aligned}
\quad (68)
$$

This equation is a modified version of the one provided in (44). Additionally, it is worth mentioning that equations (49) and (68) can be recursively employed to demonstrate the symmetry of the admittance submatrix within the P-matrix. As a result, only 6 out of the 9 elements of the matrix need to be calculated.

The final admittance $Y = Y_C + Y_A$ where Y_A is the acoustic admittance resulting from the cascading and Y_C is expressed as follows:

$$Y_C = \begin{pmatrix} jnC_0\omega & 0 & -jnC_0\omega \\ 0 & jmC_0\omega & -jmC_0\omega \\ -jmC_0\omega & -jmC_0\omega & j(n+m)C_0\omega \end{pmatrix}, \tag{69}$$

where n is the number of odd electrodes and m is the number of even electrodes, if one neglects the electrostatic couplings between adjacent transducers.

P-Matrix for HSB resonator with added reflectors

To prevent lateral leakage of waves out of a transducer, reflectors may be added on the left and right sides [61]. These reflectors consist in additional transducers which are, by analogy with reflector implementations for SAW devices, either short-circuited or left floating.

The modelling of the first case is shown in Figure 197. For the sake of simplicity, we consider that the reflectors have different ports connected to their electrodes. Each group of pillars can be represented by a P-matrix with three electrical ports. Figure 197 shows ports 1 through 9.
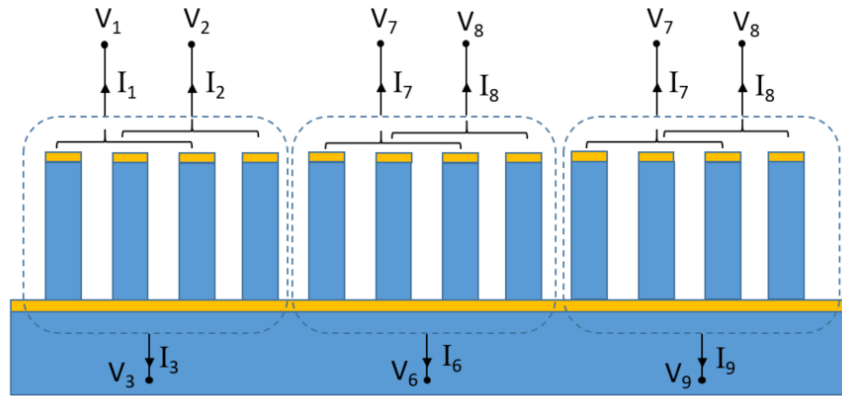

Figure 197: A schematic of HSBR with right and left reflectors

Under this assumption, each group is treated separately using an elementary P-matrix like in equation (49) and then cascading it over the number of fingers in the group using equations (58), (59), (60), (63), (64) and (68). This results in 3 P-matrices, each of size 5×5. Using the general cascading definitions from equations (44), the three matrices can be cascaded without losing generality by adding the ports to the matrix, and expanding it into 11×11.

For a P-matrix with 9 ports:

$$\begin{pmatrix} b_L \\ b_R \\ I_1 \\ \vdots \\ I_9 \end{pmatrix}_{11\times1} = \begin{pmatrix} r_L & t & \boldsymbol{\alpha_L^t} \\ t & r_R & \boldsymbol{\alpha_R^t} \\ -\boldsymbol{\alpha_L} & -\boldsymbol{\alpha_R} & \boldsymbol{Y_{9\times9}} \end{pmatrix}_{11\times11} \begin{pmatrix} a_L \\ a_R \\ V_1 \\ \vdots \\ V_9 \end{pmatrix}_{11\times1} \tag{70}$$

If the reflector electrodes are in a short-circuit, the top electrodes of the right and left reflectors are connected to the bottom electrode. A common potential then connects the three ports of the first group, the third port of the second group and the three ports of the third group. In turn, this common potential can be connected to ground, or left floating itself.

The electrical boundary conditions write therefore

- For short-circuited reflectors, with grounded bottom electrode:
  $V_C=V_1=V_2=V_3=V_6=V_7=V_8=V_9=0$

- For short-circuited reflectors, with floating bottom electrode: $V_C=V_1=V_2=V_3=V_6=V_7=V_8=V_9$, $I_C=0$

First, b_L is written as

$$b_L = r_L a_L + t a_R + \alpha_{L1} V_1 + \alpha_{L2} V_2 + \alpha_{L3} V_3 + \alpha_{L4} V_4 + \alpha_{L5} V_5 + \alpha_{L6} V_6 \\ + \alpha_{L7} V_7 + \alpha_{L8} V_8 + \alpha_{L9} V_9 \tag{71}$$

If $V_1 = V_2 = V_3 = V_6 = V_7 = V_8 = V_9 = V_C$`

$$b_L = r_L a_L + t a_R + (\alpha_{L1} + \alpha_{L2} + \alpha_{L3} + \alpha_{L6} + \alpha_{L7} + \alpha_{L8} + \alpha_{L9}) V_C \\ + \alpha_{L4} V_4 + \alpha_{L5} V_5 \tag{72}$$

Similarly

$$b_R = t a_L + r_R a_R + \left(\sum_{i\in\{1,2,3,6,7,8,9\}} \alpha_{Ri} \right) V_C + \alpha_{R4} V_4 + \alpha_{R5} V_5$$

$$I_j = -\alpha_{Lj} a_L - \alpha_{Rj} a_R + \left(\sum_{i\in\{1,2,3,6,7,8,9\}} Y_{ji} \right) V_C + Y_{j4} V_4 + Y_{j5} V_5 \tag{73}$$

The currents add up for all ports connected to the common port. The common port current can then be written as in the following expression:

$$I_C = I_1 + I_2 + I_3 + I_6 + I_7 + I_8 + I_9$$
$$I_C = -\left(\sum_{j\in\{1,2,3,6,7,8,9\}} \alpha_{Lj} \right) a_L - \left(\sum_{j\in\{1,2,3,6,7,8,9\}} \alpha_{Rj} \right) a_R$$
$$+ \left(\sum_{j\in\{1,2,3,6,7,8,9\}} \sum_{i\in\{1,2,3,6,7,8,9\}} Y_{ji} \right) V_c \tag{74}$$
$$+ \left(\sum_{j\in\{1,2,3,6,7,8,9\}} Y_{j4} \right) V_4 + \left(\sum_{j\in\{1,2,3,6,7,8,9\}} Y_{j5} \right) V_5$$

The result is a reduced P-matrix

$$\begin{pmatrix} b_L \\ b_R \\ I_4 \\ I_5 \\ I_C \end{pmatrix} = P_{5\times5} \begin{pmatrix} a_L \\ a_R \\ V_4 \\ V_5 \\ V_C \end{pmatrix} \tag{75}$$

If the common port is grounded i.e. $V_C = 0$, the P-matrix is directly reduced to 4×4 by removing the last row and column.

If the common port is floating, the expression

$$I_C = P_{5,1} a_L + P_{5,2} a_R + P_{5,3} V_4 + + P_{5,4} V_5 + P_{5,5} V_C = 0 \tag{76}$$

can be used and the elements may be reduced by substituting for V_C as follow:

$$b_L = P_{1,1}a_1 + P_{1,2}a_R + P_{1,3}V_4 + +P_{1,4}V_5$$

$$+ P_{1,5}\left(\frac{-1}{P_{5,5}}\left(P_{5,1}a_L + P_{5,2}a_R + P_{5,3}V_4 + P_{5,4}V_5\right)\right)$$

$$b_L = \left(P_{1,1} - \frac{P_{1,5} \cdot P_{5,1}}{P_{5,5}}\right)a_L + \left(P_{1,2} - \frac{P_{1,5} \cdot P_{5,2}}{P_{5,5}}\right)a_R + \left(P_{1,3} - \frac{P_{1,5} \cdot P_{5,3}}{P_{5,5}}\right)V_4 \qquad (77)$$

$$+ \left(P_{1,4} - \frac{P_{1,5} \cdot P_{5,4}}{P_{5,5}}\right)V_5$$

This can be repeated for b_R, I_4 and I_5. The P-matrix is reduced from 11×11 to 4×4

$$\begin{pmatrix} b_L \\ b_R \\ I_4 \\ I_5 \end{pmatrix} = P_{4\times4} \begin{pmatrix} a_L \\ a_R \\ V_4 \\ V_5 \end{pmatrix} \qquad (78)$$

We also consider two cases with open-circuit reflectors. In these devices, only the bottom electrode of the reflectors is connected to the bottom electrode of the active transducers. The top electrodes are always left floating. As in the previous case, the common bottom electrode can be either grounded or with floating potential.

The fact that each transducer has its top electrode floating makes the situation is a bit more complicated because the top electrodes of each group of reflectors are not interconnected: they don't share the same voltage. The assumption of Equation (47) is therefore no longer valid. Accordingly, each pillar has to have its own two ports on top and bottom as shown in Figure 198.
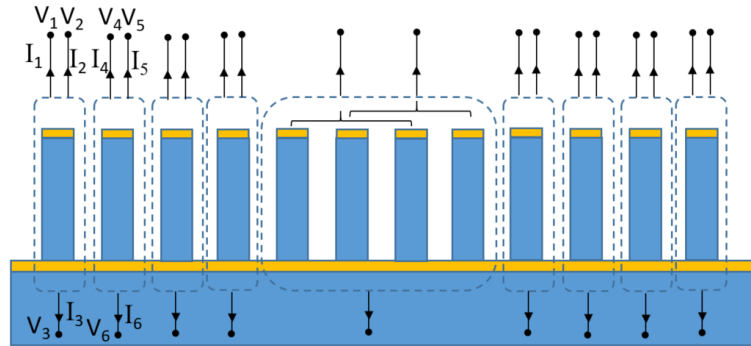

Figure 198: A schematic of HSBR with right and left reflectors; for an open-circuit reflectors, each pillar has its own top and bottom ports

An elementary P-matrix built as in Equation (49) for the first reflector pillar with two top ports can still be used since it assumes that one voltage is active and the other has zero current. When cascading this matrix with the following reflector pillar using general cascading of Equation (44), an 8×8 matrix of only two pillars is observed.

Clearly, this approach cannot be extended to a larger number of electrode pillars as the size of the matrix becomes computationally challenging. But we can use the following equalities to reduce the matrix size.

- $I_1 = I_2 = I_4 = I_5 = \cdots = 0$: by expanding each current expression, solving for an expression for its respective V and substituting, the P-matrix is reduced to 4×4. This is the same process as in Equation (76) and (77)
- $V_3 = V_6 = V_c$: the bottom voltages are always connected to a common port.

$$\begin{pmatrix} b_L \\ b_R \\ I_C \end{pmatrix} = P_{3\times3} \begin{pmatrix} a_L \\ a_R \\ I_C \end{pmatrix} \tag{79}$$

- This can be continued for all reflector pillars without changing the matrix size.

The final P-matrix after cascading all the left reflectors, the matrix of the active part, and the right hand reflectors all have a 5×5 size identical to Equation (75). This can be reduced further by considering whether the bottom electrode is floating $I_C = 0$ or grounded $V_C=0$

3. Parameters fitting

After having exposed the adaptation of a P-matrix method to hybrid SAW/BAW resonators, the next step before exploiting this model is to determine parameters for it. We now compare this mathematical formulation to our experimental electric findings to conclude the system parameters. The previously presented mathematical formulation is embedded using a Python script and the resulting admittance plotted. The following geometrical and wave parameters define the P-matrix and the admittance response. We attempt here to estimate them by finite element simulations. These parameters will be later validated on the basis of experimental data in chapter 3.

The parameters needed for a P-matrix model include some design parameters describing the 1-dimensional geometry considered:

1- p: the periodicity of the transducers,
2- w: the acoustic aperture,
3- The number of transducers and the respective connections of their electrodes

They also include some propagation parameters for the mode considered:

4- C_o: the static capacitance per electrode. The evaluation of this parameter requires simulating a reference structure with an arbitrary (small) number of electrodes and estimating its static capacitance from its admittance response far from the resonance.
5- V: the wave velocity
6- Δ: the arcsine of the reflection coefficient for the mode of interest when it is incident to a transducer.

V and Δ are evaluated by calculating the extent of the stop band for the mode of interest in the transducers grating, as is usually done for SAW devices [177]. Within this stop band, the reflection induced by the transducers prevents the mode from being able to propagate if the array is infinite. This frequency band is delimited on one side by the resonance corresponding to the pseudo-SAW or the pseudo-BAW mode, and on the other hand by another branch of this same mode, which is usually shifted by a quarter wavelength. Hence, while for example the maximum displacement is localized at the level of the transducers on one end of the stop band, they will be localized in-between the transducers for the mode at the exit of the stop band. An example illustrating these two modes for the case of the pseudo-SAW mode is shown Figure 199. Once the edges of the stop band (f1 and f2) are localized, the velocity and the reflection coefficient are determined by [177]:
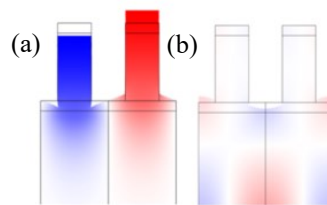

Figure 199: Representation of the mode shape of the pseudo-SAW mode at the entrance (f = 1.18 GHz) (a) and at the exit (f = 2.52 GHz) (b) of its stop-band.

- $V = p(f_2 + f_1)$
- $\Delta = \pi \left| \frac{f_2 - f_1}{f_2 + f_1} \right|$

For the example of Figure 70, the estimated wave velocity is 3700 m/s. This is not to be mixed with the *effective wave velocities* ($V = 2pf_1$) which were considered in the analysis of section 2,

and which are lower. For the same example, we obtain Δ=1.13, hence a reflection coefficient of 90%. It must be noted that the exit of the stop band lies above the sound line. A modal analysis therefore introduces many similar modes in the same frequency region, among which it is relatively difficult to identify the one of interest, what leads to some uncertainty in the evaluation of the wave velocity and the reflection coefficient. Even with some uncertainties, the later is considerably higher than what is usually encountered for SAW devices, where the reflection coefficients are usually only in the order of a small percentage [177]. This can be understood from the fact that a relatively thick piezoelectric pillar represents a noticeable obstacle to the propagation of the wave, compared to a simple thin electrode. The second reason is that the transducers store a large quantity of acoustic power which remains trapped in these structure, with little lateral power flow.

The other parameters required by the model are:

7- G: the radiation conductance. This parameter is determined through the fitting of either a simulated finite size structure response, like the static capacitance, or through the fitting of experimental data.

8- α: the wave attenuation is calculated either from the damping of the mode of interest calculated from a modal analysis, or from the quality factor of the corresponding contribution to the harmonic admittance. Eventually, it is also obtained by fitting of the response of a simulated finite size structure, or of experimental data.

9- δ: directivity. In practical cases, we considered this value as 0, since only the mode at the entrance of the stop band appeared clearly on the harmonic admittance calculations [177].

10- ψ_r: offset between reflection and transduction centers. Since we consider symmetric unit cells (centered around a transducer), we could leave this para   meter to 0.

The result of an attempt of parameters fitting is tabulated below and plotted in Figure 200. While the two lines in Figure 200 are comparable, there is clearly room for improvement and better matching. The agreement of the two lines include the frequencies of the peaks and the frequency width at half maximum of these peaks which allows to compute the quality factor.

Table 16: the final parameters fitted to the experimental device response (for the pseudo-SAW mode on h/p=1, a/p=0.5, open-circuited reflectors and floating bottom potential, 80 Electrodes, aperture of 40λ, no SiO₂)

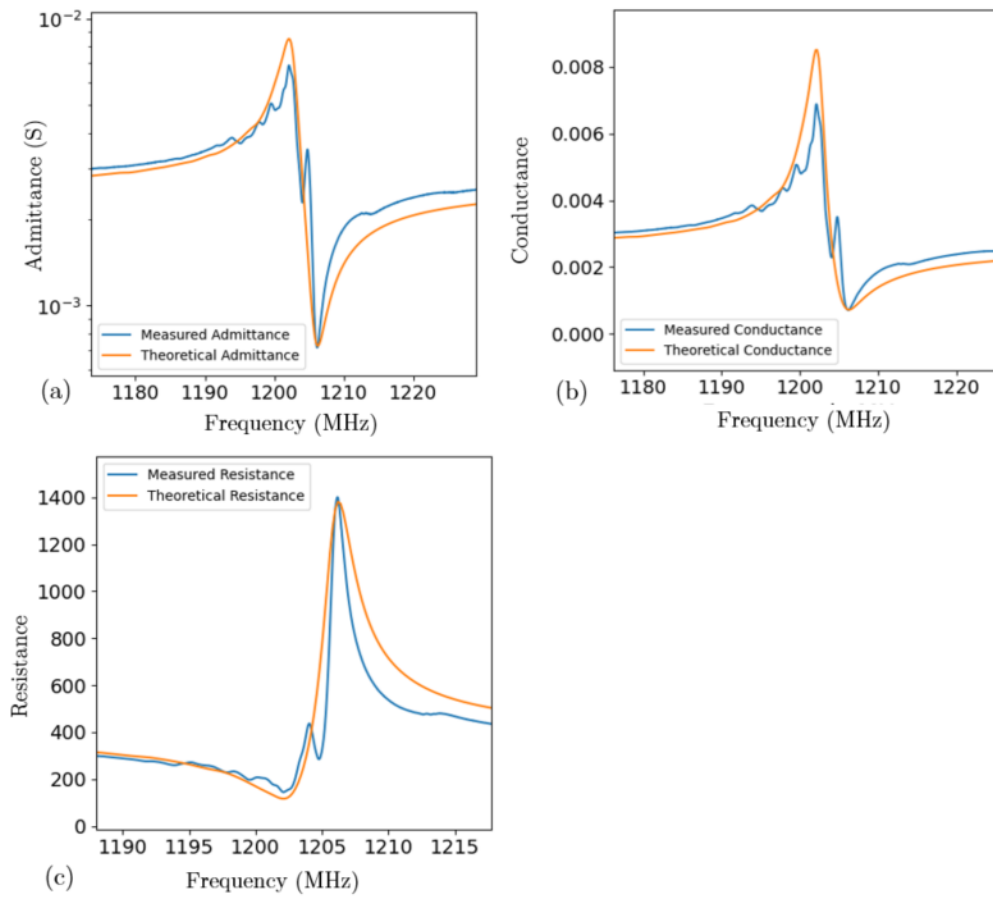| Parameter	value	unit
P	1	μm
w	80	μm
No Reflectors	30	
No Active Pillars	80	
C_0/w	205	pF/m
V	3756	m/s
Δ	1.13	
G/w	0.024	
α	0.05	dB/lambda
δ	1.1	
ψ_r	0	

Figure 200: P-matrix theoretical admittance (a), theoretical conductance (b) and theoretical resistance (c) fitted against measured response of the corresponding device.

Appendix D   Thickness Characterization Maps

Multiple values related to thicknesses of different layers were reported during the fabrication of devices in Chapter 3. Deposition thicknesses are never completely uniform and usually have a gradient. This appendix contains more characterization results completed during the course of the two rounds of fabrications described in chapter 3 in specific the optical reflectometry and the square resistance measurements translated into thickness profiles.

One common and straightforward technique for evaluating the thickness of thin films is square resistance measurements. This method involves the assessment of the resistance of a thin film, which is directly related to its thickness and electrical properties. By measuring the voltage across a thin film, the thickness can be deduced, assuming knowledge of the film's resistivity. Reflectometry is another powerful technique used to determine the thickness of thin films and is based on the interference in white light that is observed in correspondence with the reflection on thin films. Square resistance is suited for conductive materials such as Mo and reflectometry is better suited for non-conductive materials.

Figure 201 shows the SiO_2 profile on the surface of a wafer with a targeted 700 nm thickness. A step for smoothing of the surface is needed after the deposition of the SiO_2 to achieve the proper thickness.
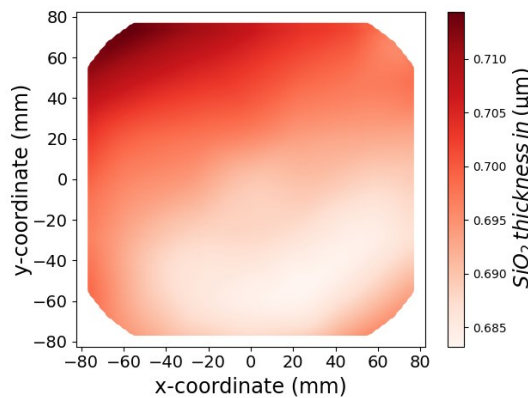

Figure 201: Thickness profiles of SiO_2 after smoothing.

Figure 202 shows the thickness measurements of the Mo after the deposition of the bottom electrode. The black dots shows the location of the square resistance measurements and the colors represent the fitted thickness map.
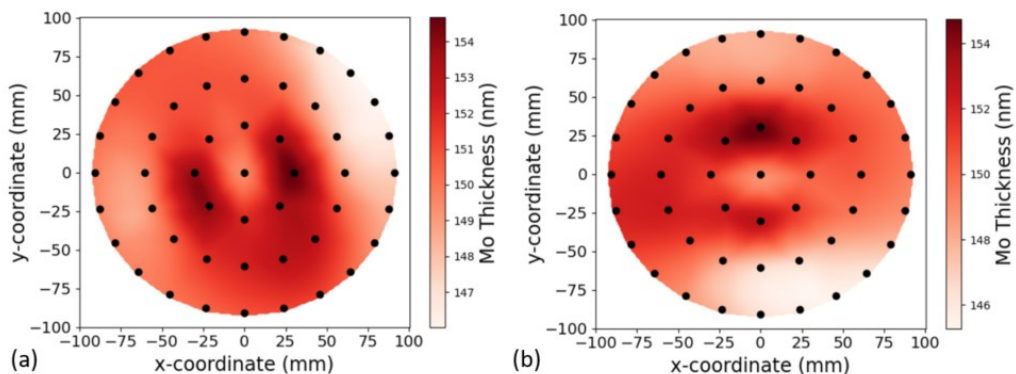
Figure 202: thickness measurements of the Mo bottom electrode on wafers with SiO$_2$ (a) and without SiO$_2$ (b).

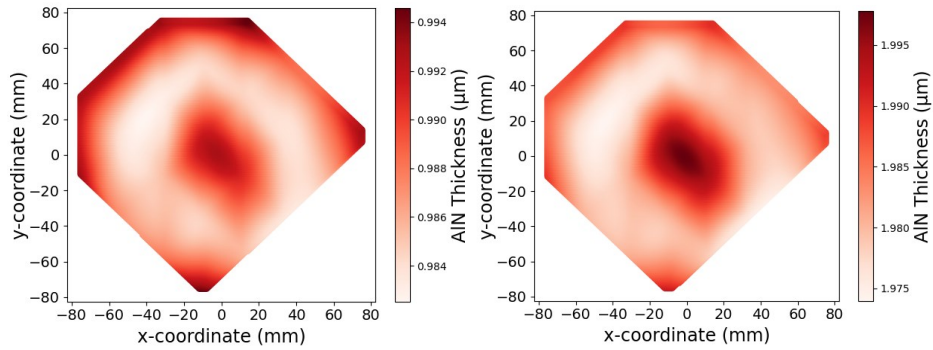Figure 203 shows the thickness measurements of the AlN after deposition for 1 and 2 μm AlN thicknesses.

Figure 203: Thickness profiles of AlN over the area of the wafer for wafer with 1 µm AlN (a) and wafer with 2 µm of AlN (b).

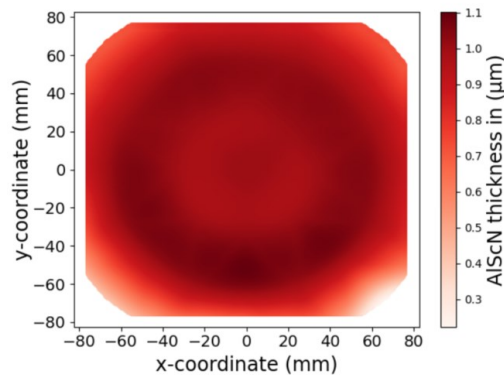Figure 204 shows the thickness map of 1 μm of AlScN after deposition

Figure 204: Characterization of AlScN films by optical reflectometry

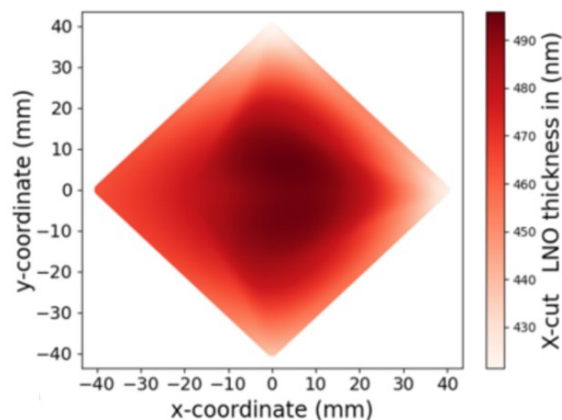Figure 205 shows thickness map of the LNO after transfer and planarization.

Figure 205: thickness profile of the LNO film over the area for different LNO orientations